Aerodynamic Performance and Particle Image Velocimetery of Piezo Actuated Biomimetic Manduca Sexta Engineered Wings Towards the Design and Application of a Flapping Wing Flight Vehicle

DISSERTATION

Anthony M. DeLuca, Lieutenant Colonel, USAF

AFIT-ENY-DS-13-D-01

DEPARTMENT OF THE AIR FORCE
AIR UNIVERSITY

AIR FORCE INSTITUTE OF TECHNOLOGY

Wright-Patterson Air Force Base, Ohio

DISTRIBUTION A: APPROVED FOR PUBLIC RELEASE; DISTRIBUTION

UNLIMITED

AFIT-ENY-DS-13-D-01

Aerodynamic Performance and Particle Image Velocimetery of Piezo Actuated Biomimetic Manduca Sexta Engineered Wings Towards the Design and Application of a Flapping Wing Flight Vehicle

DISSERTATION

Presented to the Faculty

Graduate School of Engineering and Management

Air Force Institute of Technology

Air University

Air Education and Training Command

in Partial Fulfillment of the Requirements for the

Degree of Doctor of Philosophy

Anthony M. DeLuca, BS, MBA, MS

Lieutenant Colonel, USAF

December 2013

AFIT-ENY-DS-13-D-01

Aerodynamic Performance and Particle Image Velocimetery of Piezo Actuated Biomimetic Manduca Sexta Engineered Wings Towards the Design and Application of a Flapping Wing Flight Vehicle

Anthony M. DeLuca, BS, MBA, MS
Lieutenant Colonel, USAF

Approved:

_____   _____
Mark F. Reeder, PhD   Date
Chairman

_____   _____
Richard G. Cobb, PhD   Date
Member

_____   _____
Captain Kevin R. Pond, PhD   Date
Member

Accepted:

_____   _____
HEIDI R. RIES, PhD   Date
Interim Dean, Graduate School of Engineering
  and Management

I dedicate this manuscript to my loving family. My wife has spent more days and nights than reasonable alone allowing me to focus on studying and working towards this, and my previous AFIT degree. She has borne the heaviest burden, and it has undoubtedly taken an unfair toll on her and 'us' collectively; however, she has remained steadfast in her support, and has done a prodigious job running our household to free me from intractable encumbrance while pursuing this achievement. I am eternally grateful for her beauty and patience in allowing me to pursue my dreams, and spread my intellectual wings, without which, I am confident all that is after would not be possible. She will surely never fully understand the depth of the love and admiration I hold for her. For my one and only son, who embodies the very best of all that I am, I hope this endeavor inspires in him confidence and motivation that through Christ, ordinary people can accomplish extraordinary feats.

The Spirit of the Bayonet—Always Forward, Never Back.

Beat Navy!

Acknowledgments

Preface

The pursuit of manned flight dates back millennia to early Chinese records of tethered kite flights, and crude, lighter-than-air containment vessels. Leonardo Da Vinci's 15th century fanciful human powered ornithopter was one of the earliest records documenting the intersection of the dream of flight, and the requisite scientific query into the mechanics of flight. Da Vinci's inquisition into flight inspired more than a century of rigorous scientific and mathematical exploration into the atmosphere, and the mechanics of flight, led by Newton's extensive development of the mathematical constructs necessary to quantify, and explain his seminal work in establishing the laws of classical mechanics—the foundation of aerodynamic principles.

As man took to the skies in the early part of the 20th century, the field of aerodynamics produced an immense amount of scientific research, and made considerable contributions to our practical understanding of the interaction between the atmosphere and moving machines. Great engineers and scientists like Prandtl, von Kármán, Schlichting, von Braun, Theodorsen, Timenshenko, Rutan and countless others, dedicated their lives investigating varying aspects of the science and phenomenology behind the physics of the action and reaction between man-made machines and fluid mediums. Their research spanned from very slow, laminar flow fields, where viscous forces predominate the flow physics; to supersonic flow fields, whose velocities surpass the dynamic speed of sound, and are dominated by the inertial forces of the flow field, which are primarily defined by turbulent properties; and finally to hypersonic flows, with velocities of such considerable magnitude, their flow physics are no longer governed by the same underlying assumptions about the fluid properties, which are utilized in traditional aerodynamic analysis.

However, with all the remarkable discoveries, and the litany of impressive military and civilian aircraft developed over the past 100 years, it was not until the

last two decades that aerodynamicists have earnestly investigated the flight physics of nature's smallest fliers—*insects*. To borrow an old colloquialism, *necessity is the mother of invention*, and heretofore, the civilian and military market demanded—*bigger, faster, farther*—from the aeronautics industry, not—*smaller, slower, lighter*. As with life, military objectives notwithstanding, all things change, and so has the demands on military strategic and tactical intelligence. Human Rights watchdog groups conspicuously monitor military action, forcing the current political climate to demand accurate, and real-time intelligence, and flawless precision attack, which minimizes, if not completely eliminates collateral damage, and guarantees first strike success. These particular demands have refocused the efforts of researchers to study the flight physics of birds and insects. Flapping flight provides a coupled relationship between the lifting surfaces, guidance and control, thrust generation, and power supply, in addition to providing the unique capability to 'hide in plain sight', a requirement to enable such vehicles to provide the level of precision attack, and intelligence fidelity necessary to meet an evolving military mission.

A confluence between biologists and engineers over the past 10–20 years have produced considerable research into the aerodynamics and flight mechanisms responsible for insect flight. Research, mainly from biologists, has revealed these amazing fliers generate more lift than their wings alone can produce if held *static*, meaning the additional lift is generated through the flapping motion of the wings themselves. It is the study of this aerodynamic phenomenon, its characterization, and its particular application to the Air Force Institute of Technology (AFIT), Flapping Wing Micro Air Vehicle (FWMAV) program, which is the topic of this research effort—to aid in the design, modeling, and ultimately, fabrication of a full-scale flight vehicle.

AFIT-ENY-DS-13-D-01

Abstract

Considerable research and investigation has been conducted on the aerodynamic performance, and the predominate flow physics of the *Manduca Sexta* size of biomimetically designed and fabricated wings as part of the AFIT FWMAV design project. Despite a burgeoning interest and research into the diverse field of flapping wing flight and biomimicry, the aerodynamics of flapping wing flight remains a nebulous field of science with considerable variance into the theoretical abstractions surrounding aerodynamic mechanisms responsible for aerial performance. Traditional FWMAV flight models assume a form of a quasi-steady approximation of wing aerodynamics based on an infinite wing blade element model (BEM). An accurate estimation of the lift, drag, and side force coefficients is a critical component of autonomous stability and control models. This research focused on two separate experimental avenues into the aerodynamics of AFIT's engineered hawkmoth wings—forces and flow visualization.

1. Six degree of freedom force balance testing, and high speed video analysis was conducted on 30°, 45°, and 60° angle stop wings. A novel, non-intrusive optical tracking algorithm was developed utilizing a combination of a Gaussian Mixture Model (GMM) and ComputerVision (OpenCV) tools to track the wing in motion from multiple cameras. A complete mapping of the wing's kinematic angles as a function of driving amplitude was performed. The stroke angle, elevation angle, and angle of attack were tabulated for all three wings at driving amplitudes ranging from A=0.3 to A=0.6. The wing kinematics together with the force balance data was used to develop several aerodynamic force coefficient models. A combined translational and rotational aerodynamic model predicted lift forces within 10%, and vertical forces within 6%. The total power consumption was calculated for each of the three wings,

and a Figure of Merit was calculated for each wing as a general expression of the overall efficiency of the wing. The 60° angle stop wing achieved the largest total stroke angle and generated the most lift for the lowest power consumption of the wings tested.

2. Phase averaged stereo Particle Image Velocimetry (PIV) data was collected at eight phases through the flap cycle on the 30°, 45°, and 60° angle stop wings. Wings were mounted transverse and parallel to the interrogating laser sheet, and planar velocity intersections at the wing mid-span, one chord below the wing, were compared to one another to verify data fidelity. A Rankine-Froude actuator disk model was adapted to calculate the approximate vertical thrust generated from the total momentum flux through the flapping semi-disk using the velocity field measurements. Three component stereo u, v, and w-velocity contour measurements confirmed the presence of extensive vortical structures in the vicinity of the wing. The leading edge vortex was successfully tracked through the stroke cycle appearing at approximately 25% span, increasing in circulatory strength and translational velocity down the span toward the tip, and dissipating just after 75% span. Thrust calculations showed the vertically mounted wing more accurately represented the vertical forces when compared to its corresponding force balance measurement than the horizontally mounted wing. The mid-span showed the highest vertical velocity profile below the wing; and hence, was the location responsible for the majority of lift production along the span.

Table of Contents

List of Figures

xiv

xvi

List of Tables

List of Symbols

Symbol   Page

List of Abbreviations

Aerodynamic Performance and Particle Image Velocimetery of Piezo Actuated Biomimetic Manduca Sexta Engineered Wings Towards the Design and Application of a Flapping Wing Flight Vehicle

I. Introduction

KNOWLEDGE is of little ufe, when confined to mere fpeculation: But when fpeculative truths are reduced to practice, when theories, grounded upon experiments, are applied to the common purpofes of life; and when, by thefe, agriculture is improved, trade enlarged, the arts of living made more eafy and comfortable, and, of courfe, the increafe and happinefs of mankind promoted; knowledge then becomes really ufeful. That this Society, therefore, may, in fome degree, anfwer the ends of its inftitution, the members propofe to confine their difquifitions, principally, to fuch fubjects as tend to the improvement of their country, and advancement of its intereft and profperity.

1.1 Overview

IN 1945, Theodore von Kármán recommended to General Hap Arnold in the 1st Army Air Force (AAF) Scientific Advisory Board report, *Toward New Horizons–Science, The Key to Air Supremacy*, that "only a constant inquisitive attitude toward science and a ceaseless and swift adaptation to new developments can maintain the security of this nation" [48]. That commitment to technological superiority, and its practical application was the fundamental commission and guidepost Benjamin Franklin gave to the first *Transactions Of The American Philosphical Society* in 1769

[40]; and it has served the United States Air Force well over the intervening decades. Today, a vigorous and properly focused science and technology program remains absolutely essential to advancing the capabilities the Air Force will need to fulfill its expanding and evolving mission areas, especially in the arena of bio-inspired Flapping Wing Micro Air Vehicles (FWMAV). This chapter will introduce the topic of small flight vehicles, provide some historical context concerning the origins of unmanned flight in the military, which naturally transitions into the genesis of why the military is interested, and therefore, supports its research; and will conclude with some introductory programmatics for the remainder of this research effort, which are expanded upon in subsequent chapters.

1.2 Motivation

The small speck in the sky approaches in virtual silence, unnoticed by the large gathering of soldiers below. In flight, its tiny size and considerable agility evade all but happenstance recognition. After hovering for a few short seconds, it perches on a fifth floor windowsill, observing the flow of men and machines on the streets below. Several kilometers away, the platoon leader watches the action on his wrist monitor. He sees his target and sends the signal. The tiny craft swoops down on the vehicle, alighting momentarily on the roof. It senses the trace of a suspected chemical agent and deploys a small tagging device, attaching it to the vehicle. Just seconds later it is back in the sky, vanishing down a narrow alley. Mission accomplished ... [58]

The above scenario, cited by Lieutenant Colonel Arthur Huber in Air War College (AWC) Occasional Paper No. 29, published by the Center for Strategy and Technology in 2002, encapsulates the excitement and fervor surrounding Micro Air Vehicles (MAVs) at the beginning of this millennium [44]. The anticipation of swarms of small, Unmanned Air Vehicles (UAVs), conducting a litany of military enterprise missions—on-time, targeted, reconnaissance and surveillance; tracking Persons of In-

terest (PoI); Battle Damage Assessment (BDA) in denied or otherwise austere and unfriendly confines; targeted assignations or material attacks, designed to minimize collateral human or property damages; and any other host of missions the tactical commander could envision for this promising technological scepter, was an intoxicating precept for strategic thinkers and future planners at capstone flag officer conferences like *Corona*. These are the places where 10, 20, and 50 year strategic plans are envisioned, the ideas planted, and the precepts proposed to the greater global military audience, and in a sense, the public at large, for the next generation of airmen— it is where ideas like the 'tractor beam' and 'weaponized flying insects' are transformed from science fiction, to actionable acquisition research.

The excitement was echoed and championed by Department of Defense (DoD) long range strategic planners, and captured in documents like *Joint Vision 2020*; however, there was a rift between the technological outlook for the roles MAVs were aspiring *to*, and the vision tactical commanders were inspired to use MAVs *for*, and thus, the prominent guiding Air Force doctrine documents, *AFDD1– Air Force Basic Doctrine*, did not stipulate MAV missions, nor their accompanying training, tactics, and techniques, but rather referenced MAVs as functions, or force multipliers; essentially another 'tool' at a commanders disposal to execute their primary objective [44]. As a result, potential military operationalization of MAVs on the battlefields of tomorrow began as a 'technological push'—*an answer in search of a question*— with little tangible 'requirements pull' from the operational war fighting community. A gross simplification of the military acquisition system: war fighters codify operational needs at the tactical level, those needs (or deficiencies) are translated into well defined technical requirements by a flag officer requirements group compromised of representatives from the acquisition, research, production, logistics, and operational disciplines, then the Science and Technology (S&T) community develops technical so-

lutions to meet the requirements within a specified budget and time constraint, and finally the war fighter community develops an appropriate CONcept of OPerations (CONOPS) to employ the technological answer to their original need. Accordingly, CONOPS deriving from the war fighting community were virtually nonexistent because the need, which would specifically, and identically be satisfied by MAVs, had not been identified heretofore. At a higher level; however, strategists and engineers envisioned a new set of military missions MAVs, rightly sized and sufficiently equipped, were uniquely qualified to execute, revealing new possibilities in the formulation of military strategies, which have driven intense scientific investigation and technical research [45]. The prevailing wisdom, fueling and supporting this leading edge research has been, *if we can build it, they will come.*

The forerunner of these technical inquiries can be traced back to the early 1990's from studies such as RAND Corporation's investigation into Microsystems [10], and the Massachusetts Institute of Technology (MIT), Lincoln Laboratory's early investigations of micro flyers [17], cited numerous times by the Joint Chiefs of Staff, *Joint Vision 2020*, which laid the ground work for a Defense Advanced Research Project Agency (DARPA) technical report entitled, *Micro Air Vehicles—Toward a New Dimension in Flight* [58]. The excitement and anticipation about the future role of MAVs initially proposed by these strategic 'think-tank' centers' reports formed the genesis of two RAND workshops in the early–1990's to study the technical feasibility of MAVs in military applications. As a corollary to the RAND seminars, Lincoln Laboratory conducted rigorous technical prototype analyses of the feasibility of MAVs in military applications, and developed a conceptual design and presented it to then Vice Chairman of the Joint Chiefs of Staff, Admiral William Owens. Admiral Owens was sufficiently impressed with Lincoln Lab's concept vehicle, that he ordered DoD researchers to continue pursuing technical solutions, which ultimately laid the foun-

dation for a four year, $35M DARPA program to fund investigation and Research and Development (R&D) into 'weaponizing' this new dimension of flight [44]. DARPA's vision was then to develop and field a MAV capable of providing direct support to the soldier on the ground, and hence their program set forth the following initial vehicle parameters [58]:

- A dimensional limit of 15cm in length, width, and height

- A nominal vehicle weight of 50g *(10g min / 100g max)*

- A useful payload weight of 20g

- A nominal endurance of 40 minutes *(20 minutes min / 60 minutes desired)*

- A operating range out to 10km

- A nominal cruising speed of between 15m/s *(10m/s min / 20m/s desired)*

- A unit production cost of $5,000 *(near term)* down to $1,000 *(far term)*

The ultimate goals are thus:

- ***increase*** battle space awareness

- ***decrease*** the lag in OODA loop (Observe, Orient, Decide, and Act) outcomes

- ***reduce*** real-time mission decision cycle times

Several promising prototype designs and candidate vehicles were developed during this first fully funded government MAV R&D program. The U.S. Joint Special Operations Command (JSOC), were the first suitors to postulate a tangible, visceral operational need for an operational MAV, and in 1998 submitted the "first operational requirements document for a MAV" to the Joint Requirements Oversight Council (JROC) [44]. Therefore, MAVs are then an extension of information assurance or information denial, by means of collecting information, using the appropriate mixture of on-board sensors, communications, and relay infrastructure; or denying our

adversarys access to information by precisely and accurately employing counter communications, relay, or sensor equipment against a time sensitive target—via jamming or destruction. To the extent MAVs contribute favorably to these goals, compared to the analysis of alternatives, buttressed against the immutable trend towards antiseptic, asymmetric warfare, their appeal, and in some instances, necessity, in military contexts, has been firmly entrenched in this generation's war fighters. To that end, Air Force leadership fully supports the Joint Staff's vision of the role MAVs have in our future military-industrial complex. In *America's Air Force Vision 2020*, the Air Force leadership stipulates the following technological paradigm movement:

> *[W]e'll provide the ability to find, fix, assess, track, target and engage anything of military significance, anywhere . . . Information superiority will be a vital enabler of that capability . . . Capitalizing more fully on a set of revolutionary technologies—like stealth, advanced airborne and spaceborne sensors and highly precise all-weather munitions—well operate with greater effectiveness . . . With advanced sensors and a range of precise weapons, from large to very small, we'll be able to strike effectively wherever and whenever necessary with minimum collateral damage [45].*

The anticipated spectrum of conflict for 21st Century war fighters has influenced, and motivated this new technological frontier of powered flight. The shift towards low intensity conflicts, and surgical strike capabilities, often involving small teams of individual soldiers, Special Operating Forces (SOF), or clandestine intelligence gathering personnel, operating in non-traditional environments (e.g. urban centers), has become the norm, rather than the exception in the post-cold war experience. Accordingly, this new reality has forced commanders to accept the realities of current combat operations, embrace the asymmetric nature of the part-time civilian/part-time militant adversary, and reexamine the need MAVs can fulfill on today's battlefield. The days of preparing for a mass phalanx, assaulting through the *Fulda Gap* have passed; and are instead replaced forthwith by small unit tactics, building-to-building engage-

6

ments, accomplishing strategic objectives, by neutralizing one terrorist, one militant, or disarming one Improvised Explosive Device (IED) at a time. This type of arduous combat demands precise, timely, and a multi-disciplined technical solution, owned and operated at the small unit level, enabling complete autonomous control over tactical asset tasking, with minimal information delay in order to maintain the tactical advantage over the indigenous, and usually entrenched adversaries. These evolving circumstances have *a priori* dictated, and shaped the evolution of our total DoD UAV R&D approach over the past few decades—the result is a paradigm shift away from viewing MAVs as an optional tool, to an operational Intelligence, Surveillance, Reconnaissance (ISR) asset, that is becoming fully integrated into the DoD's war fighting arsenal.
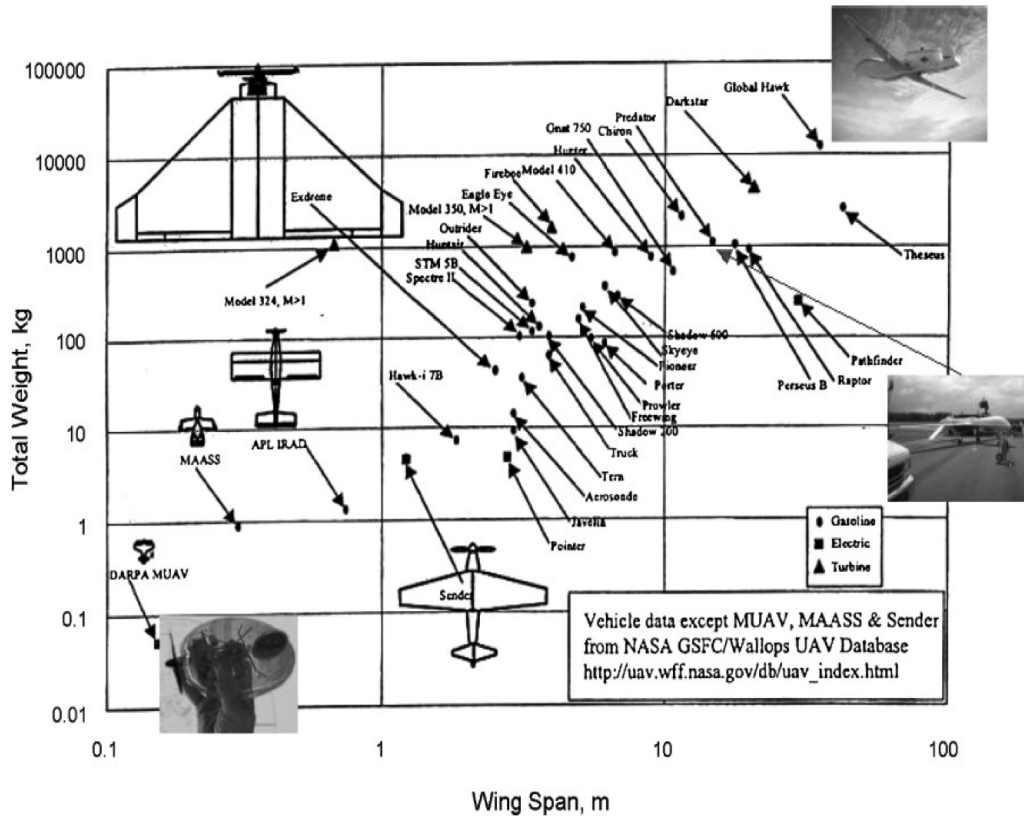
Figure 1.1: Snapshot of recorded operational UAVs worldwide in 2006 [69].

7

Figure 1.1 shows Gross Take-Off Weight (GTOW) vs. wing length (R) of the over 40 UAVs worldwide in 2006 that were currently listed in their country's respective operational inventory. As expected, for every one of the successfully fielded UAV systems, there was a host of unsuccessful iterations, and numerous technical and scientific papers written during their research and development journey. The DoD inventory of UAVs has since rapidly expanded/evolved from long loiter, high altitude, persistent ISR UAVs, covering thousands of square miles like the Air Force's Global Hawk (RQ-4), whose mission profile is to provide a multi-intelligence, multi-sensor phenomenology suite for an entire strategic theater of operations; to the Army's medium range, medium altitude, medium endurance Hunter (RQ-5A), equipped with off the shelf sensor suites for battalion sized ISR missions, or alternatively, they can be equipped with optional external weapon hard points for offensive operations in austere, and denied territory; to the backpack carried, and hand-launched Army Raven (RQ-11B) or the Air Force Special Operations Command (AFSOC) BATMAV WASP III, whose mission is to provide the small tactical unit, or SOF with 'eyes-on' ISR in the next building, over the next hill, or down the street, before initiating an offensive action [1]. Table 1.1 lists the pertinent scaling factors of the DoD inventory of UAV fleet aircraft catalogued in the 2009 volume of the United States Air Force (USAF) *Weapons File* [1]:

Table 1.1: **Span of DoD Inventory UAVs From Micro to Full Size Airframes**

UAV	Altitude *(feet AGL)*	Endurance *(hours)*	Wing Span *(feet)*	External Payload *(lbs_m)*	Max Speed *(mph)*	Max Range *(nm)*	Thrust *(lb_f)*
Global Hawk	60k	36	131	3000	357	8700	7600
Hunter	25k	30	54.5	130	138	125	114
Raven	1.0k	1.3	4.3	4	60	6.2	200w DC
Wasp III	0.5k	0.75	2.3	0.45	30	3.1	10w DC

Figure 1.2 shows an illustration of the size progression of current DoD UAVs, from full-sized UAV, down to the smallest inventory UAV, Aeroenvironment's WASP III

MAV.
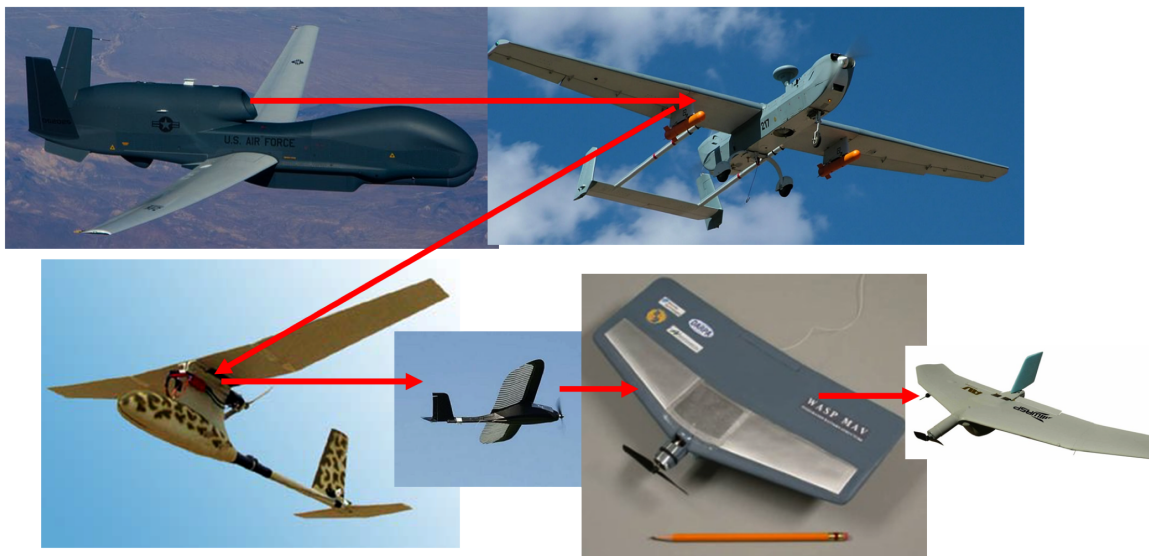
Figure 1.2: Scaling of the Defense Department's Active UAV Inventory. *From top left-to-right:* Global Hawk, Hunter, Raven, BATCAM, WASP I, WASP III.

In response to the success of the initial DARPA MAV research effort, and subsequent operational fielding of several MAVs with wing spans less than 24″, DARPA initiated a second MAV research effort in September 2005 through a Broad Agency Announcement (BAA), DARPA BAA#06-06: Nano Air Vehicle Program (NAV), to solicit innovative proposals for the R&D of very small (< 7.5cm), very lightweight (< 10g) NAVs. The goal of this program was to prove the feasibility and viability of UAVs on this extremely small-scale. Such a capability would provide the military services with a highly effective tool for the collection of battlefield intelligence. Technological feasibility follows from advances in several micro-technologies, including the rapid evolution of Micro-Electro-Mechanical Systems, also known as MEMS. These systems combine micro electronics components with comparably sized mechanical elements of varying complexity to achieve useful, and often unique functionality (e.g. integrated systems of sensors, actuators, processors, propulsion systems, energy delivery etc) [44]. In many cases, these devices are produced with established micro fabrication techniques, providing a high degree of optimism for eventual low-cost production

9

potential. Other maturing micro systems such as tiny CCD-array cameras, equally small infra-red sensors, alternative power sources, miniature Global Positioning System (GPS) receivers, and satellite and communications receivers powerful enough to maintain a reliable connection with ground operators have been catalytic in providing the motivation for like-sized delivery platforms [44, 63]. However, formidable technical challenges must be met to successfully integrate these payloads into functional NAV systems. Innovative technical solutions must be found for challenges in all the major systems of NAV design and fabrication: *aerodynamics, guidance and control, propulsion, power, navigation and communication.*

At this diminutive size, the flow physics, aerodynamic principles, practical engineering realities, and vehicle design methodologies diverge from traditional aircraft design and analysis practice, and beg for a novel approach. This fertile ground has sparked a renewed interest in the field of low Reynolds number aerodynamics, and has resulted in the coalescence of many diverse, and once disparate fields of science and engineering, into a new interdisciplinary engineer, that is simply defined as a *MAV engineer*, which demands knowledge and skill in the fields of electrics, structural dynamics, aerodynamics, flight mechanics, guidance and control engineering, signal processing, biology, anatomy, energy transport systems, and image processing. The motivation and genesis of this research is squarely attributed to the quest to design and build, small, silent, undetectable, flying NAVs that no longer loiter at 60,000 feet, but fly almost inside the personal space of our adversaries undetected. Although not specifically stipulated in the DARPA BAA, the new mission requirement to operate undetected in close proximity to the target necessitates a natural camouflage and concealment to enable the NAV to hide in plain sight, leading inexorably to bio-mimicry—*emulating nature's fliers.*

The first and most obvious component of a bio-inspired vehicle is flapping flight. Flapping wings provide several advantages over the traditional aircraft power plant and wing designs—specifically, the propulsion, control, and lifting surfaces are the same—which naturally reduces vehicle weight, required power, and the total size footprint. In order to design and build such a vehicle, a fundamental understanding of the peculiar flow physics associated with flapping flight is necessary. The Air Force Institute of Technology (AFIT) has a dedicated FWMAV research group currently comprised of three PhD and two Master's students, with approximately three active research faculty members. The current research areas are structures/design, aerodynamics and controls. Some areas in the need of additional work are in the field of wing optimization andpiezoelectric actuator (PZT) design. Recent AFIT graduates, Norris, McLung, Sladek, Anderson, DeLeón, Hollenbeck and O'Hara, covered a wide range of FWMAV topics, marrying various engineering disciplines in their research, which assisted in developing and furthering our collective understanding of the relationship between the physics of nature's fliers, and its application to the design and fabrication of manmade FWMAVs [2, 19, 43, 57, 63, 66, 80].

1.3   Research Focus

The focus of this effort is to experimentally characterize the aerodynamic performance of the AFIT biomimetic wing and drive system, documented and developed first by Anderson, and later improved upon by O'Hara, which is modeled after the hawkmoth, *Manduca Sexta*, through force measurements, and stereoscopic flow visualization techniques, to develop an aerodynamic model of the *Manduca Sexta* class sized flapping mechanism, which can be utilized in future control law algorithm development in preparation of fielding a full-scale flight vehicle. Figure 1.3(a) depicts a graphic of Reynolds number as function of Mach number and weight for different

class flying bodies, Figure 1.3(b) provides some context of the payload envelope of various natural fliers and proposed FWMAV's, and Figure 1.3(c) illustrates a range of payload versus wing span (b) for a number of different sized DoD UAVs.

(a) Mach

(b) Bio Payload

(c) UAV Payload
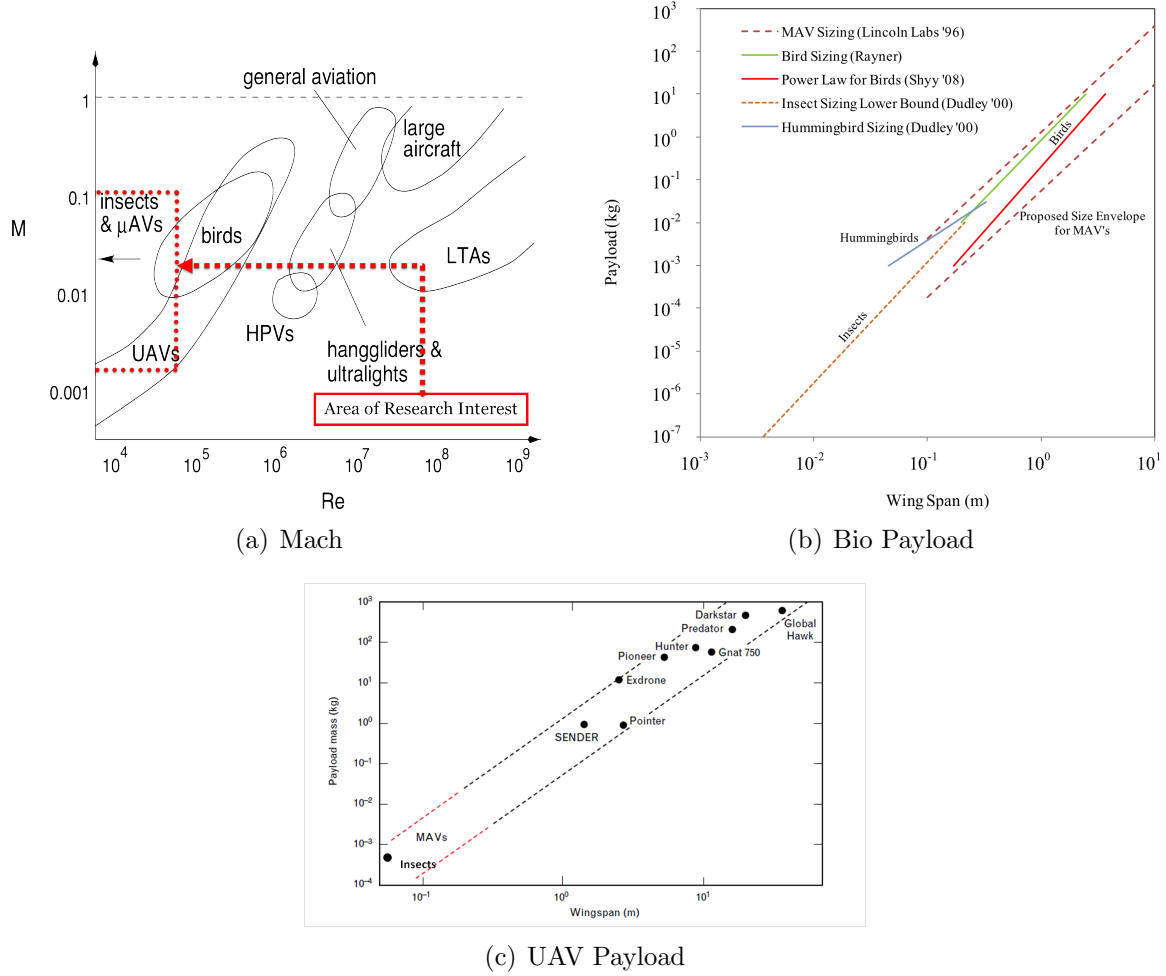
Figure 1.3: Reynolds number vs. Mach and payload for various flying bodies. *Left:* Re vs. Mach. *Right:* Payload vs. wing span for various natural flapping fliers and proposed FWMAVs. *Bottom:* Gross payload carrying capacity vs. wing span for various fixed wing DoD UAVs [22].

Anderson and O'Hara have implemented considerable actuator and wing modeling, design of experiments, finite element analysis, heuristic practice and experimentation towards the optimization of the AFIT *Manduca Sexta* class size engineered wing and flapper mechanism [2, 66]. Figure 1.4 shows an example of the wing flapper apparatus, configured in a dual wing, dual PZT version of the AFIT flapping mechanism, which

is the object of this experimental investigation.
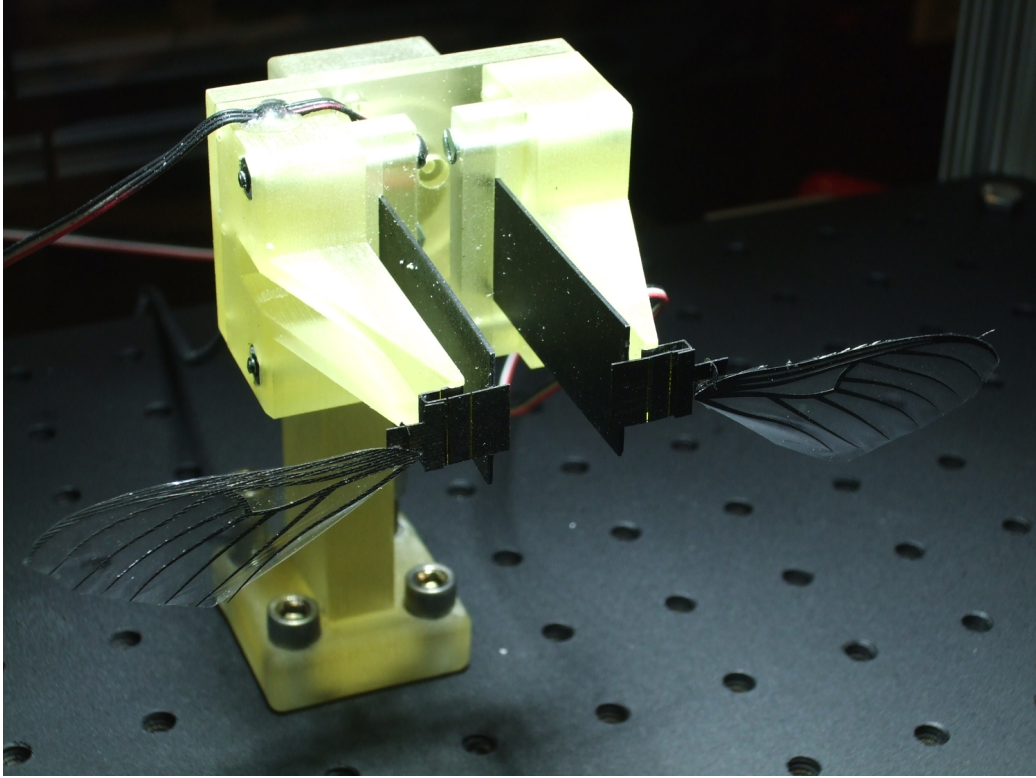
Figure 1.4: **AFIT dual wing flapper designed by Anderson and O'Hara.**

Therefore, to avoid duplicating their efforts in hopes of possibly contributing *modest* gains in efficiency, decreases in mass, changing stiffnesses to favorably shift system resonant responses, etc., this research effort did *not* address the merits of wing design, or attempt to redesign the wings or the drive system itself. However, if through the course of investigation into the causation of specific aerodynamic characteristics, certain wing characteristics are clearly revealed to heavily influence favorable aerodynamic performance—optimize lift-to-drag ratio ($^{L}/_{D}$), ↑ *lift,* ↑ *thrust,* ↓ *required power,* ↓ *drag*—then those design recommendations will obviously be included in the final results and conclusions.

The novelty in this research arises through the experimental methods and techniques of taking a biomimetically engineered wing and the associated drive mechanism, and completely characterizing its aerodynamic responses, by a combination

of:

I) Incorporating complete displacement, velocity, and acceleration FRF measurements to capture the system harmonics to ensure flapping power efficiency is maximized by identifying the system resonant frequency, which is equivalent to the damped natural frequency (ω_d), and is approximately equal to the undamped natural frequency (ω_n), for lightly damped systems, which are typical of flexible wing FWMAVs.

II) Creation of an automated feedback auto-tuning program, essentially creating an 'engine-map' or 'operating envelope' of the wing and PZT-driven flapper by automatically adjusting the drive signal trim parameter (A_{trim}), between the up and downstroke, to perfectly harmonize the wing with its drive mechanism to ensure symmetric flapping at every combination of drive amplitude (A), wing flapping frequency (ω), and $^{up}/_{down}$ stroke bias offset (η).

III) Collecting simultaneous 6-Degrees of Freedom (DoF) force and moment measurements, PZT linear displacement and velocity data, power consumption, and stereoscopic high speed video of the AFIT FWMAV's Leading Edge (LE) and Trailing Edge (TE) locations, which will employ a novel combination of ComputerVision algorithms and techniques to completely map the wing's kinematic matriculation through the flap cycle.

IV) Conducting stereoscopic Particle Image Velocimetry (PIV) to capture the x-dir velocity (u), y-dir velocity (v), z-dir velocity (w) unsteady aerodynamic velocity vector field, $\vec{V}(u, v, w, t)$, as it changes as a function of stroke angle ($\phi(\text{t})$), mechanical angle stop, and drive signal modulation.

These results are the foundation to create an aerodynamic model, which will define the aerodynamic parameters: mean lift coefficient ($\overline{C_L}$), mean drag coefficient ($\overline{C_D}$),

mean side force coefficient ($\overline{C_S}$), mean vertical force coefficient ($\overline{C_v}$), mean horizontal force coefficient ($\overline{C_h}$), mean axial force coefficient ($\overline{C_a}$), pitch moment coefficient (C_m), roll moment coefficient (C_ℓ), and yaw moment coefficient (C_n), for inclusion into future control law algorithm development as functions of easily changeable flapping parameters via the piezo drive signal shape.

1.3.1 Declarative Thesis Statement.

A robust analysis of the forces and moments on AFIT's Manduca Sexta class, bio-inspired, designed and fabricated engineered wings and PZT drive mechanism, coupled with an experimental fluid dynamics investigation through stereoscopic flow visualization methods, will: i) enhance understanding of the complex three-dimensional fluid/structure interactions in hover, and further elucidate the sometimes nebulous aerodynamic principles, which will facilitate development of an enhanced quasi-steady aerodynamic model as a function of kinematic parameters such as stroke angle, angle of attack, and elevation angle; and ii) aide in the design and development of future refinements including those related to the wing and linkage design, as well as stabiliy and control, supporting the evolution towards a fully functional, air vehicle platform.

1.4 Organization

This remainder of this dissertation flows in a logical manner, and the document organized as follows: *Chapter II* will discuss: *i*) a topical survey of the applicable aerodynamic theory, and associated flight postulates biologists and engineers have documented in the literature on both natural fliers and their manmade flapping analogs; *ii*) discuss some of the experimental techniques and results specific to the hawkmoth, and hawkmoth-based flapping mechanisms, found in the literature to buttress the AFIT hawkmoth bioinspired FWMAV; *iii*) describe the AFIT flapper mechanism,

diagram its constituent components, and discuss the impact its design parameters have on overall wing stroke kinematics; and *iv*) the physical characterization of the AFIT *Manduca Sexta* bioinspired wing. With an introduction of the historical context surrounding the genesis of MAV research leading to the motivation driving this, and numerous other FWMAV related research efforts, *Chapter III* will outline the techniques and methods employed in the experimental work accomplished, specifically:

I) Frequency Response Function (FRF) implementation and system resonance identification;

II) Automatic tuning of flapper mechanism as a function of amplitude by auto-tuning the sinusoid drive signal using trim, much like in an airplane, to achieve symmetric PZT actuator tip displacement $\approx$ symmetric wing flapping;

III) Stereoscopic high speed video wing tip tracking from a custom built program using the ComputerVision (OpenCV) tools Canny Edge Detection and Gaussian Mixture Model;

IV) Force, moment, actuator power, displacement, and velocity data processing; and

V) Stereoscopic PIV system set-up, equipment description, PIV methodology, and the taxonomy of achieving stereoscopic velocity vector fields from 2-D camera image planes.

Chapter IV will present the results of the optical wing tracking, and then integrate the angular kinematic results with the raw 6-DoF force and moment balance measurements to calculate aerodynamic coefficients. *Chapter V* will show flow visualization results created from the stereoscopic PIV measurements, then present a quantitative analysis of the velocity flow field, and offer an application of the velocity data by estimating the vertical thrust (*lift*) produced during each captured phase. *Chapter VI* will summarize the major research advancements and milestones achieved during the

course of this research, and *Chapter VII* presents opportunities for future researchers to pursue and recommendations for follow-on students where the author thinks the present work has left room for deeper investigation.

II. Background & Literature Review

2.1   Overview

NATURAL fliers operate effectively in flow regimes where the propulsive efficiency of conventional systems decrease with size, and demonstrate flight maneuvers not currently capable by FWMAVs. One of the features differentiating small flapping wing fliers from engineered, fixed, and rotary wing systems is the use of unsteady aerodynamic phenomena to produce the aerodynamic forces necessary for sustained flight. By understanding how natural fliers utilize and control the unsteady physics responsible for their enhanced aerial abilities, engineers can design FWMAV systems that take advantage of, and hopefully emulate, similar unsteady aerodynamic mechanisms. Thus, bio-inspiration offers a means to enhance the performance of the next generation of FWMAVs over existing fixed and rotary wing MAVs.

This chapter present a survey of the extensive literature on the subject of both biological and manmade flapping flight, relay the salient theoretical and aerodynamic mathematical constructs useful in application to study of the AFIT FWMAV, outline some of the related FWMAV work at contemporary laboratories and universities, and then introduce with sufficient specificity the AFIT engineered wing and drive mechanism.

2.2   Literature Review

The explosion in FWMAV related research over the past 10 years has been astounding. A informal, but thorough, survey of the AIAA *E-Library* using the following key-word searches: *unsteady aerodynamics, flapping wing(s), flapping flight, oscillating airfoils, Micro Air Vehicl(s), MAV or insect flight*, provided immutable proof to the overwhelming growth in FWAMV related research. From the date of

the first AIAA paper publication in 1913, to 1950, there were *zero* papers published with any of the key words related directly to flapping flight, and *four* published on unsteady aerodynamics, of which ALL were concerning the physics of the novelty of rotorcraft dynamics. Between 1950 and 1980 there were *zero* papers published with any of the key words related directly to flapping flight, and 29 published on unsteady aerodynamics, of which ALL were concerning rotorcraft dynamics and pitching and plunging traditional airfoils in near transonic flow regimes. Between 1981 and 2000 there were 43 articles published on flapping flight, *four* specifically published on MAVs, and over 200 published under the unsteady aerodynamics topical heading, of which there was a fairly even distribution of inflatable space structure submissions, flexible and adaptive airfoils, and the aerothermo-mechanics of wing flexure and high transonic / high Angle of Attack (AoA) flight regimes. However, in the last 10 years, between 2001-2011, there were nearly 750 articles with direct title matches to searches for *Flapping Wing* or *Micro Air Vehicles*, with another 200+ articles revealed under searches for *flexible wing, insect flight, insect aerodynamics, or low Reynolds number flight.* This staggering number of directly related peer reviewed, and published literature is just from AIAA, which does not include the near 1,000 articles on the aerodynamics and flight physics of natural fliers chronicled in cross-discipline publications like the *Journal of Guidance, Control, and Dynamics; Journal of Experimental Biology; Nature; Journal of Biology; Bioinspiration & Biomimetics* and *Philosphical Transactions of the Royal Society—Biological Sciences*, where many of the pioneering articles on flapping flight research have were published. The sheer volume of published literature on the subjects of flapping wing aerodynamics and insect flight cannot be reasonably compartmentalized, read, and digested in a short span—realities of the duration of the ascribed course of study, the peculiarities of the military institution, and associated periphery duties preclude a comprehensive review

of every researcher's work in this sprawling field. Therefore, the background material presented in this review attempts to build upon, not duplicate, the extensive literature reviews performed by previous AFIT students as part of their research into building the AFIT FWMAV program, and present that material which bolsters the present research in the speciality topics of flapping flight aerodynamics, force generation, and PIV measurements.

Scientists like Ellington, Maxworthy, Nachitgall, Norberg, Thomas, Walker, Weis-Fogh, and Willmott were studying and performing remarkable experimental inquiry on live insect flight dating back to the early 1970's. The majority of their work was published in journals catering to *earth and life sciences*, and therefore; their style and mathematical approach are a departure from the pure technical writing formula most modern engineers are accustomed to reading in a typical *AIAA*, *SPIE*, or *IEEE* publication. Not intended to be denigrating or pejorative towards their work, but their audience, and therefore, their research, and its corresponding reports are often organized and presented with different priorities than an engineering oriented research effort. Their experimental methods were innovative, and their quest was to capture the natural phenomenon of flight using actual specimens in confinement, in order to understand the mechanics and design of nature's fliers. From there, they formulate theories, and fit mathematical explanations around what their set of experiments revealed. Their efforts then can be viewed as a search for an answer to an ontological quest to identify the quiddity— *"whatness"*—of nature's fliers. This is in contrast to the standard engineering approach of formulating theoretical explanations, through a more rigorous mathematical derivation, and then conducting stepwise controlled experiments, fixing the independent variables, thereby isolating a single dependent variable, recording the results and verifying whether the results match the mathematical derivation. If not, the theory is adjusted, assumptions revisited, and the theory

reformulated. Controlling base organisms like insects is nearly impossible—*it's not like training dolphins at Sea-World.* Dr. Thomas Mueller of the University of Notre Dame classified the difference between the science used to explain natural flight versus the research to design a flapping flight vehicle in the following excerpt from a paper on the aerodynamics of flapping wing flight:

> *There is a fundamental difference between an orinthopter [an aircraft that flies by flapping wings at the same scale as nature's analogs] designer's interest in flapping wing flight and that of a biologist or zoologist. The primary motivation for studying animal flight is to explain the physics for a creature that is known to fly. That is, the fact that it achieves successful [lift] and propulsion is given. Therefore, various analytical models are adjusted to match measured results, and conclusions are reached regarding energitics, migration capabilities, etc. An orinthopter designer, in contrast, is trying to develop a flying [flapping] wing aircraft, and its ability to achieve this is no given fact. What such a person needs is a design-oriented analyisis, which is not what is offered from animal-flight studies. For a designer with an aerospace engineering background, publications from the animal-flight community can be fairly puzzling. That is, they may seem either too simplistic, involving inappropriate quasi-steady aerodynamic models, or too qualitative, presenting hypotheses regarding the supposed benefits of various free and bound vortices. What makes an engineer most comfortable is a comprehensive analysis verified with rigorous experiments over a wide range of parameters.* [60]

Isolating specific variables, precisely controlling wing motion, stroke angle, stroke plane angle, feathering angle, differentiating between forward motion and hover, maintaing constant wing angle of attack, etc. is nearly impossible using live insect specimens to discern acute, and minuscule aerodynamic phenomenon with reliable and repeatable certainty. However, their work elucidated the complexity and convoluted interrelation between insect musculature, body composition, wing design, operating Reynolds number, wing flap geometry, wing and body harmonics, flapping frequency, stroke kinematics, and the general Fluid-Structure-Interaction (FSI) used to generate net positive lifting forces, and forward thrust. These revelations, coupled with the

move inside the defense industry to collect situational awareness information in increasingly smaller error ellipses, coalesced to motivate engineers to take the proverbial *baton*, and begin increasingly more acute examinations into every facet of flapping flight phenomenon. Their results established a set of taxonomical invariant observations and theoretical abstractions about the causation of natural flight, and which parameters can be manipulated to harness and control those flight forces towards the goal of building an autonomous man-made FWMAV.

The AFIT FWMAV wing design is wholly predicated on the size, shape, and structural response of the hawkmoth, *Manduca Sexta*; and therefore, the aerodynamics used here to describe the research documented in the literature will naturally focus on studies of hawkmoth flight characteristics, and bioinspired hawkmoth mechanical flapping devices, especially concentrating on hover in particular. For live hawkmoth species, Weis-Fogh reported a mean lift coefficient of $\overline{C_L}$=1.2; a Reynolds number (Re)= 5400; a wing beat frequency (n)= 26Hz; a stroke amplitude (Φ)= 110°; an aspect ratio ($\mathcal{R}$)= 5.4; and a mean wing length (R)= 48.5mm, from the averages of a number of live specimens [31]. Willmott and Ellington reported more modest mean lift coefficients in the range of $0.7 < \overline{C_L} < 0.95$ over a range of Re $= 4200 - 6500$ [32, 92]. For values of $n = 20 - 22$Hz, $R = 50$mm, $S = 0.002$m^2; $\mathcal{R} \approx 5.5$, mean chord ($\bar{c}$)=20mm, $\Phi \approx 110°$, the AFIT FWMAV has a Re $= 5900$, and a $\overline{C_L} \approx 1 - 2$.

2.3 Aerodynamics

Any discussion about the theoretical underpinnings of the mechanism of flight typically begins with the fundamental generalized Navier-Stokes (NS) fluid dynamics equations of motion, which are then transformed and applied to the specific flight conditions, and platform characteristics pertinent to the problem under investigation. The NS equations are actually an application of a general conversation law

which describes the physics of fluid motion. The conversation law is quite simple in its formative logic, but becomes exceedingly more obtuse in its internal detail. The conservation law describes the amount of change, *flux*, of a conserved quantity, U, across a confined boundary, is due to the combination of internally acting sources and externally acting forces. These changes are a result of the mechanical and thermodynamic intrinsic properties of the fluid. The fluxes and sources are then determined by the spatial and temporal coordinates, as well as the bulk fluid motion. Without being overly pedantic, and rederiving the NS equations from first principals, the equations will be presented here, and the reader can refer to graduate texts on fluid dynamics for the detailed derivations. The conservation laws applied to *i*) Mass; *ii*) Momentum in 3-directions (x, y, z); and *iii*) Energy, completely describe the laws defining fluid flows.

The generalized conservation law defined over an arbitrary control volume (Ω), that has a continuous boundary (S), is given by Equation 2.1 below [41].

$$\frac{\partial}{\partial t} \int_\Omega U \, d\Omega + \oint_S \vec{F} \cdot d\vec{S} = \int_\Omega Q_V \, d\Omega + \oint_S \vec{Q}_S \cdot d\vec{S} \qquad (2.1)$$

Where U is any scalar conservation quantity; $\vec{F} \cdot d\vec{S}$ is the net total flux along the unit outward normal across the differential surface element ($d\vec{S}$); Q is the sources from the scalar property U, which can be broken down further into volume sources (Q_V) and surface sources ($\vec{Q}_S$) [41]. If the conserved property, U, is a vector quantity, like velocity, $\vec{v}$, then the general conservation law can be written in tensor form shown in Equation 2.2 below [41].

$$\frac{\partial}{\partial t} \int_\Omega \vec{U} \, d\Omega + \oint_S \overline{\overline{F}} \cdot d\vec{S} = \int_\Omega \vec{Q}_V \, d\Omega + \oint_S \overline{\overline{Q}}_S \cdot d\vec{S} \qquad (2.2)$$

The volume integral $\left(\int_\Omega d\Omega \right)$ is defined over a three dimensional control volume, and in cartesian coordinates is equivalent to:

$$\int_\Omega d\Omega = \iiint_\forall dx\,dy\,dz$$

A more common form used in engineering is obtained by applying Gauss' divergence theorem to the surface integral of the flux tensors, which states the integral of a flux around a closed surface is equivalent to the volume integral of the divergence of that flux through the boundary [41]:

$$\oint_S \vec{F} \cdot d\vec{S} = \int_\Omega \vec{\nabla} \cdot \vec{F}\, d\Omega$$

The general conservation law in tensor form is then written in the form shown in Equation 2.3 [41]:

$$\frac{\partial}{\partial t} \int_\Omega \vec{U} d\Omega + \int_\Omega \vec{\nabla} \cdot \vec{F} d\Omega = \int_\Omega \vec{Q}_V d\Omega + \int_\Omega \vec{\nabla} \cdot \overline{\overline{Q}}_S d\Omega \qquad (2.3)$$

Finally, if the control volume is constant, the solution is valid for any locally continuous point in the flow, and the integrals must then be identically zero at every point. The integral form of the conservation law can be written in derivative form, shown in Equation 2.4 below [83].

$$\frac{\partial \vec{U}}{\partial t} + \vec{\nabla} \cdot \left(\overline{\overline{F}} - \overline{\overline{Q}}_S \right) = \vec{Q}_V \qquad (2.4)$$

Equations 2.3 and 2.4 give the general law governing the physics of fluid matriculation through a control surface. The general conservation law is a mathematical expression describing a physical phenomena. The NS equations that completely define a fluid flow are a direct result of applying the conservation laws to the fully defined

expressions for the general transport quantity $(\vec{U})$, the general flux terms $(\overline{\overline{F}})$, and the source terms $(\overline{\overline{Q}})$, which are the three basic fluid properties: *mass, momentum, and energy.* The fluxes are further broken down into convective fluxes $(\overline{\overline{F_C}})$, and diffusive fluxes $(\overline{\overline{F_D}})$. $\overline{\overline{F_C}}$ is defined mathematically in Equation 2.5 [41, 83].

$$\left(\overline{\overline{F_C}}\right)_{ij} = U_i \vec{v}_j \tag{2.5}$$

Where U_i is defined as

$$U_i = \rho u_i$$

F_D is given by Equation 2.6.

$$\left(\overline{\overline{F_D}}\right)_{ij} = -\kappa\rho\frac{\partial u_i}{\partial x_j} \tag{2.6}$$

κ is a diffusivity constant (κ); ρ is the fluid density (ρ), u_i is the fluid velocity, and x_j is the cartesian direction.

2.3.1 Continuity.

The first of the NS equations is a statement of the conservation of mass, which is a convective transport of mass through a boundary, and simply states that mass cannot be created nor destroyed within a system. The convective flux is expressed as, $\overline{\overline{F_C}} = \rho\vec{V}$, and the diffusive flux is zero. The general integral form of the mass conservation equation is given below in equation 2.7 [41].

$$\frac{\partial}{\partial t}\int_\Omega \rho \, d\Omega + \oint_S \rho\vec{v}\cdot d\vec{S} = 0 \tag{2.7}$$

Applying the assumptions used to transform the integral form of the generalized

conservation law into the more practical differential form shown in Equation 2.4 above, the differential form of the mass equation is given by Equation 2.8 [83].

$$\frac{\partial \rho}{\partial t} + \vec{\nabla} \cdot (\rho \vec{\nu}) = 0 \tag{2.8}$$

Expanding the divergence operator unpacks Equation 2.8 further to [41].

$$\frac{\partial \rho}{\partial t} + (\vec{\nu} \cdot \nabla) \rho + \rho \vec{\nabla} \cdot \vec{\nu} = 0 \tag{2.9}$$

Employing the definition of the *substantial* or *material* derivative, a four term operator, which breaks down the total acceleration of a particle into its *local* and *convective* acceleration terms in an *Eulerian* frame given in Equation 2.10.

$$\frac{D\,()}{Dt} \triangleq \underbrace{\frac{\partial\,()}{\partial t}}_{Local} + \underbrace{(\vec{\nu} \cdot \nabla)}_{Convective} \tag{2.10}$$

Equation 2.9 can be expressed in *non-conservative* or *quasi-linear* form given in Equation 2.11 below [83].

$$\frac{D\rho}{Dt} + (\nabla \cdot \vec{\nu})\,\rho = 0 \tag{2.11}$$

Incompressible flows are typically defined for Mach numbers less than 0.3, and insect flapping wing flight is far below $M = 0.3$, and therefore the flows associated with it are classified as incompressible. Wang determined the Mach number for insect size class flapping wings is typically 0.003 and the wing beat frequency is in the range of $10 - 100$Hz [87]. The addition of the incompressibility assumption implies the time rate of change of the density is constant, meaning,

$$\frac{D\rho}{Dt} = 0$$

which further reduces the continuity Equation 2.11, to Equation 2.12 [83].

$$\nabla \cdot \vec{\nu} \equiv \frac{\partial u}{\partial x} + \frac{\partial v}{\partial y} + \frac{\partial w}{\partial z} = 0 \tag{2.12}$$

2.3.2   Momentum.

Momentum is a vector quantity characterized by the product of mass and velocity. The momentum transport quantity, $\vec{U}$, is defined as $\rho\vec{\nu}$. The convective flux applied to the momentum vector is given by Equation 2.13 [41].

$$\overline{\overline{F_C}} = \rho\vec{\nu} \otimes \vec{\nu} \tag{2.13}$$

where $\otimes$ is shorthand notation for the tensor product ($\otimes$) between $\rho\vec{\nu}$ and $\vec{\nu}$. The convective flux through the surface, $d\vec{S}$, is given by Equation 2.14 [41].

$$\overline{\overline{F_C}} \cdot d\vec{S} = \rho(\vec{\nu} \cdot d\vec{S}) = \vec{\nu}\, d\dot{m} \tag{2.14}$$

The diffusive fluxes are zero for a fluid at rest, and the momentum equation in conservative integral form is given by Equation 2.15 [41].

$$\frac{\partial}{\partial t} \int_{\Omega} \rho\vec{\nu} d\Omega + \int_{\Omega} \vec{\nabla} \cdot (\rho\vec{\nu} \otimes \vec{\nu})\, d\Omega = \int_{\Omega} \rho\vec{f_e}\, d\Omega + \int_{\Omega} \vec{\nabla} \cdot \overline{\overline{\vartheta}}\, d\Omega \tag{2.15}$$

Where $\vec{f_e}$ are the external volume forces, namely gravitational, centrifugal, Coriolis, and electromagnetic—except for gravitational, all others are negligible in flapping wing flight—and $\overline{\overline{\vartheta}}$ is the internal forces or *stresses* acting on the surface element, $d\vec{S}$, in the direction of the unit normal vector ($\vec{n}$). For an isotropic, *Newtonian* fluid, the internal stress/strain curve on a fluid element is linear, which implies a constant viscosity, rendering the total internal stress tensor ($\overline{\overline{\vartheta}}$) acting on the surface of a fluid boundary equal to:

$$\overline{\overline{\vartheta}} = -p\overline{\overline{I}} + \overline{\overline{\tau}} \tag{2.16}$$

where $-p$ is the isotropic pressure, $\overline{\overline{I}}$ is the identity tensor $(\overline{\overline{I}})$, and $\overline{\overline{\tau}}$ is the viscous shear stress tensor $(\overline{\overline{\tau}})$ of the internal friction forces of fluid layers acting in concert against one another, given by Equation 2.17 [41].

$$\tau_{ij} = \mu \left[\left(\frac{\partial \nu_j}{\partial x_i} + \frac{\partial \nu_i}{\partial x_j} \right) - \frac{2}{3} \left(\vec{\nabla} \cdot \vec{\nu} \right) \delta_{ij} \right] \tag{2.17}$$

Where the dynamic viscosity (μ) of the fluid, and can be used interchangeably with the kinematic viscosity (ν), or *absolute viscosity*, and is equal to μ/ρ. The differential form of the momentum equation yields the more commonly known NS equations for a Newtonian, viscous fluid, given in Equation 2.18.

$$\rho \frac{D\vec{\nu}}{Dt} \equiv \rho \frac{\partial \vec{\nu}}{\partial t} + \rho \left(\vec{\nu} \cdot \vec{\nabla} \right) \vec{\nu} = -\vec{\nabla} \rho + \mu \left[\Delta \vec{\nu} + \frac{1}{3} \vec{\nabla} \left(\vec{\nabla} \cdot \vec{\nu} \right) \right] + \rho \vec{f_e} \tag{2.18}$$

In x,y,z cartesian tensor form, the NS equations are given by Equation 2.19 [83, 88].

$$\rho \frac{D\vec{\nu}}{Dt} = \rho \vec{f_e} - \vec{\nabla} \rho + \frac{\partial}{\partial x_j} \left[\mu \left(\frac{\partial u_i}{\partial x_j} + \frac{\partial u_j}{\partial x_i} \right) - \frac{2}{3} \delta_{ij} \mu \frac{\partial u_k}{\partial x_k} \right] \tag{2.19}$$

The reader is referred to two very good fluid dynamics texts by Hirsch and Tannehill for the fully expanded cartesian x,y,z scalar coordinate NS equations, and to White's standard viscous flow text for the less common, but nonetheless important, polar and spherical coordinate derivations. Finally, the incompressible form of the NS equations, subject to the no-slip boundary condition, are given below in Equations 2.20 and 2.21 [41, 83, 87, 88].

In integral form:

$$\frac{\partial}{\partial t} \int_\Omega \rho \vec{v} \ d\Omega + \int_\Omega \rho \left(\vec{v} \cdot \vec{\nabla} \right) \vec{v} \ d\Omega = - \int_\Omega \vec{\nabla} P \ d\Omega + \mu \int_\Omega \Delta \vec{v} \ d\Omega + \int_\Omega \rho f_e \ d\Omega \quad (2.20)$$

In differential form:

$$\underbrace{\left[\rho \frac{D\vec{v}}{Dt} = \rho \vec{f_e} - \vec{\nabla} \rho + \mu \nabla^2 \vec{v} \right]}_{quasi-linear} \equiv \underbrace{\left[\rho \frac{\partial \vec{v}}{\partial t} + \rho \left(\vec{v} \cdot \vec{\nabla} \right) \vec{v} = \rho \vec{f_e} - \vec{\nabla} \rho + \mu \Delta \vec{v} \right]}_{conservative}$$

where: $\qquad\qquad\qquad\qquad\qquad\qquad\qquad\qquad\qquad\qquad\qquad\qquad$ (2.21)

$\vec{v}(\vec{x}, t)$ defines the flow field, and

$\vec{v}_{bd} = \vec{v}_{solid\ wing}$ states the no-slip boundary conditon at the wing surface

For completeness, Equation 2.21 is expanded into cartesian scalar form below in Equation 2.22 [83].

x-dir momentum:

$$\frac{\partial v}{\partial t} + u\frac{\partial u}{\partial x} + v\frac{\partial u}{\partial y} + w\frac{\partial u}{\partial z} = -\frac{1}{P}\frac{\partial \rho}{\partial x} + \frac{\mu}{\rho}\left(\frac{\partial^2 u}{\partial x^2} + \frac{\partial^2 u}{\partial y^2} + \frac{\partial^2 u}{\partial z^2} \right)$$

y-dir momentum: $\qquad\qquad\qquad\qquad\qquad\qquad\qquad\qquad\qquad$ (2.22)

$$\frac{\partial v}{\partial t} + u\frac{\partial v}{\partial x} + v\frac{\partial v}{\partial y} + w\frac{\partial v}{\partial z} = -\frac{1}{P}\frac{\partial \rho}{\partial y} + \frac{\mu}{\rho}\left(\frac{\partial^2 v}{\partial x^2} + \frac{\partial^2 v}{\partial y^2} + \frac{\partial^2 v}{\partial z^2} \right)$$

z-dir momentum:

$$\frac{\partial w}{\partial t} + u\frac{\partial w}{\partial x} + v\frac{\partial w}{\partial y} + w\frac{\partial w}{\partial z} = -\frac{1}{P}\frac{\partial \rho}{\partial z} + \frac{\mu}{\rho}\left(\frac{\partial^2 w}{\partial x^2} + \frac{\partial^2 w}{\partial y^2} + \frac{\partial^2 w}{\partial z^2} \right)$$

Although there are no formal diffusion terms in the NS equations, the viscous stress tensor is a second order derivative, and diffusive effects are mathematically expressed as the negative gradient of concentration, where peaks in concentration tend towards uniformity, proportional to a diffusivity constant, κ—which is a second order phenomenon [41]. Therefore, viscosity tends to diffuse the concentration of momentum in a fluid, proportional to the kinematic viscosity, ν, which is effectively a diffusion.

Now is probably a good time to introduce a critical parameter aerodynamicists use to compare, and characterize various flow regimes—the *Reynolds number*—it is defined as the ratio of *inertial* to *viscous* forces, or in terms of the development of the NS equations above, it is the ratio between the convection and diffusion of momentum through the fluid. A low Re describes a laminar flow where the viscous forces, those close to an impenetrable boundary in the flow, dominate, inferring that flow momentum is highly diffused as the flow matriculates through the control volume. A high Re describes a highly turbulent flow, dominated by the inertial energy of the flow itself, where the effects of viscosity are negligible, and momentum is transported, *convected*, by the bulk fluid motion, with little dissipation. The Re is given by Equation 2.23 below.

$$Re = \frac{V_\infty L}{\mu_\infty/\rho_\infty} = \frac{\rho_\infty V_\infty L}{\mu_\infty} \tag{2.23}$$

In dimensionless terms, the Re is expressed as:

density scale: $\quad \rho^* = \frac{M}{L^3} \to \frac{\rho}{\rho_\infty}$

velocity scale: $\quad V^* = \frac{L}{T} \to u^* = \frac{u}{V_\infty}, \ v^* = \frac{v}{V_\infty}, \ w^* = \frac{w}{V_\infty}$

length scale: $\quad L$

viscosity scale: $\quad \mu^* = \frac{L^2}{T} \to \frac{\mu}{\mu_\infty}$

Where the dimensionless variables are denoted by *, the ∞ is the free stream condition, and L is the reference length scale of the flow. Non-dimensional forms of equations are scale-invariant, thereby making it possible to compare flight physics across a wide range of scales. The choice of parameters used to nondimensionalize the applicable equations is somewhat arbitrary. The method used here, and most conventionally used by most insect and flapping wing flight analysis is the one developed by Ellington in his seminal series of six manuscripts published in the 1984

Transactions of the Royal Society [31, 32, 33, 34, 35, 36]. Equation 2.24 gives the dimensionless form of the viscous, incompressible NS equations, nondimensionalized by the Reynolds number.

$$\frac{\partial \vec{\nu}^{\,*}}{\partial t^*} + (\vec{\nu}^{\,*} \cdot \nabla^*) \vec{\nu}^{\,*} = -\nabla^* P^* + \frac{1}{\mathrm{Re}} \nabla^{2^*} \vec{\nu}^{\,*} \tag{2.24}$$

Ellington proposed a form of the Re number used in flapping flight analysis, adapted from Equation 2.23, which is the convention both biologists and aerodynamicists have adopted in comparing flapping flight regimes and their associated flows, given below in Equation 2.25.

$$\mathrm{Re} = \frac{\bar{c} U_t}{\mu / \rho} = \frac{4 \rho \Phi n R^2}{\mu \mathcal{R}} \tag{2.25}$$

where Ellington defined the mean maximum tip velocity $(\bar{U}_t)$ as $U_t = 2\Phi nR$, Φ is in radians, n is in Hz, R is the wing length (*half span*) and the $\mathcal{R}$ is defined below in Equation 2.26. The Re for typical insect flight ranges from $10^2 - 10^4$, well within the laminar region of flow.

$$\mathcal{R} = \frac{4R^2}{S} \tag{2.26}$$

The wing area (S) is given by Equation 2.27 below [32].

$$S = 2 \int_0^R c(r) \; dr \tag{2.27}$$

The mass and momentum NS equations provides the fundamental theoretical basis for understanding forces and flows from arbitrary or measured kinematics. However, the pressure above and below the wing is not easily measured in a laboratory; therefore, the NS equations are not easily applicable to real world flapping flight analysis.

An alternative, and sometimes more convenient form of the NS equations is achieved by taking the curl of both sides of Equation 2.24, which eliminates the pressure term because the curl of a gradient is identically zero, yielding Equation 2.28 [71, 88].

$$\frac{\partial \omega^*}{\partial t^*} = \nabla^* \times (\vec{\nu}^* \times \omega^*) + \frac{1}{\text{Re}} \nabla^{2^*} \vec{\nu}^* \tag{2.28}$$

Where $\omega^* = \nabla^* \times \vec{\nu}^*$ is the nondimensional vorticity of the fluid. The flow is said to be irrotational when $\omega^* = 0$, and obtains a non-zero value when the derivatives of the velocity field at a point in space are emanating mutually orthogonal vectors [41, 71, 88].

The NS equations are not complete without a statement of the conservation of energy equation; however, if the flow is incompressible and isothermal, then the energy equation is decoupled from the mass and momentum equations, and it can be left out of the aerodynamic equations of motion. Therefore, the continuity and momentum equations alone are sufficient to solve problems in flapping wing flight. These equations can be shown in short-hand vector form as

$$\frac{\partial U}{\partial t} + \frac{\partial f}{\partial x} + \frac{\partial g}{\partial y} + \frac{\partial h}{\partial z} = \vec{Q} \tag{2.29}$$

Where the components of the flux tensor (f,g,h) are vector quantities given by

$$f = \begin{bmatrix} \rho u \\ \rho u^2 + p - \tau_{xx} \\ \rho uv - \tau_{xy} \\ \rho uw - \tau_{xz} \end{bmatrix}, g = \begin{bmatrix} \rho v \\ \rho vu - \tau_{xy} \\ \rho v^2 + p - \tau_{yy} \\ \rho vw - \tau_{yz} \end{bmatrix}, h = \begin{bmatrix} \rho w \\ \rho wu - \tau_{zx} \\ \rho wv - \tau_{zy} \\ \rho w^2 + p - \tau_{zz} \end{bmatrix} \tag{2.30}$$

and the source term vector, $\vec{Q}$, is given by:

$$Q = \begin{bmatrix} 0 \\ \vec{f_x}e \\ \vec{f_y}e \\ \vec{f_z}e \end{bmatrix} \tag{2.31}$$

all of which are 5x1 column vectors, *the energy equation terms are not shown*, leaving 4x1 column vectors.

2.3.3 From NS → Lift and Drag Forces.

The lift and drag resultant forces exerted by the flow on a solid body are obtained from the integral form of the momentum equation given above in Equation 2.20. If the control volume, Ω, contains a solid body such as a wing, then an additional reaction force $(-\vec{R})$ must be added to the right-hand side of Equation 2.20. The reaction forces, $-\bar{R}$, are comprised of a normal component, lift force $(\vec{L})$, and a parallel component, drag force $(\vec{D})$, in the direction opposite to the relative velocity. If the surface (S) or solid boundary is located in the far-field, the viscous forces are negligible and their contribution can be removed from Equation 2.20, resulting in the incompressible, viscid form of the NS equations, with the addition of the lift and drag forces, shown in Equation 2.32 below [41].

$$-\vec{R} \equiv -\left(\vec{L} + \vec{D}\right) = \int_\Omega \vec{\nabla} P \, d\Omega + \int_\Omega \rho \left(\vec{\nu} \cdot \vec{\nabla}\right) \vec{\nu} \, d\Omega \tag{2.32}$$

A more common solution technique is to place the boundary of the control surface (S) on the solid body surface of the wing S_b. This geometric definition forces the velocity field at the surface to zero due to the no-slip condition, which has an ancillary benefit of removing the complex integral of the divergence of velocity from the NS equations, and replacing it with a scalar integral of the product of the viscosity coef-

ficient and velocity in incompressible flows. Equation 2.33 gives the incompressible, viscous NS equations, absent external forces, at the wing surface [41].

$$\vec{R} \equiv \vec{L} + \vec{D} = -\int_{\Omega_b} \vec{\nabla} P \, d\Omega + \mu \int_{\Omega_b} \Delta \vec{\nu} \, d\Omega \qquad (2.33)$$

The solution to the NS equations yield information about the flow physics in the near-field control volume, and the resultant wake in terms of the velocity components and pressure gradients. The lift and drag forces acting on the wing surface can be evaluated from the pressure and stresses along its surface. The local forces acting perpendicular and parallel to the wing, *lift and drag*, are a summation of the viscous and inviscid fluxes along the wing, influenced by the pressure distribution above and below the surface, which is determined by the vortex wake in the near-field flow [53].

2.4   Insect & Flapping Wing Flight

The application of the NS equations developed in section 2.3 above to the analysis and design of FWMAV is a difficult problem. The flow fields surrounding flapping wings in general are characterized as unsteady; although portions of the flow are completely steady. The flow produced by a flapping wing can be broken down into periods of steady flight separated by unsteady transitions between phases. Flapping wings are characterized by a steady period of translation in the forward or *down* stroke where the wing translates with a constant velocity and feather angle (ψ_f), the angle between the wing and the vertical after rotation; a rapid deceleration to *supination*, which then is followed by a steady rotation of the wings to reverse the orientation of the wings, maintaining the leading edge into the direction of the relative wind; followed by a rapid acceleration that transitions the wing to another period of steady translation in the rearward, or *up* stroke, and the cycle is finalized by deceleration

to pronation, and rotation of the wings back to the downstroke posture. Figure 2.1 shows the a sequential progression of a hawkmoth's flap cycle.
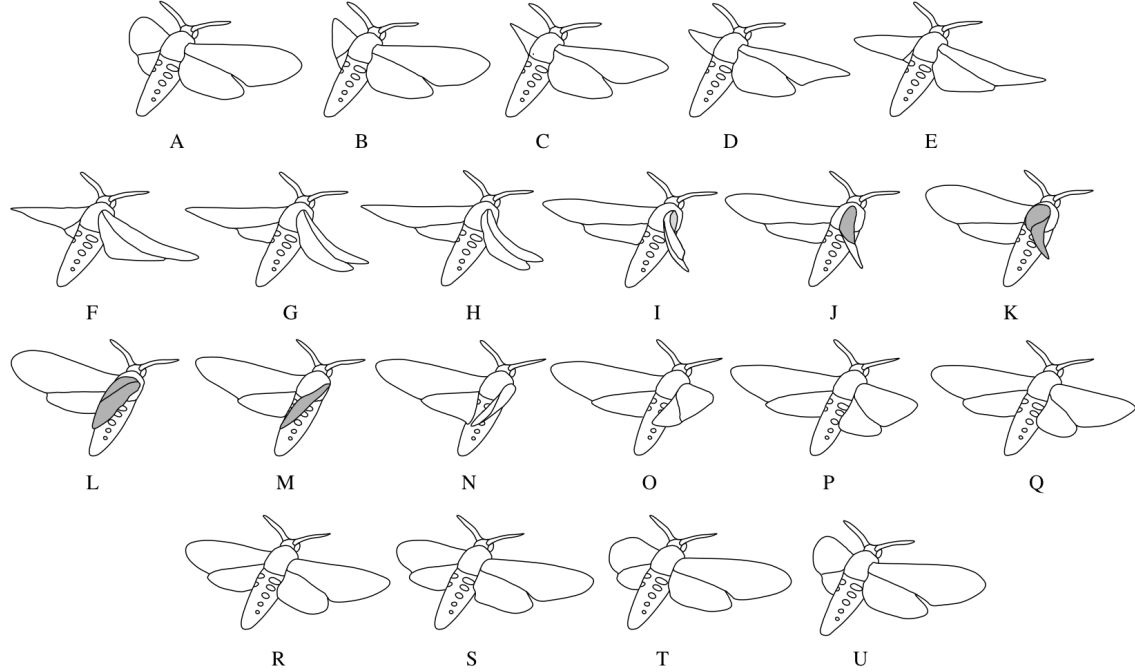
Figure 2.1: A complete Manduca Sexta flap cycle from high-speed video capture sequence. (A) & (U) signify the mid-point of supination. The white wings surfaces are the *dorsal* or *top* view, and the shaded areas are the *ventral* or *bottom* wing surfaces, which illustrate the amount of wing flip and flexion during a single cycle [91].

Figure 2.2 depicts a graphic of the the upstroke and the downstroke phases of insect flight with a horizontal stroke plane. Three degrees of freedom, given by three body centered cartesian angles: *i*) mean stroke plane angle ($\bar{\beta}$)—the angle between the mean plane of the wing's $^3/_4$ chord point and the horizontal; *ii*) elevation angle ($\theta(t)$)—the angle between the $^3/_4$ chord point and β, when not in the stroke plane, ($+\theta$) is above β, and ($-\theta$) is below β; and *iii*) wing position angle ($\phi(t)$)—the angle of the wing at a specific time in the stroke phase; these three Euler angles, in conjunction with a single wing rotation angle, the angle of attack ($\alpha(t)$)—the angle between the leading edge and the relative wind measured from the horizontal—completely describe the wing orientation in space as well as the rotation of the wing about a longitudinal axis [31, 32, 33, 60].

35

(a) Downstroke   (b) Upstroke
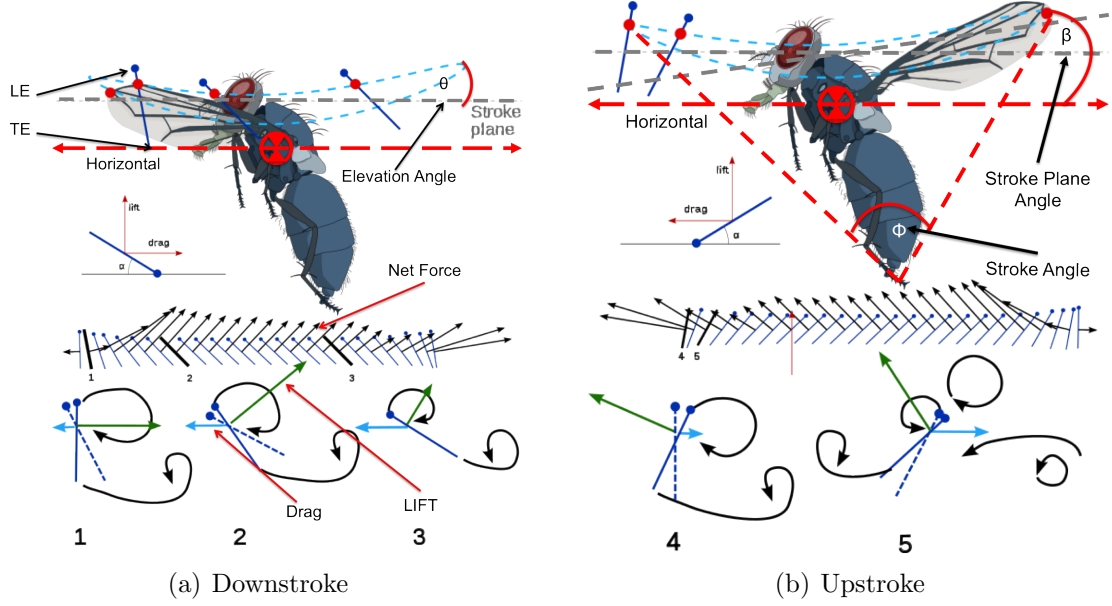
Figure 2.2: Depiction of insect flight during a complete flap cycle. *Left:* downstroke. *Right:* upstroke. The *blue* line represents a 2-D chord slice of the wing with the Leading Edge (LE) shown with a dot, and the Trailing Edge (TE) without. The *red* dot represents the $^3/_4$ chord point or Center of Mass (CoM) of the wing from which the cartesian angles are determined. The three kinematic cartesian angles shown completely describe the wing orientation during the stroke cycle. The bottom of each cartoon shows a 2-D wing trace schematic of the wing and the oreintation progression of the lift and drag forces during the flap cycle. Lastly, the *black* curved lines show the growth and development of Leading Edge Vortex (LEV) and Trailing Edge Vortex (TEV) sections at each stage in the flap cycle.

A fourth parameter; the mean body tilt angle ($\bar{\chi}$), the angle between the body Center of Gravity (CG) and the horizontal, specifies the angle of the body above or below the horizontal, which is used to describe the body attitude of the entire flight vehicle *or* insect body during forward flight, assuming the body is oriented with the relative wind, and is not *crabbing* into the wind; is a necessary parameter when analyzing flight conditions other than hover [32, 33]. In all the experiments conducted in this research, the wing is mounted to a fixed stationary sting, resulting in strictly hover simulated flight conditions, and $\chi = 0$.

Since so much of the discussion surrounding flapping flight analysis relies upon a tacit understanding of the nuanced definitions of steady and unsteady flows, it is appropriate to define the nature of steady and unsteady flows. Within the context of force and flow dynamics, the term *steady* signifies explicit time independence of

fluid forces; and therefore, *unsteady* flows have an explicit temporal evolution due to inherently time-dependent phenomena within the fluid [71]. Specifically, in flapping flight aerodynamics, *steady* does not imply time invariance. The forces exerted on airfoils may change with time as the wing feather angle changes during the wing stroke, which changes the lift and drag forces developed, without being explicitly dependent on time itself, because the underlying motion of the airfoil varies, causing a corresponding change in the resultant forces. If the forces at each instant are modeled by the assumption of inherently time-independent fluid dynamic mechanisms, then such a model is called *quasi-steady*, i.e. the forces are steady at each instant in time, but vary with time progression during the flap cycle due to kinematic time dependence of the wing position with respect to the relative wind, which is ultimately a function of the control dynamics of the insect or the digital feedback control system of the FWMAV [71, 73].

The unsteady aerodynamic phenomena driving small-scale flapping wings, which generate sufficient aerodynamic forces for lift and forward flight, are produced by high speed dynamic rotations of the wing. The bulk wing motion, comprised of a coupling of translation and rotation, are oscillatory in nature, and encompass a large variety of motion profiles and associated tip paths for different species of insects. The tip path associated with a specific winged flier depends on the morphology, the configuration of the wing and body structures and joints, and the physiology, which determines how the wing is actuated [9, 31, 32, 52]. Figure 2.3 shows a graphic depiction of a typical wing stroke tip trace with a slightly inclined stroke plane. Determination of the wing position with respect to its body axis coordinates will be essential later during analysis of the aerodynamic forces and moments created by the AFIT FWMAV.
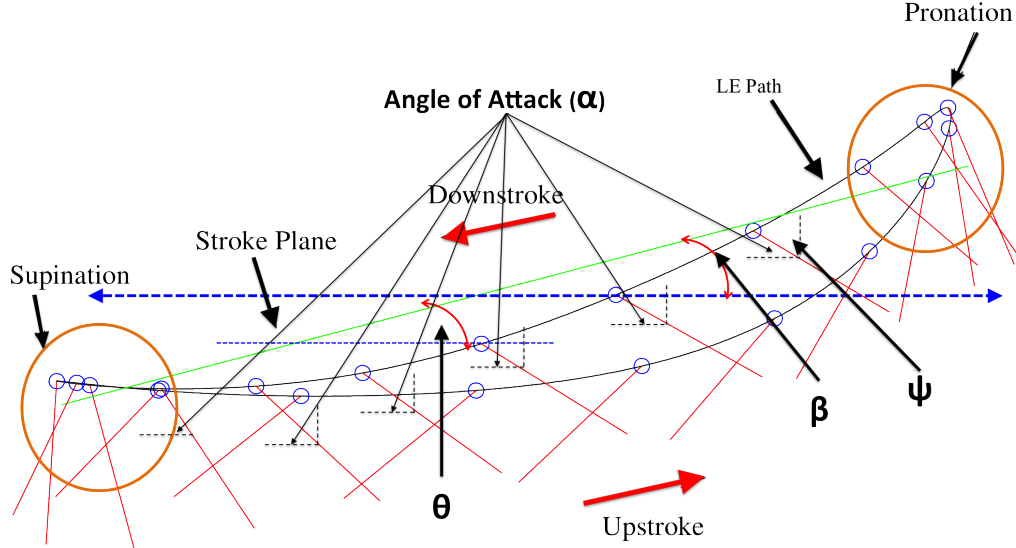
Figure 2.3: Graphic depiction shows a typical wing LE trace of a slightly inclined stroke angle. The 2-D wing section is shown in red. The LE is denoted by a blue circle. The rotations at the end of the each translation half-cycle are circled. The LE path during the stroke is shown by a black arc, and the mean stroke plane is drawn through the tip trace by a green line. The stroke plane angle, β, and the elevation angle, θ are shown relative to the horizontal and stroke plane respectively—modified from [57].

Sane summarized in his text on the aerodynamics of insect flight, all of the effects on a flapping wing may be reduced to three major sources of aerodynamic phenomena: *i*) the creation and sustainment of a leading edge vortex; *ii*) the quasi steady-state aerodynamic forces on the wing observed during translation; and *iii*) the wing's contact, and subsequent recapture, with its shed wake from previous strokes, which is a form of dynamic stall [71]. Of course, the mathematical rigor to fully characterize these seemingly innocuous flight mechanisms are time dependent and ephemeral. There is no clear delineation between the start of one mode and the end of the previous, and the prevalence of one varies as the size of the flight system changes. The size of flying insects ranges from about 20μg to about 3g; and as flight mass increases, there is a corresponding increase in wing area, and a decrease in wing beat frequency [31, 32, 37, 60, 61, 71]. For larger insects, the Reynolds number may be as high as 10^4, and for smaller insects, it may be as low as 10^2. This means that viscous effects are much more important to the more diminutive fliers, although the flow is still in

the laminar region, even up to the largest flapping wing fliers [71].

2.4.1   Finite vs. Infinite Wings.

Since much of the theoretical literature addresses the aerodynamic performance of idealized 2-D sections of wings, it is important to distinguish between finite and infinite wings. *Finite wings* refer to an actual 3-D wing with two tips, and thus a finite length span. From the perspective of fluid dynamics, the importance of the wing tips is they create a component of fluid velocity that runs along the span of the wing, perpendicular to the direction of far-field flow during linear translation, and of course upon pronation and supination. The pressure differential between the upper and lower wing surfaces forces the high pressure air beneath the wing to migrate towards the low pressure region, spilling over and around the wing tips into the upper low pressure region [70, 59]. This mixing forms vortices that stream from behind the wing, and continue to roll-up into two main vortex structures, one aft of each wing, of opposing sense [47, 70]. The vortical structures have a downward spiral, which causes an induced velocity, whose vertical component is called *downwash*, and whose horizontal component is called *induced drag* [49, 70, 59]. Where the 2-D infinite wing theory postulates constant circulation along the span, real 3-D finite wings have a tapered circulation, diminishing from root to tip, where the circulation is identically zero at the wing tip—an elliptic distribution results in the theoretical minimum induced drag [47, 49, 70]. Every time the circulation changes, i.e. when the lifting angle of attack changes, a vortex is shed into the free stream, and the shed vortices on a given wing share the same rotational direction; and therefore, merge into a single trailing vortex. Prandtl theorized the trailing vortices from each wing are essentially a single, but bifurcated horseshoe vortex extending across the entire span from tip to tip, running through the center of pressure, and closed along the back by the starting vortex,

39

which extends to infinity, and is equal in strength to the bound vortex along the span—preserving Helmholtz's first two vortex laws [47, 49, 59, 70].

Infinite wings are theoretical abstractions of 2-D structures creating strictly chordwise flow from LE to TE, eliminating spanwise flow from wing root to wing tip. Experimentally, 2-D wings can be simulated by positioning baffles close to the wing tips with rigid walls, which limit spanwise flow, thus constraining the fluid to move in two dimensions. Since the wing is constrained at the tips, by definition, an infinite wing cannot perform flapping motions since the theoretical tip blocking should extend infinitely. In 2-D flow, thin-airfoil theory states the airfoil is replaced with a mean camber line, and viscosity forces an irrotational circulation around the wing, which is proportional to the lift, causing a streamline to flow smoothly over the sharp TE of the wing, which results from the superposition of a uniform flow and flow induced by the circulation distribution [47, 59]. An empirical observation, known as the *Kutta condition* states a body with a sharp TE creates a circulation sufficient to hold the rear stagnation point at the TE of a finite angle to force the flow where the upper and lower surfaces meet tangentially, parallel to the mean camber line; thereby implying there is a singular value for the circulation which prevents an infinite velocity at the trailing edge [70, 59]. Prandtl's method of sections, or blade element approximation states: *In each cross section of a wing of finite span, the velocity distribution in the immediate neighborhood of the wing is assumed identical to the velocity distribution of the two-dimensional flow around the same section, with $\vec{V}$ as the velocity vector at infinity* [47, 59]. However, 2-D formulations based on the infinite wing assumption, breaking the wing into differential blade elements and integrating across the span, have often proved useful in the study of flapping wing flight, specifically yielding decent approximations to measured wing flight vertical forces, but fails to capture the significance of any spanwise side forces, by definition assuming they are zero (F_y=0),

which are instrumental in developing precise autonomous control algorithms.

2.4.2 The Translational Quasi-Steady Approximation.

Conventional aerodynamic analysis of flapping wing flight attempts to reduce the problem of revolving wing dynamics to a succession of static flight conditions, called the *quasi-steady approximation.* This approximation invokes the assumption that the instantaneous forces on a flapping wing are equivalent to the forces generated for a static wing at the same instantaneous velocity and angle of attack to the relative wind.

Weis-Fogh first posed the quasi-steady assumption as the method to analyze insect flight in 1972. The assumption can only be tested theoretically in proof-by-contradiction. The mean forces produced by the wings during a flap cycle are calculated using the quasi-steady assumption; if the forces do not satisfy the net force balance—vertical force balances weight, and horizontal force balances drag—then the assumption is rendered incorrect. If the mean quasi-steady forces do satisfy the force balance, then it cannot be discounted as a valid flight mechanism [31]. Ellington showed the quasi-steady approximation is much more valid for fast forward flight because of the low value of the reduced frequency parameter (K), which is the ratio of the flapping velocity to the forward flight velocity, given in Equation 2.34 [53].

$$K = \frac{2\pi f \bar{c}}{2U_{ref}} \tag{2.34}$$

Where f is the flapping frequency, $\bar{c}$ is the mean wing chord, and U_{ref} is the reference velocity at the radius of the second moment of wing area ($r_s(S)$), defined by Equation 2.35,

$$\bar{\omega} r_2(S) R \tag{2.35}$$

where $\bar{\omega}$ is the mean rotational velocity ($\bar{\omega}$) of the wing ($\omega = \dot{\alpha}$), equal to the product of twice the wingbeat amplitude (or total stroke angle), Φ, (in radians) and the wingbeat frequency [53]. Ellington gave a general expression for the k$^{\text{th}}$ moments of wing area (S_k), applied to a generalized wing length and area, as a function of the distribution of the normalized chord ($\hat{c}$) $= {}^{c_i}/_{\bar{c}}$, given in Equation 2.36 [32].

$$S_k = 2 \int_0^R cr^k dr = SR^k \int_0^1 \hat{c}\hat{r}^k d\hat{r} \tag{2.36}$$

Where the *hatted* ('∧') variables denote dimensionless values, $\hat{r}$ is the nondimensional radius ($\hat{r}$), expressed as ${}^{r_i}/_{R}$, and the nondimensional radius of the k$^{\text{th}}$ moment of wing area ($\hat{r}_k^k(S)$) is given in Equation 2.37 [32, 51, 84].

$$\hat{r}_k^k(S) = {}^{S_k}/_{SR^k} = \frac{SR^k \int_0^1 \hat{c}\hat{r}^k d\hat{r}}{SR^k} = \int_0^1 \hat{c}\hat{r}^k d\hat{r} \tag{2.37}$$

A simplifying approximation can be made to eliminate the integrals by assuming the area of the wing is concentrated at a single distance, $\hat{r}_k(S)$, from the wing base, then the k$^{\text{th}}$ moment of area is exactly S_k. After making all the appropriate substitutions, the final form of K is shown in Equation 2.38.

$$K = \frac{\bar{c}}{4\Phi r_2(S)R} \tag{2.38}$$

A low value of K represents a steady flight velocity dominated flow, which reduces the viscous effects on the spatial derivatives of the NS equations, thereby mitigating the unsteady effects, and bolstering the contribution of the macro quasi-steady aerodynamic effects [31]. However, at slow flight speeds, the value of K is much higher, and in the limit, as forward velocity approaches zero in a hover, $K \to \infty$. Here the unsteady viscous effects dominate. The wings transition quickly between upstroke

and downstroke, undergoing rapid acceleration and decelerations in only a few chord lengths, which makes the virtual mass of air surrounding the wings, and the unsteady circulatory effects of rapid pronation and supination, critical aerodynamic considerations in the understanding of the complete aerodynamic picture of flapping wing flight [31].

Hovering flight presents one of the most challenging aerodynamic problem for FWMAV designers, while simultaneously relaxing other mathematical complications. The force and moment balance is simplified by creating a stationary coordinate system, permitting easy application of the NS equations in an Eulerian fixed coordinate system, over the more onerous mathematical treatment required for a Lagrangian moving reference frame. Hover is defined as the flight condition governed by a zero net force balance where lift equals weight, and drag equal thrust, with zero resulting translational velocity parallel to the horizontal. Hover flight does not have a net forward thrust or velocity component, which eliminates the need to consider body lift, interference drag, and the other aerodynamic prescriptions usually employed for assessing total vehicle dynamics. However, hover does require the highest lift coefficients because the relative velocity of the wings is not aided by the forward flight velocity, and hover demands the greatest total power expenditure, which gives FW-MAV designers a useful minimum power threshold necessary to meet in vehicle design [31].

The mathematical expression of the quasi-steady approximation can be expressed through either the Rankine-Froude propeller actuator disk model, or realized through application of Prandtl's blade element method described above in section 2.4.1. The actuator disk theory is a momentum transfer method which models the net force developed on the airfoil by the induced velocity jet imparted to the surroundings, which is a convection of momentum through the control volume, whose boundaries

include a vertical cylindrical column of air surrounding the wing [33, 34, 35, 72, 73, 74]. Calculation of forces from PIV velocity measurements is a proven application of this method. The equations used to calculate the net downward vertical force, *thrust*, and force results from reduced PIV data are presented later in *Chapter V*.

The blade element method (BEM), and its variations, are used very frequently in control models because its application is straightforward, and it facilitates easy linearization of the constitutive force equations control engineers use to develop models of vehicle behavior [26, 74, 77]. The BEM model solves for the forces in the body, or wing reference coordinate system, by defining a differential wing section (dy) and utilizing classic thin airfoil theory proposed by Prandtl, calculates the instantaneous differential lift and drag force on the differential wing element, and solves for the instantaneous aerodynamic wing forces by integrating the differential lift and drag along the wing span, R, [2, 31, 33, 74]. Refer to figure 2.4 for a diagram of the wing and the wing section definitions used in the blade element approximation.
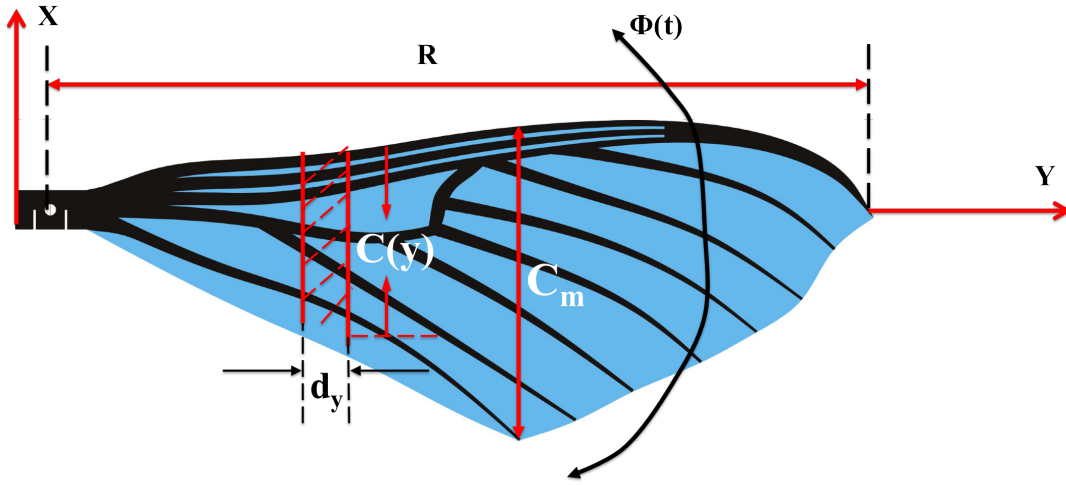
Figure 2.4: Diagram of a wing with the blade element sections identified—adapted from [2, 26].

For a given wing stroke angular velocity, $\dot{\phi}(t)$, and angle of attack, $\alpha(t)$, the instantaneous differential lift and drag, produced by a differential wing element, is found through the classic lift and drag equations shown below in equation 2.39 [31, 49, 70]

$$L = \tfrac{1}{2}\rho C_L V_\infty^2 S$$
$$D = \tfrac{1}{2}\rho C_D V_\infty^2 S \tag{2.39}$$

when differentiated with respect to span position, they yield the differential lift and drag equations for a wing element (dy), given below in Equation 2.40 [2, 26, 31, 34, 74].

$$dL = \tfrac{1}{2}C_L \rho y^2 c(y)\alpha(t)\dot{\phi}^2(t)\ dy$$
$$dD = \tfrac{1}{2}C_D \rho y^2 c(y)\alpha(t)\dot{\phi}^2(t)\ dy \tag{2.40}$$

where $\dot{\phi}(t)$ is the wing stroke angular velocity $(\dot{\phi}(t))$, and $c(y)$ and dy are defined in Figure 2.4 above. Now that the elemental forces have been derived for a differential wing element, integrating Equation 2.40 across the span, results in the instantaneous aerodynamic wing forces, given below in Equation 2.41 [2, 26, 34, 51, 74]

$$L = \int_0^R dL = \tfrac{1}{2}C_{L,t}\rho\alpha(t)\dot{\phi}^2(t)I_A$$
$$D = \int_0^R dD = \tfrac{1}{2}C_{D,t}\rho\alpha(t)\dot{\phi}^2(t)I_A \tag{2.41}$$

where $C_{L,t}$ and $C_{D,t}$ are the approximate instantaneous aerodynamic coefficients, given in 2.49, and the second moment of wing area (I_A) is given by Equation 2.42 below, and uses the nondimensional radius of the 2nd area moment obtained from Equation 2.37 [32, 51, 84, 92].

$$I_A \equiv S_2 = 2\sum_i^N r_i^2 c_i dr_i$$
$$S_2 = \hat{r}_2^2(S)\,(SR^2) \qquad (\text{in } \text{m}^4) \tag{2.42}$$

Equipped with information about the wing's morphological parameters, and knowing either discrete values of $\phi(t)$ and $\alpha(t)$ at specific time intervals, or having an equation specifying ϕ and α as a function of time, the quasi-steady aerodynamic forces can be solved as a function of time during the wing beat cycle. Ellington [32],

O'Hara [65], and Usherwood [84] have tabulated morphological parameters from extensive allometry studies of *Manduca*, and those values, along with the basic geometric properties—span (R) and mean chord ($\bar{c}$)—of the engineered wing, were use to interpolate to compute the necessary morphological parameters used in the subsequent aerodynamic analysis performed herein. The values of ϕ and α can be computed from video estimation and tracking (see section 3.2.3 for more details on the present work done on wing tracking), cyclic lift and drag forces are recorded with a force balance, and the cycle average forces are used to calculate the $\overline{C_L}$ and $\overline{C_D}$.

Ellington's 1984 six paper manuscript series chronicled his series of experiments on six different *orders* of insect, spanning multiple male and female samples, from twenty different *families* of insects, and his results on the proof-by-contradiction were inclusive as to the validity of the quasi-steady approximation first posed by Weis-Fogh. He concluded the quasi-steady assumption's validity was a function of kinematic group, *horizontal stroke plane, inclined stroke plane, vertical stroke plane, or clap-and-fling / peel-n-fling*, rather than an absolute ubiquitous flapping wing explanation or not [31]. He found the value of the measured $\overline{C_L}$ was greater than the value of $C_{L_{max}}$ calculated from the quasi-steady approximation in both the clap-and-fling and the vertical stroke plane insect classes, which proves the assumption false, but the results were less conclusive, and much closer, in the other kinematic groups, including the horizontal stroke plane insects, of which the hawkmoth belongs; thereby revealing the quasi-steady approximation as a plausible physical explanation of enhanced lift [31].

Sane and researchers at the University of California at Berkeley conducted a series of much more controlled experiments on a dynamically scaled fruit fly, *Drosophila Melanogaster*, wing with precisely prescribed wing motions, and a larger wing area, which made both the measurements of the wing morphological parameters, the wing

kinematics, and the subsequent dual-axis force measurements more repeatable and accurate, and therefore more reliable [73]. They examined 191 separate sets of kinematic patterns by changing stroke amplitude, angle of attack, rotation timing, rotation duration, and the shape and magnitude of stroke deviation to determine what influence, if any, wing kinematics have on the production of unsteady aerodynamic forces in insect flight [73]. They used the formulation for generalized force coefficients developed by Ellington [33] and Dickinson [24], given in Equation 2.46 below to calculate force coefficients.

$$C_{Force_i} = \frac{8\rho_w \overline{\hat{F}}_i \cos^2(\beta_r)}{\rho n^2 \Phi^2 R^2 (\hat{r}_2^2(S)) \left(\overline{d\hat{\phi}/d\hat{t}}\right)^2 \cos^2(\beta)} \tag{2.43}$$

where:

$\rho_w \equiv$ wing loading $= \frac{mg}{s}$

$\overline{\hat{F}} \equiv$ nondimensional force $= \frac{\overline{F}}{mg}$

$\beta_r \equiv$ effective stroke plane angle

$r_2^2(S) \equiv$ nondimensional radius of 2nd moment of wing area, given in 2.37

the nondimensional stroke angle $(\hat{\phi})$ is calculated by Equation 2.44

$$\hat{\phi} = \frac{2(\phi - \bar{\phi})}{\Phi} \tag{2.44}$$

using a horizontal stroke plane, and the small angle approximation, $\frac{\cos^2(\beta)}{\cos^2(\beta_r)} \approx 1$, substituting and reducing for a single wing reduces the expression for C_F to:

$$C_{F_i} = \frac{8\overline{F_i}}{\rho n^2 \Phi^2 \bar{c} R^3 (\hat{r}_2^2(S)) \left(\overline{d\hat{\phi}/d\hat{t}}\right)^2} \tag{2.45}$$

substituting:

$$\bar{c} = \frac{S}{R}$$

$$S = \frac{R^2}{\mathcal{R}}$$

further reduces the equation for C_{F_i} to the final form below:

$$C_{F_i} = \frac{8\overline{F_i}\mathcal{R}}{\rho n^2 \Phi^2 R^4 \left(\hat{r}_2^2\left(S\right)\right)\left(\overline{d\hat{\phi}\big/d\hat{t}}\right)^2} \tag{2.46}$$

where $\bar{F}_i$ designates the generalized forces—*vertical, horizontal, and spanwise*—and the mean nondimensional angular velocity $\left(\overline{d\hat{\phi}\big/d\hat{t}}\right)$, defined in Equation 2.47 below, is used as the characteristic velocity in subsequent body force calculations.

$$\frac{\overline{d\hat{\phi}}}{d\hat{t}} = \frac{d\left(\frac{2\left(\phi-\bar{\phi}\right)}{\Phi}\right)}{dt} \tag{2.47}$$

A 2$^{\text{nd}}$ order central difference approximation, with an accuracy of $\text{O}\left(\Delta t^2\right)$, was used to numerically compute the derivative of the wing flap angle, ϕ:

$$\left(\frac{d\phi}{dt}\right)_i = \frac{\phi_{i+1} - \phi_{i-1}}{2\Delta t} + \text{O}\left(\Delta t^2\right) \tag{2.48}$$

They fit curves to the measured cyclic lift and drag forces from 180° Φ sweeps conducted at various values of prescribed α to provide an equation of the quasi-steady force coefficients as a function of α (in rads), given below in Equation 2.49, which were used to calculate forces using the 'quasi-steady' 2-D approximation, to compare to the measured force balance values at the specified kinematic test conditions [73].

$$C_{L,t} = 0.225 + 1.58\sin\left(2.13\alpha - 7.2\right)$$
$$C_{D,t} = 1.92 + 1.55\cos\left(2.04\alpha - 9.82\right) \tag{2.49}$$

The results showed the quasi-steady estimates failed to capture the time-history mea-

sured lift for nearly all the kinematic variations, but results improved when compared to the cycle averaged values of $\overline{C_L}$. The quasi-steady approximation also underestimated the magnitude of the $\overline{C_D}$ for all conditions [73]. Anderson plotted 6-DoF force balance results for symmetric flapping of his prototype FWMAV against the quasi-steady approximation obtained from Equation 2.49. His results confirmed the quasi-steady approximation under-predicted the vertical force (F_x), and due to its 2-D finite wing origin, did not offer any prediction of the presence of a side force (F_y) or axial force (F_z), nor an airfoil generated moment about any axis. Figure 2.5 shows the individual cartesian force and moment plots against the quasi-steady prediction trends.
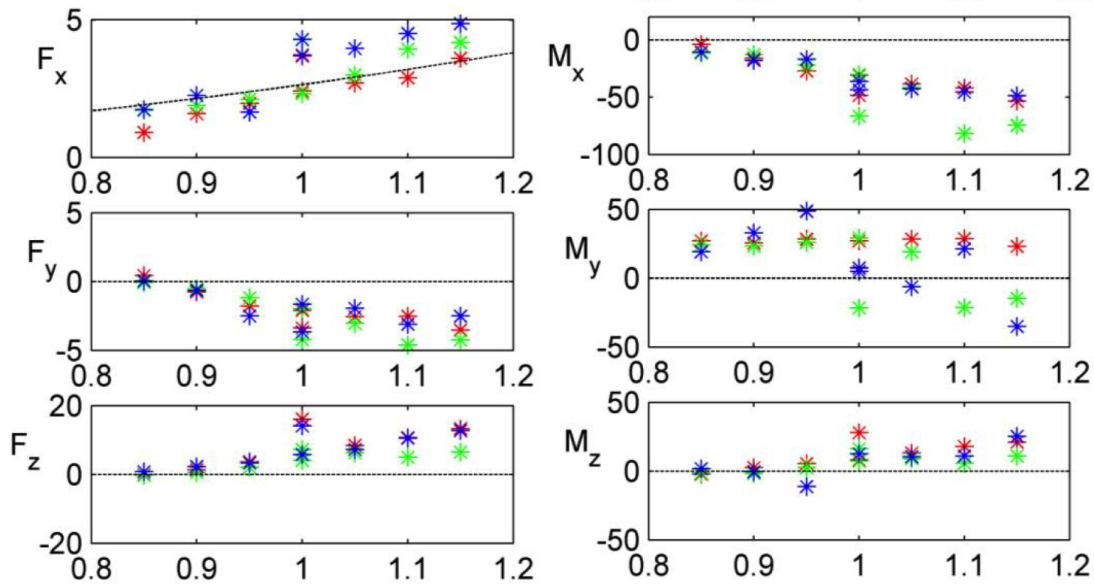
Figure 2.5: Force balance results from Anderson's symmetric flapping tests vs. the quasi-steady approximation obtained from Equation 2.49 plotted against drive amplitude. The dashed line represents the predicted quasi-steady trend and the color asteriks represent different test groups. *Left:* Force data in [gF]. Top is F_x, Center is F_y, Bottom is F_z. *Right:* Moment data in [gF-mm]. Top is M_x, Center is M_y, Bottom is M_z—modified from [2].

Sane concluded the discrepancy was due to the contribution of rotational effects that steady-state estimates do not capture, which implies prior estimates of the required mechanical power necessary to design and build a viable FWMAV based on wing kinematics were most likely grossly underestimated, because the required me-

chanical power is directly related to the amount of drag force to overcome. Therefore, in 2002, Sane and Dickinson set out to develop an improved quasi-steady approximation that accounted for the rotational effects, albeit, steady in nature, but still an improvement over the straight translational blade element approach developed by Prandtl, Glauert, Theordorsen, and Munk in the infancy of aerodynamics as a core discipline. They used the same mechanical fruit fly setup cited previously in [73], and tested a wing in steady translation at varying angular velocities, across the same series of constant stroke angles (Φ), and feathering angles (α), as before. They compared the instantaneous forces to the translational quasi-steady approximation using Equation 2.49, and the differences between the measured and estimated forces were attributed to a combination of rotational and inertial effects [74]. Figure 2.6 shows the measured vs. the translational net forces for two different rotational speeds.
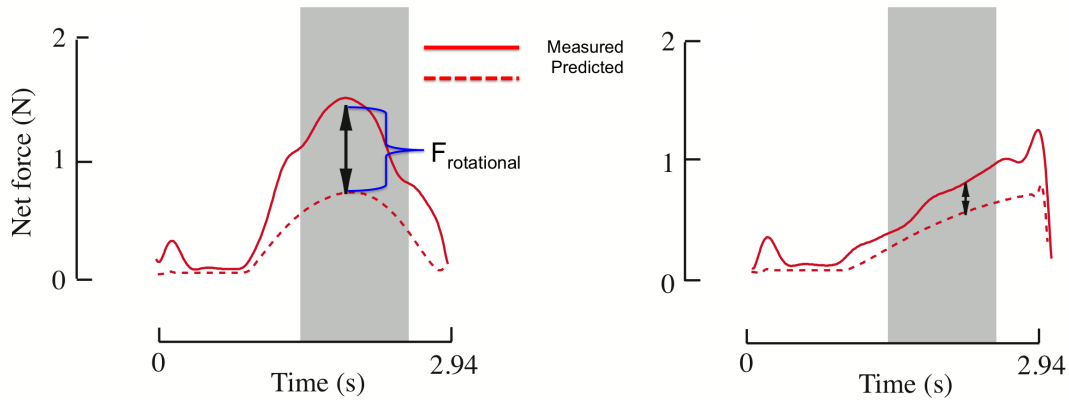
Figure 2.6: Measured vs. translational quasi-steady prediction at a constant translational velocity of $0.27 \ ^m/_s$. Measured values are indicated by soild lines, predicted values are indicated by dashed lines. *Left:* rotational velocity = 14.2**RPM**. *Right:* rotational velocity = 6.36**RPM**—modified from [**74**].

Since the translational and rotational velocities were held constant within a prescribed α test sweep, the inertial effects were minimized, and therefore neglected, leaving the difference between actual and predicted forces essentially attributable to the rotational effects alone. They developed a mathematical model based on a 2-D inviscid approximation, and used the experimental rotational coefficients determined above

to transform the inviscid 2-D rotational model into a 3-D model using blade element theory. The improved quasi-steady model was born from the merger of the rotational coefficients and the translational quasi-steady model, as well as a consideration for the added virtual mass effects [74]. In the absence of skin friction drag, the forces acting normal to the wing are the summation of four forces, $F_{inst} = F_{vm} + F_{rot} + F_{trans} + F_{us}$ [74]. F_{vm} is the force due to the inertia of moving the virtual mass of air, approximated by a right circular cylinder, with the major axis running coincident with the leading edge; F_{rot} is the rotational force, F_{trans} is the translational force, and F_{us} is the unsteady aerodynamic force [32, 34, 74].

The force due to virtual mass (F_{vm}) can be approximated by calculating the differential force acting on an infinite 2-D blade element, and integrated across the span to get a 3-D approximation, given in Equation 2.50 below [74]. The F_{vm} on an infinitely thin wing acts normal to the surface of the wing at all times, and ostensibly during symmetric flight, in a horizontal stroke plane, the net overall force contribution would be approximately zero [24, 25, 71, 84]

$$F_{vm} = \frac{\pi}{16}\rho\bar{c}^2 R \left[4R \left(\ddot{\phi}(t)\sin\alpha(t) + \dot{\phi}(t)\,\dot{\alpha}(t)\cos\alpha(t) \right) \int_0^1 (\hat{c}(r))^2\,\hat{r}dr - \ddot{\alpha}(t)\,\bar{c} \int_0^1 (\hat{c}(r))^2\,dr \right]$$
$$(2.50)$$

Where $\dot{\alpha}(t)$ is the wing rotational velocity ($\dot{\alpha}(t)$), $\dot{\phi}(t)$ is the wing stroke angular velocity ($\dot{\phi}(t)$), given above in 2.44, $\ddot{\phi}(t)$ is the wing stroke angular acceleration ($\ddot{\phi}(t)$) and $\ddot{\alpha}(t)$ is the wing rotational angular acceleration ($\ddot{\alpha}(t)$), which can be found by differentiating the expression for $\dot{\phi}(t)$ and $\dot{\alpha}(t)$ respectively with respect to the flap cycle time (t).

The net force due to translation (F_{trans}) is comprised of the vector sum of the orthogonal components of the lift and drag translational forces, and is shown in

Equation 2.51 below [74].

$$F_{trans} = \frac{\rho S U_t^2 \hat{r}_2^2(S)}{2} \sqrt{\left(C_{L,t}^2(\alpha) + C_{D,t}^2(\alpha)\right)} \tag{2.51}$$

where the translational values of $C_{L,t}$ and $C_{D,t}$ were given in Equation 2.49 above.

The force due to rotation (F_{rot}) was calculated by rearranging the statement for F_{inst}, to $F_{rot} = F_{inst} - F_{trans}$, whereby the rotation force is found by subtracting the translational quasi-steady estimate from the steady-state measured instantaneous forces. The rotational theoretical model was derived buttressed against idealized assumptions, whose applicability to real-world flapping flight is suspect: i) the direction of the fluid velocity vector is equal to the slope of the airfoil surface at every instant, effectively the no-slip condition; ii) the vorticity at the trailing edge must be zero to fulfill the *Kutta* condition; and iii) the small angle approximation used in the *Kutta-Jukowski* assumption was applied to the large amplitude shifts in the rotational angle of attack, resulting in the d'Alembert paradox associated with inviscid non-real flows of *zero* net induced drag, which conveniently makes the net aerodynamic force on the wing equal to the net lift found by integrating the differential lift across the span. This results in the net instantaneous rotational forces equal to the rotational component of the total aerodynamic force [74]. Equation 2.52 gives the rotational circulation after applying the assumptions enumerated above.

$$\Gamma_{rot} = C_{rot}\omega\bar{c}^2 \tag{2.52}$$

where the rotational coefficient (C_{rot}) is given by Equation 2.53

$$C_{rot} = \pi \left(\frac{3}{4} - \hat{x}_o\right) \tag{2.53}$$

and $\hat{x}_o$ is the nondimensional distance from LE to the axis of wing rotation ($\hat{x}_o$). We

will see later that, although these assumptions make it possible to mathematically express F_{rot}, they are physically unrealistic, and therefore result in force estimates that do not match the measured values. Equation 2.54 gives the finalized equation for the rotational force [74].

$$F_{rot} = C_{rot}\rho U_t \omega \bar{c}^2 R \int\limits_0^1 (\hat{c}(r))^2 \hat{r} dr \tag{2.54}$$

Figure 2.7 shows the lift and drag for the measured vs. improved quasi-steady model for a symmetric rotation about the wing axis; meaning the wing rotated at supination and pronation at the exact half-stroke.
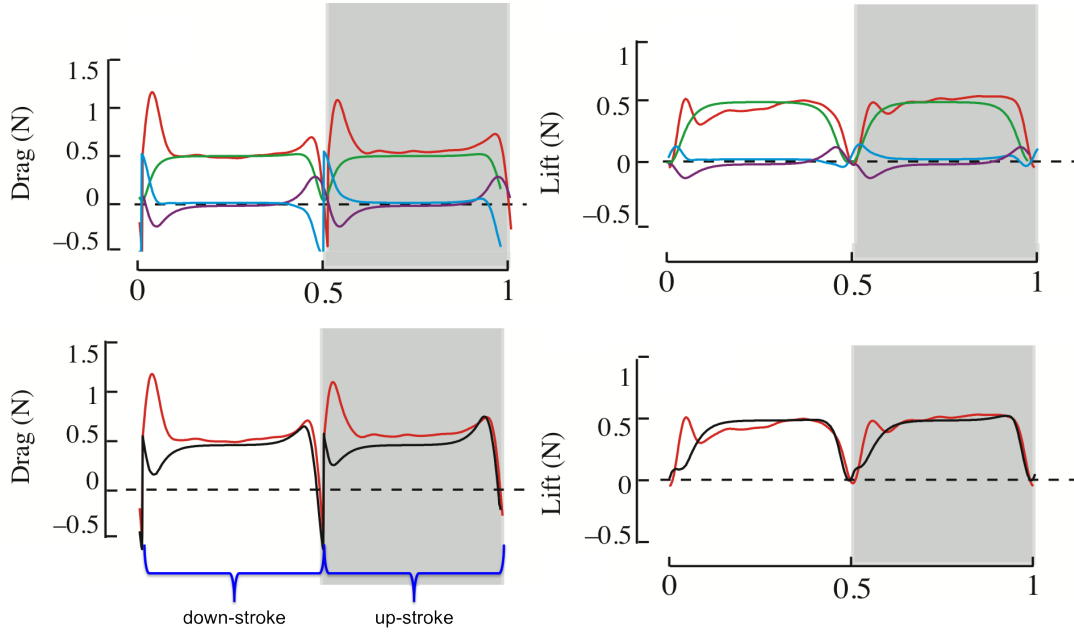
Figure 2.7: Measured vs. the improved quasi-steady prediction for a symmetric rotation at the half cycle. *Top*: The individual componets of the predicted F_{inst} vs. measured values. Red = measured forces, green = quasi-steady translational component (F_{trans}), purple = quasi-steady rotational component (F_{rot}), blue = added virtual mass force (F_{vm}). *Bottom*: Summation of all the predicted quasi-steady contributions vs. measured values. Red = measured values and black = improved quasi-steady model estimates. *Left*: Drag and *Right*: Lift–modified from [74].

Although the revised quasi-model displayed an improvement over the original translational quasi-steady model, it still underestimated the lift and drag produced by the actual wing. Sane concluded the remaining difference must be the unsteady

aerodynamic effects of what Ellington, Usherwood, Van den Berg, and Willmott identified at Cambridge as the development of a stable and sustained leading edge vortex and wake recapture [74].

2.4.3 Leading Edge Vortex.

At wing lengths on the order of 50 millimeters, the dominant unsteady aerodynamic phenomenon assumed to be responsible for aerodynamic lift is a LEV produced by a laminar flow separation near the leading edge of the wing [34, 35, 85, 86, 93]. For illustration purposes, Figure 2.8 shows the development of a laminar separation bubble over a fixed, but flexible, traditional wing.
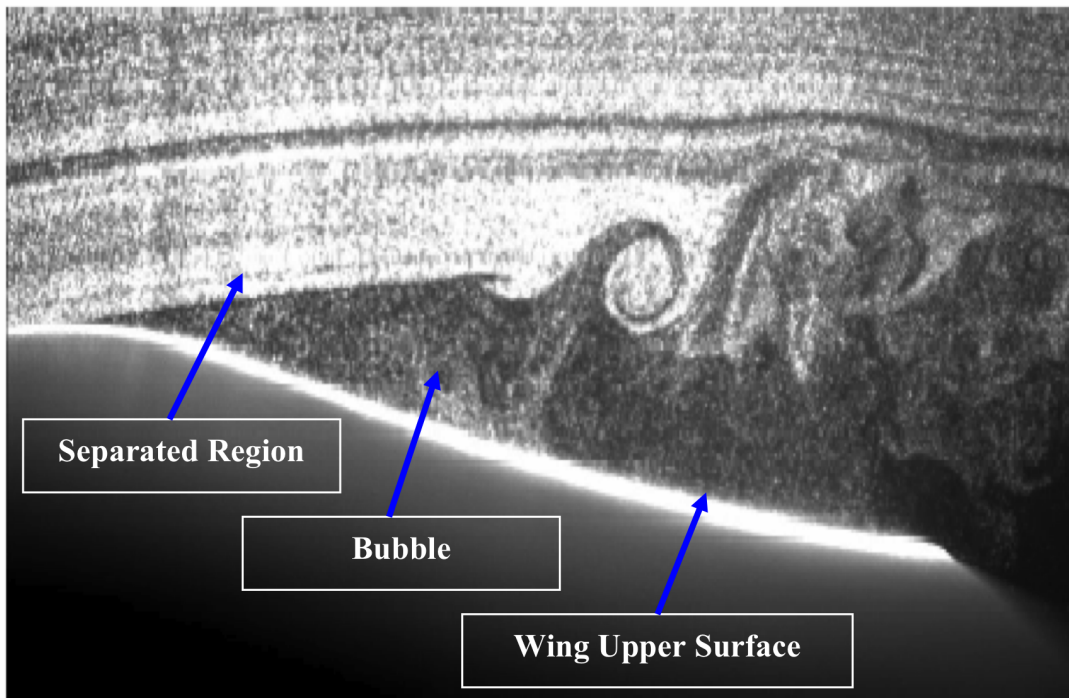
Figure 2.8: Laminar separation bubble caused by the viscous boundary layer where the flow slightly separates past the mid-chord and then rapidly reattaches aft of the separated streamline, causing a recirculation rear of the mid-chord, which entrains non-circulatory air, forming a bubble of energized air along the wing surface—modified from [22].

The finite length hawkmoth wing exhibits significant three-dimensional tip effects, which produce a strong vortical structure at the wing tip. The three-dimensional tip

effects are exacerbated by the spanwise pressure distribution, which features a region of low pressure near the wing tip. The spanwise flow, and the LEV coalesce with the tip vortex to form a continuous vortical structure that extends along the length of the wing from near the wing root until it is shed into the wake along the path of the wing tip as illustrated in Figure 2.9. The vortex wake produced by the LEV tip vortex, and the combined Starting and Stopping (SS) vortices produced by each wing, form a vortex ring [38, 86, 85, 93]. When the phase and orientation of the vortical structures align, the vortex ring produces a linear momentum jet, which provides the thrust necessary for sustained hovering, as shown by the streamlines outside the vortex system in Figure 2.9(D).
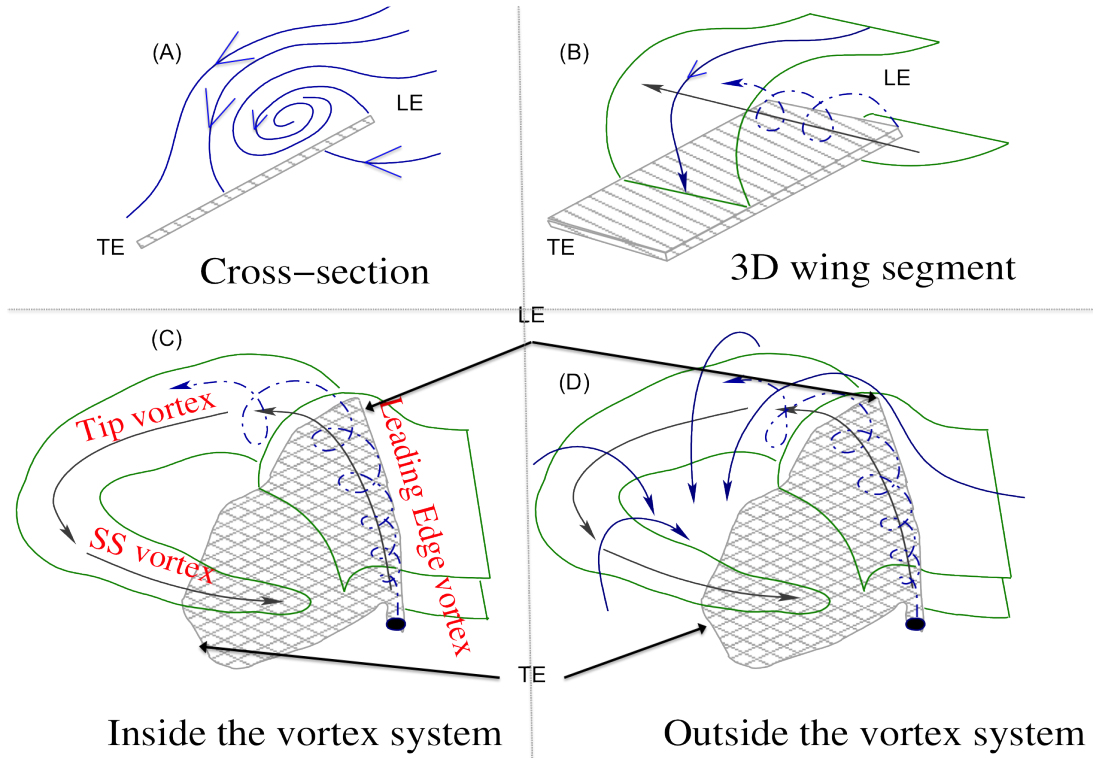
Figure 2.9: **3-D perpsective diagram of a LEV on a finite flapping wing. Blue dashed lines indicate the vortex structures, bounded by green solid lines. Solid blue lines are individual stream lines, and the wing surface is shown in gray. (A) Cross section of the LEV. Compare to the cross sectional cut of the smoke visualization from a mechanical hawkmoth flapper in the bottom pane of Figure 2.12. (B) Three dimensional wing segment demonstrating the axial, or spanwise transport of the LEV, and the streamlines shown feeding the LEV are moving into the paper. (C) Inside the flow between two streamlines during mid-downstroke. The spanwise transport of the LEV is feeding the tip vortex. (D) Outside the LEV. The flapping motion creates a large downwash, or *induced velocity*, which results in a linear momentum jet during hover—modified from [86].**

The end of each half-stroke is characterized by a deceleration of the wing stroke until the translational velocity component reaches zero, where the wing exhibits either a pronation or supination, and the direction of wing motion changes. This deceleration is accompanied by a feathering rotation along a spanwise axis, which reorients the leading edge of the wing into the relative wind for the following half-stroke. As the wing changes direction of motion, the strength of the LEV developed during the preceding half-stroke decreases until it is shed into the wake, assisted by the deformation of the last 25% of the posterior section of the wing, a combination of the first bending and first torsion modes [34, 35]. The decrease in the strength of the LEV and bound circulation about the wing is balanced by a release of vorticity into the wake at the TE. The vorticity shed from the TE of the wing forms a stopping vortex, shown in Figure 2.10. As the direction of motion changes and the wing accelerates into the next half-stroke, a new LEV is formed in addition to another starting vortex, balancing the change in bound circulation about the wing. A complete two dimensional stroke cycle is illustrated in Figure 2.10 adapting the descriptions used by [57] and [86] .
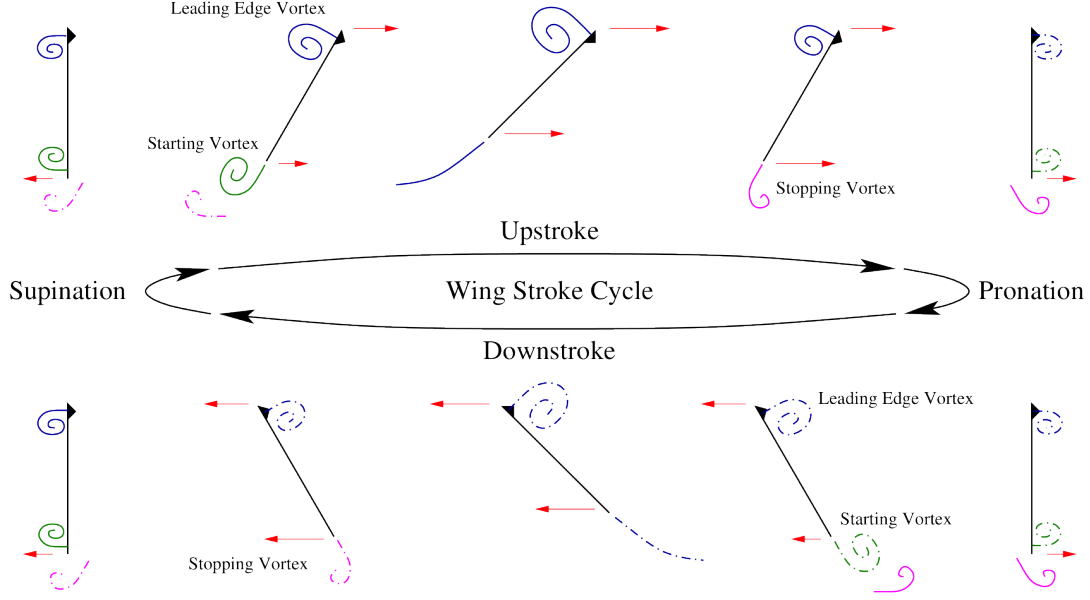
Figure 2.10: Development of LEV and SS vortex during a single stroke cycle. Solid lines indicate vortex structures produced during the upstroke. Dashed lines indicate vortex structures produced during the downstroke. The velocity of the wing at the leading and trailing edges is shown in red. The wing tip is signified by a black triangle—modified from [57, 86].

The vortical structure produces a region of low pressure near the wing surface, and increases the strength of the bound circulation about the wing, proportional with the pressure gradient above and below the wind. Invoking the *Biot-Savart* law, the strength of the vortex core, Γ, induces an increment of velocity at a fixed point at an angle (β) along its radius, r, which when integrated across a differential vortex filament line element, dL, gives the velocity of a finite vortex induced at the point (r_{ab}), given in Equation 2.55 [49],

$$u_\theta = \frac{\Gamma}{4\pi} \int_b^a \frac{\vec{dL} \times \vec{r}_{ab}}{\vec{r}_{ab}^3} = \frac{\Gamma}{r\pi} \left(\cos(\beta_a) - \cos(\beta_b) \right) \tag{2.55}$$

together with *Helmholtz's* first theorem that the strength of a vortex filament is constant along its length, the vorticity along the LE can be used to calculate the bound circulation, which can then be used to estimate the mean lift [49]. This LEV is similar to the vortical structure produced during dynamic stall observed for conventional

57

configurations undergoing rapid pitch or plunge maneuvers [34, 37]. Unlike the vortex produced during a dynamic stall, the leading edge vortex observed in flapping wing flight is stable for the duration of the flap half-cycle. In addition to circulatory aerodynamic phenomena, there are aerodynamic forces associated with the rapid acceleration and deceleration of the volume of entrained air in the immediate vicinity of the wing, attributable to viscous effects, as the wing flips and changes its direction of motion at the end of each half-stroke, maintaining the leading edge into the direction of the relative wind. This non-circulatory phenomenon influences the pressure distribution along the wing surface as well as the pressure and velocity field about the wing. The circulatory and non-circulatory aerodynamic phenomena each produce localized wake structures. These local wake structures interact to form the complex wake structures observed for natural fliers. Sustained flight is achieved when the vortical wake structures align in space and time to form a coherent momentum jet of air normal to the direction of travel; which in hover, is vertical towards the earth.

Researchers at Cambridge University have conducted extensive studies on the hawkmoth flight characteristics, and although their live insect experiments may not provide the engineering rigor necessary to conclude definitively what the essence of the mechanism of flight is attributed to; their subsequent flow visualization, mechanical flapper, and Computational Fluid Dymamics (CFD) studies are very thorough, and their conclusions are credible to use as a foundation for further FWMAV design and analysis. At wing lengths on the order of 50mm, the dominant unsteady aerodynamic phenomenon assumed to be responsible for aerodynamic lift is a LEV produced by a laminar flow separation near the leading edge of the wing [33, 34, 37, 38, 93, 91, 92]. Tip vortices associated with fixed finite wings are traditionally seen as phenomena that decrease lift and induce drag [76]. Willmott, Shyy, and others have discovered in their testing of hawkmoth sized fliers, tip vortices increase lift by creating a low-

pressure region near the wing tip, thereby increasing leading edge suction, and by anchoring the LEV to delay, or even completely prevent it from shedding into the wake [38, 76, 93]. Furthermore, for certain flapping kinematics, the LEV remains attached along the spanwise direction, and the tip effects are not prominent; in such situations, the aerodynamics are less affected by the aspect ratio of a wing [76].

The formation of a LEV was first reported in a seminal study by Ellington and his colleagues at Cambridge. Ellington explored high-speed video of a hawkmoth in a confined test section seeded with talcum powder. He used stereographic video captures, and an in-house holographic illustrator to distill the 3-D wing kinematics from 2-D images, wing cartesian angles, and visualize the LEV developed during fleeting moments of hover. He reported an intense LEV was generated on the downstroke, of sufficient strength to explain the high-lift forces encountered in insect flight studies [38].

Willmott reported the formation of an intense LEV on high-speed video captures of a tethered hawkmoth, attached to a single DOF scale, flapping in a smoke seeded wind tunnel. He reported a sustained wake consisting of an alternating series of horizontal and vertical vortex rings generated by successive up and downstrokes, respectively [93]. The downstroke produced significantly more lift than the upstroke due to the formation of a LEV, which was stabilized by a spanwise flow moving out from the wing root towards the wing tip [38, 93]. The LEV grew in size with increasing forward flight velocity. During supination, vorticity is shed from the LE as postulated by what Ellington described as a structural *torsional wave*, which develops along the last 25% of the wing, posterior to the median flexion line, whilst the anterior portion of the wing remained a rigid body [33]. A small linear momentum jet provided additional thrust as the trailing edges approach the end of the upstroke [93]. They concluded from their experiment that the presence of vorticity, and hence,

the LEV, is created by dynamic stall, and not by the rotational lift, or quasi-steady mechanisms that had been initially postulated for insect flight [38]. The vortex spirals out towards the wingtip with a spanwise velocity comparable to the flapping velocity. Willmott stipulated the three-dimensional flow seen by the propagating LEV, and the subsequent system of vortex shedding and wake recapture, is similar to the conical leading-edge vortex found on delta wings, with the spanwise flow stabilizing the vortex [38]. Figure 2.11 shows a sample of video stills during a single flap cycle from two offset high-speed cameras.
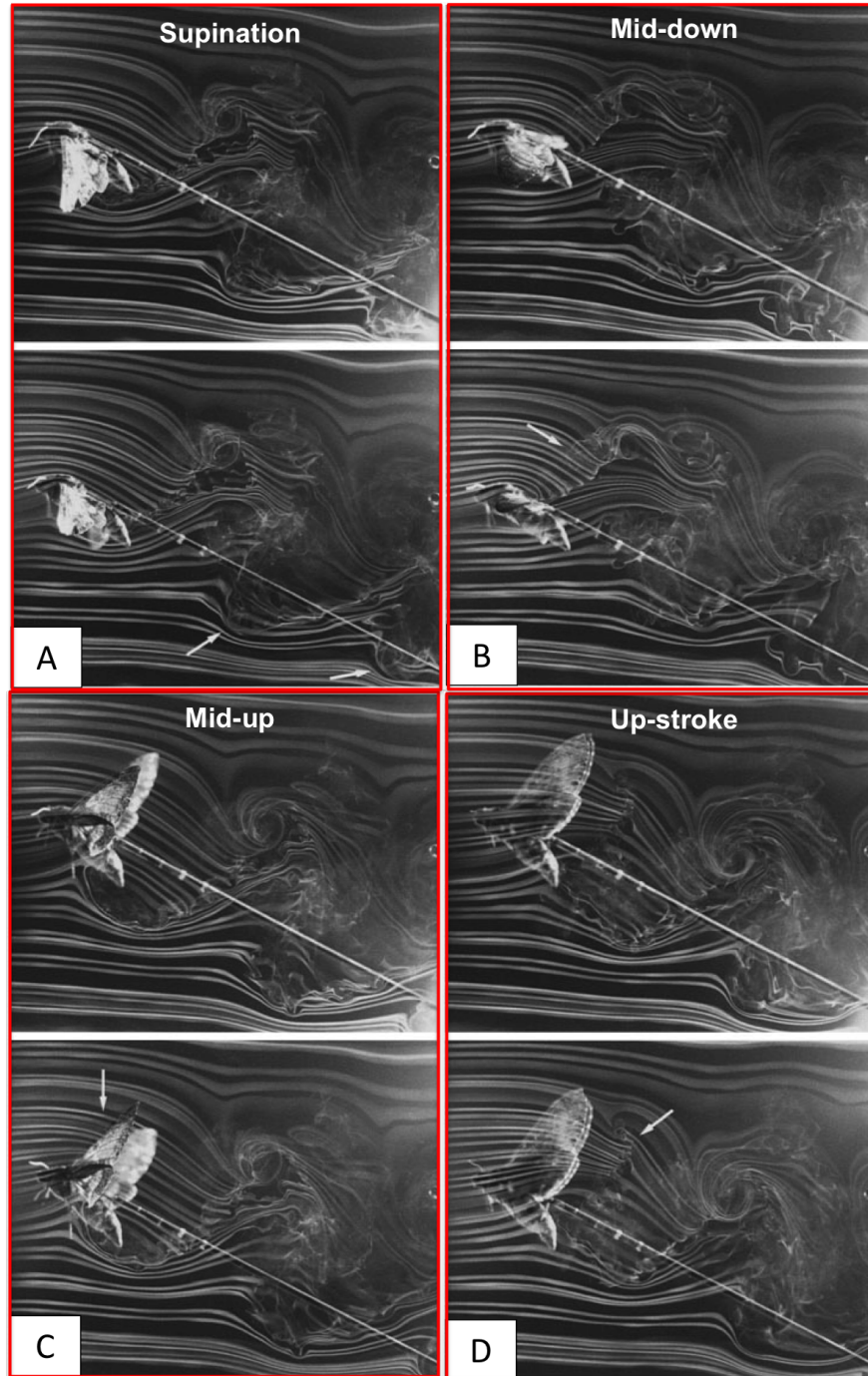
Figure 2.11: Smoke visualization on a tethered hawkmoth. (A) downstroke. Sequence begins at the downstroke supination with the vortices due to wing rotation are indicated by arrows. (B) Mid-downstroke. The downstroke tip vortices are clearly marked spiraling from the TE. (C) Mid-upstroke. The bound circulation maintaining attached flow to the wing is evident along the span. (D) upstroke. The sequence ends at upstroke pronation where the LEV is seen to be diffusing, and the generation of a secondary, counter rotating wake is seen—modified from [93].

Aside from the obvious issues of exercising experimental discipline, variable con-

trol, and the limitations inherent in trying to get insects to perform exactly as the experiments demands, Van den berg identified mathematical limitations in Willmott's tethered hawkmoth smoke experiments, specifically the position of vortices can only be inferred indirectly from smoke flowing around them, making detailed measurements on the strength of bound circulation, and hence vertical force impossible [86]. Building upon the tethered hawkmoth visualization studies, Van den berg explored the LEV in a controlled environment on a $10\times$ dynamically scaled mechanical hawkmoth flapper, with $n = 0.3$Hz, $R = 465$mm, $\beta = 15°$, $\Phi = 180°$, and $\theta = +30°$, which maintains a Re range of $\approx 5000 - 8000$, and achieves aerodynamic similarity, ensuring the forces exerted on the mechanical flapper are of the same magnitude as those generated by the live specimen [86]. He constructed a DC servo motor, spur gear driven mechanical flapper device, which used cloth wings designed by R.J. Wooten, stretched over a brass frame. The LE of the brass frame was perforated so it could emit vaporized oil smoke during flapping. Van den berg's experiments on a model mechanical hawkmoth flapper revealed the flow visualization results were in excellent agreement with the visualization results from Willmott's live hawkmoth experiments. Figure 2.12 shows the Cambridge mechanical flapper at two different stroke angle positions, $\phi = 0°$ and $\phi = -25°$, with smoke emanating from its leading edge smoke rake, and a cross sectional cut through the LEV at various span locations as $\%R$.
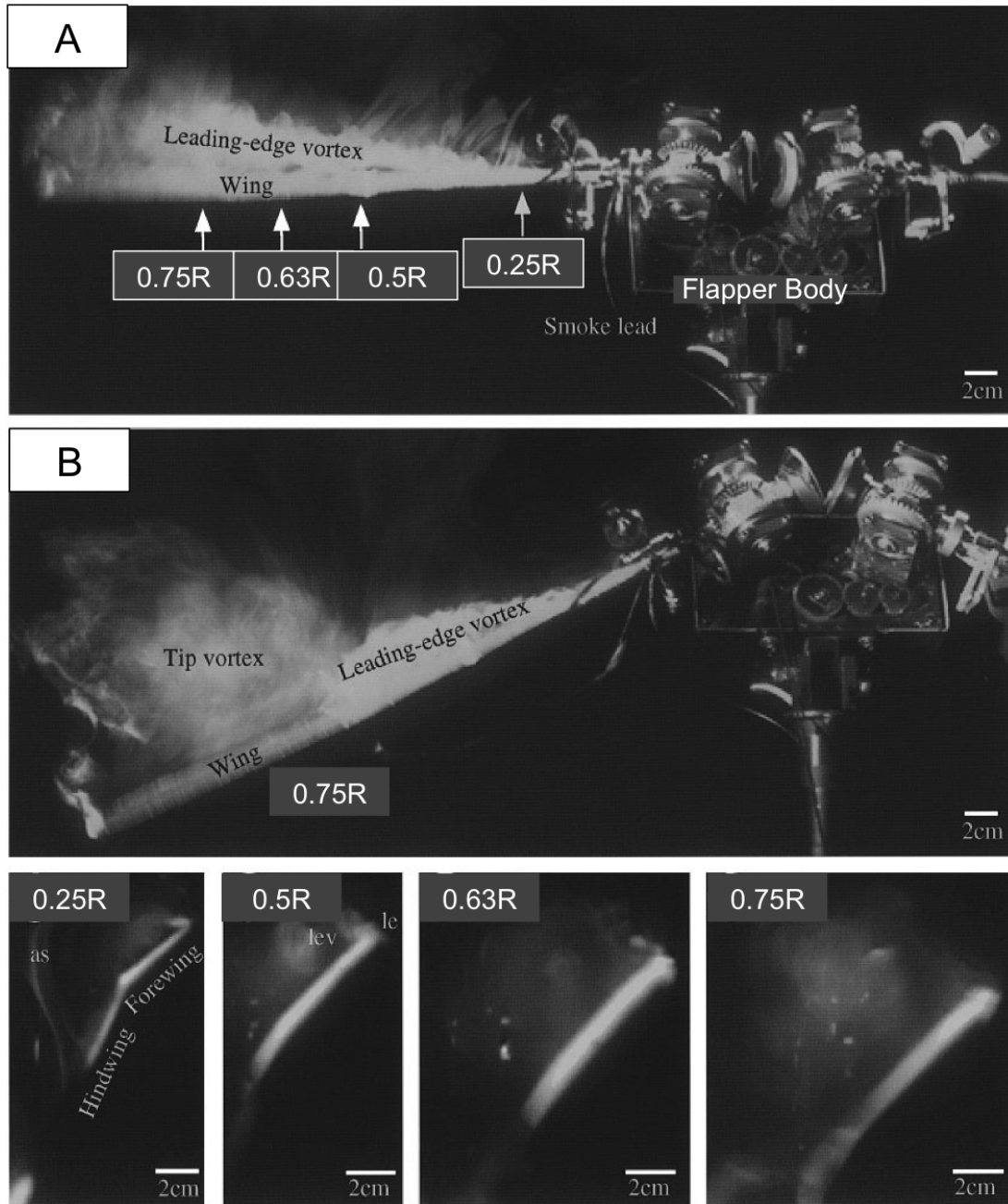
Figure 2.12: Flow visualization of the LEV during downstroke. The view is parallel to the wing surface, corresponding to a top view of a hovering hawkmoth. (A) LEV shown at $\phi = 0°$. (B) LEV shown at $\phi = -25°$. The development of a large tip vortex, with a broken core, at $0.75\%R$ is evident. *Bottom:* Cross sectional cut through the LEV from a perpendicular camera view. The diameter of the vortex increases moving spanwise from base to tip. Towards the wing tip, the LEV is less distinct, evidence it is dissipating, losing momentum, and begining to blend into the tip vortex—modified from [86].

At wing beat velocities equitable to hover, the downstroke wake for both Van den berg's mechanical flapper and Willmott's live hawkmoth experiments are seen as a

small, *tightly wrapped*, strong, and stable LEV with a strong axial flow component increasing in diameter from wing base to tip, separating from the wing at approximately $R = 0.75R$ during the 2nd half of the downstroke, and merging with a large tip vortex with a nonuniform core, which connects to a combined SS vortex generated by pronation [86]. At the end of the downstroke, the wake is best approximated as one vortex ring per wing. The air flow over the wings of both the hovering insect, and those of the flapper were highly three-dimensional. The high angles of attack the wing traverses from cyclic pronation and supination phases is the genesis of the LEV [38, 86]. The flapping motion itself induced a strong axial flow in the LEV, which stabilized it, preventing it from dispersing down the chord and breaking off at the TE, and instead convected it towards the tip. The spanwise convection kept the diameter comparatively small, but very intense. The velocity of these rings corresponds well with the predicted impulse of the wake, indicating that sufficient lift is produced for weight support. Based on the size and velocity of the vortex rings, Van den berg estimated the mean lift force during the downstroke was $\approx 1.5\times$ the body weight of a hawkmoth, confirming the downstroke provides the majority of the lift force during a flap cycle [86, 85]. He applied the method developed by Ellington [32, 34, 36] to analyze the mean lift of hovering vortex wakes, using the initial geometry of the vortex sheets, and the impulse imparted by the vortex sheet created by circulatory lift. The mean circulation ($\bar{\Gamma}$) of an isolated vortex ring can be calculated using the self-induced velocity (V_i) of the vortex core, the vortex ring diameter (D_{vr}), and the vortex core diameter (D_{vc}) given below in Equation 2.56.

$$\bar{\Gamma} = \frac{2\pi D V_i}{\ln\left(8D_{vr}/D_{vc}\right) - 0.25} \tag{2.56}$$

From measurements of the LEV and the shed vortex ring, Van den berg calculated circulation values of $\bar{\Gamma} = $ 1350-1650 $^{\mathrm{cm}^2}/_{\mathrm{s}}$. With the value of the mean circulation

known, the mean downstroke lift ($\bar{L}_{DS}$), can be estimated by the impulse of the wake (I_w) divided by the duration of the downstroke (T_d), show in Equation 2.57 below [32, 34, 35, 36].

$$\bar{L}_{DS} = \frac{I_w}{T_d} = \frac{0.25\pi\rho D_{vr}^2 \bar{\Gamma}}{T_d} \tag{2.57}$$

Yielding values of $\bar{L}_{DS} = 9.5 - 11.75$mN ($\approx 1075$gF), which is $\approx 35\%$ more than what is required to support the 7.8mN weight of the average hawkmoth [32, 86]. O'Hara attached several desiccated hawkmoth wings, with and without scales, see Figure 2.13, to the AFIT FWMAV flapper and measured forces with the Nano-17 force balance, and recorded vertical forces on order of ≈ 1040mgF with scales, and ≈ 970mgF with the scales removed.
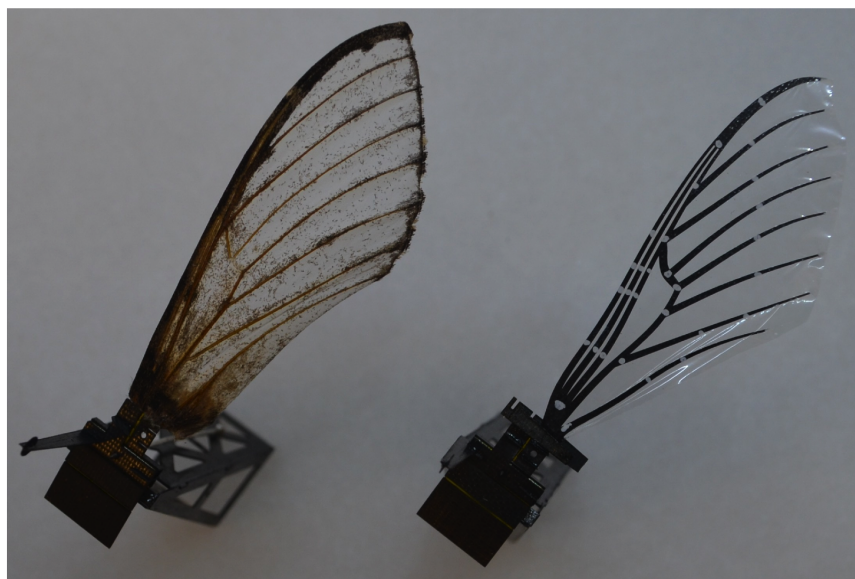
Figure 2.13: *Left:* **Hawkmoth wing (scales removed) mounted on the AFIT FWMAV test flapper,** *Right:* **Engineered wing mounted on AFIT FWMAV test flapper—modified from [66].**

Liu *et.al.* conducted a CFD analysis on the mechanical flapping hawkmoth wings used by Van den berg *et.al.*, and their numerical simulations confirmed the presence of a LEV in much the same way the flow visualization experiments illustrated it. They discretized the three-dimensional incompressible, unsteady NS equations, Equation

2.20, in the conservative integral form, nondimensionalized in a local wing based, fixed, coordinate system. The governing equations were discretized using a Finite Volume Method (FVM) employing a first-order, two-point, backward-difference implicit formulation. The governing PDE's are hyperbolic, meaning the conservation equations are well-posed, initial value problems, which are most generally expressed by solutions to the general *wave* equation, $U_{tt} - \lambda^2 U_{xx} = 0$. The solutions behave in a *wave-like* manner where a disturbance in the initial conditions is not felt simultaneously everywhere in the domain, but travel with a finite propagation wave speed along *characteristic* lines, requiring the use of a time-marching technique to solve the temporal derivatives. Their analysis revealed a complex interaction between the viscous dissipation forces and unsteady flow around the flapping wing, and of the time dependence of instantaneous force production; which revealed hovering flight is dominated by a combination of the unsteady aerodynamics of the instantaneous time-dependent dynamics, and the past history of the wing [53].

More specifically, the CFD results rendered a coherent LEV with axial flow during translational motions of both the up and downstrokes. The attached LEV resulted in a negative pressure region, which produced a leading edge suction, and hence, is responsible for enhancing lift production [53]. The axial flow, derived from the spanwise pressure gradient, stabilized the numerical vortex, and rendered its characteristic spiral conical shape. Interestingly, Liu was able to verify what Willmott and Van den berg could only postulate from their smoke visualizations, that the LEV created during previous steady translational motion, *during the constant angle of attack potions*, remains attached during the rotational transitions of pronation and supination [53]. Although it remains attached at the end of the translational phase of the stroke, its shape, and therefore its kinetic energy is considerably altered due in large part to coupling between the translational and rotational motions, which developed into a

complex tangled structure, and is ultimately shed before the subsequent translational motion, where it interacts with the SS vortex, forming a counter-rotating vortex ring. Figure 2.14 shows a comparison between Van den berg's mechanical smoke flow visualization experiments and Liu's CFD simulations at the same three stroke angles.
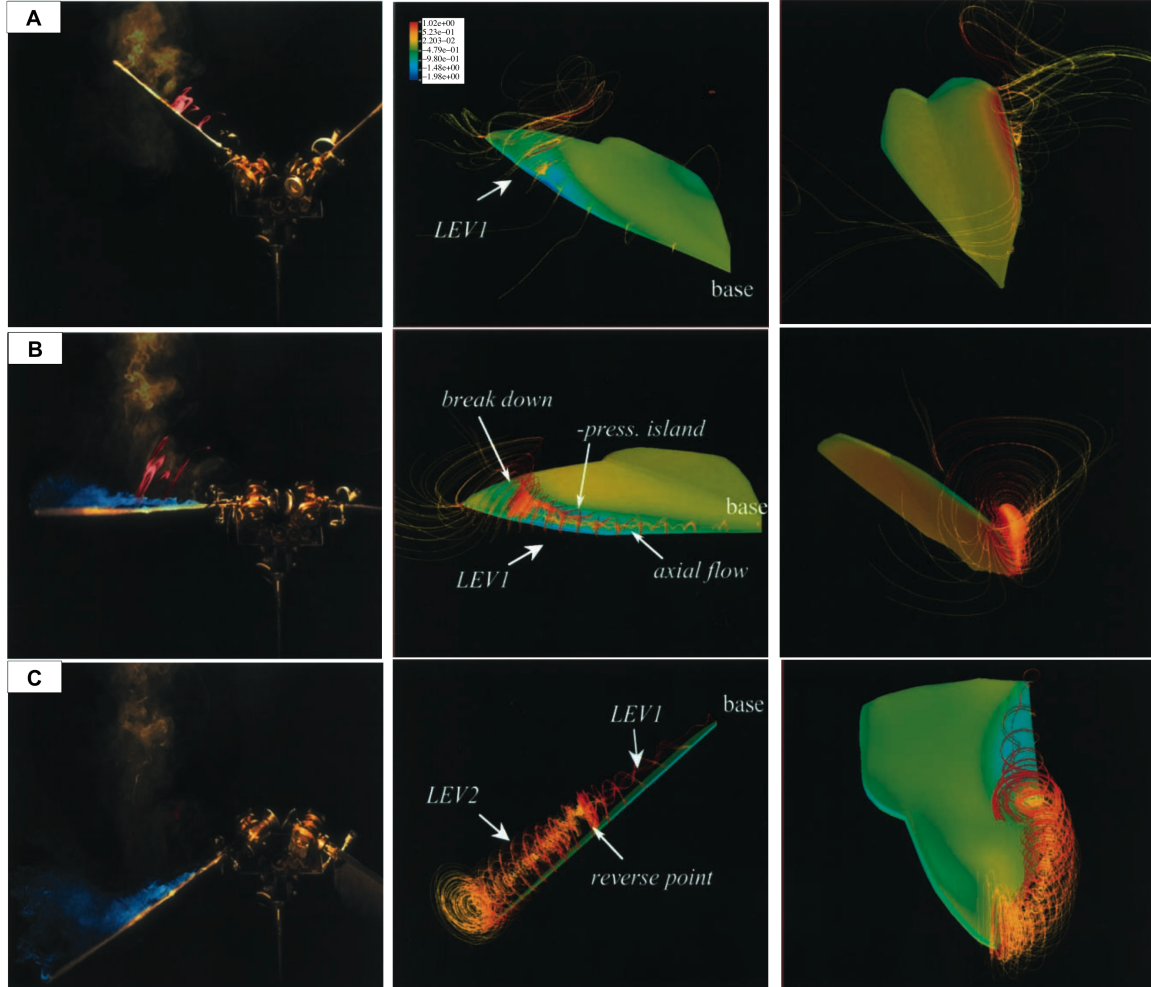
Figure 2.14: Comparision of smoke visualization to a CFD analysis on the mechanical hawkmoth flapper. *Smoke images*: The LEV in the smoke frames is colored in blue. The red smoke is the LEV from the early downstroke that is still attached. *CFD images Top & Side views:* In the CFD frames, blue indicates low pressure, while red indicates high pressure regions. The LEV is clearly evident in CFD frames B & C: LEV1 is the original LEV produced at the onset of rotation, a probable dynamic stall artifact, which is subsumed into the tip vortex at $\approx 0.7R$, and LEV2 begins between the break down of LEV1 and the tip, and displays a large axial velocity gradient towards the tip, maintaining attachment through to rotation, and breaking down into the tip vortex during subsequent translation. (A) $\phi = +30°$. (B) $\phi = 0°$. (C) $\phi = -36°$—modified from [53, 86].

Figure 2.15 gives a graphic depiction of Liu's LEV qualitative observations shown

macroscopically applied to the hawkmoth during a single flap cycle from downstroke through upstroke and back to the start of the downstroke.
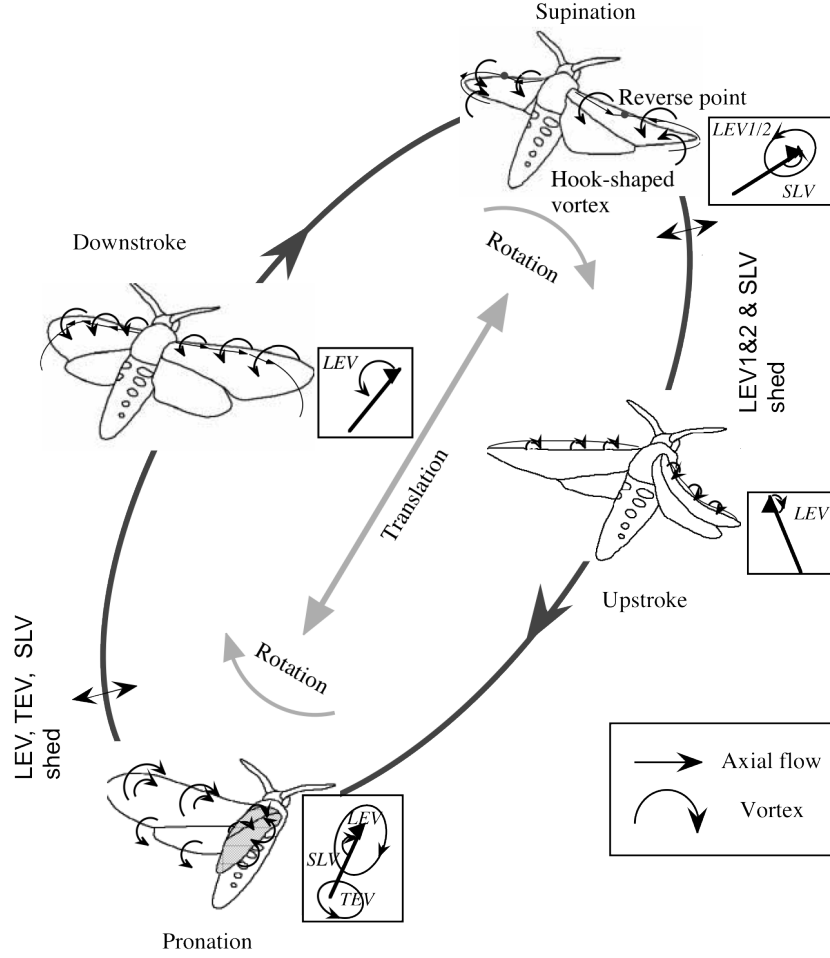
Figure 2.15: Graphic shows an illustration of Liu's CFD results depicted across a single flap life cycle.

Liu calculated the lift and drag forces in the body fixed coordinates using Equation 2.58

$$L = \tfrac{1}{2}\overline{C_L}\rho U_{ref}^2 S_{wing}$$
$$D = \tfrac{1}{2}\overline{C_D}\rho U_{ref}^2 S_{wing}$$

$$(2.58)$$

where $\overline{C_L}$ and $\overline{C_D}$ are the wing mean lift and drag coefficients given in [31], S_{wing} is the wing area given in [32], and U_{ref} is a reference velocity from the hawkmoth

flapping in hover. The lift and drag are local forces, meaning they are with respect to the wing position angle, and are in an inertial, or body fixed coordinate system, and remain orthogonal and parallel to the relative wind as it moves throughout its flap cycle. To determine the net vertical and horizontal forces in a non-inertial reference frame, the lift and drag are converted to the global earth-centered coordinates, as vertical and horizontal force coefficients, $\overline{C_v}$ and $\overline{C_h}$, given in Equation 2.59, with respect to the the angle between the mean stroke plane and the horizontal, β [53].

$$
\begin{aligned}
F_v &= L\sin\beta + D\cos\beta \\
F_h &= L\cos\beta - D\sin\beta
\end{aligned}
\tag{2.59}
$$

If the empirically derived lift and drag coefficients are known for a particular wing, then the fixed reference frame forces can be found through the standard trigonometric relation, $\tan\beta = \left(\overline{C_L}/\overline{C_D}\right)$ [53]. The results showed the forces developed during one complete flapping cycle are produced primarily during the downstroke, and the latter half of the upstroke, with little force generated during the rotational transitions. The vertical force generated during simulated hover was 11.05mN (1126mgF), $\approx 40\%$ greater than the weight of an average hawkmoth [53]. Figure 2.16 shows a CFD contour map of the wing, looking at the LE, showing the build-up of vortex rings as the wing flaps, which influences the vertical forces recorded.
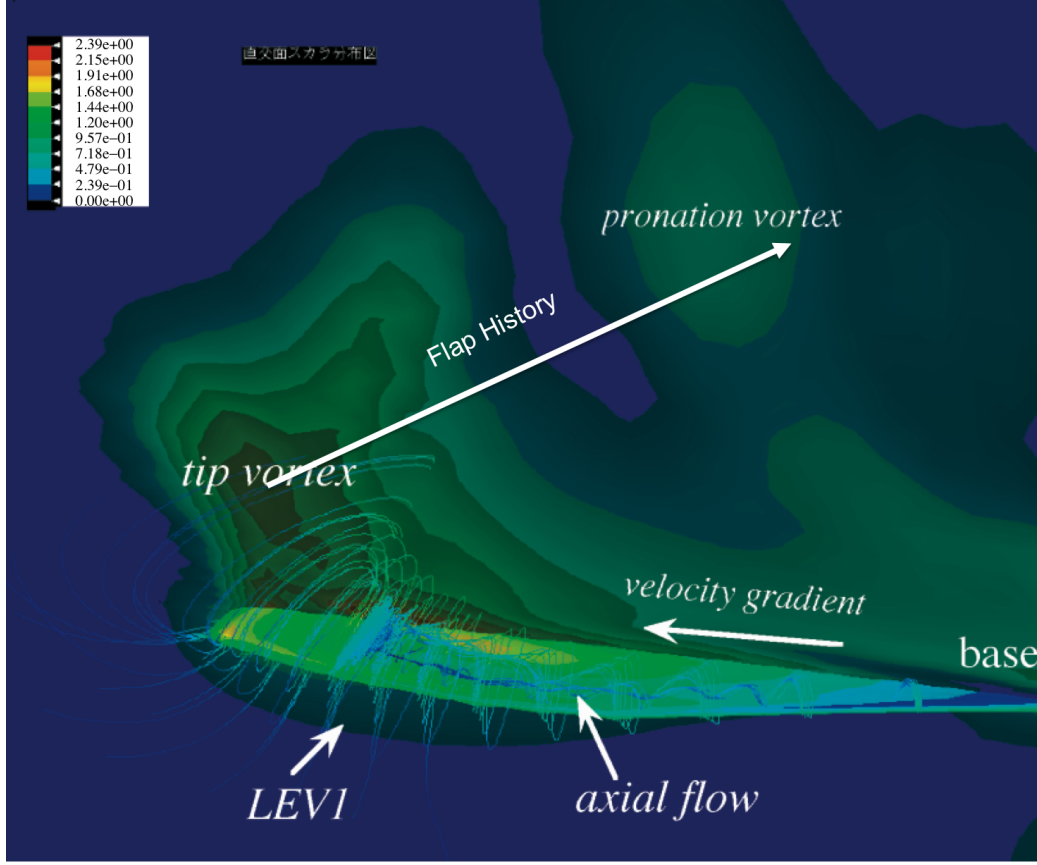
Figure 2.16: CFD contour map plot. View is perpendicular to the LE, base is on the right and tip is on the left. Plot shows the development of the LEV and the axial (*towards the tip*) transport of vorticity. The LEV breaks down at $\approx 0.7R$. Shed vorticity from previous downstrokes is visible above and rear of the wing plane—modified from [53].

Maybury and Lehmann conducted force and PIV experiments on the effect of forewing and hindwing phase lag in model dragonfly wings, and found that altering the two wing system independently changed the shape, size, and nature of the LEV, which in turn changed the cyclic growth and decay of vertical forces [56]. Singh *et.al.* conducted thrust and PIV experiments on various high-speed biomimetic flapping wing mechanisms. Their experiments discovered the inertial power effect of wing mass had a great impact on the flapping frequency, and a passive pitch flapping mechanism generated greater thrust than a prescribed motion biomimetic flapping mechanism [78]. Shyy *et.al.* performed NS numerical simulations on a pitching and plunging flat plate, 2% thickness, $R = 4$, $Re = 100$, and reported for a low aspect-

ratio flapping wing, tip vortices can increase lift both by creating a low-pressure region near the wing tip, and by anchoring the LEV to delay, or even prevent it from shedding [76]. Their simulations at Reynolds numbers an order of magnitude lower than that seen by the hawkmoth, demonstrated enhanced wake capture and a linear momentum jet found in the wake and tip vortices [76]. Researchers at Georgia Technological University conducted dual axis force measurements, and limited PIV flow visualization on a rather large, $R = 20$in, set of flexible wings, and concluded thrust was sustained through the flap cycle, while vertical force was periodic, generating lift on the downstroke, and a small amount of negative lift was produced during the upstroke [55]. DeClerq *et.al.* conducted PIV measurements on the efficacy of the *clap and peel* mechanism used on the Delft University of Technology's Delfly II FWMAV; revealing an influx of velocity on the peel, but no corresponding expulsion of a momentum jet during the clap. The PIV results showed the growth of a LEV on the initial in-to-out stroke, which served to augment lift, with evidence of a destroyed vortex core during the out-stroke [18]. University of California researchers, Birch, Dickinson and Dickson, conducted two axis PIV experiments on dynamically scaled model fruit fly, *Drosophila Melanogaster*, wings, ($R = 260$mm), immersed in a oil bath to control the viscosity and fluid density, thereby allowing Reynolds number scaling, and found contrary evidence to earlier results of a ubiquitous spanwise, spiraling, stable LEV for any size flapping wing. They found no evidence of an attached LEV on their wings at $Re = 120$, but did see evidence of similar results reported by the aforementioned studies when they changed the viscosity of the oil fluid medium to increase the operating Reynolds number to 1400 [8, 9]. These differences suggest the transport of vorticity that maintains prolonged attachment may take different forms at different Reynolds numbers. Their results indicate the presence of spanwise axial flow in the vortex core on model *Manduca* wings, and the absence on model

71

Drosophila wings is a Reynolds number effect, and not an artifact of differences in experimental methodology or wing morphology [8].

2.5   Mechanism Design

To reliably measure the aerodynamic forces and moments of the wing apparatus, a drive mechanism had to be designed to mimic the flap and stroke cycle of the *Manduca Sexta* as closely as possible. Extensive rod and gear driven mechanisms have been design and tested in FWMAV designs in the past, but they are limited in their variability to only being able to vary the flapping frequency without changing the drive linkages, or disassembling the mechanism and changing the rod lengths [2, 54, 89, 94]. Mechanical flappers are limited then to a fixed flapping waveform (the drive signal), drive bias (drive signal shape), and amplitude (wing tip angular arc), all governed by the mechanical components of the assembly mechanism itself [2, 54, 89, 94]. Further, as the entire scale of the flapping mechanism decreases, the ratio of inertial to structural loads decreases, making frictional losses critical to power and transmission efficiency when dealing with scales of milligrams of force, and driven by milliwatts of power [2]. A programmable drive system was desired to fine-tune the flap cycle without altering the mechanism itself. The AFIT FWMAV design is comprised of a flapping mechanism and transmission, a drive train, the AFIT engineered wing (designed from the hawkmoth), mounting apparatus, and the associated electronics, connections, and sensing and diagnostic equipment. The following sub-sections detail the important aspects of the flapper anatomy and system design.

2.5.1   Powerplant & Drive Train.

Integral to the design of the AFIT FWMAV is the flapper mechanism. Anderson provided a thorough review of the typical mechanism designs presently being

72

explored and implemented in a number of MAV research centers [2]. Table 2.1 details a summary of different power plant drive mechanisms that have been studied and implemented in different FWMAV designs.

Table 2.1: **Survey of Research Based Flapper Powerplant Drive Options**

Actuator Type	Strain (%)	Stress (MPa)	Frequency (Hz)	Specific Energy density($^{J}/_{g}$)	Efficiency (%)
Synchronous Flight Muscle	17[a]	0.35[c]	5.5-100[d]	0.003[f]	2-13[h]
Asynchronous Flight Muscle	2[b]	—	100-1046[e]	0.002[g]	5-29[i]
PZT[j]	0.2	110	10^8	0.013	90
PVDF[j]	0.1	4.8	10^7	0.0013	90[k]
SMA (TiNi)[j]	5	200	10^1	15	10
Solenoid[j]	50	0.1	10^2	0.003	90
EAP[j]	63	3	10^4	0.75	90

Note: energy density $= {}^{power\ density}/_{flapping\ frequency}$

[a]Monarch butterfly[30], [b]Bumblebees[30], [c]Locust[12], [d]&[e][30], [f]Hawkmoth[30], [g]Bumblebee[30], [h−j][30], [k][12]

Anderson's survey of the available power plant options for the myriad of design constraints the FVMAV designer must contend with, *i.e. payload, vehicle size, flapping frequency, power requirements, power electronics*, almost exclusively implicates the PZT driven actuator as the most sensible and practical choice. Wood explored two different methods to drive a PZT configured for FWMAV designs. The first method is an alternating drive where the dual source drives each layer independently. Each source is 180° out of phase with the other, each driven unipolar. The advantage of this method is it drives each layer only in the positive direction, which gives the most tip deflection; however, the disadvantage is it requires two independent power sources for each actuator—a total of $2n + 1$ wires, and $2n$ sources for n actuators, which is impractical for designing and integrating into a FWMAV [96]. The second PZT driving technique is simultaneous drive, which biases the entire actuator; therefore, the bias and ground source can be common for multiple actuators—requiring

$n+2$ wires, and $n+1$ sources for n actuators [96]. The result of testing different PZT combinations show the alternating method exhibits greater saturation, while providing approximately 5% less displacement than the simultaneous drive for a given maximum velocity field. Under cyclic actuation, however; the simultaneous drive shows slightly greater hysteresis [96]. Figure 2.17 shows the electrical schematic of how each drive method is physically connected, and Figure 2.18 shows the difference in the hysteresis—how much the tip position varies from nominal center at zero displacement—after repeated application and removal of a cyclic input voltage [96].
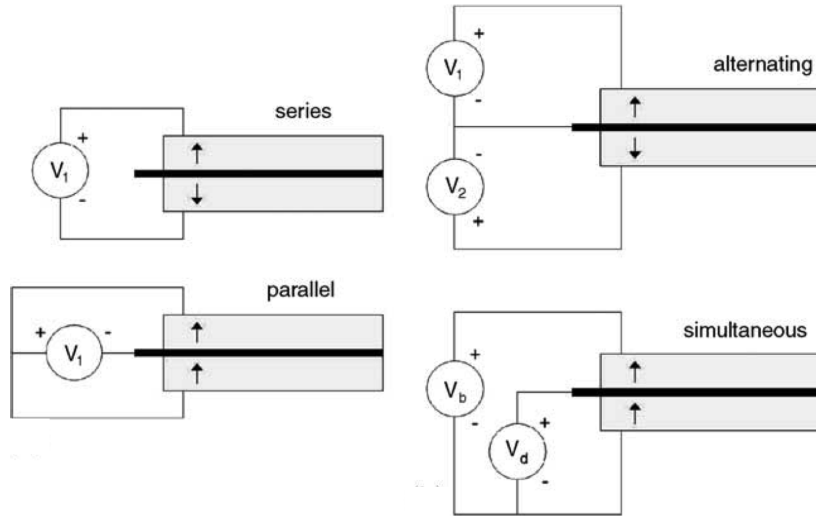
Figure 2.17: **PZT actuator drive methods.** *Left:* **Single source,** *Right:* **Dual source—modified from [96, 94].**
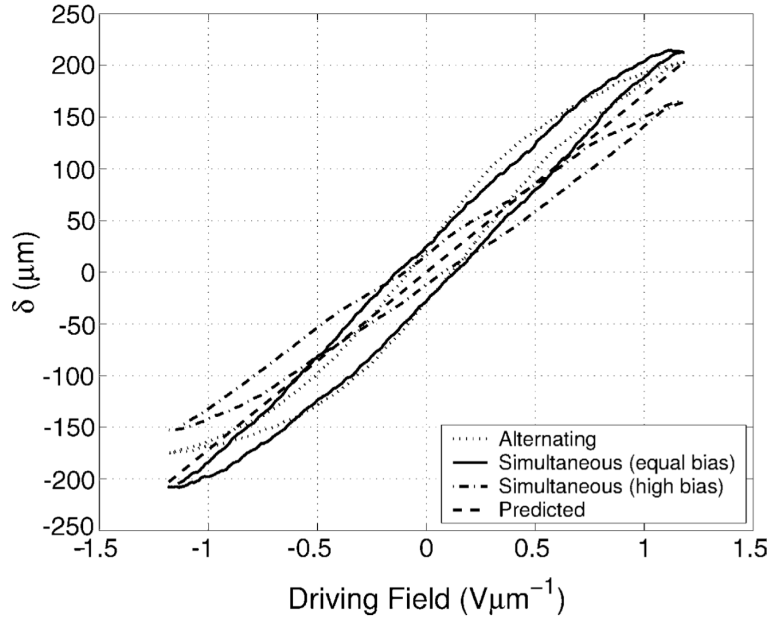
Figure 2.18: The hysteresis in displacement developed between the different drive methods from cyclically loading the PZT with a maximum input voltage of $300V$—modified from [96].

Biologists have reached a unifying consensus that insects generate aerodynamic flapping power by flapping their wings at resonance, through a series of ventral and dorsal muscular contractions originating in the mesothorax and metathoracic cavities; whereby the muscles contract linearly to produce an angular wing motion, which can be effectively modeled as a mechanical linear actuator. The bimorph cantilevered PZT driven actuator connected to a dual crank-slider transmission was selected as the most efficient adaptation of biological fliers. Their flight mechanism is a complex system-of-systems of protein synthesis, which activate dorsoventral and basalar muscles, which then apply forces to the tergum exoskeletal plate and sclerites respectively, activating and driving the wing in a hemispherical arc. This complex biomechanical machine is most accurately simplified as a dual linear actuator model of the thoracic flight muscles, whose mechanical analog is a simple-crank slider mechanism [2, 6, 12, 54, 66, 90, 94]. Figure 2.19 illustrates a cross section cut-away of an indirect

drive insect thorax, and how its biomechanical flapping mechanism is modeled as a simple mechanical model.
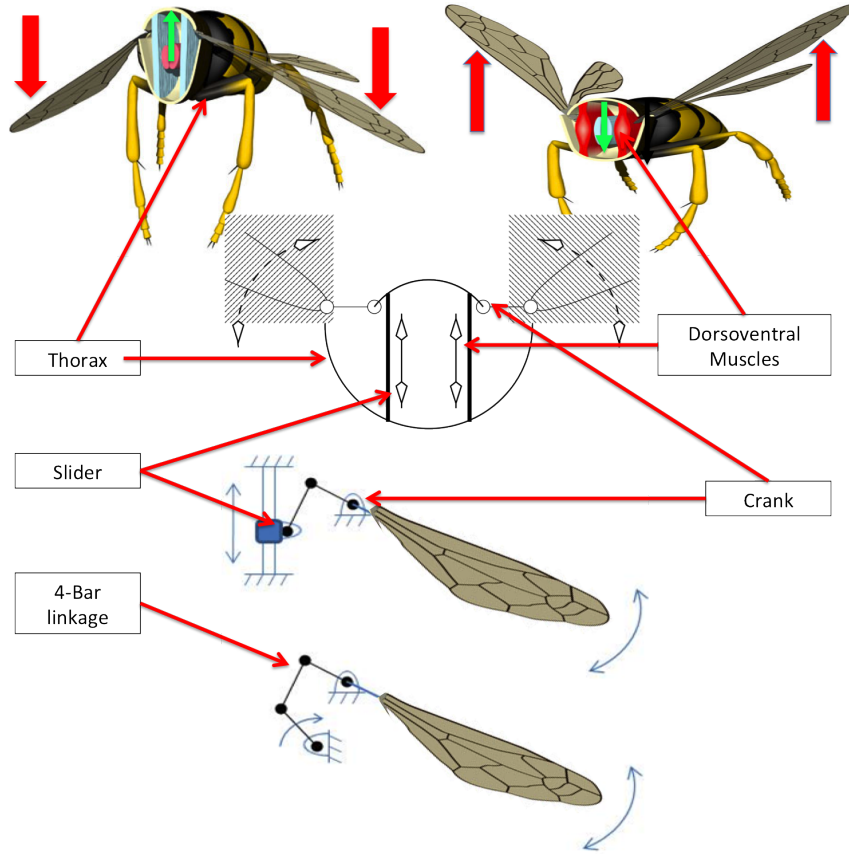
Figure 2.19: Insect flapper mechanics modeled as a mechanical 4-bar linkage.

The slider can be replaced with the addition of another pinned bar linkage, simplifying the model to a straight four-bar linkage mechanism. The free, unclamped tip of the PZT traverses more of an arc than straight translational motion, and therefore its motion can be used in place of the driving crank in the model flapping mechanism [94]. However, this design forces the PZT tip to be aligned along the rotational plane, which increases the tip load, or *blocking force*, and minimizes the actuator's drive potential [2, 94]. The greater the cantilevered length, the greater the tip displacement, and the higher the blocking force is generated at the tip. Essentially, the PZT length should be aligned along the maximum dimension of the FWMAV to maximize its

effective length; and therefore, its output capacity. When it is aligned in the stroke plane, it creates a large and undesirable moment about the body centroid [2]. If the PZT is oriented 90° out of plane with the rest of the linkage assembly, in the longitudinal plane along the vertical axis, tip deflection, and therefore wing stroke angle, will be maximized, while reducing the tip strain of the actuator. This configuration change requires an additional joint to transfer the linear motion of the PZT tip to the angular motion of the wing, transforming the assembly into a double crank-slider mechanism, first introduced by researchers at the University of California Berkeley in their *Micromechanical Flying Insect (MFI)*, and refined by researchers at Harvard in their *RoboFly* [4, 5, 95]. The top graphic of Figure 2.20 illustrates the difference between in-plane, and orthogonal to the stroke plane PZT orientations, while the bottom graphic depicts the Harvard RoboFly's double crank-slider drive mechanism. The PZT replaces the crank, and the blue joints are the rotational joints *(sliders)*, which are not as durable as a traditional mechanical slider collar. However, their ability to store elastic energy greatly reduces the friction penalty inherent in mechanical sliders, which is crucial when weight and power conservation are paramount design considerations [2]. The AFIT FWMAV's PZT and linkage drive train move in the same plane, aligned with the z-axis, which minimizes the number of moving joints, and provides for a robust testing architecture. Future flight vehicles, with miniaturized actuators, would require orienting the PZT 90° out-of-plane with the rest of the linkage assembly, in the longitudinal plane, along the vertical axis, which maximizes tip deflection, and therefore wing stroke angle, while minimizing the actuator tip strain.
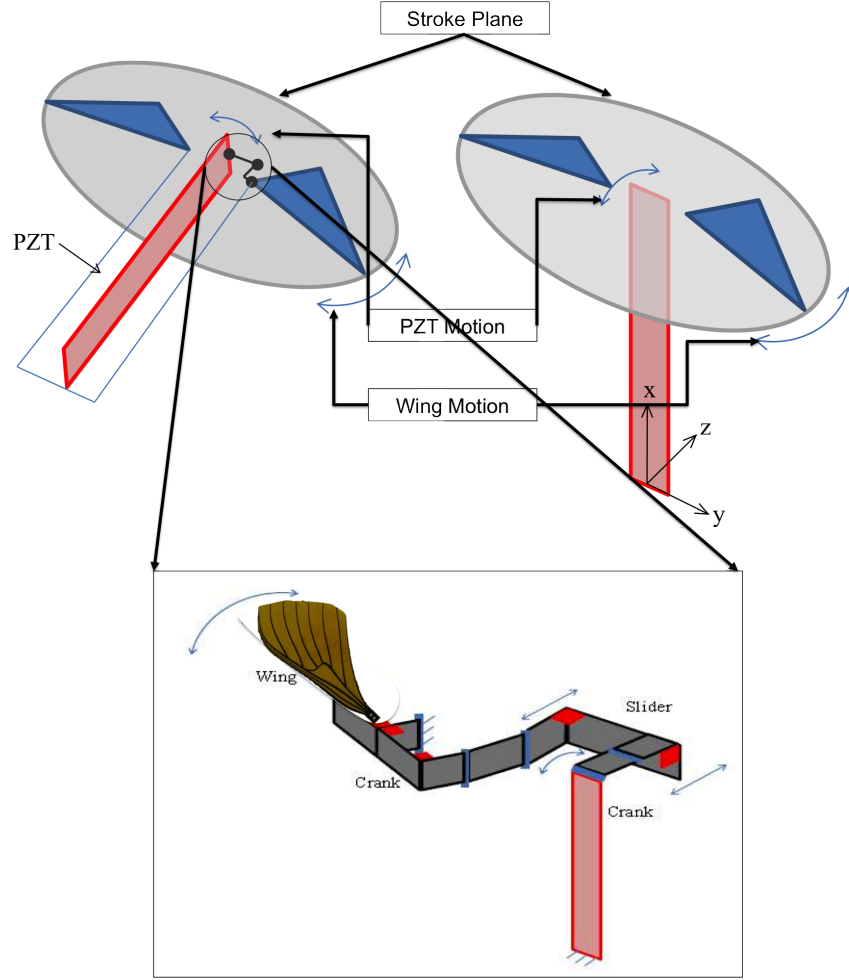
Figure 2.20: PZT orientation. *Right:* **in-stroke plane,** *Left:* **perpendicular to the stroke plane, and** *Bottom:* **exploded view of Harvard** *RoboFly* **double crank-slider model where the rotation joints are shown in blue; fixed angle joints are shown in red, which keep the alignment of the entire assemble along a neutral axis—modified from [2, 94].**

The first crank-slider transforms the arc motion of the PZT tip, which acts like a crank, in the $x - z$ plane into a linear motion, parallel to the z-axis and the PZT tip. This tip linear motion is transformed into rotary flapping motion in the $y - z$ wing stroke plane through the shared slider and second crank, see the bottom pane of Figure 2.20 for a visual schematic of these motions [2].

Flapping at resonance is critical to generate the greatest translational displacement of the longitudinally mounted PZT, which is tantamount to maximizing the total wing stroke. Flapping at resonance is the optimal flapping frequency to maxi-

mize the total $\pm$ PZT displacement, which corresponds to the maximum total wing stroke angle, Φ, for the lowest possible power output [2, 94, 95]. Biologists have shown insect analogs also flap at thoracic resonance, exciting the first natural frequency of the linear actuator musculature-wing flight system [30]. Both the dorsal and ventral components of the thoracic flight control mechanism are used to store and release elastic kinetic energy, transferring small displacements of the scutum and tergum plates, which compress and release the dorsoventral and dorsolongitudinal muscles, into large wing rotations, and this action is enhanced by moving those muscles at resonance to minimize the chemical-protein synthase required to sustain flight [94].

Researchers at Harvard developed a kinematic relationship between the transmission component lengths and the half cycle stroke angles [39, 89, 94]. Anderson implemented those kinematic relations into a MATLAB® script to predict total wing tip travel, animate the motion, and output the ϕ_{max} and ϕ_{min} angles, given a PZT cantilever length and transmission linkage lengths. The geometry of the flapping mechanism and the resulting rigid body kinematics are chosen based on the expected displacement of the drive actuator and the desired wing motion. Figure 2.21 shows a diagram of the generalized AFIT 4-bar linkage flapper drive train. For illustration purposes, the PZT is replaced here by a rotating link, not a cantilevered beam.
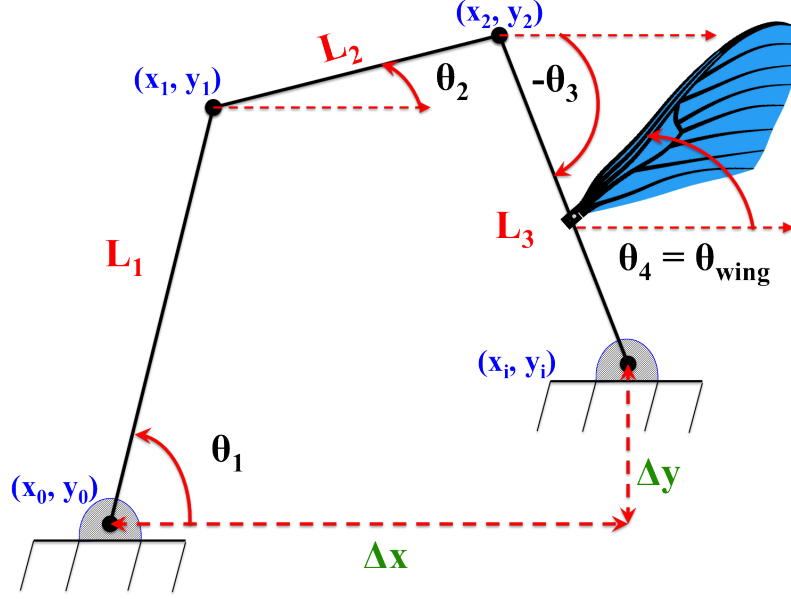
Figure 2.21: Schematic of the 4-bar linkage assembly used in the AFIT FWMAV drive transmission. Linkages, L_i, shown in red, displacement angles, θ_i, shown in black, coordinates shown in blue [2, 39, 94].

To define the linkage, the link lengths, L_i, and the relative location of the fixed rotation points, $(\Delta x, \Delta y)$ must be specified, which serve as the inertial, or global reference coordinates. For a given angular actuator deflection (θ_1), δ defines the cartesian location of the linkage during the stroke. Given a specified actuator deflection, δ, the location of point (x_1, y_1) can be calculated. The distance from point (x_2, y_2) to point (x_i, y_i) is spanned by a two-link planar manipulator [2]. Equation 2.60 gives the trigonometric solution to the relative wing displacement angle, θ_3 [2, 94].

$$\theta_3 = -\left| \, 2\arctan\sqrt{\frac{(L_2 + L_3)^2 - (x^2 + y^2)}{(x^2 + y^2) - (L_2 - L_3)^2}} \, \right| \tag{2.60}$$

where x & y are coordinate distances between the last two pivots of the linkage. For completeness, the intermediate angle, θ_2 can be calculated as follows in Equation 2.61 [2].

$$\theta_2 = \arctan 2(y, x) + \arctan 2\left(L_3 \sin \theta_3, L_2 + L_3 \cos \theta_3\right) \tag{2.61}$$

80

$arctan2$ is the four-quadrant arctangent function. The actual wing stroke angle, θ_4, is θ_3 plus its mounting position offset relative to L_3. Figure 2.21 shows an angle just past 90°. The position of the wing along L_3 is not fixed, but it is most beneficial to make L_3 as small as possible to maximize the amplification of the small amount of actuator displacement into a large amplitude wing stroke angle [2]. The AFIT drive mechanism mimics this principle through the use of a linear actuator in the form of a cantilevered end PZT actuator, connected to a replicated robotic four bar linkage. Equation 2.62 is the transmission ratio, T, of the replicated 4-bar linkage assembly, relating the wing flap angle to the linear PZT displacement, and is approximately equal to the inverse of the length of L_3 [2, 94].

$$T \equiv \frac{\theta_{wing}}{\Delta} \approx \frac{1}{L_3} \tag{2.62}$$

Where Δ is the off-set in the vertical alignment between the flexures at $L1/L2$, and between $L4$ and the mounting block, while L_3 is the length of the second crank. The length of the second crank determines the transmission ratio of the mechanism—how much the linear input motion is amplified to create angular output wing motion. For the largest amplitude, hence the greatest wing motion, the crank length, L_3, should be as small as possible. The lengths of the other links are not critical to the wing motion, but they must be chosen circumspectly to avoid binding the entire assembly, and to ensure the flexures are not over rotated and ruptured, causing them to separate. Figure 2.22 shows a close-up of the linkage assembly. The design of the individual lengths of the transmission, as well as their positional relation to each other, determine the maximum *up* and *down* stroke angle, ϕ_{max} and ϕ_{min}, achieved by the flapper drive train.
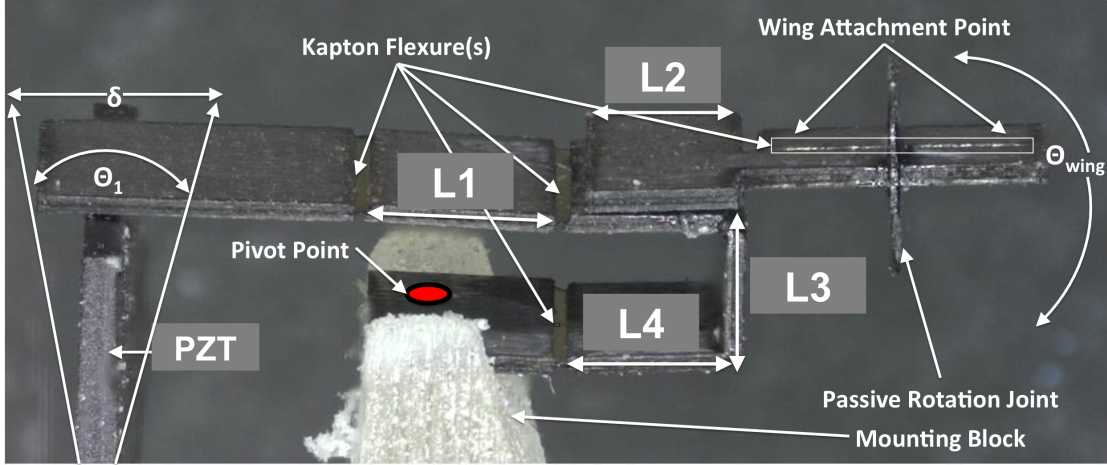
Figure 2.22: Close-up of the linkage assembly with the parts labeled used in the desgin and assembly process. $L_1 = 2.96$mm, $L_2 = 2.36$mm, $L_3 = 1.25$mm, $L_4 = 2.50$mm.

Using the linkage lengths, L_i, provided in Figure 2.22, and the time history of the PZT displacement, δ, from the displacement sensor, the theoretical wing angle, $\theta(t)_{wing}$ (*this nomenclature is utilized by the Harvard Microrobotics Lab, and describes the same kinematic motion as the actual stroke angle, ϕ, which is used in subsequent aerodynamic analysis*), can be calculated at any time during the stroke cycle using Equation 2.63 [39, 66].

$$
\begin{aligned}
\theta(t)_{wing} = -\frac{\pi}{2} + \arccos\Big\{ &\left[L_3^2 + (L_1 + L_2 - L_4 - \delta)^2 + L_3^2 + (L_2 - L_4)^2 - L_1^2 \right] \\
&\times \left[2\sqrt{L_3^2 + (L_2 - L_4)^2} \times \sqrt{L_3^2 (L_1 + L_2 - L_4 - \delta)^2} \right]^{-1} \Big\} \\
&+ \arctan\left(\frac{L_3}{L_1 + L_2 - L_4 - \delta} \right) + \arctan\left(\frac{L_2 - L_4}{L_3} \right)
\end{aligned}
\tag{2.63}
$$

2.5.2 The AFIT FWMAV Design.

The flapping mechanism used in this research was designed to have a maximum positive stroke angle, $\phi_{max} = +55°$, and a maximum negative stroke angle,

$\phi_{min} = -55°$, for a total stroke amplitude, $\Phi \approx 110°$. The wing venation structure is manufactured of a high modulus lamina carbon fiber, YSH-70A, impregnated with RS-3C epoxy resin, multi-layered in a $0-90-0°$ sandwich, which was heated, pressed, and cured in a LPKF Multipress S at 192°, 100N/cm², for 120 minutes. The wing planform area is covered by a polyethylene terephthalate (PET) mylar film, with an elastic modulus of 3.7GPa, which is higher than its biological analog of 2.45GPa [65]. The linkages consist of $160\mu m$ carbon fiber with joint flexures created by sandwiching $12.5\mu m$ thick Kapton HN 50 between two pieces of carbon fiber, then cured at 192°, 30N/cm², for 4 minutes. The cured carbon fiber components are cut on a precision laser-machining center LPKF Protolaser U. Figure 2.23 shows the AFIT FWMAV components after the laminated carbon fiber sheets are cut on the laser and ready for assembly.

(a) Structure   (b) Linkage   (c) Passive rotation joint

(d) Rotation stop   (e) Alignment clips   (f) Wing
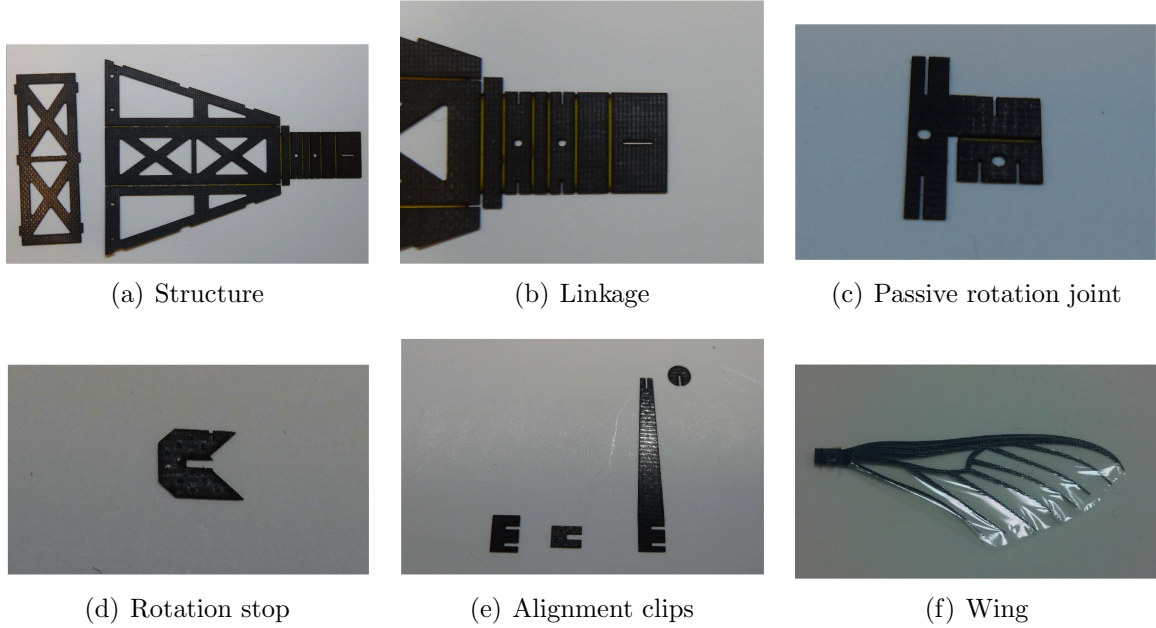
Figure 2.23: **AFIT FWMAV cut-out laminated carbon fiber assembly parts.**

The PZT and linkage transmission are fixed to a rapid prototype mounting assembly. The wing is attached to L_3 with crystal bond adhesive, and the rotation is controlled by a passive rotation stop made from $25\mu m$ thick Kapton HN 100, cut at

either 30°, 45°, or 60°. The flapper mounting structure consists of a rapid prototype resin polymer structure, which is rigidly mounted to a Nano-17 Titanium force transducer with three $2Mx$10mm hex cap screws. Figure 2.24 shows the assembled flapper and the flapper fastened to the mounting structure, and attached to the wired PZT.
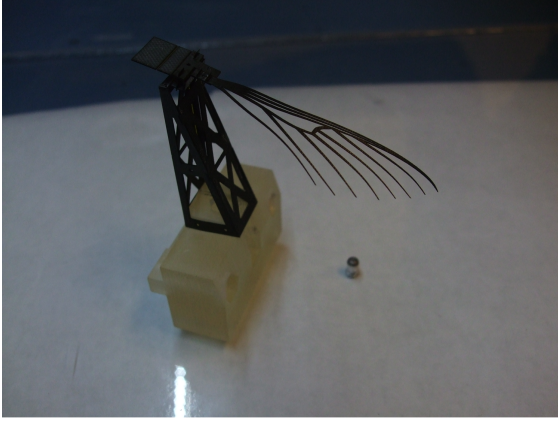
(a) Wing venation without mylar wing surface
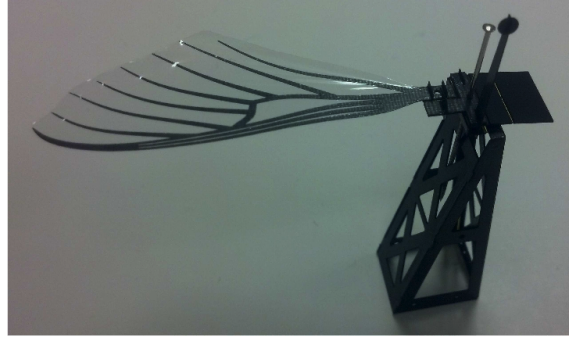
(b) Completed flapper
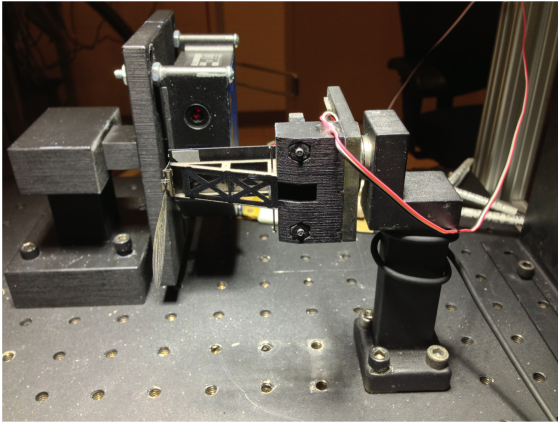
(c) Mounted flapper (front)
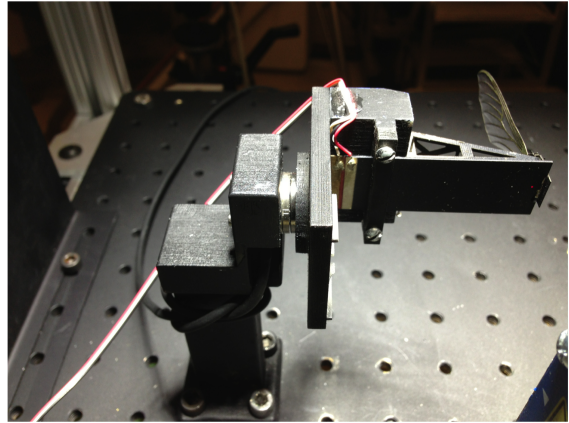
(d) Mounted flapper (back)

Figure 2.24: **Assembled and mounted flapper in test chamber.**

The PZT used to drive the AFIT FWMAV in this research is a 50mm (43mm effective) cantilevered length, Omega Piezo, OPT 60/20/0.6 strip actuator, with a maximum desired displacement of ±1.0mm of tip deflection. The piezo is driven in parallel (simultaneous) by a dual source with the crystals energized by a scaled DC bias ($A \cdot 200$V) to maximize the drive potential of the actuator, which deflects more in the positive (elongation) direction. The drive signals originate from a desktop PC via

MATLAB®, to a data acquisition box (DAQ) (National Instruments USB-6229 ±10V), amplified 30×, and then connected to the PZT actuator via a BNC interface card. The waveform shape of the drive signal can be altered in the MATLAB® interface. The flapper drive signal sent to the DAQ box is generated in MATLAB® using Equation 2.64.

$$\text{Drive Signal} = \frac{(A \cdot V_{gain}) \left(\frac{1}{2} + \sin(\omega t) + \eta + A_{\text{trim}}\right)}{30} \tag{2.64}$$

where A is the signal amplitude expressed as a fraction of the max voltage (-150V to $+300$V), which can be varied from $0 \to 1$, $V_{gain} = 200V$, η is the stroke bias parameter, and A_{trim} is a wing trim parameter used to obtain symmetry between the up and downstroke ($\phi_{min} = \phi_{max}$) from an unperturbed, fixed wing position. A_{trim} is an artifact of the manual manufacturing and assembly process, and is dependent on the wing and assembly structure. It is calculated through an automated auto-tuning procedure, and must be determined for each individual flapper system under test, as described in detail in [23]. The signal can be further biased toward either the up or downstroke with the bias parameter (η) while maintaining period invariance. The factor of $\left(\frac{1}{2}\right)$ is added to the equation to oscillate the PZT more in the ($+$) direction, where it has greater displacement potential. A factor of (1) would cause the PZT to exceed its maximum voltage of $V = +300$V at the higher amplitude settings. Figure 2.25 illustrates the difference in both the drive signal and the resulting wing flap angle, $\phi(t)$ between the symmetric (trimmed) and asymmetric (untrimmed) flap cases, where $\phi(t)$ was calculated with Equation 2.63, using the values for δ from the PZT displacement sensor data.
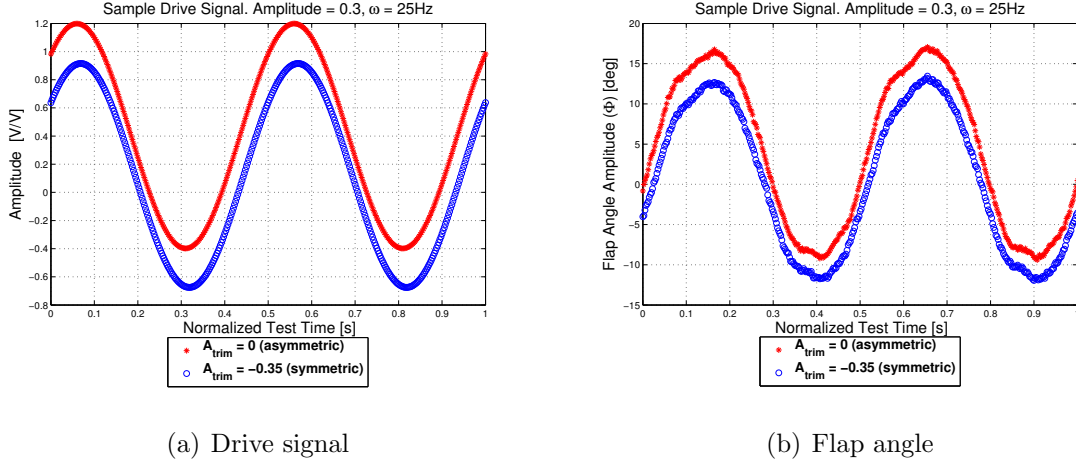
Figure 2.25: Example of two cycles of wing flap angle at A=0.3 and ω=25Hz for a trimmed and untrimmed drive signal, where $A_{\text{trim}}=-0.35$ for the symmetric example. *Left:* Drive signal sent to the DAQ box. *Right:* Flap angle as a function of cycle time, $\phi(t)$, calculated using PZT displacement and Equation 2.63.

The speed of either the up or downstroke can also be varied through a technique postulated by Anderson called Bi-harmonic Amplitude Bias Modulation (BABM) by adding integer values of the resonant frequency to specific phases of the stroke while also maintaining period invariance. However, without a traditional bar, gear, and linkage drive design, the wing by virtue of its attachment, rotates around the spanwise axis independently during the stroke, and its motion cannot be prescribed. Therefore, to ensure the wing rotates without needless oscillation, and recaptures inertial losses at the end of the stroke, a passive rotation joint was added to the wing-linkage attachment to ensure the leading edge was ahead of the trailing edge during both the up and downstroke phases [2]. Figure 2.26 depicts the AFIT wing/flapper mechanism with its 45° passive rotation joint, and the reference coordinate system used by the Nano-17 Titanium force balance.
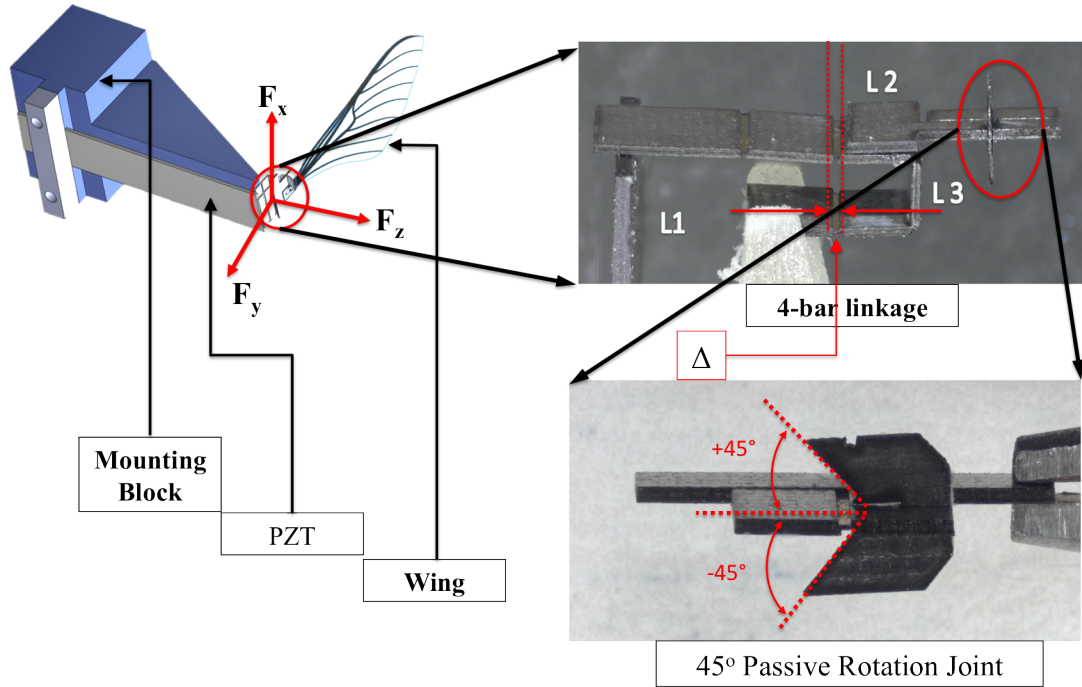
Figure 2.26: The AFIT FWMAV flapper assembly shows the PZT and wing mounted to the assembly block, the linkage assymbly, and the passive rotation joint. The body axis system is also displayed.

Figure 2.27 shows the complete wing cycle from upstroke to downstroke, normalized by time from $^t/_\tau$, where t is the specific time during the wing cycle, and τ is the total cycle time required to complete a single up-to-downstroke flap cycle.
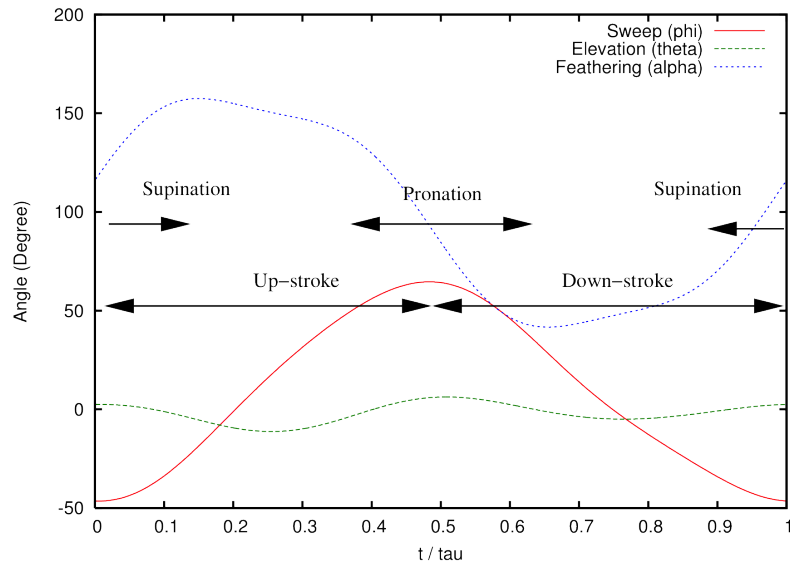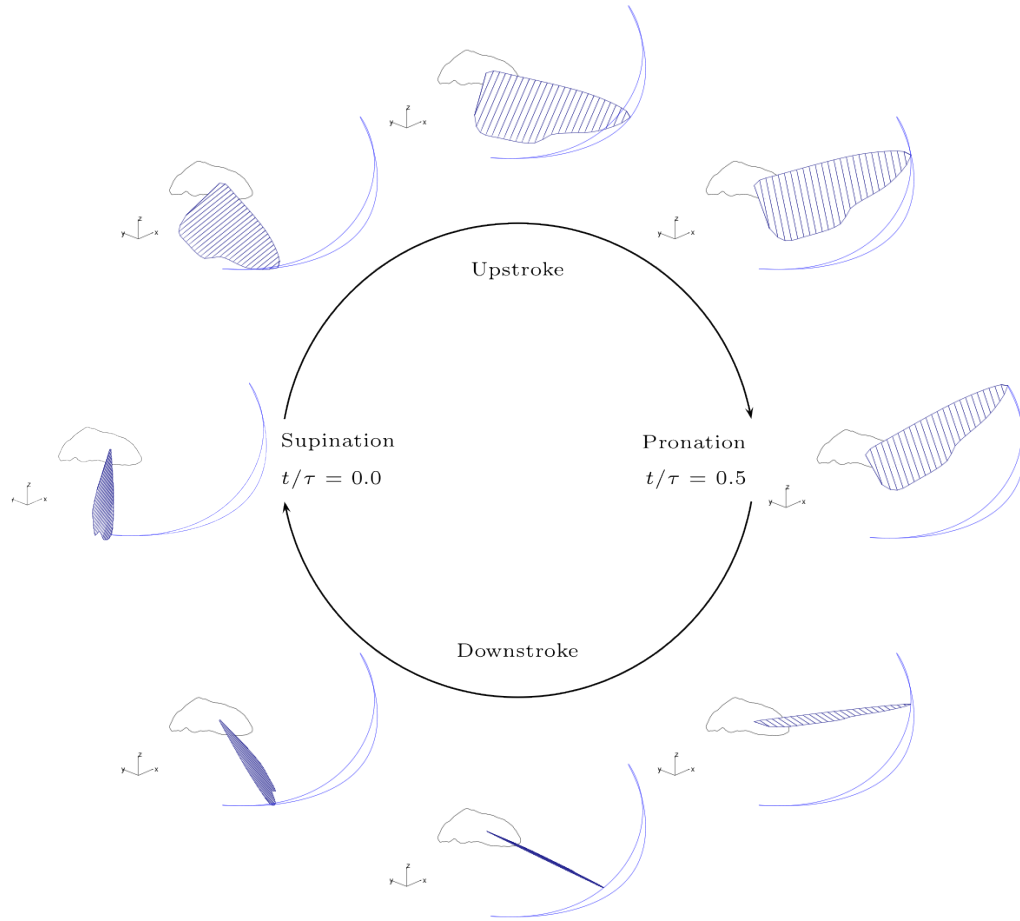
Figure 2.27: Notional graphic showing the sinusoidal change in stroke angle, ϕ (red line), elevation angle, θ (green line), and angle of attack, α (blue line), during a normalized $\left[{}^t/_\tau \right]$ single flapping cycle—from [50, 53, 57].

2.5.3   Wing Design.

O'Hara designed a biomimetic wing model with material properties, and structural responses closely matching those of the hawkmoth, *Manduca Sexta*. They were designed through *i*) careful dissection of numerous biological specimens; *ii*) medical Computer Tomography (CT) scanning of the inner venation patterns to catalogue their thickness and stiffness; *iii*) 3-D scanning laser tomography, with and without scales, to capture the precise wing planform shape; *iv*) 3-D finite element modeling to model the wing's bending and torsion modes to aide in the design of a carbon fiber lay-up schematic to accurately mimic the thickness, taper, and stiffness of the manmade analogue, to reproduce the same system structural dynamics; and *v*) an exhaustive precision laser CNC cutting technique developed to ensure accurate and repeatable manufacturing.

Figure 2.28 shows the biological mapping of the hawkmoth wing's structural members.
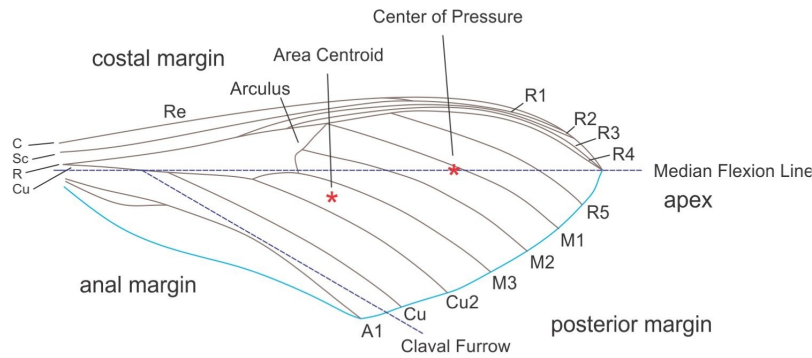
Costa (C) – the leading edge of the wing
Subcosta(Sc) – second longitudinal vein (behind the costa), typically unbranched
Radius (R) – third longitudinal vein, one five branches reach the wing margin
Media (M) – fourth longitudinal vein, one to four branches reach the wing margin
Cubitus (Cu) fifth longitudinal vein, one to three brances reach the wing margin
Anal Vein (A) – unbranched veins behind the cubitus

Figure 2.28: Diagram of the hawkmoth, *Manduca Sexta*, schematic of the typical forewing venation map—modified from [66].

Fifteen separate slices, at $2.5mm$ intervals, were made through the wing from root to tip with a microtome to assess the cross-sectional taper of the veins. The microscope

has a resolution accuracy on order of ≈ 1 micron, while the vein cross sectional areas were on order of ≈ 25 microns. Figure 2.29 shows an example of how the hawkmoth wing was sliced to make the venation slides used in examination and measurement, and a CT scan of the venation cross-section itself after being dyed and set on the optical slide.
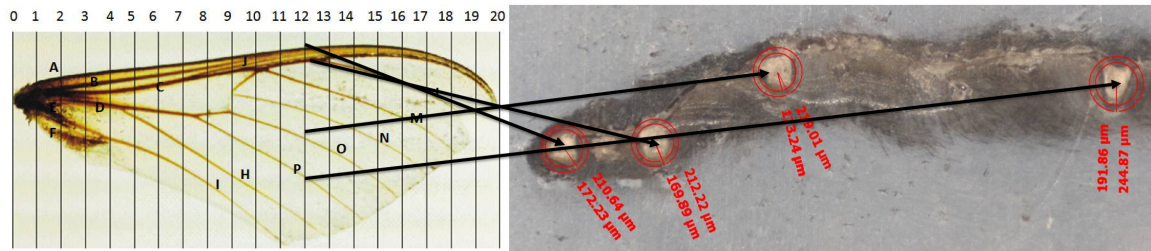
Figure 2.29: Slice locations of an examined Hawmoth wing *Left:* Schematic of the spacing and locations of slices made along the biological hawkmoth wing, post descalation, made chordwise from root to tip. *Right:* Venation cross section, cut with a microtome through the median flexion line of a typical *Manduca Sexta* specimen, suspended in paraffin wax, dyed, and then photographed with a scanning electron microscope— modified from [66, 65].

Figure 2.30 shows the finite element model of the engineered wing made from the material properties, modal testing, and 3-D rendering of the *Manduca Sexta* biological representative.
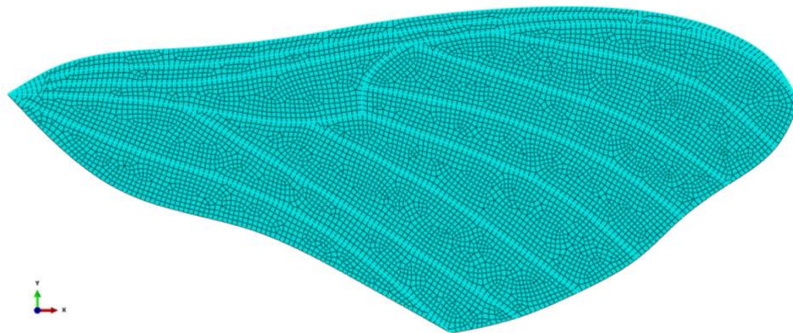
Figure 2.30: Finite Element Model of the hawkmoth wing, which is used as the basis of the manufactured engineered wings used in this research [66, 65].

Table 2.2 below lists the material properties of the hawkmoth, *Manduca Sexta*, O'Hara experimentally determined through his exhaustive testing on 30 male and female specimens [64, 65, 66].

Table 2.2: Hawkmoth Wing Structural Properties Measured by O'Hara *et.al.*

mass = **28.6**mg			
Mass Property ‖	**x-axis**(m)	**Y-axis**(m)	**Z-axis**(m)
Center of Area	22.1E-03	4.0E-03	0
Center of Mass	16.2E-03	0.5E-03	0
Moment of Inertia ‖	$I_{xx}(kg-m^2)$	$I_{yy}(kg-m^2)$	$I_{zz}(kg-m^2)$
Origin	2.99E-10	1.14E-08	1.16E-08
Center of Mass	2.91E-10	3.89E-09	4.18E-09
Product of Inertia ‖	$I_{xy}(kg-m^2)$	$I_{yy}(kg-m^2)$	$I_{zz}(kg-m^2)$
Origin	-2.54E-10	1.01E-29	-5.92E-29
Center of Mass	-1.64E-11	1.01E-29	-5.92E-29

Table 2.3 below lists the material properties of the AFIT engineered wing, which were modeled from the properties calculated through the structural analysis of the hawkmoth wings, and calculated through use of finite element modeling using ABAQUS commercial modeling software [65, 66].

Table 2.3: Engineered Wing Structural Properties Measured by O'Hara

mass = **38.2**mg			
Mass Property ‖	**x-axis**(m)	**Y-axis**(m)	**Z-axis**(m)
Center of Area	22.1E-03	4.0E-03	0
Center of Mass	20.9E-03	4.7E-05	0
Moment of Inertia ‖	$I_{xx}(kg-m^2)$	$I_{yy}(kg-m^2)$	$I_{zz}(kg-m^2)$
Origin	7.69E-10	3.05E-08	3.13E-08
Center of Mass	7.68E-10	8.1E-09	8.87E-09
Product of Inertia ‖	$I_{xy}(kg-m^2)$	$I_{yy}(kg-m^2)$	$I_{zz}(kg-m^2)$
Origin	-1.13E-10	-2.00E-32	-1.37E-31
Center of Mass	-6.24E-11	-2.0E-29	-1.37E-31

Figure 2.31 below shows a liberated hawkmoth wing (left), prototypes of the AFIT designed thin (center), and thick (right) ribbed engineered wing trials.

Figure 2.31: Biological vs. engineered hawkmoth wings. *Left:* Liberated hawkmoth wing, *Center:* AFIT designed thin engineered wing, *Right:* AFIT designed thick ribbed engineered wing. [66, 65].

Table 2.4 lists the 1st bending and 2nd torsion modes of all three wings depicted in figure 2.31 above, evaluated in both air and in a vacuum, in the AFIT MAV lab [65, 66].

Table 2.4: Biological and Engineered Wing Modal Analysis Results Measured by O'Hara

Wing	Mass [mg]	1st mode air [Hz]	2nd mode air [Hz]	1st mode vac [Hz]	2nd mode vac [Hz]
Hawkmoth	55.8	46.8	71.8	87.5	152.5
Thin vein	52.5	52.1	72.8	58.1	80.3
Thick vein	61.7	68.4	77.8	68.4	84.6

The descriptions of the wing, flapper, and drive train design used in this research are an abbreviated summary, for further details into the design, manufacturing, and equipment used to fabricate the AFIT flapper system, the reader is encouraged to refer to [2, 20, 65, 66, 79] for more thorough analysis, description, and details on the AFIT wing and flapper design. This description was only meant to provide a topical coverage of the most salient points in the design, so a basic understanding and familiarity is gained, sufficient to follow the basis of the experimental work presented following this chapter.

III.   Experimental Methodology

3.1   Overview

C HAPTER III will detail the experimental equipment, tactics, techniques, and procedures employed in this research program. The experimental methodologies and numerical methods used to operationalize the flapper will be explained along with the novel procedures developed specifically for this research to characterize the AFIT FWMAV. Methods for obtaining the AFIT FWMAV system resonant frequency, and the auto-tuning procedure used to set A_{trim} to achieve a symmetric wing stroke angle are presented. Details and operating specifications of the measurement equipment used in the force and moment, and PIV experiments are presented, in addition to a high level description of the data processing and analysis methods required to transform raw data into actionable engineering parameters.

3.2   Flapper Operationalization

3.2.1   Flapper Auto-Tune Mapping.

As previously stated in *Chapter* II, flapping at resonance is necessary to generate the greatest displacement of the PZT in order to maximize the total wing stroke. Anderson's MATLAB® script to predict total wing tip travel, given a PZT cantilever length and transmission linkage lengths, was used to animate a moving graphical rendering of the designed wing flapping, with the linkages and wing modeled as linear beams. Figure 3.1 shows three still shots of the MATLAB® animation file developed by Anderson to predict the total stroke angle, given an input parameter set of PZT and transmission component lengths.
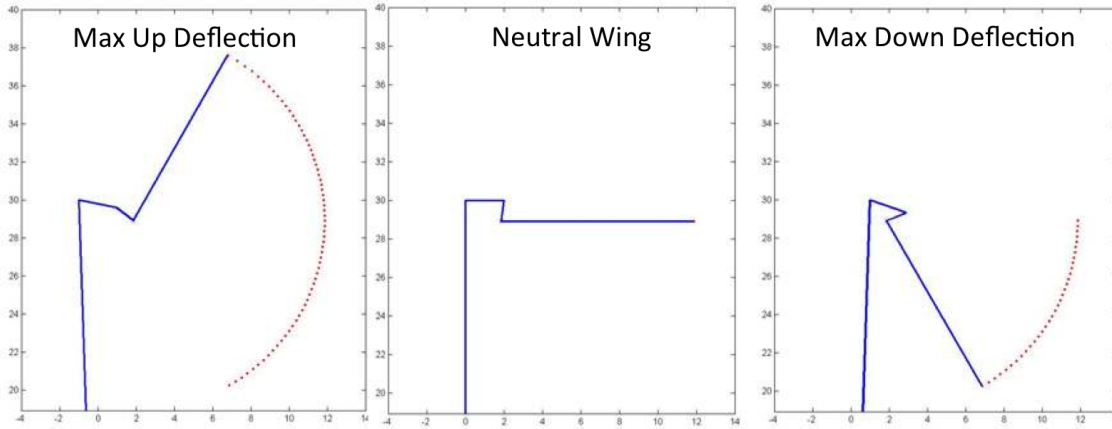
Figure 3.1: Plot of the Matlab®wing stroke angle design tool developed by Anderson [2].

Although it is possible to design the linkages to achieve a prescribed wing travel with Equations 2.62–2.61, originally stipulated by Wood and Finio at Harvard, and implemented by Anderson; the practical implementation of the fabrication and assembly of such diminutive designs rarely translates into the expected actual performance. Previous researchers relied on high-speed video analysis of the flapping mechanism to determine if the wing was flapping symmetrically. At worst, the analysis relied on judgement; and at best, used rudimentary video fiducials to determine wing symmetry [8, 38, 86, 93]. O'Hara used a white tipped carbon beam, glued to the flapping mechanism, rotated 90° to the wing mount, as a fiducial point during high-speed video capture. A MATLAB® script written by Sladek was used to translate the high-speed video into a series of photographic stills used to track the painted edge, which was used to calculate the wing tip position in pixel coordinates, which could, in theory, be used to calculate the wing position, and ostensibly then, the *up* and *down* stroke angles could be extracted from the matrix of pixel locations [66]. This method proved more accurate than using visual clues alone; however, the code was susceptible to error if any of the still images were blurry, or the pixel resolution between the popsicle stick and the background was not distinct enough to register a pixel threshold intensity difference. Additionally, gluing the painted stick to the flapper altered the

94

physical dynamics of the system under test, changed the flapped mass, the 1st mode resonant frequency, and ultimately the actual wing motion. Figure 3.2 shows a video grab of the AFIT flapper with a popsicle stick mounted, and an added rough tracking course overlaid on the video still.
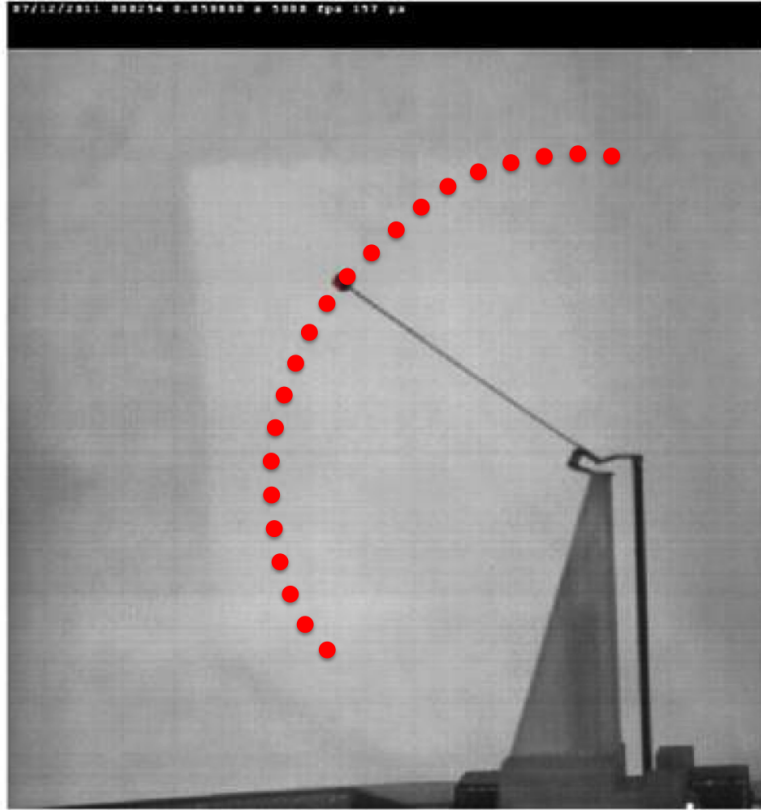
Figure 3.2: **Popsicle stick optical tracking used by O'Hara [67].**

It is desired to be able to track the motion of the PZT, and therefore the wing, reliably and accurately to determine symmetry, without altering the system dynamics or changing the flapping configuration of the wing-flapper system. A Micro-Epsilon optoNCDT 1700 laser displacement sensor, with a 2.5kHz sampling rate, 0.1μm resolution, and 2.0μm maximum linearity was used to capture the PZT tip displacement. A rapid prototype mounting structure was designed and fabricated to mount the sensor in close proximity to the flapper mechanism without interfering with the flapper itself or the surrounding aerodynamic forces created during wing motion. Figure 3.3

shows the displacement sensor in the test chamber.
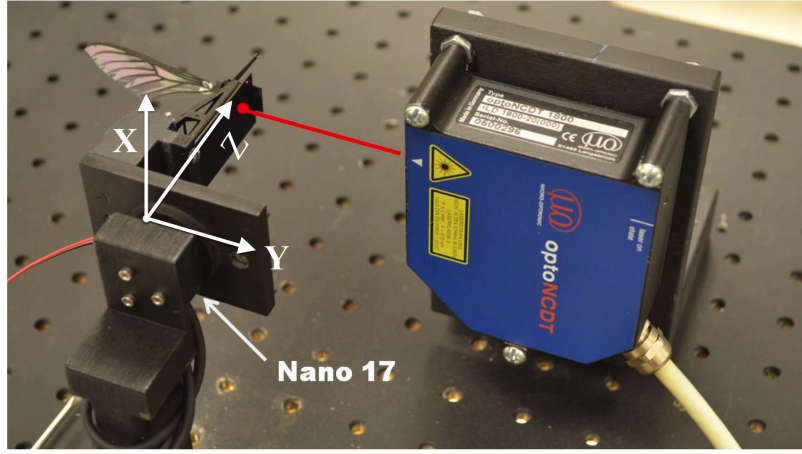
Figure 3.3: $\mu\epsilon$ optoNCDT 1700 displacement sensor.

A calibration procedure was developed to determine the conversion ratio from volts to millimeters. A sensitive calibration tool, comprised of a rotating metal drum, sub-scale accurate to 0.0025in, full-scale accurate to 0.025in, per rotation, was used to calibrate the displacement sensor. The sensor was connected to an oscilloscope, and voltage readings were taken at five complete rotations of the calibration tool from 0.10in to 0.20in. A straight difference was taken between voltage readings, and an average slope was calculated by Equation 3.1.

$$\overline{S} = \frac{1}{S_n} \sum_{i=1}^{n} S_i \tag{3.1}$$

The average slope was found to be 12.53 $^{v}/_{in}$. Given the slope and the input from the sensor, the standard form for an equation for a line is used to calculate the displacement (in inches) as follows in Equation 3.2.

$$x_{disp} = \frac{y_{volts} - b}{12.53 \ ^{v}/_{in}} \tag{3.2}$$

A MATLAB® routine was developed to perform an automated, real-time adaptive tuning of a PZT/flapper/wing assembly. When the *Auto-Tune PZT* function

96

is selected in the custom developed user interface menus, the operator is prompted to enter the design limits of the system under test, a beginning and maximum amplitude, a beginning and maximum amount of wing trim (A_{trim}), and the symmetry error tolerance. The symmetry error tolerance is a user specified threshold of how close the ratio of $^+/_-$ PZT tip deflection is to ≈ 1 . The value of A_{trim} determines how much of the drive signal is forced to bias the peak amplitude of either the *up* or *down* stroke by adding more energy to either the $+$ or $-$ PZT drive signal given in Equation 2.64. The program will then start the symmetry analysis, starting with the beginning amplitude, and calculate the ratio of *up* to *down* stroke as a percentage, where a value of one is *perfectly symmetric flapping*, using the real-time displacement sensor data, and adjusts the trim values, based on a sensitivity switching function that automatically adjusts the amount of PZT bias correction based on the magnitude of the error between the *up* to *down* stroke travel—the *greater* the error, the more bias correction; the *smaller* the error, the less the bias correction. Once the user specified symmetry tolerance is achieved, the flap settings and all the associated force, moment, power and displacement, data is saved to a structured array file. The program then increments to the next amplitude setting, repeating the above process until the error bounded symmetry value is reached for all the amplitude settings up to the user specified maximum amplitude setting, *or* the PZT displacement reaches the user specified upper design limit, which causes the program to stop the tuning at that amplitude setting, and reports the maximum amplitude, and symmetrical flapping conditions attainable within the maximum allowable PZT displacement. It is essential that the experimentalist confirm that the location of the PZT lie within the measurement range of the non-contact displacement sensor.

Symmetry values were verified by manually tuning wing symmetry at a few amplitudes. Still frames of high speed video were analyzed using the coordinate capture

features of the MotionStudio^{tm} software . A stationary pixel location at the attachment point was chosen as the base coordinate, $(x_o, \ y_o)$, and the coordinate locations at the maximal translation position of the up and downstrokes in space are $(x_i, \ y_i)$. The image origin, $(0, 0)$, is located at the top left corner of the video image. To make the angular position calculations more tenable, and keep the angles restricted to a two-quadrant tangent, the origin of the video image is shifted to the base coordinate location by an offset coordinate pair, $(x_n, \ y_n)$. The wing tip coordinates in space, $(x_i, \ y_i)$, must be shifted by the same offset amount to maintain the proper spatial relationship. These two points are used to calculate the wing stroke angle, ϕ, as follows:

$$\phi(t) = \tan^{-1} \left| \frac{(x_o - x_n) - (x_i - x_n)}{(y_o - y_n) - (y_i - y_n)} \right| \tag{3.3}$$

Figure 3.4 shows an example of manually extracted maximal up and downstroke images superimposed of a image of the wing at rest. For the $45°$ wing shown, at A=0.5 and A_{trim}=0.035, $\phi_{max} = 55.45°$ and $\phi_{min} = 56.65°$, for a total stroke angle of $\Phi = 121.1°$.

Figure 3.4: Example of three superimposed images from a $45°$ wing at **A=0.5** and $\mathbf{A_{trim}}$**=0.035, used in manually checking wing symmetry.** $\phi_{max} = 55.45°$ **and** $\phi_{min} = 56.65°$.

3.2.2 System ID.

As previously stated, it is necessary to flap at the system resonance (PZT/flapper/wing) to maximize the amount of total wing stroke travel using the minimum amount of system power. A MATLAB$^®$ routine was incorporated in the flapper GUI allowing the user to drive the flapper with a linear frequency sweep utilizing a built-in signal processing *chirp* function that excites a user specified frequency range at a specified amplitude setting. The function subsamples the frequency response data from the force, velocity, and distance sensors to eliminate the starting and stopping transient responses, and stores that data in a three dimensional array, comprised of a two-dimensional matrix of force balance data, and a third-dimension stores the data from subsequent tests, until the user specified total number of frequency sweep tests are accomplished. All of the individual frequency test data is then averaged, yielding a single multi-run frequency response data set. The input signal (X_1) (*drive*

signal from the amplifier to the flapper) and the output signal (Y) {$Y_1=F_z$ *(mgF)*,

$Y_2=$*distance (mm)*, $Y_3=$*velocity (* $^m/_s$*)*} are separated, and the data is put into 10

bins; the size of each bin is determined from the overlap percentage (50%) and the to-

tal number of data points, N. The input and output data is filled into each bin, with

50% of each bin being filled from the previous bin. A *Hanning* window, the size of

each bin, is applied to the input and output to force each bin to start and end at *zero*,

making the data *periodic*, thereby reducing data *leakage*. The windowed data is used

to calculate the cross and auto Power Spectral Density (PSD) for each sensor, and are

then averaged to determine a composite auto and cross PSD. The size of the averaged

auto and cross PSD data sets are reduced by eliminating 20% of half the sampling

frequency, $\omega_s \gg \omega_o$, of the discrete data signals, or the Nyquist frequency. Identifying

the Nyquist frequency removes aliasing from the data set, preventing high frequency

content from "wrapping", and biasing, (*creating noise*), in the lower frequency con-

tent. Retaining the first 80% of the data eliminates "folding" as a result of applying

an anti-aliasing filter (*low-pass filter*) ahead of the sampling device. {*Since this is*

not a treatise on signal processing, the derivation of the discrete-continuous Nyquist-

Shannon Sampling Theorem upon which the data conditioning used here is predicated,

is not presented here, but can be found in any standard text on signal processing}.

The resulting auto and cross PSD data is then used to calculate the FRFs of each

data signal.

A Bode plot of the acceleration, velocity and displacement FRF is used to deter-

mine the 1$^{\text{st}}$ mode (*system resonance*) of the system under test. Figure 3.5 shows

the averaged time history of the acceleration (*axial force*: F_z), velocity, and displace-

ment sensors compared to the their respective percent coherence from an ensemble

average of 10 frequency sweeps from $\omega = 0 \rightarrow 125$Hz, $A = 0.05$, $t = 10$sec, sample

rate $= 5$kHz. If the data sets are: *i) ergodic* signals, data which the statistical prop-

erties, namely the *mean* and *variance*, have properties that are both time averaged and spatially invariant; and *ii*) possesses a linear transfer function, which satisfies the properties of superposition, scaling, and homogeneity. Mathematically, linearity is expressed by: given two system inputs, $x_1(t)$ and $x_2(t)$, and an operator, H that maps the inputs to the outputs,

$$y_1(t) = H\{x_1(t)\}$$

$$y_2(t) = H\{x_2(t)\}$$

then a linear system is one which satisfies Equation 3.4 for any value of α and β:

$$\alpha y_1(t) + \beta y_2(t) = H\{\alpha x_1(t) + \beta x_2(t)\} \tag{3.4}$$

the coherence is then a measure of the causality of the output, Y_i, (*force, velocity, displacement data*) to the input, $X_1(t)$, (*flapper drive signal*). The percent coherence is calculated from Equation 3.5

$$\gamma^2 = S_{xy} = \frac{H_1(\omega)}{H_2(\omega)} = \frac{|S_{xy}|^2}{S_{xx}S_{yy}}$$

where: $\tag{3.5}$

$$0 \leq S_{xy} \leq 1$$

where S_{xy} is the cross-spectral density between x and y, and S_{xx} and S_{yy} are the auto-spectral density of x and y respectively. Equation 3.6 gives the auto and cross correlation, and Equation 3.7 give the expressions for the auto-spectral density (S_{xx} or S_{yy}) and cross-spectral density (S_{xy}) respectively.

$$\text{auto correlation } X \rightarrow X = S_{xx} = X_k^* \cdot X_k$$

$$\text{auto correlation } Y \rightarrow Y = S_{yy} = Y_k^* \cdot Y_k \qquad (3.6)$$

$$\text{cross correlation } X \rightarrow Y = S_{xy} = X_k^* \cdot Y_k$$

where:

$$S_k^{xy} = DFT\left(R_r\right) = \frac{1}{N} \sum_{r=0}^{N-1} R_r e^{-\left(\frac{2\pi k_r}{N}\right)}$$

and:

$$R_r = \text{cross correlation } = R_{xy}\left(\tau\right)$$

$$R_{xy}\left(\tau\right) = R_r = \frac{1}{T} \sum_{s=0}^{N-1} X_s Y_{s+r} \Delta$$

let $T = N\Delta$, then:

$$R_{xy}\left(\tau\right) = R_r = \sum_{s=0}^{N-1} X_s Y_{s+r}$$

therefore:

$$S^{xy} = \frac{1}{N} \sum_{r=0}^{N-1} \left(\sum_{s=0}^{N-1} X_s Y_{s+r} \right) e^{-i\left(\frac{2\pi k_r}{N}\right)}$$

$$= \frac{1}{N} \left(\underbrace{\sum_{s=0}^{N-1} X_s e^{-i\left(\frac{2\pi k_s}{N}\right)}}_{DFT(X_r)=X_k^*} \cdot \underbrace{\sum_{r=0}^{N-1} Y_s e^{-i\left(\frac{2\pi k_{s+r}}{N}\right)}}_{DFT(Y_r)=Y_k} \right) \qquad (3.7)$$

Where the k indices indicates discretely sampled data, *(e.g. displacement, velocity, acceleration)*, * denotes the conjugate transpose of the indicated data set, and

DFT(N_x), is the Discrete Fourier Transform (DFT) of the discrete data set. If $x(t)$ and $y(t)$ are completely unrelated, the coherence will be zero. A value of S_{xy} less than one, but greater than zero, indicates either *i)* a noisy measurement; *ii)* the system relating $x(t)$ and $y(t)$ is not linear; *iii)* or that $y(t)$ *might* be generating its output due to its input $x(t)$, but it is also being influenced necessarily from other input signal streams. With the equations defined for the discrete auto and cross PSDs, Equation 3.8 is used to calculate the discrete FRF, or transfer function, $H(\omega)$:

$$
\begin{aligned}
H_1\left(\omega\right) &= \frac{S_{xy}(\omega)}{S_{xx}(\omega)} \\
H_2\left(\omega\right) &= \frac{S_{yy}(\omega)}{S_{yx}(\omega)}
\end{aligned}
\tag{3.8}
$$

Where $H_1(\omega)$ is susceptible to noise on the input signal, and represents the lower bound of the transfer function; while $H_2(\omega)$ is susceptible to noise on the output signals, and represents the upper bound of transfer function. The drive signal, *input channel*, is conditioned and filtered by the amplifier and the National Instruments (NI) box before being sent to the flapper mechanism, but the force data, *output channel*, is not conditioned before it is sent to the NI box, making it more likely to be contaminated by environmental noise, electrical noise in the connections, or low threshold data signals. Therefore, because $H_1(\omega)$ is insensitive to noise on the output channel, it was used to determine the resonant frequencies. Figure 3.5 shows a representative example of the force, velocity, and displacement time history signals, percent coherence, and their respective normalized FRFs.
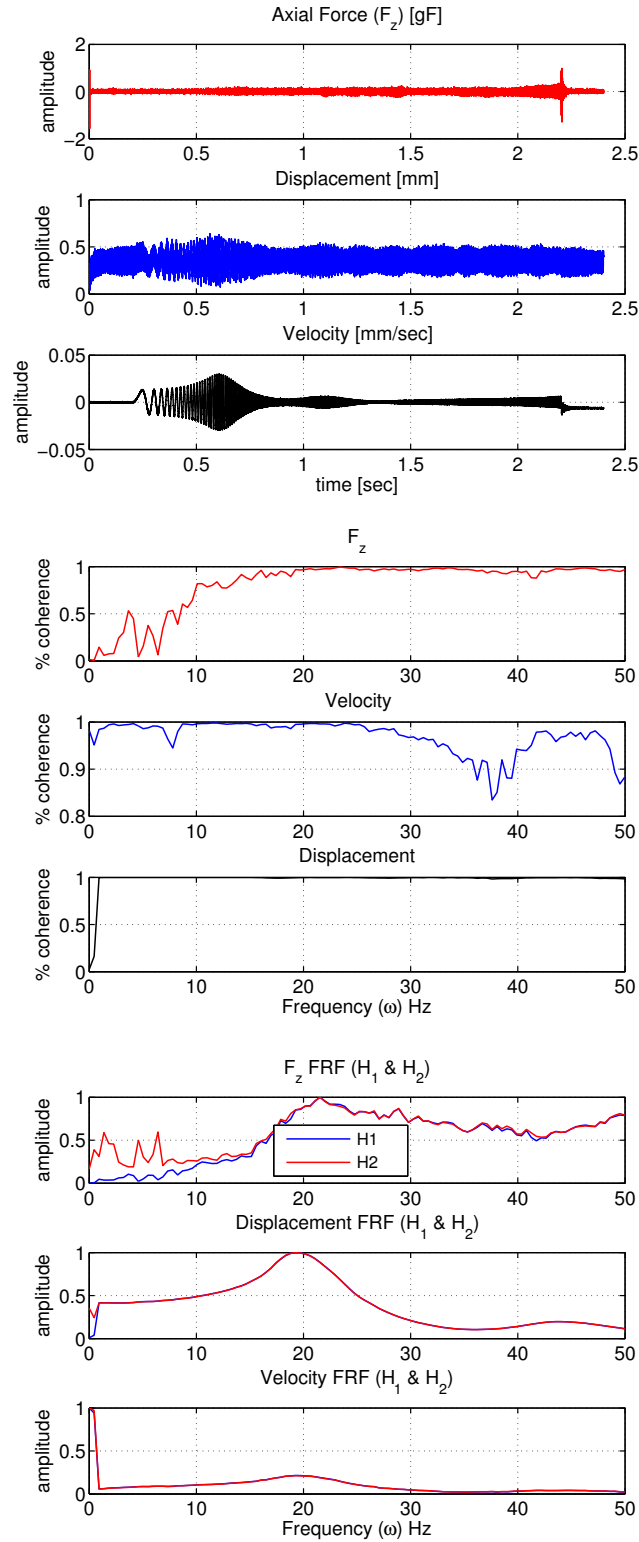
Figure 3.5: Example illustration of the acceleration, velocity & displacement response to a linear chirp from 0-125Hz. *Top:* raw signal time history; *Middle:* % coherence. *Bottom:* normalized FRFs.

The force data shown in Figure 3.5 had poor coherence (X_1 = input chirp signal, Y_i =F_z data) and was not used to determine the system resonant response. The most likely cause of the poor force coherence data is the low amplitude setting used in the frequency chirp did not create a large enough force to rise above the noise floor threshold of the Nano-17 Titanium force transducer (load limits and operating envelope specified in section 3.3). Figure 3.6 shows the displacement percent coherence and FRFs for the 30°, 45°, and 60° PZT/flapper/wing system under test used in the experiments detailed below. There were two clearly identifiable modes at ≈ 20Hz and ≈ 45Hz.

(a) Coherence: 30° (b) Coherence: 45° (c) Coherence: 60°

(d) FRF: 30° (e) FRF: 45° (f) FRF: 60°
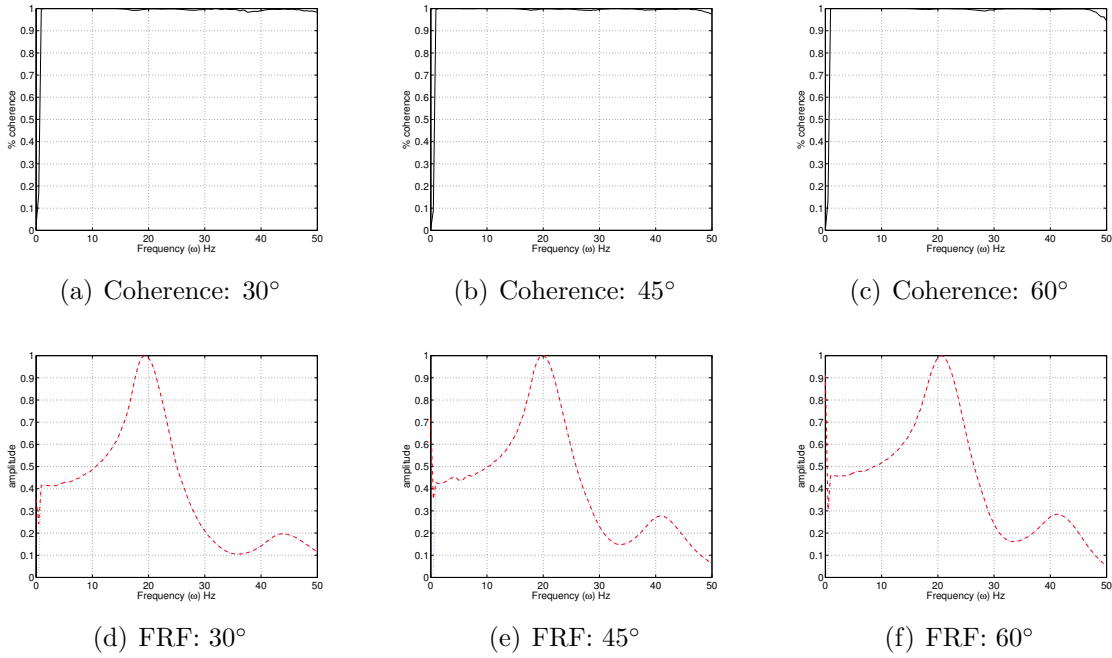
Figure 3.6: 30°, 45°, and 60° System Coherence and Frequency Response Functions.

3.2.3 Optical Wing Tip Tracking.

The position of an untwisted wing tip in relation to a fixed point, such as the wing mount spar, is necessary to calculate the wing's angular position, ϕ, in the wing stroke plane, β. Two positions, one at the leading edge of the wing tip, and another point on the trailing edge, are needed to calculate the angle of attack, α, and

the elevation angle, θ, the inclined angle of the wing tip with respect to the stroke plane. These three angles completely describe the wing position at any time during the translational and rotational stroke phase, and are used to calculate aerodynamic parameters of the wing like C_L and C_D.

Doyle *et.al.* developed a method to optically track dynamic systems in three dimensions using multiple high-speed video camera streams, see [23], [28], and [29] for detailed descriptions of the optical tracking algorithm development process. As an interim step in the progression of his research, he developed his own set of tracking algorithms by customizing a combination of routines available in the ComputerVision (OpenCV) library. Specifically, he employed a combination of Canny Edge Detection and an improved Gaussian Mixture Model (GMM), developed by Zivkovic, to video clips of the wing flapping from two perpendicularly mounted IDT X-Stream high speed cameras; one vertically mounted, downward focused, and the other horizontally mounted, focused at dorsal surface of the wing, taken at 1000Hz. The cameras have a 512×512 CMOS sensor, equipped with Giga-Ethernet and USB 2.0 communications interface. They are capable of frame rates up to 5000Hz, can be configured to fire from an internal timer, on detected motion, or externally from a 5V TTL trigger; and they can be linked together in a *master—slave* configuration where the TTL trigger signal sent to the *master* camera will simultaneously fire the *slave* camera. Table 3.1 lists the camera specifications and settings used in the optical tracking testing.

Table 3.1: **High Speed Camera Specifications & Settings Used for Optical Wing Tracking**

Camera Spec ‖	Top Camera	Side Camera
Camera model	X-Stream XS-4	MotionPro X4
Lens	Nikkor 1:28D (28mm)	Nikkor 1:28D (28mm)
f-stop	4	2.8
Sensor type	CMOS	CMOS
Sensor model	MV-02	MV-02
Sensor size	512×512	512×512
Sensor gain	1.0	1.1
Dynamic range	8-bit	8-bit
Frame rate	1000Hz	1000Hz
Exposure	$108\mu s$	$497\mu s$
Trigger type	Circular mode / edge high TTL	Slave

3.2.3.1 GMM tracking method.

The improved GMM model essentially is a background subtraction method where a current image frame, I_t is subtracted from a future image frame, I_{t+i}, to determine which pixels are not part of the preexisting background pixel intensity map. A probability density function is assigned to each pixel to determine if a pixel from the incoming image, I_{t+i}, is part of the background or foreground [28]. Zivkovic's improved GMM stipulated for a time period, T, that at any time, t, there is a training set of images, $X_T = \{x(t), ..., x(t-T)\}$, used to establish the Background (BG) image. Every new image frame is used to update the training data set, X_T, and reestimate the model, by $p\left(\vec{X}^{(t)} \middle| X_T, BG\right)$, where $\vec{X}^{(t)}$ is the pixel intensity value in some color subspace. The BG only model is given by $p\left(\vec{X}^{(t)} \middle| BG\right)$. If however, as the number of image frames propagate forward, objects appear not in the BG but belong in the Foreground (FG), the model must be updated to include both BG and FG pixels, $p\left(\vec{X}^{(t)} \middle| X_T, BG + FG\right)$. Equation 3.9 shows the GMM model for M components (*images*) [97].

$$p\left(\vec{X}^{(t)} \middle| X_T, BG + FG\right) = \sum_{m=1}^{M} \hat{\pi}_m \mathrm{N}\left(\vec{x}; \hat{\vec{\mu}}, \hat{\sigma}_m^2 I\right) \qquad (3.9)$$

107

where $\hat{\vec{\mu}}_1, \ldots, \hat{\vec{\mu}}_m$, are the estimates of the mean pixel values, $\hat{\sigma}_1, \ldots, \hat{\sigma}_m$, are estimates of the variances used to describe the Gaussian components, and the mixing weights are $\hat{\pi}_m$, and are positive, real-valued, and sum to one. The weighting factor, π_m, assigns a value describing how much of the data belongs to the m$^{\text{th}}$ component of the GMM, which is the probability density that a specific sample comes from the m$^{\text{th}}$ component, or *image* frame [97].

The GMM model was implemented in a C++ program, and 301 frames of wing flapping video, from a single camera were used to track a single point on the wing tip to assess its efficacy for future use in tracking multiple points, with multiple cameras, along the wing's leading and trailing edges, to provide pixel coordinates necessary to calculate all three wing positional angles, $\phi(t), \theta(t), \alpha(t)$. The initial GMM model wing tip tracking was able to track the general motion of the wing, but produced a large number of spurious data points. A 3$^{\text{rd}}$ order polynomial was the best fit to the data, and used to plot against the raw data, this data, along with the interpolating polynomial, were used to filter spurious $x - y$ data pairs, and a second 3$^{\text{rd}}$ order polynomial was fit to the filtered $x - y$ data set, which more accurately tracks the wing tip arc, see [21, 23, 28, 29, 97] for further details on this optical tracking implementation. Figure 3.7 shows the raw GMM track data with the initial and improved curve fit, and Figure 3.8 shows the improvement the polynomial approximation renders over the standard GMM optical tracking model implementation.
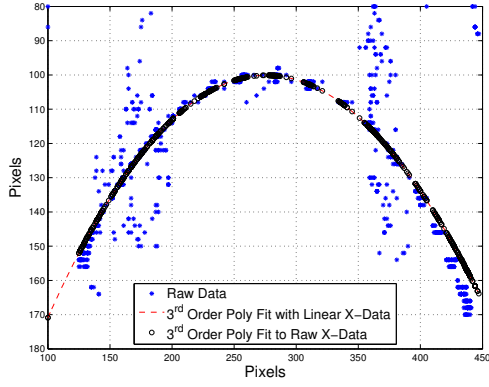
(a) Raw data & 1st fit
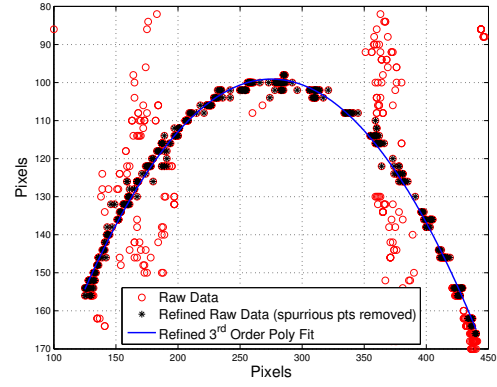
(b) 2nd fit

Figure 3.7: **Results of Gaussian Mixture Model optical wing tip tracking.** *Left:* **Blue data shows $(x,\ y)$ pixel coordinates from GMM tracking model, black data shows a 3rd order polynominal fit using GMM x-coordinate data, and red line is a 3rd order polynominal fit to a linearized x-vector spanning the left and right most GMM pixels.** *Right:* **Results of improved linear least squares approximation. Red data shows $x - y$ pixel coordinates from GMM tracking model, black data shows filtered GMM optical tracking data, and the blue line is the improved 3rd order polynominal fit to the filtered GMM tracking points.**

TEST CONDITIONS: A = 0.35, ω = 25Hz, η = −0.39

Raw Tracking Data | Filtered & Smoothed Tracking Data
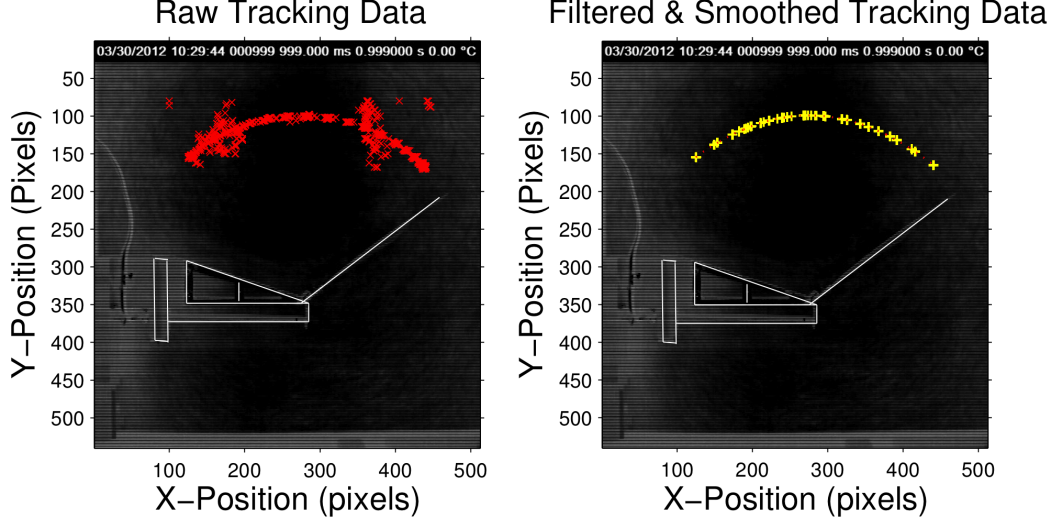
Figure 3.8: Results of optical wing tip tracking—TOP VIEW. *Left:* Raw GMM tracking points overlayed on the wing video; *Right:* Improved tracking points from a 3$^{\rm rd}$ order least squares regression approximation.

However, since this initial proof of concept involved a single tracking point, and a single camera, the resulting pixel coordinates can only be used to describe the wing tip's 2-D arc, which can only be used to calculate the stroke angle, Φ. Given the amount of computational overhead involved with implementing the GMM tracking model, another set of OpenCV tools were used to calculate all three kinematic angles simultaneously. The GMM model, in conjunction with a Canny Edge Detector, were employed to track multiple points along the wing, in multiple images, at the same time.

3.2.3.2   Canny Edge Detector tracking method.

The *Canny* function in the OpenCV library aims to improve upon shortcomings in background detection methods by *i*) numerically minimizing the error rate by a good detection of only existent edges, and not comparing backgrounds; *ii*) providing optimal localization by numerically minimizing the distance between detected edge pixels and real edge pixels; and *iii*) eliminating false positives by permitting only one detector response per edge. The detection algorithm applies the following numerical techniques to achieve the desired edge detection accuracy *i*) apply a Gaussian filter to reduce noise; *ii*) find the image gradient intensity and direction (to the nearest cardinal direction) using a Sobel convolution mask; *iii*) apply *non-maximum* pixel intensity suppression to ensure only thin edges are maintained in the final pixel location and intensity matrices; and *iv*) bound the solution's upper and lower limits to eliminate hysteresis [68]. An array of 301 images from the top and side cameras, for every angle stop and test condition combination, were loaded into the tracking program; each top/side image pair were dynamically resized to maintain the same wing aspect ratio relation between images, and the images rotated so the mounting block and the linkage pivot point were at the same pixel location in every frame. The Canny toolbox was used to reduce the images to their exterior outlines, and custom GMM masking techniques were utilized to block out the mounting base, PZT drive wires, and other areas that caused spurious edges to appear. Points along the wing's detected edges were designated and stored for all 301 frames at each angle stop/test case combination.

- The minimum and maximum points along the LE were stored from the *top* images to calculate the stroke angle (ϕ) at every frame through the flap cycle.

- The maximum point along the LE and the minimum point along the TE were stored from the *side* images to calculate the elevation angle (θ) at every frame through the flap cycle.

111

- 51 pairs of points at 0.01R intervals were collected from 0.4R to 0.9R along the span in both the *top* and *side* images to calculate the angle of attack, $(\alpha(r))$, as a function on span location at every frame through the flap cycle.

The wing kinematic angles as a function of time, $\phi(t)$, $\alpha(t)$, and $\theta(t)$ were calculated using standard trigonometric relations. The total average stroke angle recorded for each run, Φ, during a test run was calculated by taking the mean of ϕ_{max} and $|\phi_{min}|$. The angle of attack was defined in *Chapter II* as the angle the wing makes with the horizontal, but the angle calculated from the optical tracking is the feather angle, ψ, the angle between the vertical and the wing; therefore, $90°$ was subtracted from all the angles. On a $30°$ angle stop wing, the wing will rotate $\approx 30°$ from vertical after hitting the rotation joint, resulting in an $\approx 60°$ angle of attack. Whereas a $60°$ angle stop wing will rotate $\approx 60°$ from vertical, resulting in an $\approx 30°$ angle of attack. The average elevation angle and angle of attack for each test case was computed by separating them into their respective $(+)$ and $(-)$ components, calculating the average total $(+)$ and $(-)$ angles, and then taking the mean of the average $(+)$ angle and the $|(-)|$ angles. The angle of attack, $\alpha(r)$, is the complement of the feather angle, ψ, and its average instantaneous value was calculated by first taking the mean of all 51 angle values along the span at each instant in time, then applying the same procedure previously outlined to calculate the total average alpha for each test case. Figure 3.9 shows a sample output from the Canny Edge Detection algorithm developed to track the wing, and the associated kinematic angles calculated at those specifically captured image frames.

112
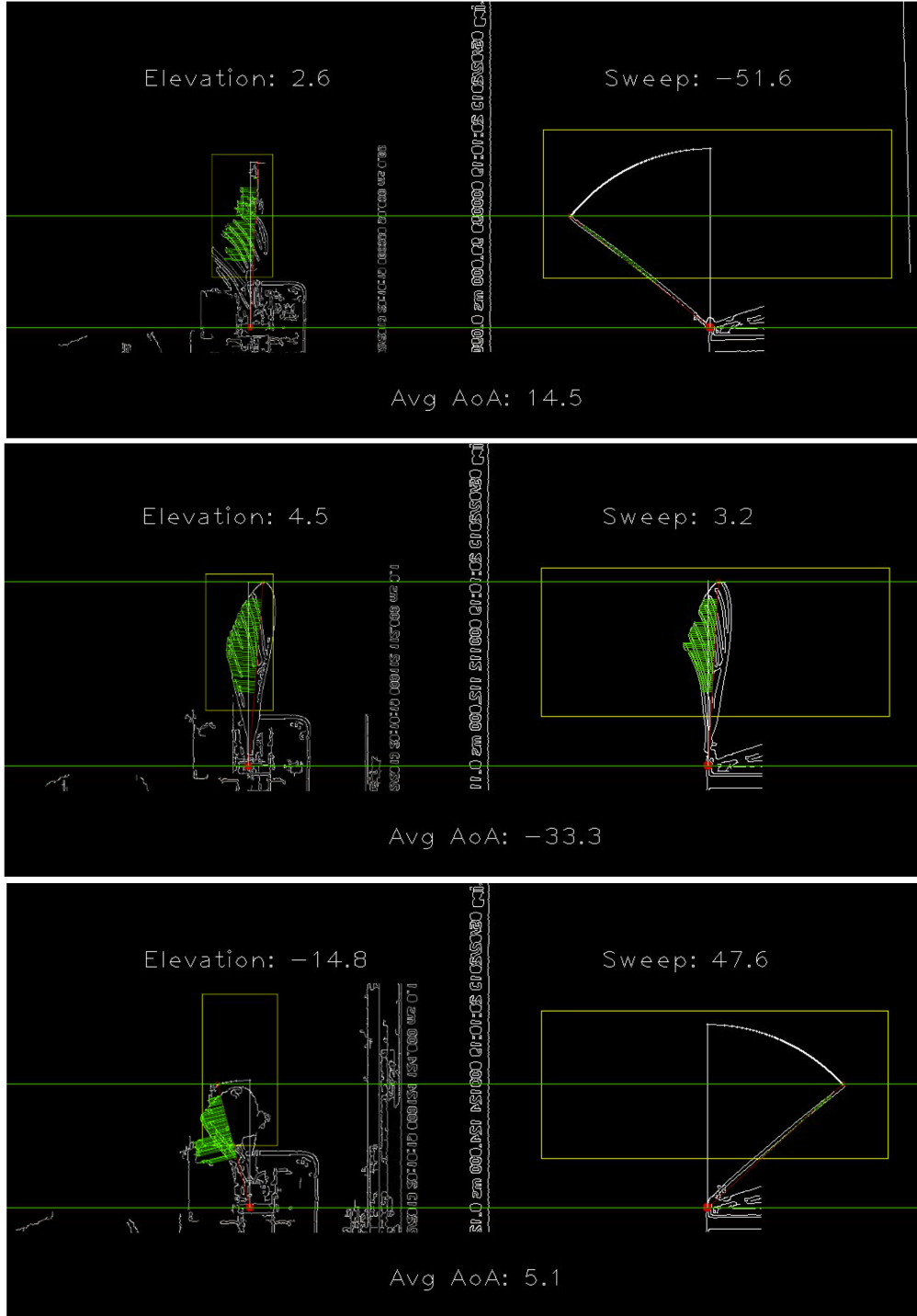
Figure 3.9: Sample video capture from the Canny Edge Detection algorithm used on a $45°$ degree wing at **A=0.5** and **A$_{\mathrm{trim}}$=0.035.** The red line tracks the fixed point and the LE. The green horizontal bisectors dynamically resize the images using the pivot and LE as fiducials. White arc tracks progression of ϕ from rest. The yellow box is the interrogation area. Green lines within the wing area connect the LE/TE pairs for ψ tracking. *Top:* Maximum upstroke. *Center:* Mid-stroke. *Bottom:* Maximum downstroke.

Figure 3.12 shows an example time history of all three kinematic angles for the 45°
angle stop wing obtained from the optical tracking algorithm plotted against flap
time.

(a) 45°: $\phi(t)$

(b) 45°: $\psi(t)$

(c) 45°: $\theta(t)$
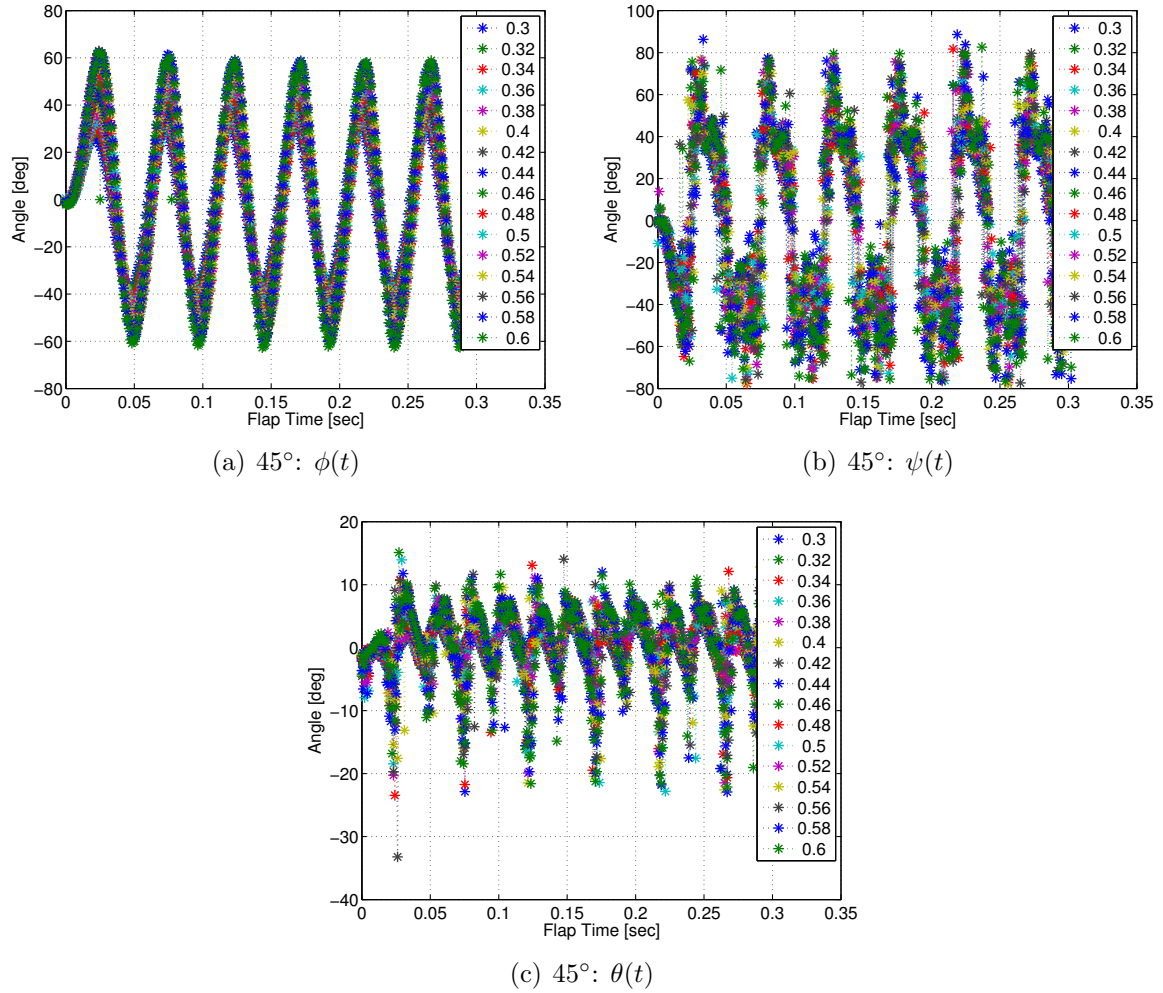
Figure 3.10: Optical tracking results for the 45° angle stop wing's kinematic angle calculations.

Figure 3.11 compares the 30°, 45°, and 60° angle stop wing kinematic angles at the
minimum, mid, and maximum amplitude tested for each wing angle stop configuration
normalized over a single flap cycle.
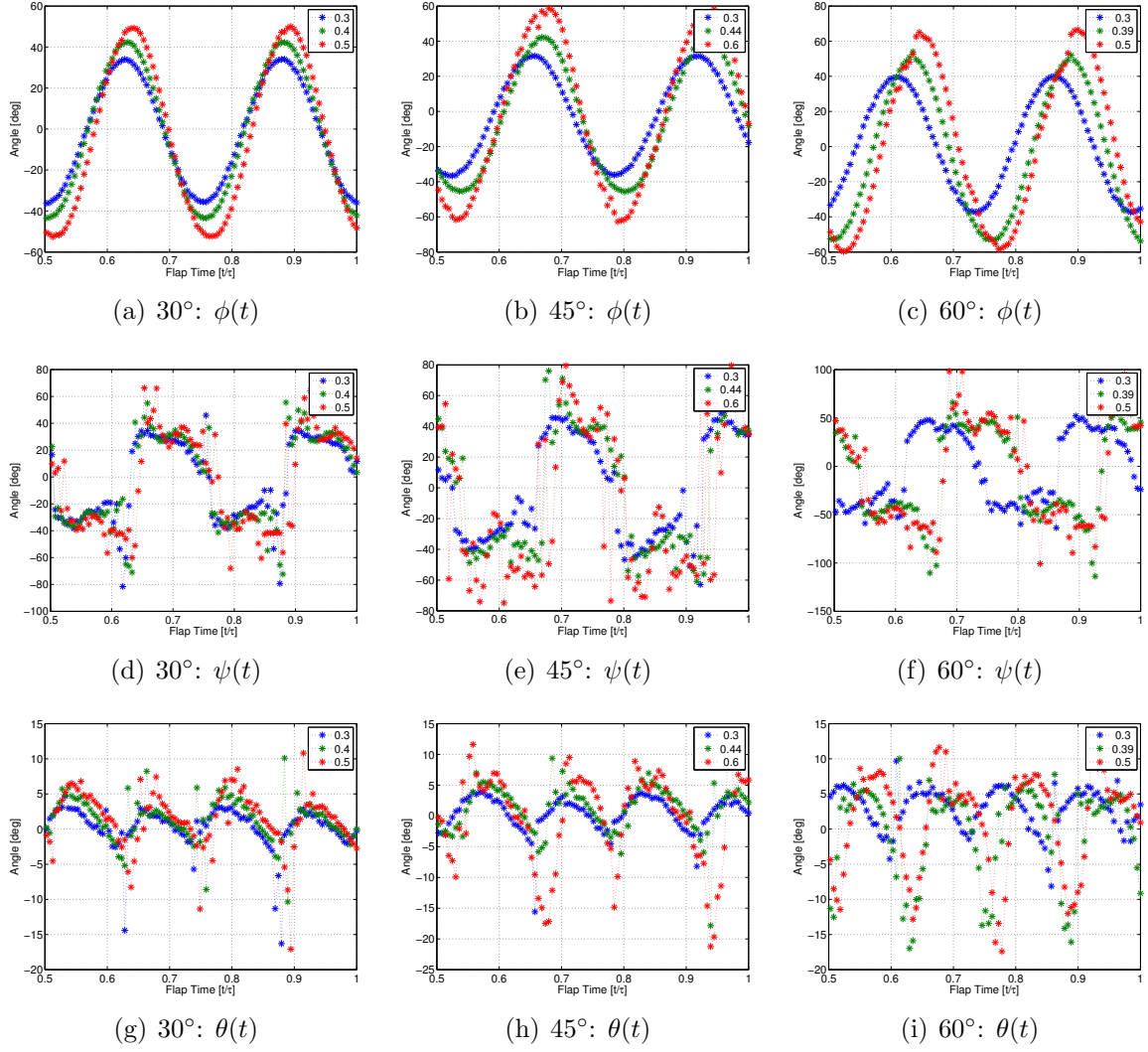
Figure 3.11: 30°, 45°, and 60° angle stop comparisons at the minimum, mid, and maximum flap amplitudes tested over a single flap cycle.

The mean kinematic angles for the 30°, 45°, and 60° angle stop wings are tabulated in Table 3.2 below for every amplitude tested, and are shown graphically in Figure 3.12 above. Figures 3.11(d)-(f) show the feather angle, ψ, measured from the vertical, which is the complement of the angle of attack, α, while Table 3.2 lists the mean angle of attack, which is used in the aerodynamic performance analysis in subsequent chapters.

Table 3.2: **Mean Wing Kinematic Angles [deg] vs. Amplitude From Optical Tracking**

	30° wing stop				45° wing stop				60° wing stop		
A	Φ [deg]	α [deg]	θ [deg]	**A**	Φ [deg]	α [deg]	θ [deg]	**A**	Φ [deg]	α [deg]	θ [deg]
0.30	70.3	63.3	1.9	0.30	69.6	60.1	2.1	0.30	77.9	55.0	2.8
0.32	74.3	61.2	2.0	0.32	72.8	58.2	2.4	0.32	83.6	52.1	3.2
0.34	78.8	60.3	2.1	0.34	76.3	58.4	2.6	0.34	92.2	50.6	3.5
0.35	79.7	60.3	2.3	0.36	78.5	58.3	2.6	0.35	96.4	50.6	3.7
0.36	81.2	60.5	2.2	0.38	83.1	56.8	2.8	0.36	102.4	49.6	4.4
0.38	84.8	60.1	2.3	0.40	88.4	55.5	3.3	0.37	101.3	48.5	5.0
0.40	87.8	59.1	2.4	0.42	92.7	53.6	3.0	0.38	103.2	48.4	5.2
0.42	91.2	57.8	2.5	0.44	97.6	52.6	3.3	0.39	110.8	46.8	5.5
0.44	94.9	58.4	2.5	0.46	101.8	50.7	3.4	0.40	107.4	45.6	5.7
0.45	94.4	58.1	2.6	0.48	106.1	50.2	3.6	0.41	109.2	45.9	5.8
0.46	99.2	58.0	2.6	0.50	112.1	49.4	4.1	0.42	110.9	45.3	6.3
0.48	102.9	58.2	3.0	0.52	115.1	49.2	4.0	0.44	118.8	45.1	6.8
0.50	107.1	57.0	3.0	0.54	118.2	48.4	4.8	0.45	119.8	45.6	6.8
–	–	–	–	0.56	121.7	47.9	5.4	0.46	125.7	45.2	5.6
–	–	–	–	0.58	123.3	46.9	5.9	0.48	127.3	42.5	7.5
–	–	–	–	0.6	125.1	46.0	6.0	0.50	130.7	41.1	6.5
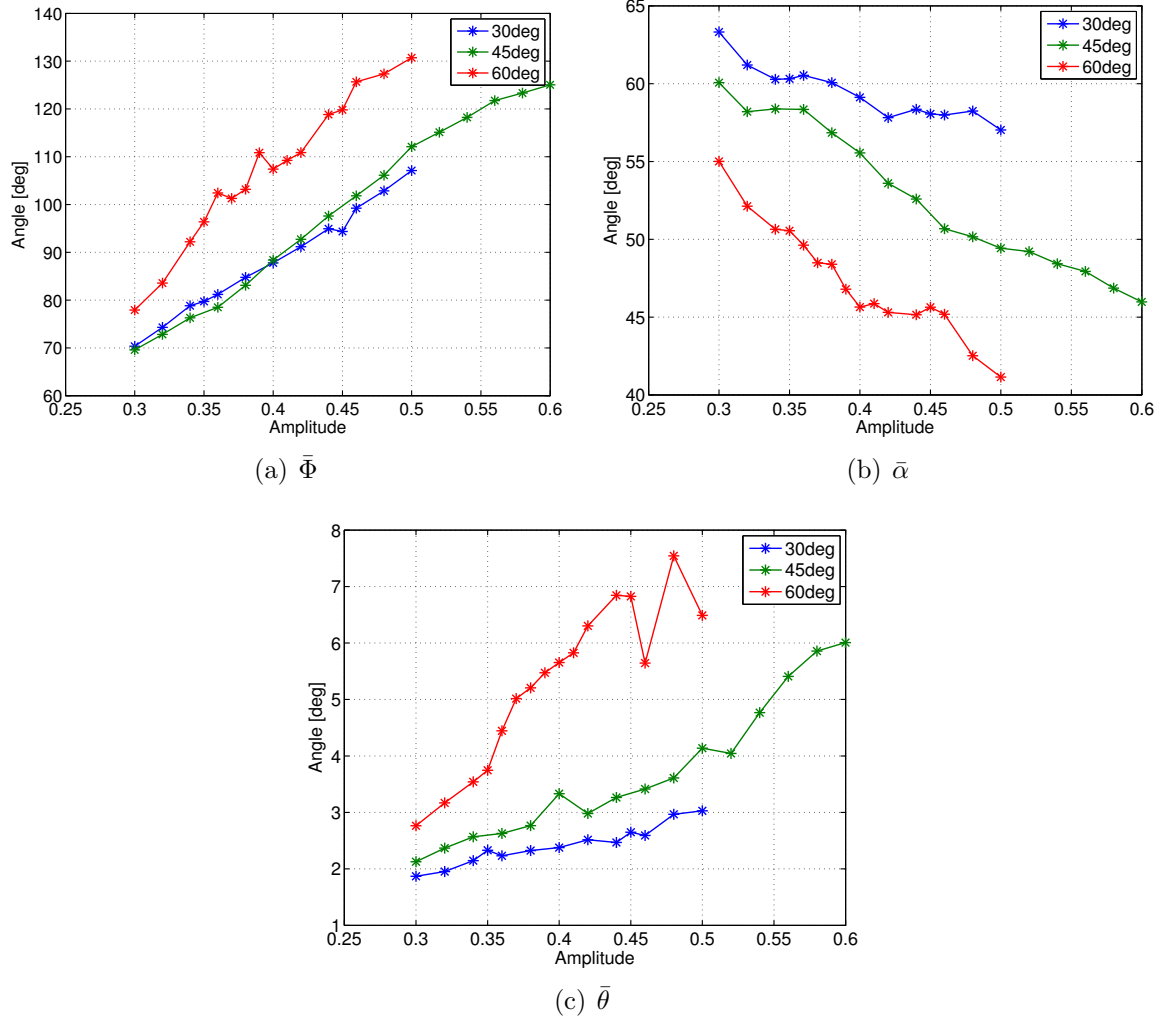
Figure 3.12: Mean kinematic angles, $\bar{\Phi}$, $\bar{\alpha}$, $\bar{\theta}$ plotted against drive signal amplitude.

The mean kinematic angles shown in Figure 3.12(c), specifically in the 60° angle stop, and to a lesser extent in the 45° stop, depict non-linear behavior near the maximum amplitude tested. At these amplitudes, the flapper exceed the linkage design and surpassed the maximum design stroke angle, resulting in non-linearities in the wing structure and excessive buckling and heaving at the ends of the stroke.

117

3.3   Force Balance Set-up

Insects generate very small, difficult-to-measure, forces and moments, and likewise, so do aerodynamically scaled FWMAVs, which are therefore, difficult to accurately measure with ordinary laboratory instruments. Specially constructed test equipment designed to capture minute forces is required to reliably measure the aerodynamic output of the AFIT FWMAV. ATI Industrial Automation specializes in robotic End Effectors, *productivity tools*, and have developed a line of force transducers for roboticists to measure forces and torques over a wide range of robotic applications and load ranges. The ATI Nano-17 Titanium Force Torque (F/T) sensor, coupled with a Netbox data communications interface, has a published sensitivity rating well below the threshold of the expected AFIT FWMAV forces. According to the manufacturer's specifications, the balance has a resolution of 0.149gF in all three Cartesian coordinates. 3.13 shows the published sensing range and resolution of the Nano-17 Titanium F/T transducer.

Calibration	Fx,Fy	Fz	Tx,Ty	Tz	Fx,Fy	Fz	Tx,Ty	Tz
SI-8–0.05	8 N	14.1 N	50 Nmm	50 Nmm	1/681 N	1/387 N	462/60815 Nmm	127/23078 Nmm
SI-16–0.1	16 N	28.2 N	100 Nmm	100 Nmm	2/681 N	2/387 N	924/60815 Nmm	127/11539 Nmm
SI-32–0.2	32 N	56.4 N	200 Nmm	200 Nmm	5/851 N	10/967 N	1848/60815 Nmm	254/11539 Nmm
	SENSING RANGES				RESOLUTION			

These system resolutions quoted are the effective resolution after dropping eight counts of noise. The effective resolution can be improved with filtering. NOTE: Applied loads must be within range in each of the six axes for the F/T sensor to measure correctly.

Figure 3.13: **Three sensitivity calibration settings of the Nano-17 Titanium F/T transducer, the AFIT balance is configured to spec # SI-8-0.05.**

The Nano-17 Titanium F/T transducer is a monolithic structure. The transducer senses applied forces and torques through three solid stainless steel sensing beams equally spaced radially around a central hub, affixed to the outside wall of the transducer housing. Applied loads are transferred to multiple sensing beams, which allows the transducer to increase its sensing range in a given axis if an adjacent axis has reduced sensing range caused by near full-scale displacement. The force applied to the

transducer flexes the three symmetrically placed beams using Hooke's law, $\sigma = E\epsilon$, where σ is the stress applied to the beam, which is proportional to the applied force, $\sigma = {}^F/_A$, E is the modulus of elasticity of the beam, and ϵ is the outer strain of the beam. Figure 3.14 shows a drawing of the Nano-17 Titanium and the coordinate reference directions provided by its manufacturer [3].
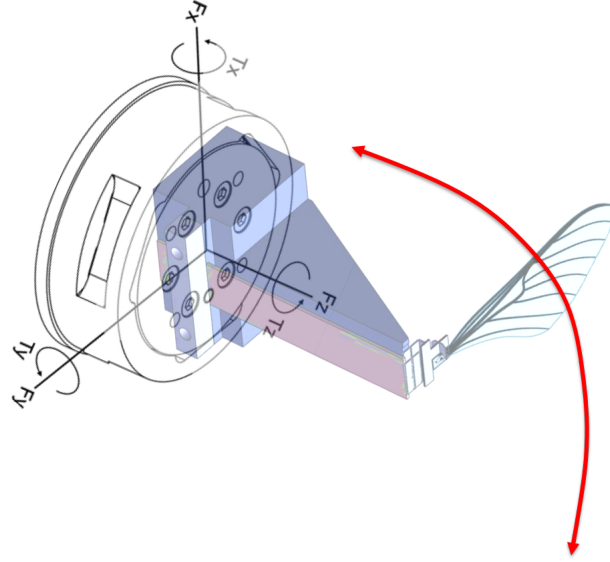
Figure 3.14: Diagram of the Nano-17 Titanium F/T transducer and orientaton of principal axes with the PZT, mounting block, and wing provided for perspective on location of the sensors with respect to the actual wing motion. Note in the orientation used in the AFIT MAV lab, the vertical force vector (*lift*), is aligned along the balance x-axis, the side force (*spanwise*) down the wing is aligned along the y-axis, and the axial force (*thrust*) is aligned out the front of the balance along the z-axis—modified from [3].

Semiconductor strain gages are attached to each beam, which are strain-sensitive resistors. The resistance of the strain gage changes as a function of the applied strain by the relation $\Delta R = S_a R_o \epsilon$, where ΔR is the changed in resistance in the strain gage after application of a load, S_a is the gage factor of the strain gage, which is an empirically derived quantity, R_o is the undeflected resistance of the strain gage, and ϵ is the resultant stain applied to the gage.

Recent AFIT students used a Nano-17 Titanium transducer borrowed from the Air Force Research Lab (AFRL), in their FWMAV research, and conducted extensive

sensitivity and repeatability testing of the balance to determine its accuracy and applicability to aerodynamic testing. Sladek evaluated the balance against calibrated loads to determine axis interactions, uncertainty, and noise thresholds. 9.81mN (1gF) was the smallest calibrated weight used in the verification tests. The 1gF load was applied and removed 30 times to the x, y, z axes individually. Table 3.3 lists the 30 test average results for the 1gF applied load [79]:

Table 3.3: Nano-17 Titanium Force Balance Test Calibration Results [79]

1gF load applied to each axis separately		
Axis ‖	Noise (gF)	% error
x	0.034	5.13
y	0.279	3.49
z	0.194	5.00

Figure 3.14 shows a drawing of the Nano-17 Titanium and the reference coordinate directions used by the balance. The balance coordinate system differs from traditional aerodynamic balances where the body axes relating the normal, side, and axial forces are x_b, y_b, z_b respectively. The moments are measured about the balance center (M_b), and are transferred to the pivot point (M_p) of the linkage/mounting block interface through Equation 3.10

$$F_p = F_b$$
$$M_p = M_b - r_{b-p} \times F_b$$

(3.10)

where r_{b-p} is the vector coordinates, $[\Delta x_p, \Delta y_p, \Delta z_p]$, from the balance to the pivot point, given here as $r_{b-p} = [0, -10, 62.25]$mm. Equation 3.11 gives the matrix equation used to transfer the moments from the balance center to the pivot point.

$$
\begin{bmatrix} M_{xp} \\ M_{yp} \\ M_{zp} \end{bmatrix} = \begin{bmatrix} M_{xb} \\ M_{yb} \\ M_{zb} \end{bmatrix} - \begin{bmatrix} 0 & -x_p & y_p \\ x_p & 0 & -z_p \\ -y_p & z_p & 0 \end{bmatrix} \begin{bmatrix} -F_z \\ F_y \\ -F_x \end{bmatrix} = \begin{bmatrix} M_{xb} + F_y x_p + F_x y_p \\ M_{yb} + F_z x_p - F_x z_p \\ M_{zb} - F_z y_p - F_y z_p \end{bmatrix}
$$
$$(3.11)$$

Figure 3.15 shows a labeled front and back view of the FWMAV experimental test chamber used in the testing detailed below. Figure 3.16 shows the data flow between the commanded input signal to the flapper and the collected aerodynamic data using the experimental set-up shown in Figure 3.15.
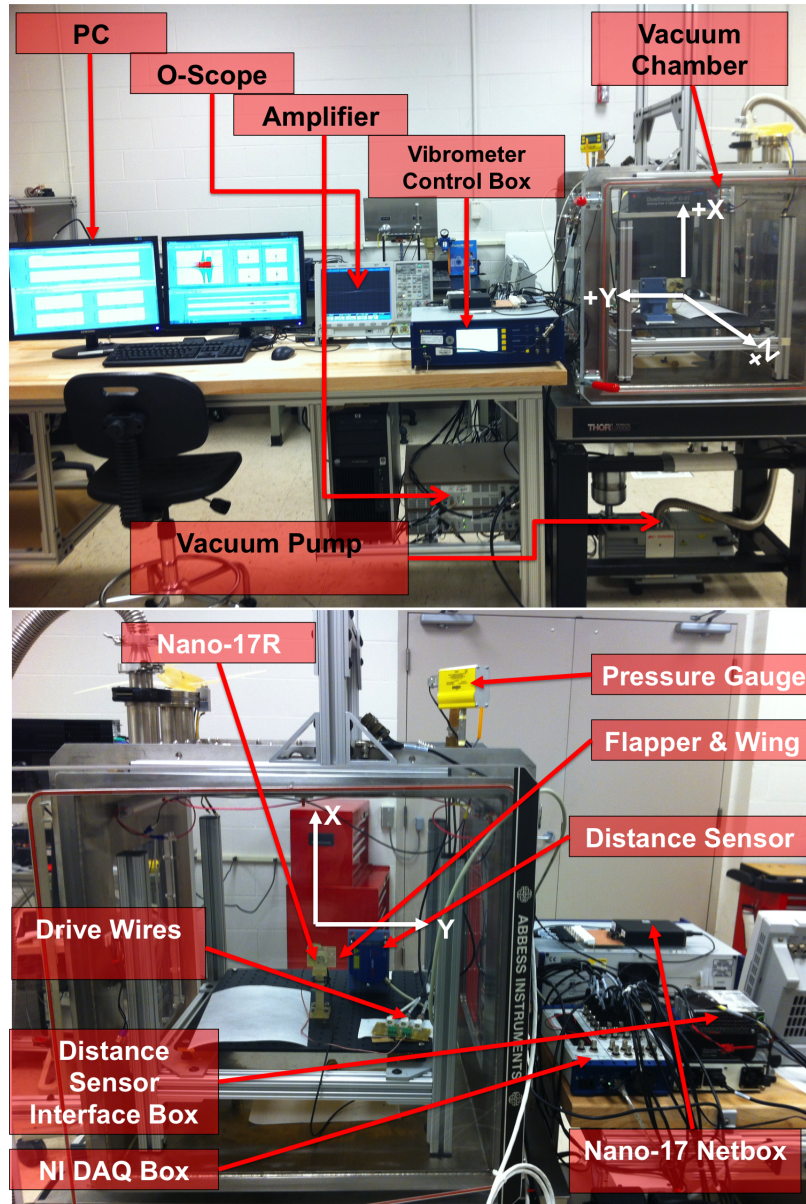
Figure 3.15: AFIT MAV Lab Set-up. *Left:* front view of the MAV Lab, not pictured, the vibrometer sensor head is located just off the right side of the frame; *Right:* rear view of the MAV test chamber, stainless steel braided hose connected to the top is the vaccum hose.
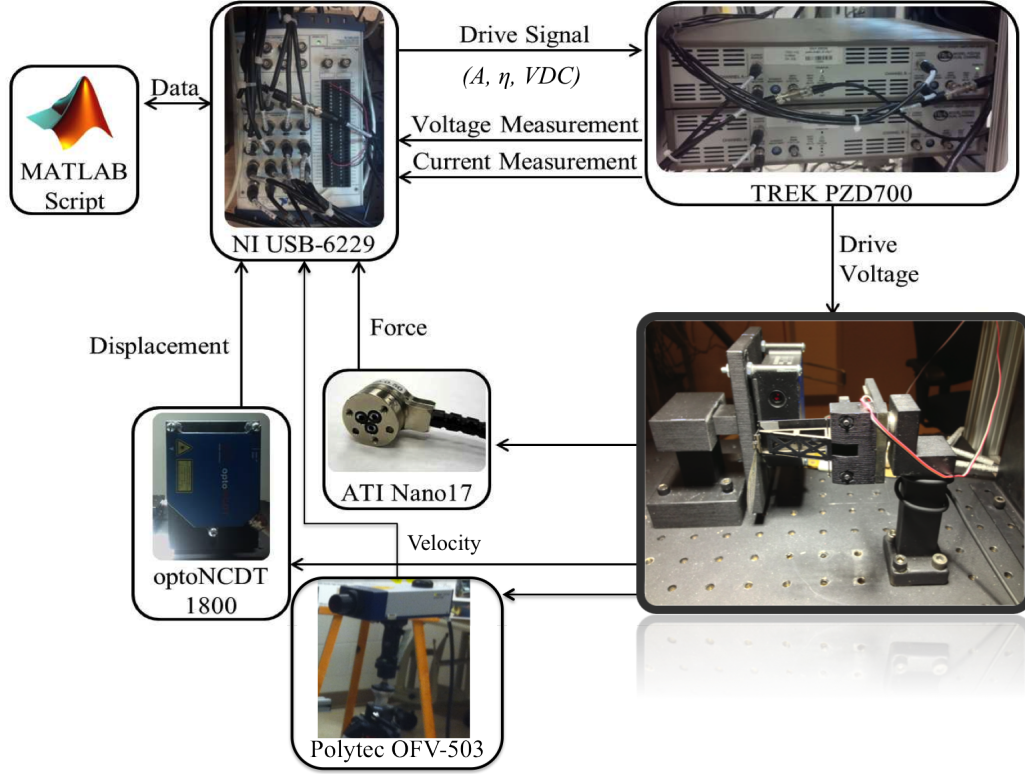
Figure 3.16: Data flow diagram shown the input signal sent to the flapper and the experimental aerodynamic force, moment, velocity, displacment data captured by the sensors and sent back to the desktop PC—modified from [11].

3.4 PIV Set-up

PIV measurements provide instantaneous velocity vector fields spatially distributed across a user defined interrogation area. The AFIT stereo PIV system was used to collect stereoscopic u, v, w velocity field data with AFIT's functional FWMAV model, operating in a closed cell seeded particulate environment. Seed material is a 6.5 $^{L}/_{min}$ by volume dilution at 25psig of air and Rosco Clear Smoke Fluid, atomized by a TSI 6-jet 9306 atomizer, with a nominal particle size $\approx 1\mu$m, which is on order of $\approx 1 - 2$ pixels, with a seed concentration of 10^7 particles/cm^3. The intention was to capture the entire flow field and visualize the aerodynamics of the FWMAV in all

123

three cartesian directions.

3.4.1 PIV Laser.

The PIV system used in these tests was a Dantec Dynamics all-in-one PIV and data processing system. The PIV system laser is a New Wave Research, Solo 200XT, model 25270, Neodymium-doped Yttrium Aluminum Garnet (Nd:YAG) ($Nd : Y_3Al_5O_{12}$) laser. An overview of how the laser functions is a dopant, triply ionized neodymium, Nd(III), replaces a small fraction of the yttrium ions, typically 1% by atomic weight, in the host crystal structure of the yttrium aluminum garnet (YAG) crystal because the two ions share a similar atomic structure. The neodymium ion provides the lazing activity in the crystal, and releases energy at a wavelength of 1064nm, or at one of its harmonic frequencies, through use of frequency doublers in the laser housing; where 532nm is the basic fundamental frequency most commonly used in PIV applications [14]. A flash lamp and the YAG crystal are placed along the major axis of a mirrored elliptical cavity, which helps maximize the energy transfer from the flash lamp to the crystal. The flash lamp is heated, exciting the cavity for approximately 250μs; which thermally dissipates the excess heat by a cooling tank of de-ionized water, before the next pulse of the flash lamp, which is preset at 10Hz [14]. The flash lamp is externally triggered by the Dantec timing and synchronizer hub, which serves as the gatekeeper between the laser, the software interface, the camera and the TTL trigger. Figure 3.17 shows the New Wave Solo 200XT laser control box front and the connection diagram in the back.
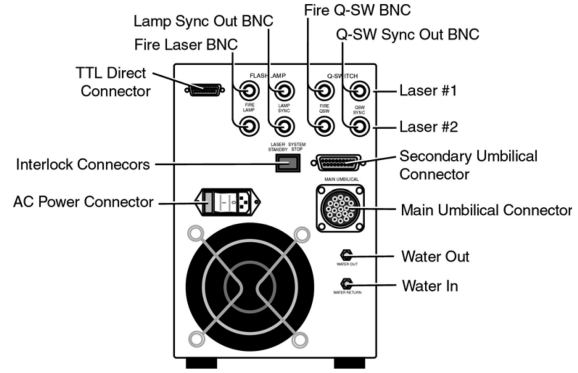
(a) Front   (b) Rear

Figure 3.17: New Wave Solo 200XT laser control box.

To increase the intensity of the laser light emitted into the test section without overdriving the YAG crystals, which decreases both its life and the laser pulse frequency, preventing consumption of excessive power, a technique called Q-switching is used to pulse the laser in PIV applications. This technique does not open the gate to the laser optic as soon as the flash lamp heats, and excites the crystals to the point where it is capable of emitting electrons—called the lazing energy minimum threshold—the Q-switch keeps the cavity closed for the majority of the duration of crystal excitation, which concentrates and intensifies the lazing electron energy, opening and firing the laser only for a few nanoseconds [14]. By delaying the opening of the lazing cavity, the Q-switch allows the YAG rod to store lazing energy to maximize the pulse energy released. Most standard off-the-shelf PIV lasers are capable of producing Q-switch energies in the range of $10 - 400$mJ per pulse, with an average Q-switched pulse duration of $5 - 10n$s [14]. The Q-switch is opened, and the laser fired $150 - 200\mu$s after the start of flash lamp excitation, which prevents the excited crystal ion energy from decaying in the cavity. The Q-switch can be externally or internally triggered by the FlowMap system hub to collect continuous or phased averaged PIV data. The Q-switch increases the output energy of the laser, which

generates a brighter laser sheet through the test section, illuminating more particles, and delivering greater fidelity to the sensing camera. More particles per image pair provides a more statistically reliable; and therefore, a more accurate velocity field characterization [14, 16]. Figure 3.18 depicts the PIV equipment setup used in this research.

(a) System interface

(b) Particle seeder

(c) Synchronizer and timing box

(d) Cameras
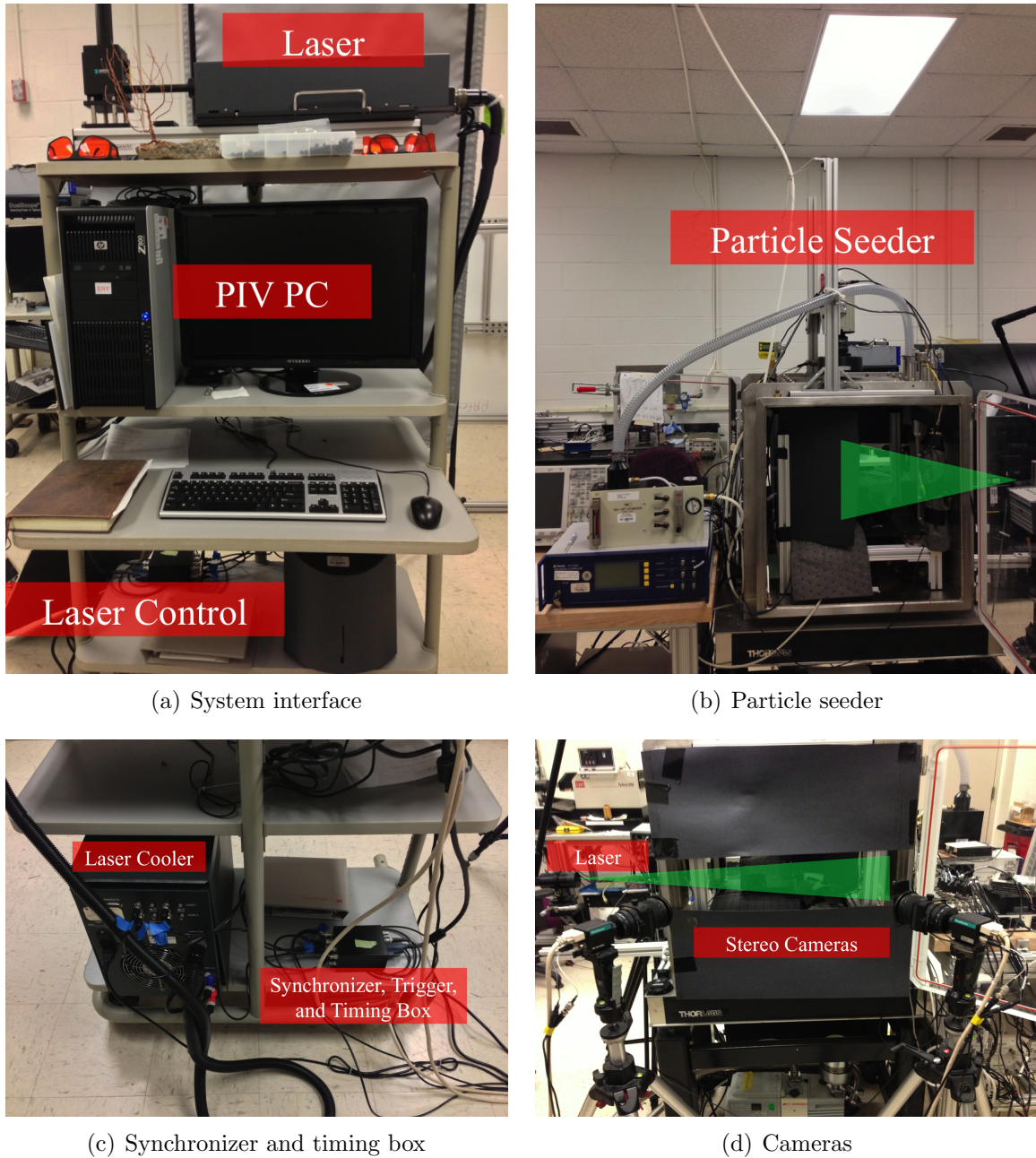
Figure 3.18: PIV equipment set-up.

An armature with straightening mirrors directs the energy emitted by the lazing cavity from the laser housing to the laser head optics, which is used to generate the planar laser sheet and adjust its thickness. The laser sheet was adjusted to a thickness of $\approx$ 4mm to accommodate the highly three dimensional nature of wake vortex structures emanating from flapping wings to illuminate particles traveling longitudinally in and out of the 2-D planar laser sheet. Nordin *et.al.* conducted extensive 3-D and stereoscopic PIV experiments on tuning PIV test parameters to minimize error on carefully calibrated inlet and outlet nozzles, and concluded the optimal laser sheet thickness was twice the size of the projected interrogation area [15, 62]. Figure 3.19(a) shows the laser head pointed into the test chamber and 3.19(b) shows the associated beam straightening optical mirror armature.

(a) Laser head
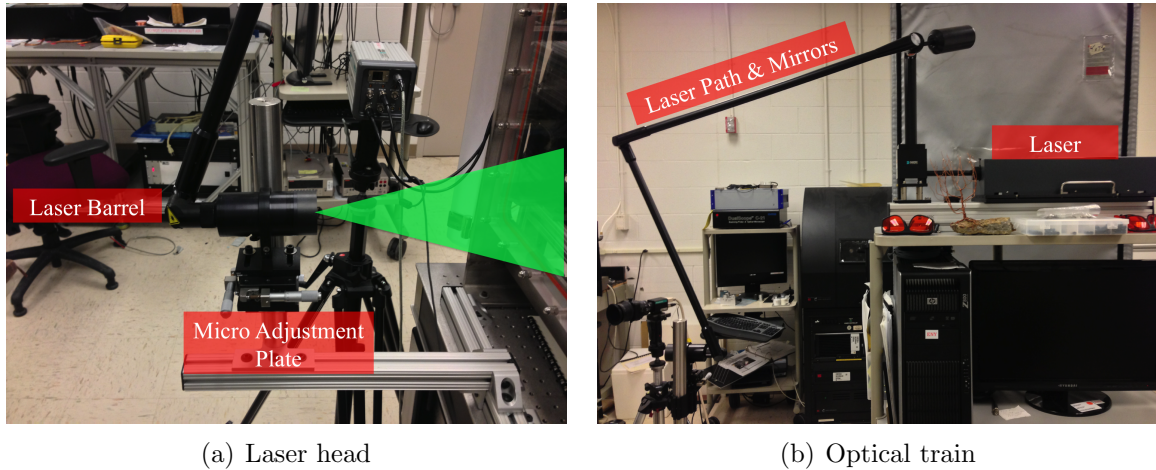
(b) Optical train

Figure 3.19: PIV laser and optical train.

3.4.2 PIV Cameras.

Two FlowSense 4M-MKII cameras were used to capture the illuminated image pairs. The cameras are a high speed, black and white, asynchronous still-frame camera with a 2048 × 2048 pixel array Charged Coulped Device (CCD), equipped with electronics to accommodate rapid inter-frame acquisition of image pair sequences. The FlowSense 4M camera uses a high performance progressive scan interline CCD

chip but with a sensitivity $\approx 55\%$ of the quantum efficiency at $532nm$. The camera resolution is 2048×2048 light sensitive cells with an equal number of storage cells, and has a depth of 12-bits per pixel [16]. When the Q-switch receives an external, or internal laser fire command, the camera aperture opens and the CCD chip is exposed to scattered light from the first pulse of the laser sheet, and a 2048×2048 pixel image is acquired. The first image is immediately stored in a temporary buffer, the CCD array is electronically wiped clean, the aperture remains open and then registers light from the second pulse of the laser sheet, and the second 2048×2048 pixel image is acquired. Both images are transferred to the Dantec DynamicStudio processing software through a BNC connection. The images pairs are streamed to the Dantec DynamicStudio project database in real time during image acquisition through the use of specially purchased National Instruments *Frame Grabber* video cards, which are designed for high bandwidth data acquisitions. Rather than using the on board PC RAM to store acquired images until after the acquisition sequence is completed, limiting the number of image pairs to the physical size of system RAM, the *Frame Grabber* cards use the high speed PCIe interface on the system motherboard, and the HDD as a buffer to stream captured images directly to the processing software, thereby only limiting the bandwidth based on the I/O speed of the processor and PCIe interface, which is many times faster and more efficient than transferring images back and forth from the system RAM. The minimum time between subsequent frames is $1\mu s$ [14]. This process is repeated for the duration of user specified image pair acquisitions. The time dependent unsteady nature of flapping wing aerodynamics makes it critical to specify exactly when the laser fires to capture flow phenomenon at specific instances in the flight profile—*phase locked or phase averaged.* The Dantec PIV system is equipped with an advanced automatic synchronization mode that has a short activation delay of $20\mu s$, which permits the ability to externally trigger the

128

laser sheet with minimal delay between fire command and laser execution, which is critical to capture and freeze wing motions on order of $\approx 20 - 25$Hz. Figure 3.20 shows a generalized schematic of the PIV camera connections.
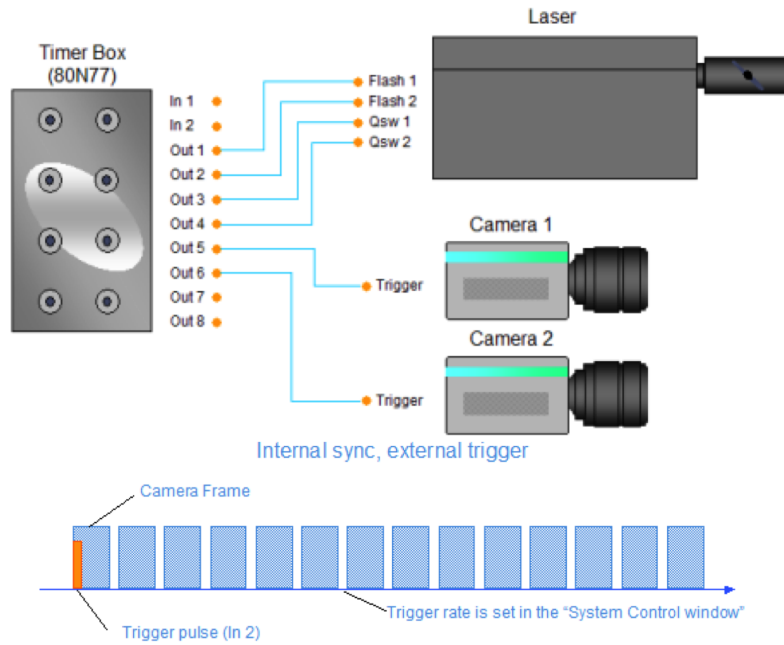
Figure 3.20: General PIV camera configuration—modified from [16].

Table 3.4 tabulates the Dantec stereo PIV system specifications.

Table 3.4: **Dantec PIV System Specifications & Settings**

Specification	Value
Solo 200XT Laser Controller Specifications	
Laser Repetition Rate	$8 - 21$Hz
Pulse Interval	$1 - 1e6\mu$s
Max Trigger Window	5000μs
Flash lamp #1 & #2 Q-switch Delay	190μs
Q_1 & Q_2 Activation Delay	0.18μs
Pre-light $\rightarrow$ 1st Flash (pulse) Delay	0.18μs
Duration of Flash Lamp & Q-switch Signal	10.0μs
New Wave Research Solo 200XT Laser Specifications	
wavelength (λ)	532nm
Pulse Energy	200mJ
Electrical	240V / 1500W
Pulse Width	$3 - 5n$s
Pulse Duration	0.01μs
Pulse Frequency	15Hz
Maximum Beam Diameter	6mm (FWHM)
# of Pulses	2
FlowSense 4M MkII Specifications	
Lens	Nikon PC-e Micro-Nikor f/2.8D
Lens size	85mm, manual focus, 5" long attached to a Scheimpflug mount
f-stop	5.6
CCD Field of View	2048×2048 pixels

The camera lenses are mounted to a *Scheimpflüg* pan and tilt mount. The *Scheimpflüg* principle is named after Captain Theodor Scheimpflüg of Austria that devised a geometric rule in 1904 describing the orientation of the Plane of Focus (PoF) of a camera lens when the lens plane is not parallel to the image plane. This principle is employed in stereo PIV to correct perspective distortion in the out-of-plane images from the two PIV cameras. In normal photographic set-ups, the user orients the camera's lens and image planes in parallel, ensuring the PoF is parallel to both the lens and image planes. Therefore, if a planar subject, such as the laser sheet from a 2-D planar PIV laser, is parallel to the image plane, it will be coincident with the camera's PoF, and the entire imaged area will be equally focused, see [21, 23] for 2-D PIV images results using a single camera, oriented parallel to the laser sheet. If the subject plane is not parallel to the image plane, it will be in focus only along a line

where it intersects that PoF. When an oblique tangent is extended from the image plane, and another is extended from the lens plane, they meet at a line through which the PoF must pass, as shown in Figure 3.21.
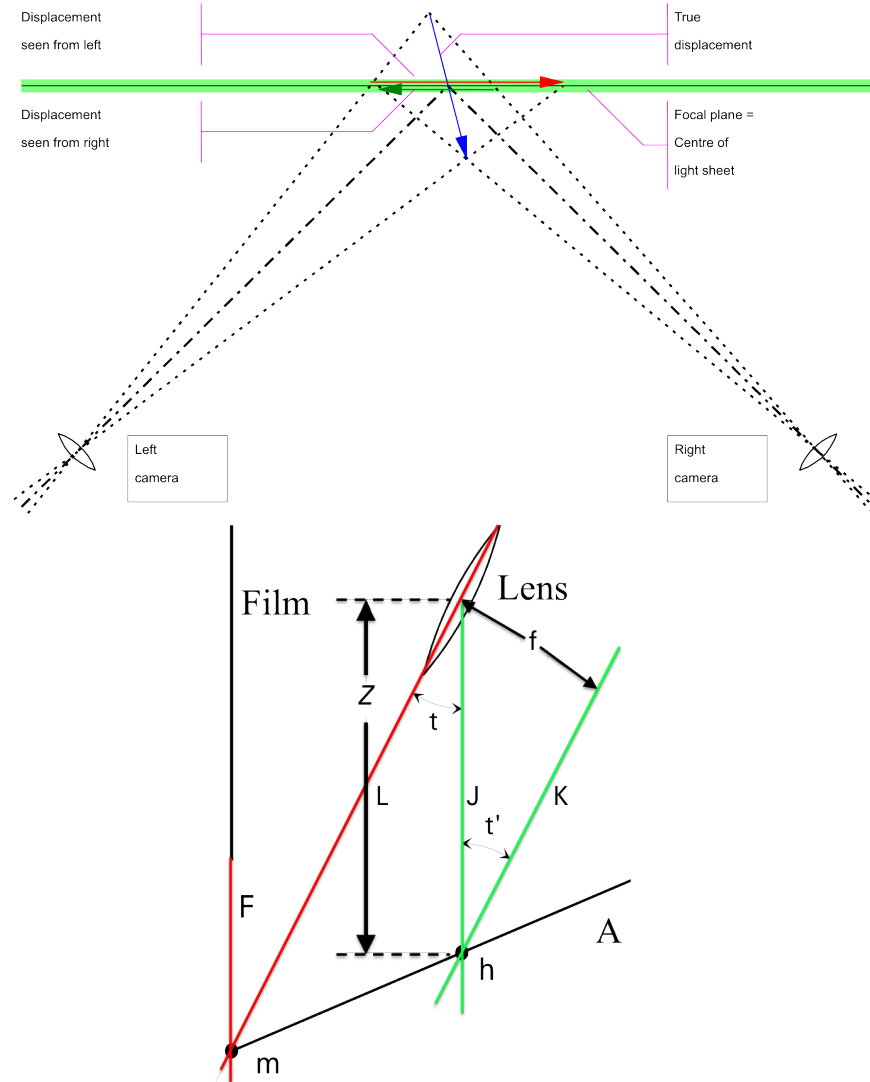
Figure 3.21: Picture of the *Scheimpflüg* principal and how it is applied to stereoscopic PIV imagery—modified from [15].

With these geometric constraints established for calculating the intersection of the PoF of a camera lens out-of-plane with the image target, a planar subject can be completely focused by manipulating the lens to the correct angle through a pan-and-tilt (*Scheimpflüg*) type mounting system. The required tilt angle (t), to maintain the

131

focus of the entire image is computed by Equation 3.12 below

$$t \equiv t' = \sin^{-1}(f/Z) \tag{3.12}$$

where L is a line representing the lens plane, A is a line representing the object plane, f is the lens focal length, K is a line representing a perpendicular bisector between the lens axis f and A at point h, J is a perpendicular bisector between point h and the centroid of the lens itself. The *Scheimpflüg* principal states planes J, K, and A must intersect at point h for the image plane to be equally focused. Z is the distance from the lens face to the object plane A, which for our PIV testing was measured to be $\approx$ 1m, and $t' \equiv t$ because planes L and K are parallel; therefore if the lens focal length and the physical distance from the lens face to the object plane (PIV laser sheet) are known, then the lens tilt angle can be computed. Figure 3.22 shows a close-up of the Nikon *Scheimpflüg* mounting lens system used on the PIV cameras in these experiments.

Figure 3.22: Picture of the Nikon *Scheimpflüg* mounts used on the PC-e micro-Nikkor lenses. *Left:* Undeflected lens. *Right:* Fully tilted lens.

3.4.3 PIV Camera Calibration.

Since the images are taken out of the PoF, the two stereo camera lenses are angled so their images are completely in focus, while also maximizing image overlap between cameras so the entire interrogation Region of Interest (RoI) is imaged by both cameras, without which, stereo velocity vector processing is not possible from the 2-D planar images. Figure 3.23 shows the planar configuration of two separate camera images, and the shift in the apparent camera coordinates of an object in the image plane compared to the actual physical coordinates of the object in Euclidean space.
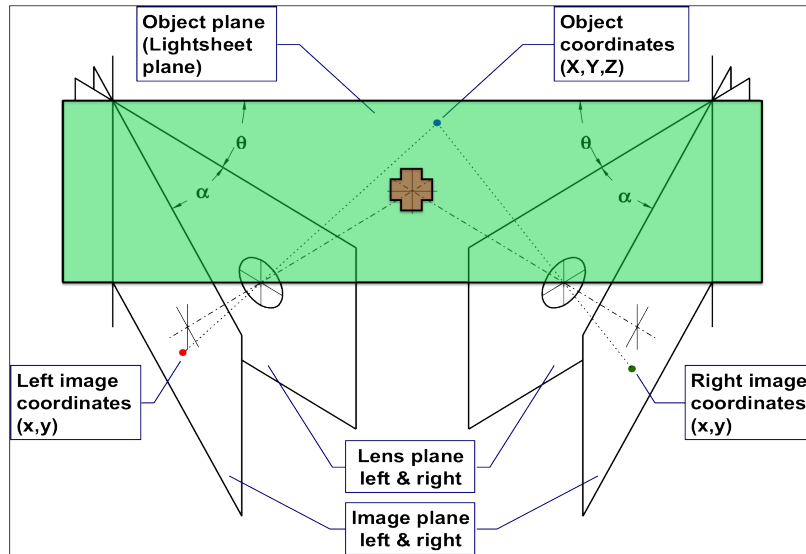
Figure 3.23: Graphic demonstrating the apparent shift in an object's spatial location on the tilted camera lens compared to their physical location in true $x - y$ space.

The calibration procedures used in this experiment to align the cameras and focus the image plane of both cameras using the *Scheimpflüg* pan-and-tilt lenses is outlined below:

1. Align cameras at $\approx 45°$ to the image plane.

2. Turn the laser on single pulse mode at the lowest power setting.

3. A 200mm × 200mm dot matrix calibration plate is aligned parallel to the laser sheet, and the thickness of the sheet is adjusted so the thickness is approximately twice that of the projected area, which is about the thickness of the calibration plate, or ≈ 4mm.

4. Center the calibration plate in the center of the RoI, adjust the cameras so the center focus dot on the calibration plate is in the center of both camera images.

5. Set the DynamicStudio acquisition software to *Free Run* and preview the images of the calibration grid with the DynamicStudio software in real time.

6. Focus both cameras on the center dot, align the camera bodies so the blurry outside edge of each camera's image plane are aligned. Ensure each camera is imaging the entire RoI and there is complete overlap of the RoI between each camera. If the camera images are not centered on the focus dot, or the blurry outer edges are not aligned, adjust the camera hight and camera lens tilt angles. See Figure 3.24 below for an example of the alignment procedure.
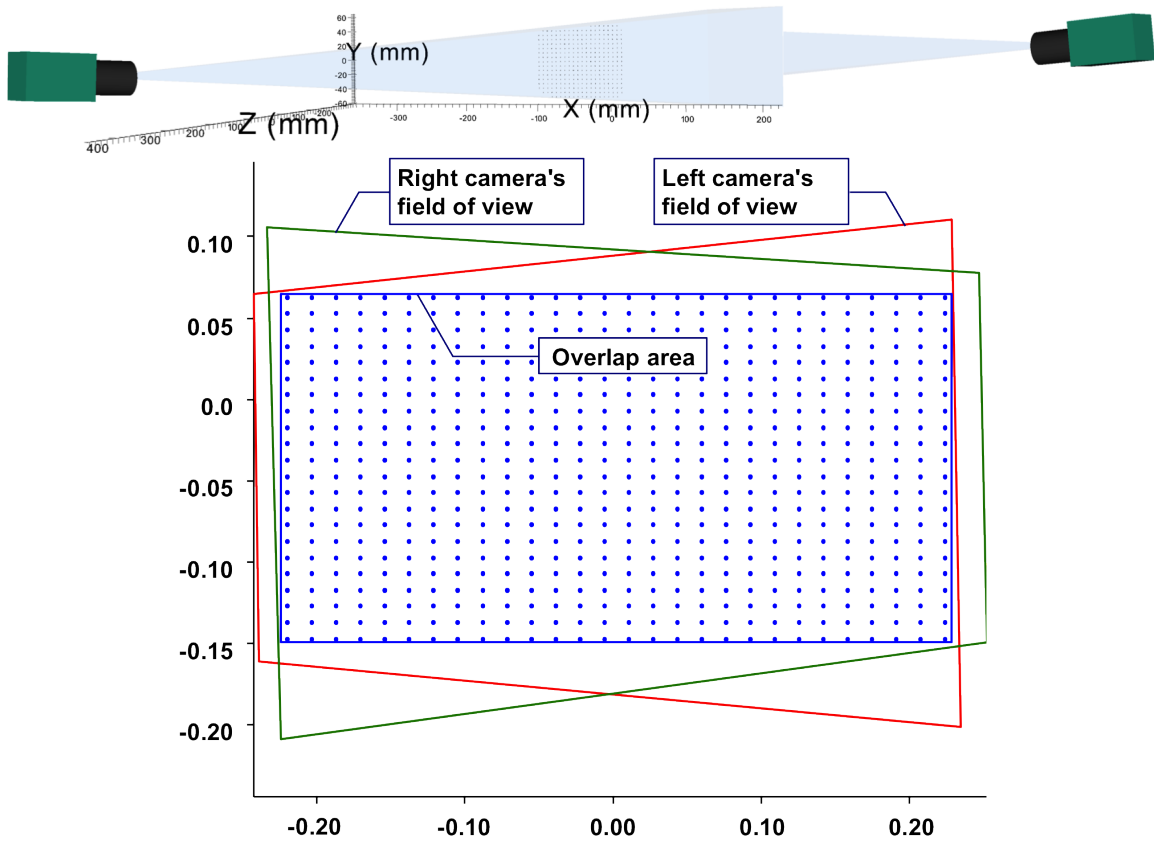
Figure 3.24: Graphic generated by the Dantec DynamicStudio software depecting the actual spatial arrangement of the camera set-up used in this experiment as determined by the calibration procedure.

7. Adjust the *Scheimpflüg* mounts on each camera so the blurry outside edge of each image plane is in focus, careful not to lose focus of the inner edge of either image plane.

8. Refocus each camera one last time to bring the entire image into crisp focus. See Figure 3.26 for an example of the complete focus and adjustment procedure.
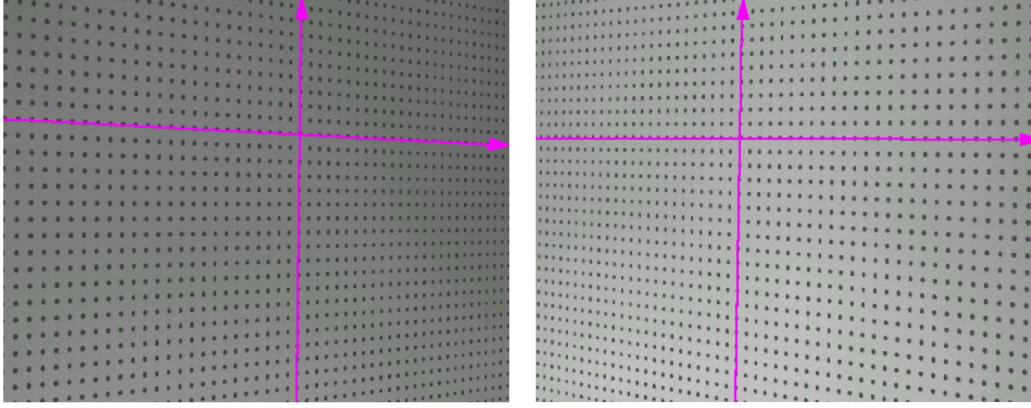
Figure 3.25: Example of the left and right camera focus procedure on the 200×200mm calibration plate. The camera's PoF are centered on the plate's center dot, and the image focus is equal from top to bottom and left to right—modified from [15].

9. Turn off the live image stream in the DynamicStudio acquisition software. Create a calibration project inside of the PIV experiment database. Open the *Acquire Data* tab in the system acquisition window and set the number of images $= 1$. Select *Free Run* to take a single image of the completely focused and aligned calibration target. Select the *Acquire Data* tab again and select *Save for Calibration*.

10. Repeat the above step of taking a single image and saving it into the calibration file for a minimum of five different calibration plate orientations. Rotate the calibration plate about its central axis, careful to keep the center point fixed in space, by alternately lowering and raising each corner, and then alternately lowering and raising the top and bottom edges. When at least five calibrations images have been acquired, save the images to the calibration file project. The calibration project file should contain the images from the initial focus shot of each camera plus the rotated and warped calibration plate images.

11. Right select camera #1 image folder and select *Calibrate*→ *Categories* →*Calibrations* → *Methods* → *Multi-Camera*.

136

12. In the calibration window Select *Automatic* target ID, select the *Standard* target type, select $200mm \times 200mm$ target size, select *Dot* as the target type, and finally select *Automatic* threshold detection.

13. Click the grid target image in the calibration window and select it with the spacebar, select camera #1 with the spacebar and drag the newly generated *multi-calibration* file onto the image target grid in the calibration window. Right click camera #1 and select *Show Contents List*, which reveals all the calibration images taken, and ensure the newly plotted green dot grid is aligned with the calibration target black dots, if it is not, right click the calibration images and delete them, check the image focus to ensure the entire image is still in focus, and adjust the f-stop to allow more light into the frames, then repeat the image collection sequence.

14. Repeat the calibration procedure for camera #2. See Figure 3.26 for an example of the completed calibration procedure.
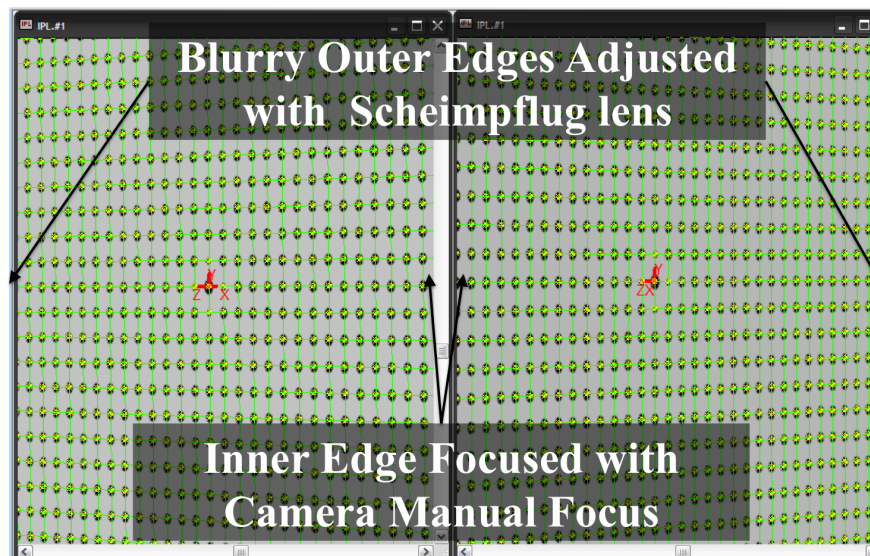
Figure 3.26: Completed camera calibration procedure–modified from [15].

3.4.4 PIV Image Processing.

The PIV images pairs are processed with the Dantec DynamicStudio software v3.21. The DynamicStudio digital processing manual provides a detail explanation of the PIV data processing procedures, and Figure 3.27 outlines the acquisition and processing methods used to process the acquired image data and calculate velocity vectors from the raw image pairs.
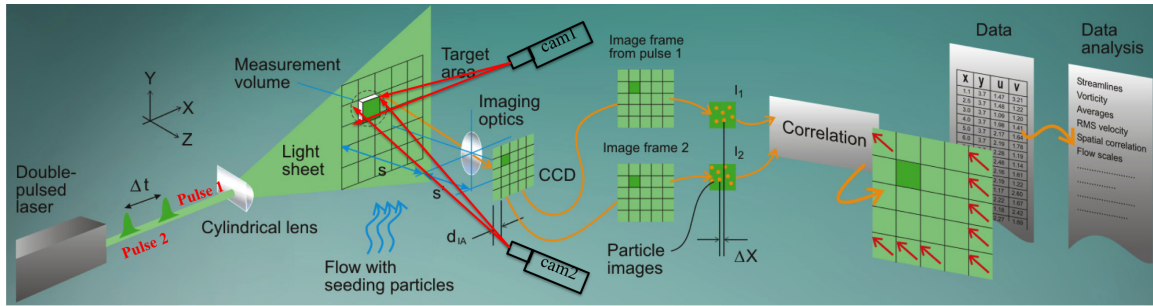
Figure 3.27: Overview of the numeric data processing methods the Dantec DynamicStudio software uses to produce velocity vectors from the pixel intensity image pairs—modified from [15].

The DynamicStudio processing software transforms the time stamped pixel data, see Figure 3.28(a)—(b), to the frequency domain by performing an FFT on each user specified integration window to correlate velocity vectors. However, the FFT process introduces noise *or* aliasing into the data. To mitigate the effect of aliasing, the software uses windowing functions to manipulate the image grey-scale by multiplying the registered pixel intensity by a variable gain between 0 and 1, which depends on the pixel position within the interrogation area [14]. This eliminates false correlations at the edge of the interrogation area, and prevents correlating edge artifacts with actual flow particles. Windowing, however, forces the data to be periodic at the edges of the interrogation window, causing data loss at the edges. Therefore, to eliminate data loss, a 50% window overlap is chosen to increase the pixel count in each window, and ensures pixels across integration boundaries are not capriciously eliminated.

The size of the interrogation window is dependent on the maximum expected par-

ticle speed in the flow region, the amount and distribution of seeding particles in the flow, the size of the camera lens, the f-stop setting, and the distance the camera is from the test section. Sample image pairs were processed using varying size interrogation windows. The most realistic and repeatable results were obtained from an interrogation area of 64×64 pixels, with 50% region overlap, and a Gaussian window. Increasing the interrogation area reduces the processing time; but produces fewer vectors, and decreases the statistical confidence in the resultant cross correlations. A smaller interrogation area, and increased overlap percentage, corresponds to oversampling, or double counting, the seeding particles [14]. A sophisticated numerical method of an adaptive correlation process was applied to the raw image pairs, see Figure 3.28(c)—(d). The adaptive correlation method employs a successive iteration of correlations to the RoI to reduce the occurrence of spurious vectors being admitted to the velocity solution and mistakenly eliminating valid ones as well. A 64×64 pixels desired final interrogation area size was selected along with three correlations in the analysis recipe menu. The adaptive correlation then picked scaled size windows and successively performed correlations to the RoI, using the previous larger correlation as the input vector space for subsequent refinement correlations. The final correlations of each image pair were further refined by applying by a moving average window, then applying velocity peak and range validation filters, see Figure 3.28(e)—(j). The peak-to-peak height ratio relative to and adjacent peak was set to 1.1—meaning a peak that is greater than 10% higher than a neighboring peak, both spatially and temporally, is eliminated—a higher ratio admits more vectors in the cross correlation matrix, but increases the probability of spurious data being included in the velocity field. The range validation filter for the magnitude of the u, and v-velocity vectors was set to 5 $^{\mathrm{m}}/_{\mathrm{s}}$, which eliminates any velocity vector in individual correlations greater than the maximum value set in the filter. The range validation filter value was based

139

on the maximum expected particle velocity, which is less than the maximum calculated wing tip velocity (U_T). Dickinson *et.al.* and Sane concluded the peak induced velocity was maximum at the wing tip just before stroke reversal through flow visualization experiments on model flappers [24, 72, 73, 74, 75]. Ellington used high speed photogrammetry to capture smoke patterns emanating from a leading edge smoke rake on a $4\times$ scale model Hawkmoth flapper, and his flow visualizations at various positions along the span demonstrated the highest span-wise velocity occurred at the wing tip during mid-translation of the downstroke [38]. Willmott *et.al.* confirmed the leading edge vortex achieved maximum velocity at the wing tip on the downstroke using smoke visualization of a tethered live Hawkmoth in a wind tunnel [93]. The average tip velocity was approximated by Equation 3.13 [34, 37].

$$U_T = 2\Phi\omega R \tag{3.13}$$

where Φ is the total mean stroke angle for each run, calculated using the optical tracking results shown in section 3.2.3.2, ω is the flapping frequency (*previous insect studies adapted the used of n to denote the wing beat frequency*)—20Hz for the 30° angle stop wing, 22Hz for the 45° angle stop wing, and 21Hz for the 60° angle stop wing—and R is the wing length from root to tip, 50mm. Table 3.5 lists the mean tip velocity in $[^{\mathrm{m}}/_{\mathrm{s}}]$ at every amplitude for each wing tested.

Table 3.5: Tip Velocities for Various Angle Stop and Amplitude Combinations

30° wing stop			45° wing stop			60° wing stop		
A	$\bar{\Phi}$ [deg]	U_t [m/s]	A	$\bar{\Phi}$ [deg]	U_t [m/s]	A	$\bar{\Phi}$ [deg]	U_t [m/s]
0.30	70.3	2.5	0.30	69.6	2.7	0.30	77.9	2.9
0.32	74.3	2.6	0.32	72.8	2.8	0.32	83.6	3.1
0.34	78.8	2.8	0.34	76.3	2.9	0.34	92.2	3.4
0.35	79.7	2.8	0.36	78.5	3.0	0.35	96.4	3.5
0.36	81.2	2.8	0.38	83.1	3.2	0.36	102.4	3.8
0.38	84.8	3.0	0.40	88.4	3.4	0.37	101.3	3.7
0.40	87.8	3.1	0.42	92.7	3.6	0.38	103.2	3.8
0.42	91.2	3.2	0.44	97.6	3.7	0.39	110.8	4.1
0.44	94.9	3.3	0.46	101.8	3.9	0.40	107.4	3.9
0.45	94.4	3.3	0.48	106.1	4.1	0.41	109.2	4.0
0.46	99.2	3.5	0.50	112.1	4.3	0.42	110.9	4.1
0.48	102.9	3.6	0.52	115.1	4.4	0.44	118.8	4.4
0.50	107.1	3.7	0.54	118.2	4.5	0.45	119.8	4.4
–	–	–	0.56	121.7	4.7	0.46	125.7	4.6
–	–	–	0.58	123.3	4.7	0.48	127.3	4.7
–	–	–	0.60	125.1	4.8	0.50	130.7	4.8
MEAN:	88.2	3.1	–	98.9	3.8	–	107.4	3.9

At the completion of all the image processing and filtering, the resulting product is the familiar *vector statistics* map for each data set, see Figure 3.28(k)—(l). The vector statistics map is the final product produced from 2-D PIV systems and is what is used in subsequent 2-D analysis. The stereoscopic PIV images are produced by selecting the left and right camera vector statistics maps and the left and right camera calibrations and processing them together using the DynamicStudio *Stereo PIV Processing* algorithm. The stereo processing takes the 2-D PIV image data and uses the calibration constants to correct spatial variances between image coordinates, producing a 3-D velocity map shown in Figure 3.28(m). The filtering and custom processing algorithms designed for these PIV experiments aided in reducing admittance of spurious vectors in the final velocity solution. However, laser sheet reflection from fasteners in the test chamber, the wing mounting structure, and even off of the mylar wing at oblique angles will result in non-physical velocity information propagating into the flow field solution. Figure 3.28 visually tracks an example of the data pro-

cessing workflow from 50 raw images/camera through to the final stereoscopic u, v, w velocity vector image.

(a) Camera 1: image

(b) Camera 2: image
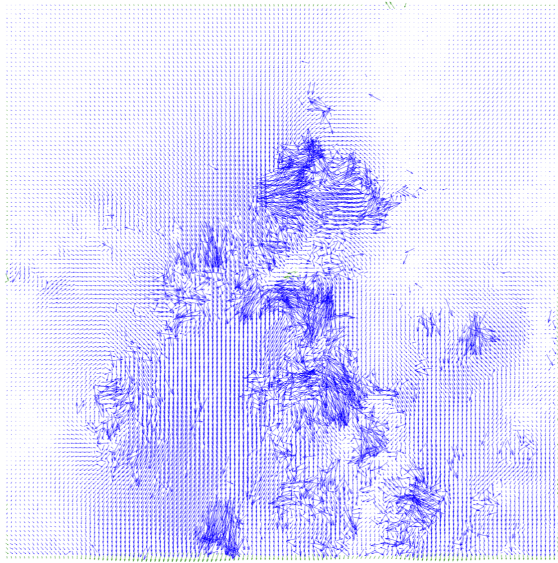
(c) Camera 1: adaptive correlation
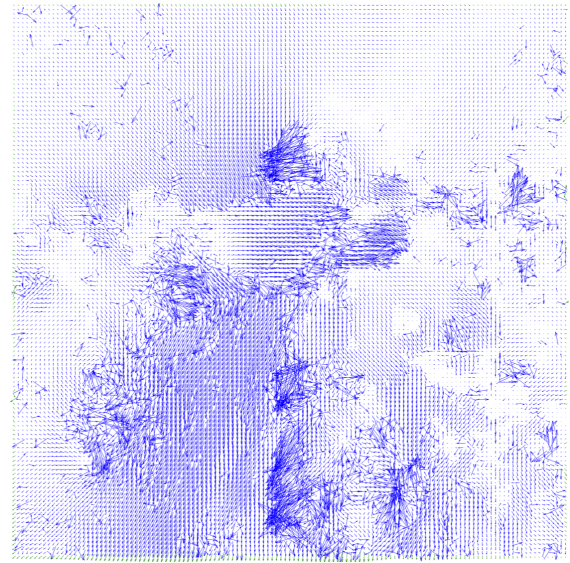
(d) Camera 2: adaptive correlation

Figure 3.28: PIV Processing Steps
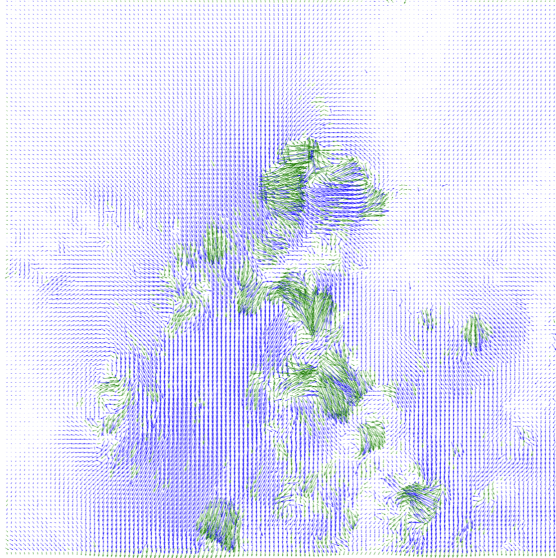
(e) Camera 1: moving average
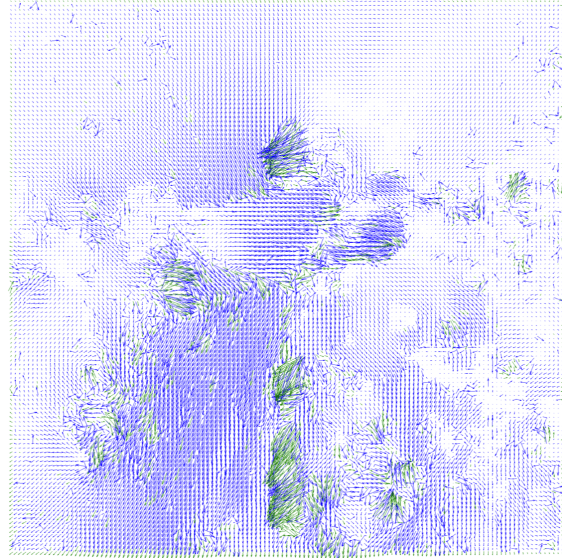
(f) Camera 2: moving average
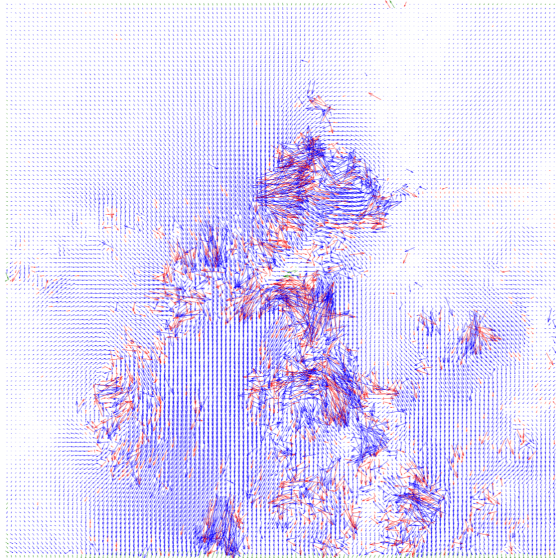
(g) Camera 1: peak validation
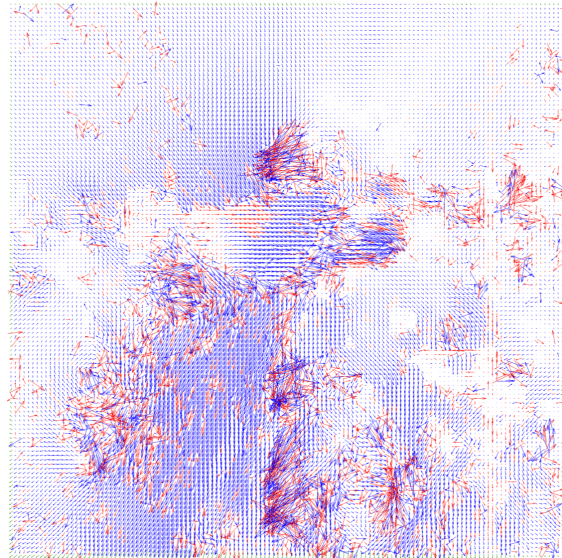
(h) Camera 2: peak validation

Figure 3.28: PIV Processing Steps
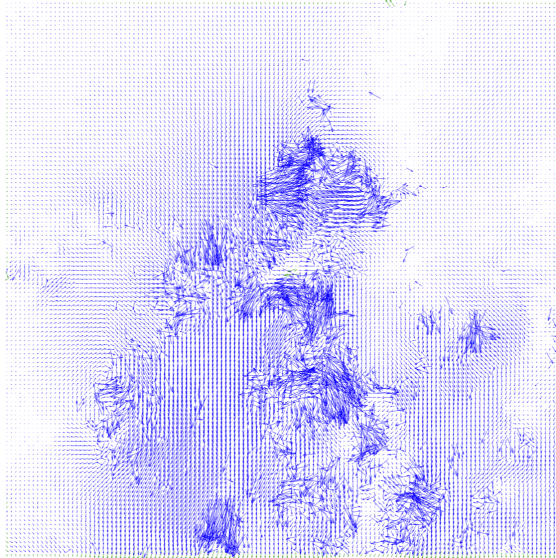
(i) Camera 1: range validation
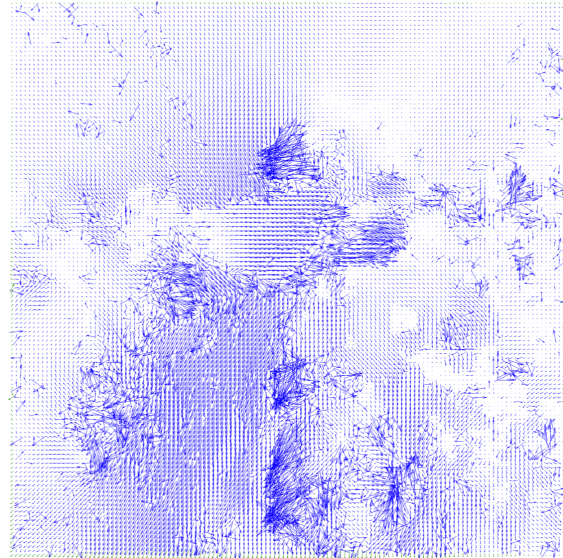
(j) Camera 2: range validation
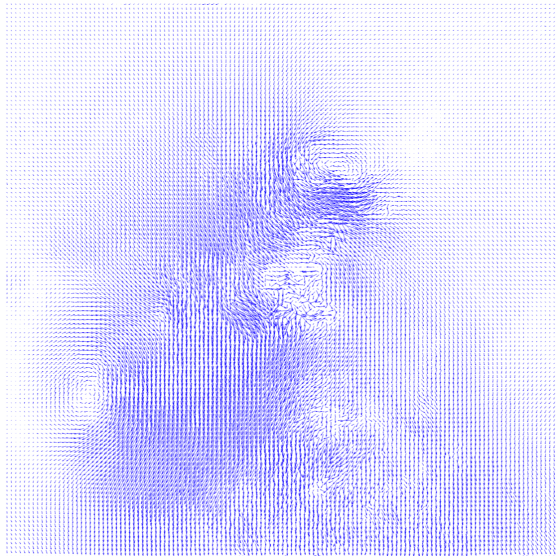
(k) Camera 1: vector statistics
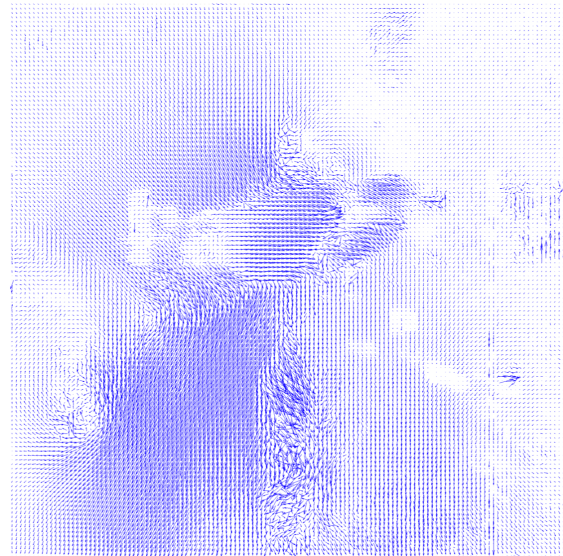
(l) Camera 2: vector statistics

Figure 3.28: PIV Processing Steps

(m) Stereo PIV image
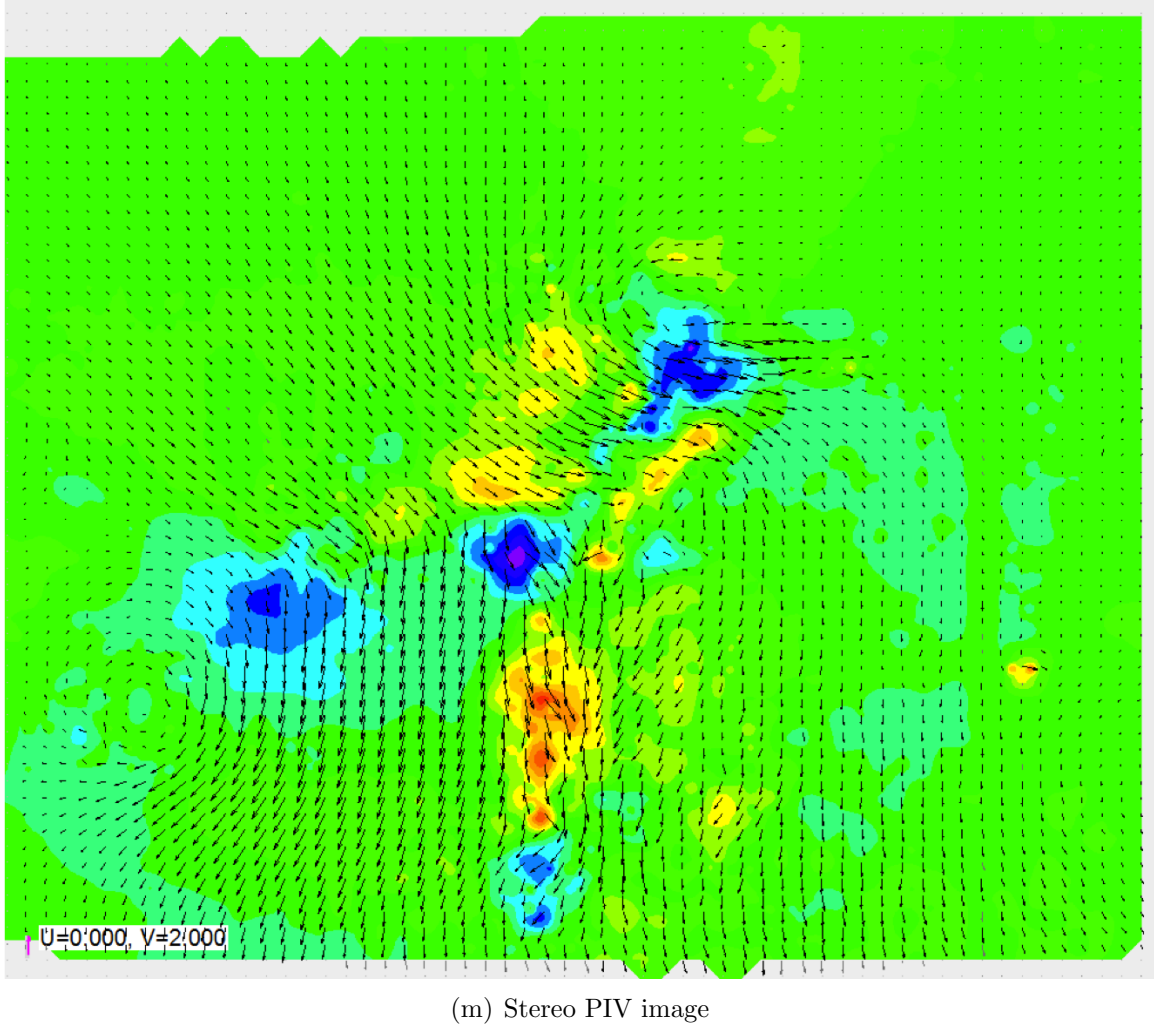
Figure 3.28: Visual example of the complete PIV processing sequence from 50 raw images to the final stereo u, v, w velocity vector map. The velocity vectors represent the horizontal and vertical velocity, u and v, and the contour map represents the stereo velocity component, w.

A MATLAB® script was written to synchronize the laser pulses, and image pair capture from the PIV system, with the flapping period of the wing, and sample rate, irrespective of the flapping frequency, amplitude, or intra-period offset (η), enabling all the image pairs to be captured at the same phase in the flap cycle—*phase locked*. The laser TTL signal was written as a carrier signal, packaged with the flapper drive signal sent to the data acquisition box. PIV images were taken at eight phases at every test condition. Figure 3.29 shows an example of the flapper drive signal for both trimmed and untrimmed flapping, with eight phases marked on the signal wave,

145

and an example of a mid-downstroke 5V TTL signal overlaid on the drive signal.
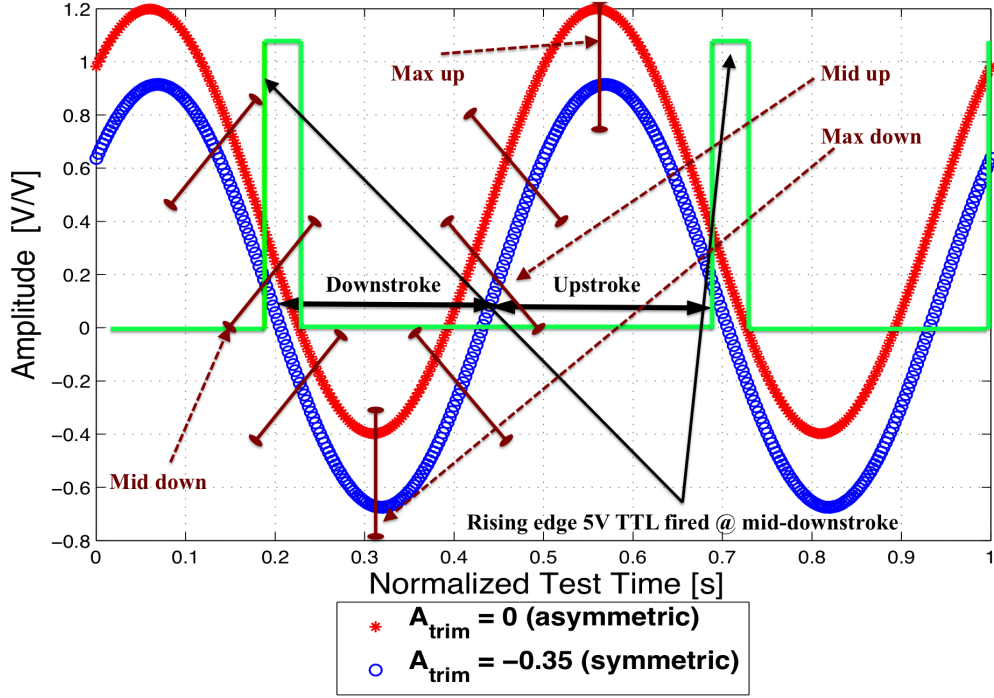
Figure 3.29: Trimmed and untrimmed drive signal. $A = 0.3$, $\omega = 22$Hz. Blue line is symmetric (A_{trim}=-0.35) and red line is asymmetric (A_{trim}=0). Green line is a $5V$ TTL trigger to fire the PIV laser at the *mid-down* stroke. Brown lines bisecting the drive signal are the 8-phases PIV images were taken at each test point.

The TTL signal was designed to send a fire pulse to the laser at the same place in the drive signal after the peak (upstroke) to give the wing a chance to initialize its motion, and overcome the initial inertial resistance of the PZT and wing mass. As a general reference, four seconds of flap time should emit 100 laser triggers, and record 100 PIV image pairs. However, the laser Q-switch and flash lamp repetition rate is not fast enough to fire the laser at every $2n\pi$ interval of wing phase, meaning the laser did not fire every time the wing passed through the specific phase under consideration. Five laser pulses were fired for approximately every second of flap time ($\approx 5 - 7$Hz repetition rate) at a 5000Hz sample rate. About 10s of flap time was required to collect 50 image pairs. The more images collected per test point, the

higher the fidelity is in the resulting vector statistics, and hence, the stereo velocity measurements. Examples of various PIV experiments in the literature recommend 100, and sometimes as many as 1000 images pairs should be collected per test point, though PIV papers have been published using 50 or fewer images pairs due to the peculiarities of certain experiments. Attempts were made to collect 100 images pairs per test point in the PIV experiments conducted here; however, the extended amount of flap time necessary to record 100 images resulted in breaking multiple flappers at the rotation joints. There was a shortage of flappers available; therefore, the number of images collected per test point was reduced to 50 in the interest of covering a wider range of test conditions before the flappers succumbed to fatigue. Note, turbulence or velocity perturbation data was not sought after in this research.

The time between pulses (Δt) is a significant variable in the set-up of any PIV testing. This test parameter governs the gross pixel movement between the first and second frame capture. The longer the Δt, the greater the particle motion between images. The Dantec DynamicStudio processing manual recommends particle motion on order of $\approx 10\%$ of the pixel size of the interrogation window [14]. The sample window used to process the data was 64×64 pixels; therefore the target particle motion between images was 6-10 pixels. A 45° angle stop wing, at A=0.4, was used to determine the correct Δt setting necessary to achieve the recommended 6-10 pixel movement between image pairs. Δt was incremented in 100μs intervals in a fully seeded test chamber, and 10 image pairs were collected per Δt. Several locations above and below the wing were zoomed in on, and specific particles were selected and followed between image pairs. A built-in reticle was used to get the coordinates of the target particle in each frame and the total number of pixels travelled between frames was calculated. The value of Δt was adjusted by 100μs until the target amount of pixel motion was reached. The value of Δt, in addition to all the other parameters

and equipment settings used in the PIV experiments, are subsequently chronicled in *Chapter* V.

IV. Aerodynamic Performace

4.1 Overview

THIS chapter will focus on the results of the Nano-17 6-DoF force balance testing. Forces and moments were collected at various passive rotation angle stop and amplitude combinations. Raw force and moment data is initially presented with 95% confidence error bars to set the baseline accuracy for subsequent calculations using the force and moment data. Aerodynamic coefficients were calculated from the raw force and moment data using blade element theory, and were contrasted with steady and rotational treatments to develop an aerodynamic coefficient model for use in future design considerations. Power consumption, along with its dimensionless coefficients, are presented as a secondary, yet nonetheless important, companion to the force data as a function of driving amplitude, and hence, stroke angle, to give designers an aerodynamic power coefficient threshold to benchmark their electrical components off when considering battery or power plant solutions.

4.2 Test Point Matrix

Forces and moments were collected on 30°, 45°, and 60° angle stop flappers at various driving amplitudes. The following flapping tests were performed on the AFIT FWMAV, listed in Table 4.1 below. Note, the 60° flap testing was not completed on the same day as the other testing because the original flapper failed at the rotation joint after A=0.36, and no more flapper bases were available to assemble another test article. An extra base and linkage was made available several months later, and another 60° wing was assembled, its resonant frequency determined, symmetry verified through manual tuning of A_{trim}, and force balance testing resumed at A=0.37. Figure 4.1 gives a visual reference for the distinction between the 30°, 45°, and 60°

angle stops mounted on the passive rotation joint.
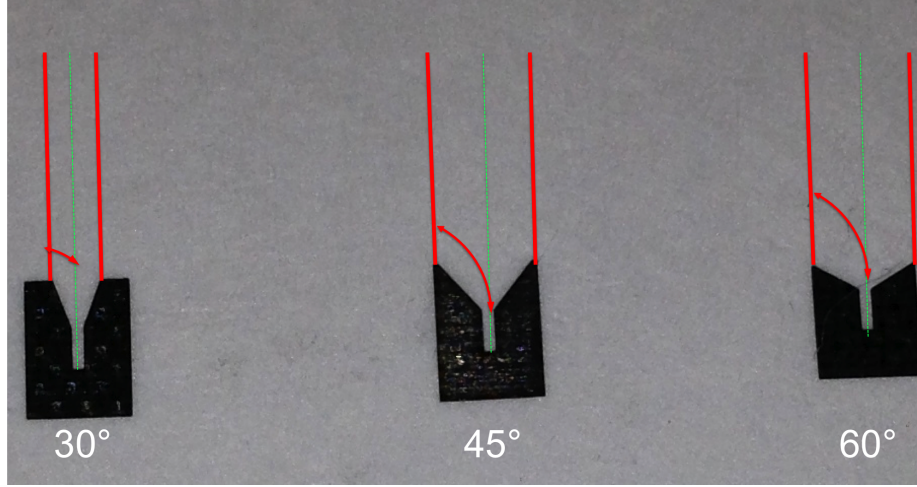
Figure 4.1: Graphic depiction of the 30°, 45°, and 60° passive rotation angle stops used in the subsequent research.

4.3   Kinematic vs. Optical Φ Comparison

The instantaneous kinematic flap angle, $\phi(t)$, was calculated with Equation 2.63 from the real time PZT displacement measurements obtained from the optoNCDT displacement sensor. The kinematic cycle averaged total flap angle, Φ, was computed by sampling the middle 70% of the $\phi(t)$ time-history data to eliminate the transient wing motions at the beginning and end of the test, and the cycle average stroke angle was calculated by taking the average of the sum of the absolute value of the local maximum and minimum values over the sample range. In all cases the stroke angle increased monotonically with drive amplitude, and the kinematic equation under predicted Φ at every test point for all three angle stops. This is a very useful design consideration. Power consumption, lift and drag are predicated on the total stroke angle, and heretofore, Φ was calculated by assuming an amount of PZT displacement, δ, and using Equation 2.63 to compute the expected amount of stroke angle. Improving over previous research efforts, this research has incorporated the real-time measured value of δ into Equation 2.63 to improve on the accuracy of the model prediction

Table 4.1: Flapping Test Point Matrix for 30°, 45°, 60° Angle Stop Flappers vs. Drive Signal Voltage

30° wing

A	A_{trim}	V^+	V^-	V_{tot}	ω	δ	Φ_{kin}	Φ_{opt}	Φ_{err}
0.30	-0.060	86.4	-33.6	120	20	1.15	54.5	70.3	22.5
0.32	-0.044	93.2	-34.8	128	20	1.20	57.2	74.3	23.0
0.34	-0.028	100.1	-35.9	136	20	1.25	59.6	78.8	24.4
0.35	-0.020	103.6	-36.4	140	20	1.27	60.7	79.7	23.8
0.36	-0.020	106.6	-37.4	144	20	1.29	61.6	81.2	24.1
0.38	-0.020	112.5	-39.5	152	20	1.32	63.5	84.8	25.1
0.40	-0.020	118.4	-41.6	160	20	1.35	65.3	87.8	25.7
0.42	-0.018	124.5	-43.5	168	20	1.39	67.4	91.2	26.1
0.44	-0.016	130.6	-45.4	176	20	1.43	69.4	94.9	26.9
0.44	-0.015	130.7	-45.3	176	20	1.42	68.6	94.4	27.3
0.46	-0.014	136.7	-47.3	184	20	1.44	70.0	99.2	29.5
0.48	-0.012	142.8	-49.2	192	20	1.50	73.3	102.9	28.8
0.50	-0.010	149.0	-51.0	200	20	1.54	75.7	107.1	29.3
–	–	–	–	–	–	–	–	–	–
–	–	–	–	–	–	–	–	–	–
–	–	–	–	–	–	–	–	–	–

45° wing

A	A_{trim}	V^+	V^-	V_{tot}	ω	δ	Φ_{kin}	Φ_{opt}	Φ_{err}
0.30	-0.070	85.8	-34.2	120	22	0.35	50.3	69.6	27.7
0.32	-0.005	95.7	-32.3	128	22	0.37	52.5	72.8	27.8
0.34	-0.036	99.6	-36.4	136	22	0.94	54.8	76.3	28.2
0.36	-0.019	106.6	-37.4	144	22	0.38	57.0	78.5	27.4
0.38	-0.002	113.8	-38.2	152	22	0.39	59.2	83.1	28.8
0.40	0.015	121.2	-38.8	160	22	0.40	61.4	88.4	30.5
0.42	0.022	127.9	-40.1	168	22	0.41	63.7	92.7	31.4
0.44	0.030	134.6	-41.4	176	22	0.42	65.9	97.6	32.5
0.46	0.037	141.4	-42.6	184	22	0.43	68.1	101.8	33.1
0.48	0.045	148.3	-43.7	192	22	0.44	70.3	106.1	33.7
0.50	0.035	153.5	-46.5	200	22	0.46	72.5	112.1	35.3
0.52	0.030	159.1	-48.9	208	22	0.48	74.8	115.1	35.1
0.54	0.010	163.1	-52.9	216	22	1.28	77.0	118.2	34.9
0.56	-0.025	165.2	-58.8	224	22	1.37	83.2	121.7	31.7
0.58	-0.050	168.2	-63.8	232	22	1.45	88.1	123.3	28.6
0.60	-0.070	171.6	-68.4	240	22	1.50	91.8	125.1	26.6

60° wing

A	A_{trim}	V^+	V^-	V_{tot}	ω	δ	Φ_{kin}	Φ_{opt}	Φ_{err}
0.30	-0.200	78.0	-42.0	120	21	1.32	63.4	77.9	18.6
0.32	-0.152	86.3	-41.7	128	21	1.38	66.3	83.6	20.7
0.34	-0.104	94.9	-41.1	136	21	1.42	68.6	92.2	25.7
0.35	-0.080	99.4	-40.6	140	21	1.44	69.5	96.4	27.9
0.36	-0.063	103.5	-40.5	144	21	1.49	72.2	102.4	29.6
0.37	-0.046	107.6	-40.4	148.0	21	1.50	72.8	101.3	28.1
0.38	-0.029	111.8	-40.2	152	21	1.52	74.1	103.2	28.2
0.39	0	117	-39	156	21	1.53	74.4	110.8	32.9
0.40	0.005	120.4	-39.6	160	21	1.57	76.9	107.4	28.4
0.41	0.022	124.8	-39.2	164	21	1.59	78.0	109.2	28.6
0.42	0.040	129.4	-38.6	168	21	1.59	77.8	110.9	29.8
0.44	0.065	137.7	-38.3	176	21	1.69	83.9	118.8	29.4
0.45	0.080	142.2	-37.8	180	21	1.71	85.3	119.8	28.8
0.46	0.090	146.3	-37.7	184	21	1.75	87.8	125.7	30.2
0.48	0.110	154.6	-37.4	192	21	1.78	89.7	127.3	29.6
0.50	0.130	163.0	-37.0	200	21	1.79	90.5	130.7	30.8

over using a δ value from the PZT manufacture's data sheet; however, the model still considerably under predicts the actual wing stroke angle. The mean percent error between the predicted and measured values of Φ was $28\%, 30\%,$ and $28\%,$ for the $30°,$ $45°,$ and $60°$ wings respectively; therefore, an adequate approximation would be to add 28% to the predicted values in future design iterations. Figure 4.2 shows the difference between the values of the predicted kinematic stroke angles and the actual stroke angles calculated from the optical tracking routine. Higher stroke angles for a specific amplitude are generally desirable, which results inexorably to higher total forces.

(a) 30° (b) 45°

(c) 60°
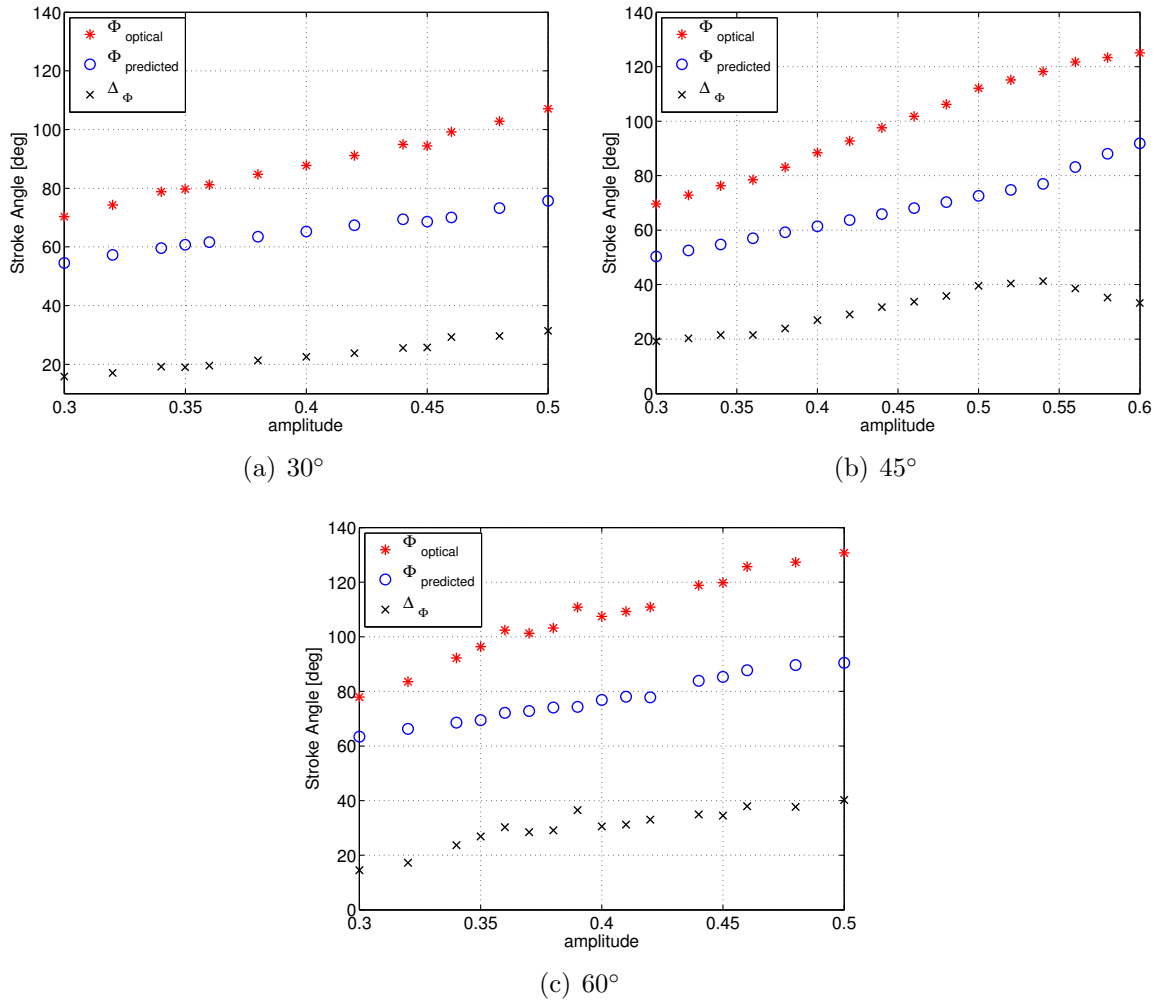
Figure 4.2: Stroke angle comparison between Φ calculated with the kinematic equation, Equation 2.63, and Φ computed with the optical tracking code for the $30°$, $45°$, and $60°$ angle stop wings. In all cases, the stroke angles increased montonically with drive amplitude.

4.4 Force Error Bars

The next series of plots show the graphical results of error analysis on the raw force data. Multiple five second tests at each test condition were executed and averaged together to get a single raw time history data set. The time history was subsampled to retain the middle 70% of the flapped data time, then the mean value was taken of the resampled raw data to calculate the cycle averaged forces and moments. Figure 4.3 shows the three cycle averaged forces plotted with their respective 95% confidence bounded standard deviations for the variable amplitude testing. The error bar plots are significant because they illustrate how sensitive the entire FWMAV field of study is to slight changes in design parameters. The forces produced by wings of such diminutive size can approach the sensitivity noise floor of the sensor's resolution capability, especially at the lower drive voltages. The error bar plots show the $\pm$ standard deviation (σ_x), at a 95% confidence interval, calculated from the subsampled force time history data, which removes the tare and the flapping start and stop transient force responses, leaving only the full-scale flapping forces as the result, representing the most stable data set possible. The sample standard deviation (σ) for each subsampled force vector is calculated using Equation 4.1 below.

$$\sigma_{(F_x, F_y, F_z)} = \sqrt{\left(\frac{1}{n-1} \sum_{i=1}^{n} (x_i - \bar{x})^2 \right)} \tag{4.1}$$

Where n is the number of data samples, here it is the length of the subsampled force vectors, and $\bar{x}$ is the sample mean ($\bar{x}$) of the data set, and is calculated numerically by Equation 4.2.

$$\bar{x} = \frac{1}{n} \sum_{i=1}^{n} x_i \tag{4.2}$$

The data set is sufficient ($n = 25,000$ data points) to assume a Normal-Gaussian

Probability Distribution ($f_n(y)$), which is a function of the theoretical mean ($\bar{\mu}$), and the theoretical standard deviation ($\bar{\sigma}$), and is given in Equation 4.3 below [7].

$$f_n(y) = \frac{1}{\sigma\sqrt{2\pi}} \; exp\left(\frac{-(y-\mu)^2}{2\sigma^2}\right) \tag{4.3}$$

The probability statement then gives a relationship between the desired confidence level (β_{cp}), $\bar{x}$, and a confidence factor (k_3). The probability the force data is within 95%, or $\pm5\%$ of the mean, is formally stated in Equation 4.4,

$$\text{Probability} \; (\bar{x} - k_3\sigma x < \mu < \bar{x} + k_3\sigma) = \beta_{cp}$$

or in terms of the confidence interval: (4.4)

$$\text{Probability} \; (\bar{x} - \Delta x < \mu < \bar{x} + \Delta x) = \beta_{cp}$$

where Δx is the confidence interval, and is calculated numerically by $\pm\Delta x = (1 - \beta_{cp})\bar{x}$, and k_3 is equal to $\Delta x/\sigma$ [7]. The error bar at each of the mean force values is the product of σ and k_3 [7]. The expected result is, as the average force increases with either increasing flapping frequency, or drive signal amplitude, the length of the error bars would decrease, as the magnitude of the force increases above the sensor resolution floor threshold. Although the error bars were small in comparison to the magnitude of the mean forces, see Figure 4.3, the size of the vertical force (F_x), error bars showed modest increase as the drive amplitude increased, something not present in either the axial force (F_z) or the spanwise or side force (F_y). The vertical lift is the largest force exerted on the balance, and as this force increases, the cyclic nature exacerbates the statistical standard deviation and variance. The increasing magnitude of the fluctuation (rise and fall) around zero increases the uncertainty in the measurement.
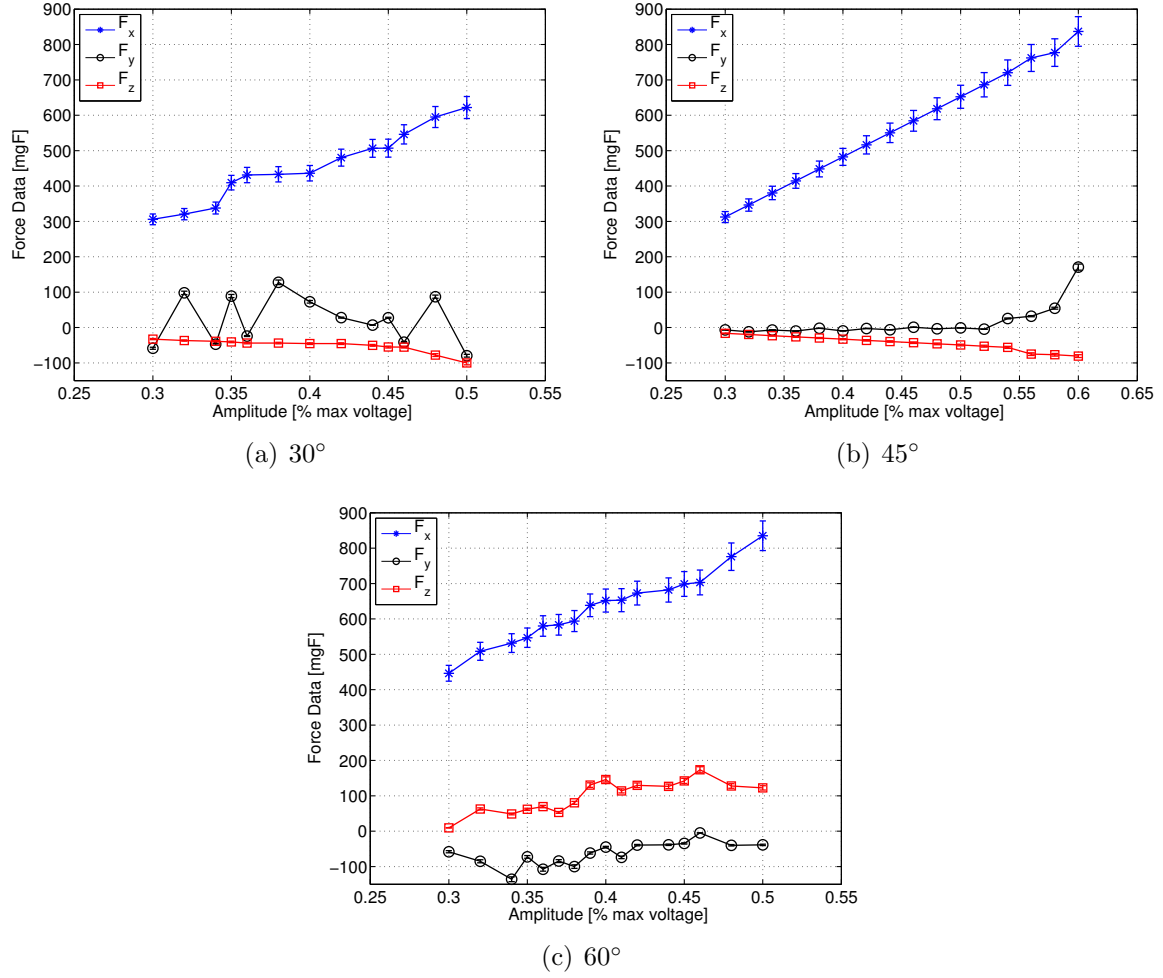
Figure 4.3: Comparison of the cycle averaged vertical force (F_x), side force (F_y), and axial force (F_z) error bar plots for the 30°, 45°, and 60° angle stop wings.

4.5 Aerodynamic Forces

This section will present the results for lift and drag calculated with the 2-D blade element model described in section 2.4.2, and then expand upon that formulation by applying a quasi-steady analysis to take the earth centered Nano-17 balance forces and convert them to body centered forces, and develop 3-DoF force coefficients in both the body and wind axes that can be used as a baseline aero model for future design and refinement of the AFIT FWMAV.

155

4.5.1 Blade Element Lift & Drag.

Previous researchers have shown the application of standard 2-D airfoil analysis to flapping wing flight, without necessarily showing the detailed results of that utilization to a specified system under test. Anderson used the BEM to model lift and drag forces using an idealized wing model and a general array of wing angles, not rooted in actual measured AFIT FWMAV angular performance. Instantaneous values of C_L and C_D were calculated using the time history of the angle of attack results from the optical tracking during the wing stroke using Equation 2.49. The force coefficients were applied to Equation 2.41 to estimate the lift and drag forces developed during the wing stroke. Figure 4.4 shows a trace of the instantaneous force coefficients, C_L and C_D, calculated for the AFIT FWMAV using a 2-D BEM and the actual angle of attack data obtained from the optical tracking routines.
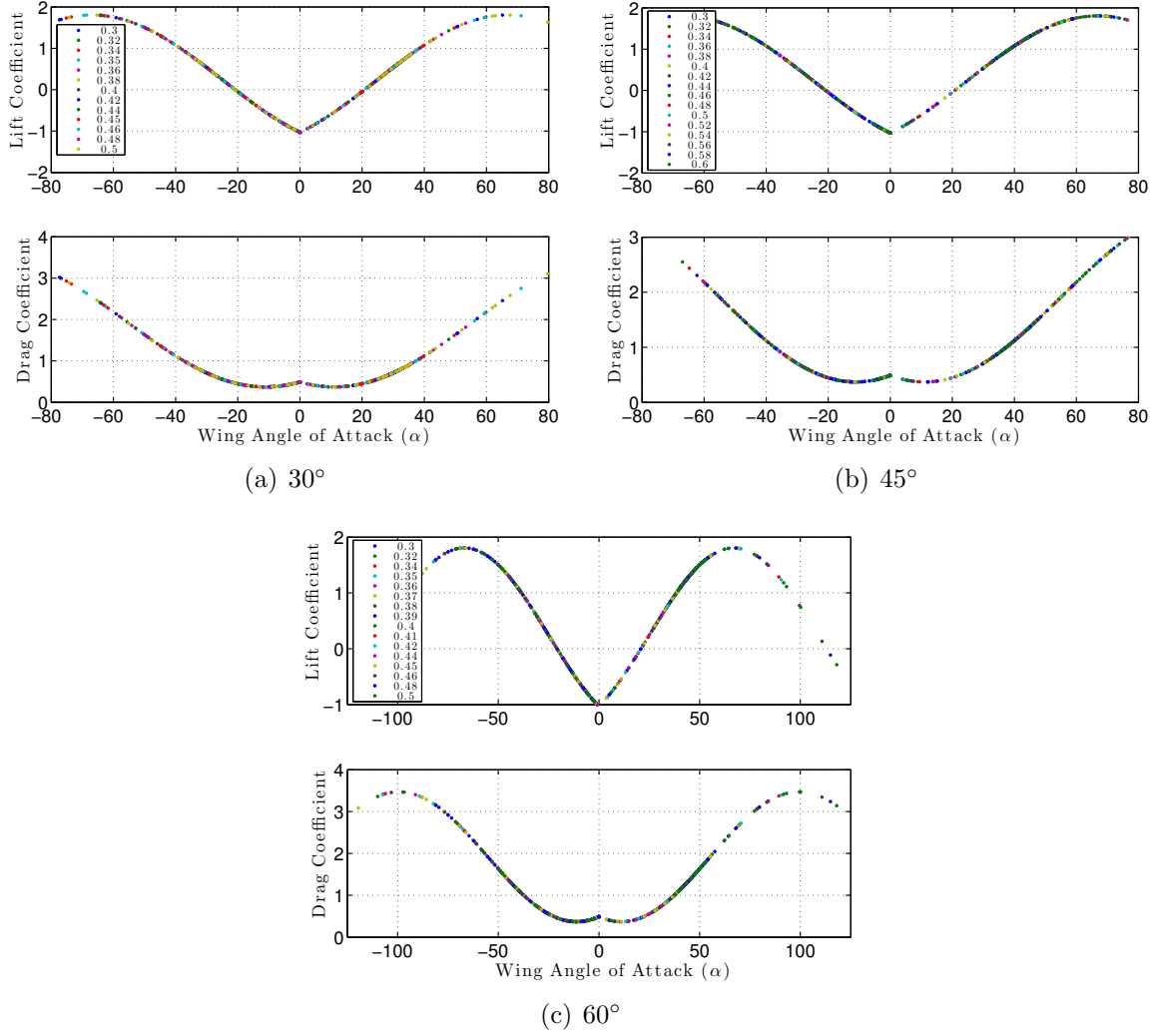
Figure 4.4: Force coefficients, C_L & C_D, obtained from BEM predictions for the 30°, 45°, and 60° wings plotted against angle of attack.

Using the estimates for the force coefficients obtained above, the lift and drag forces through the wing stroke can also be approximated by applying traditional lifting line theory, using Equation 2.41. Figure 4.5 shows an estimate of the lift and drag forces through the flap stroke as a function of angle of attack, and Figure 4.6 shows the lift and drag forces plotted for a single normalized flap cycle. The scatter in the force data at the AoA limits at the end of each half cycle is due to the wing rotation transition between supination and pronation where the forces over the wing are ameliorated by the abrupt change in AoA, stalling the wing as it rotates up through vertical

157

($\alpha = 0°$) and back over to the next half cycle AoA. The BEM predicts the forces grow during the translation phases, decrease to zero when $\alpha = 0°$ during rotation, and then increase again during the following half cycle.

(a) 30°

(b) 45°

(c) 60°
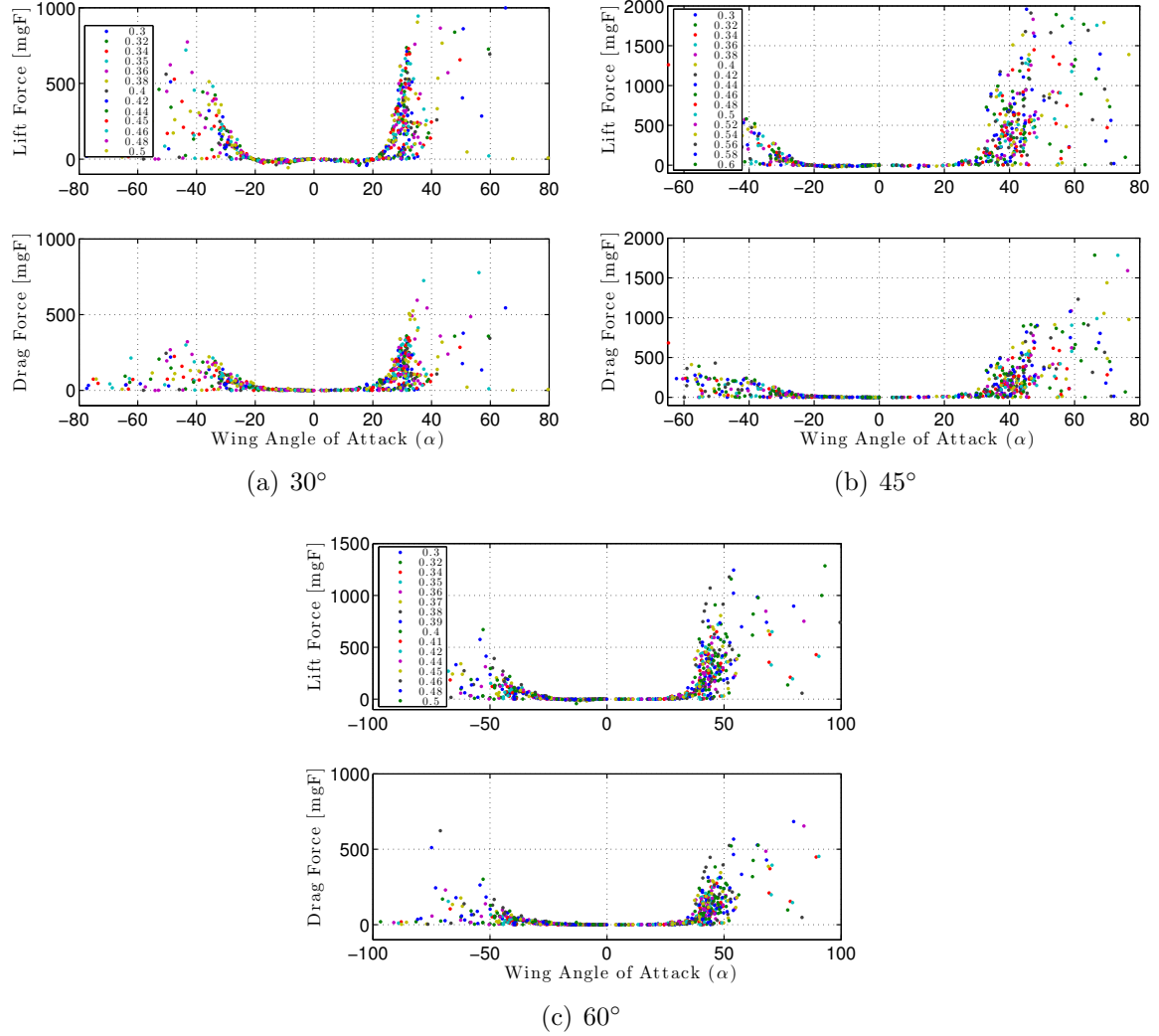
Figure 4.5: Lift and Drag calculated obtained from BEM predictions for the 30°, 45°, and 60° wings plotted against angle of attack.
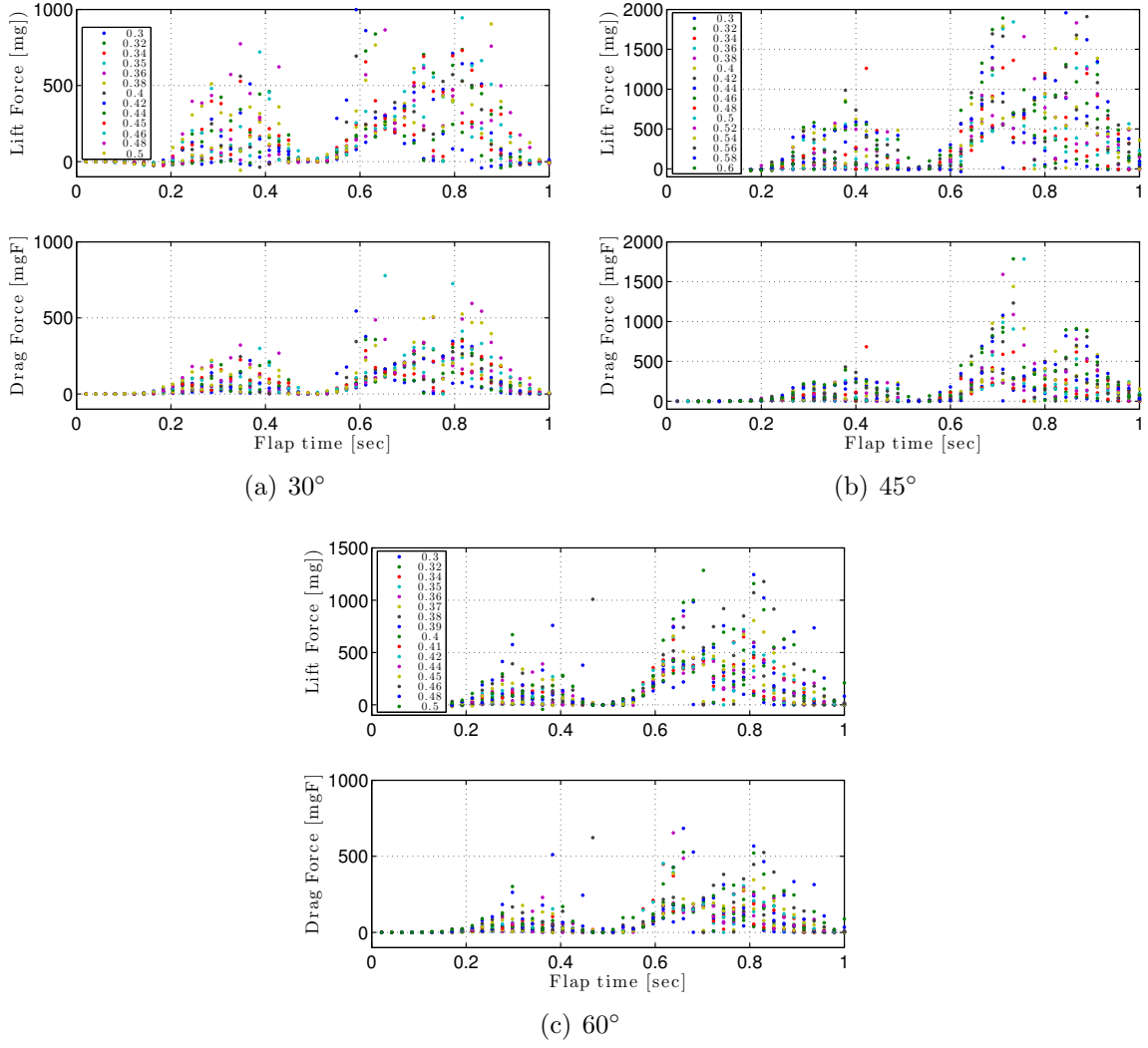
Figure 4.6: Lift and Drag plotted over a single stroke cycle for the 30°, 45°, and 60° wings.

Figure 4.7 shows the drag polar, C_L vs. C_D, plotted for the 30°, 45°, and 60° wings. The presentation of the data in this format is consistent with standard aerodynamic analysis, and can also be used to compare to published results by Sane, Usherwood, Willmott and others [73, 84, 92].

(a) 30°

(b) 45°

(c) 60°
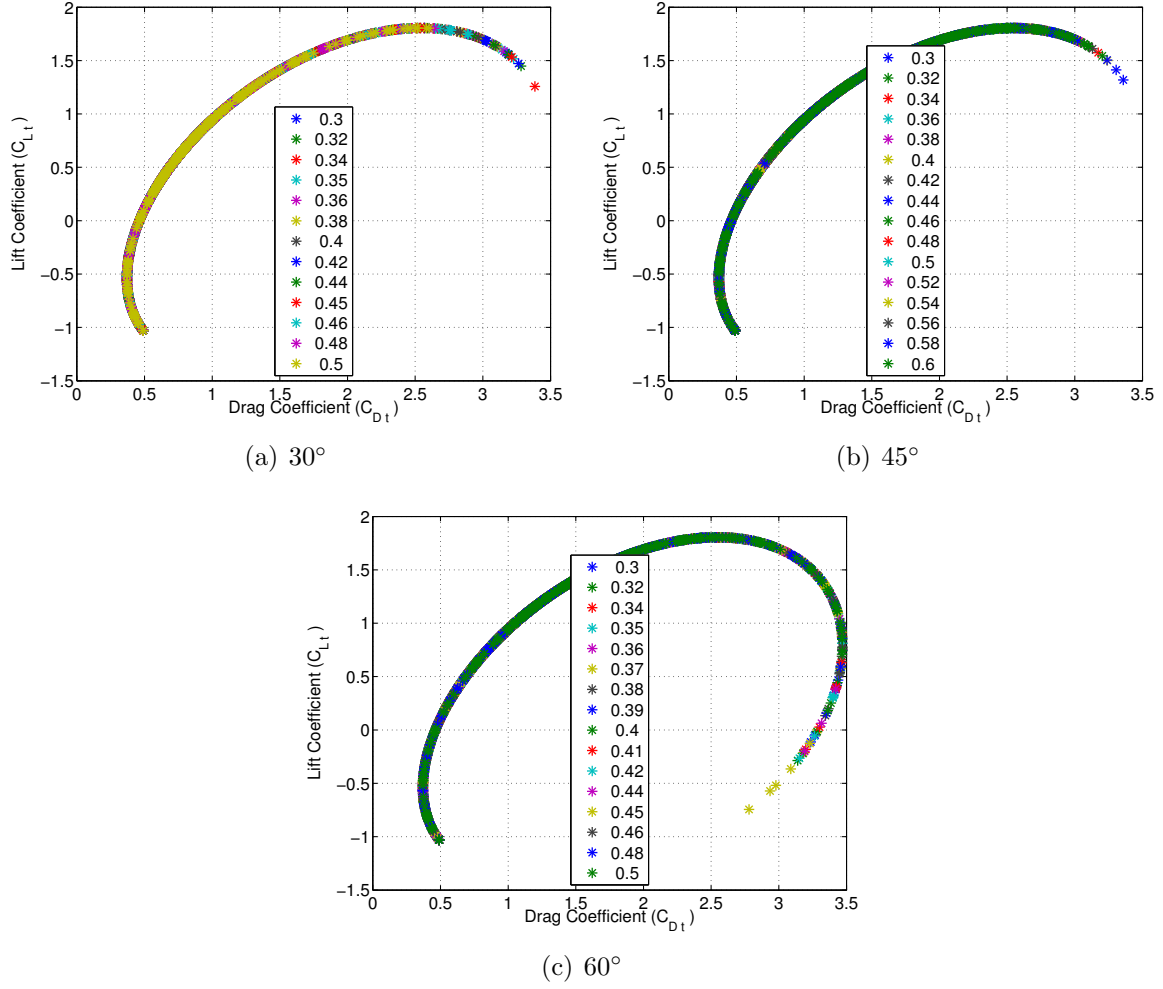
Figure 4.7: Drag polars obtained from BEM prediction plotted over an entire flap cycle for the 30°, 45°, and 60° wings.

The final series of illustrations in the blade element model analysis is the lift-to-drag ratio, $^L/_D$, at six different amplitudes for the 30°, 45°, and 60° wings, shown in Figure 4.8 below.
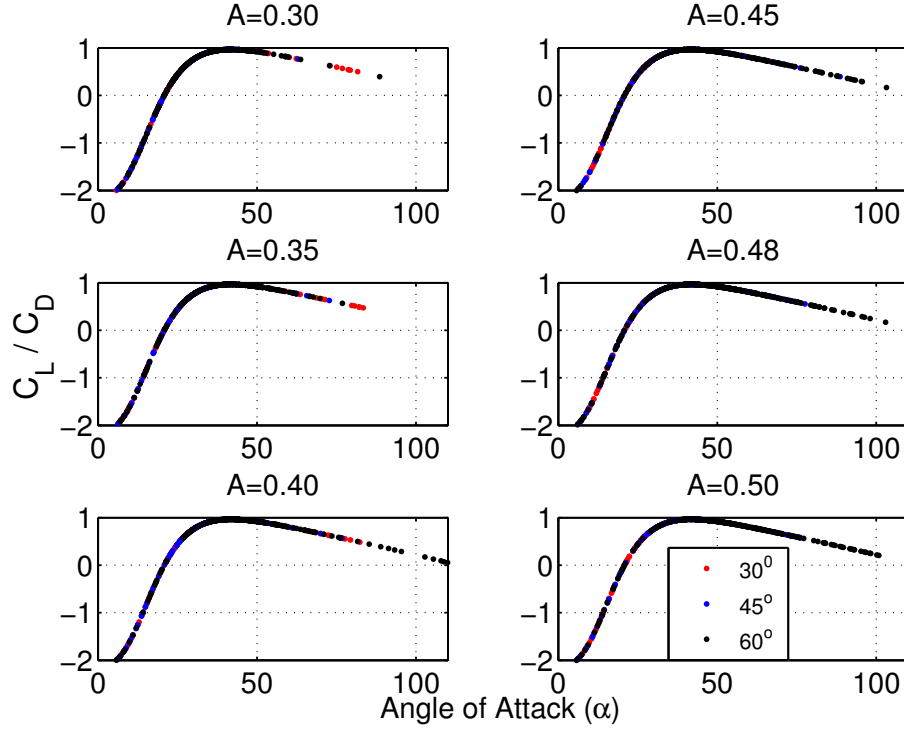
Figure 4.8: Lft-to-drag ratio, $^L/_D$, shown at A=(0.30, 0.35, 0.40, 0.45, 0.48, and 0.50) for the 30°, 45°, and 60° wings.

All of the BEM quasi-steady predictions of lift and drag forces, and their corresponding dimensionless coefficients show general agreement with published predictions by Usherwood *et.al.* on 10× scaled model revolving mechanical hawkmoth wings, and that published by Sane on 25× scaled model revolving mechanical fruit fly wings. Figure 4.9(c) shows C_v and C_h vs. angle of attack, and the corresponding drag polar for Usherwood's 10× mechanical hawkmoth wing from data collected on a 2-DoF force balance under kinematic conditions matched to live hawkmoth flight, and for a set of altered wing kinematics placing wing rotation ahead of maximal stroke apogee and perigee. Figure 4.9(d) shows measured lift and drag force development over a stroke cycle compared to BEM predictions for Sane's scaled mechanical Fruit Fly wing using a range of prescribed values of α.

(a) 10× hawkmoth: C_v

(b) 25× Fruit Fly: $\alpha = 30°$

(c) 10× hawkmoth: C_h

(d) 25× Fruit Fly: $\alpha = 50°$
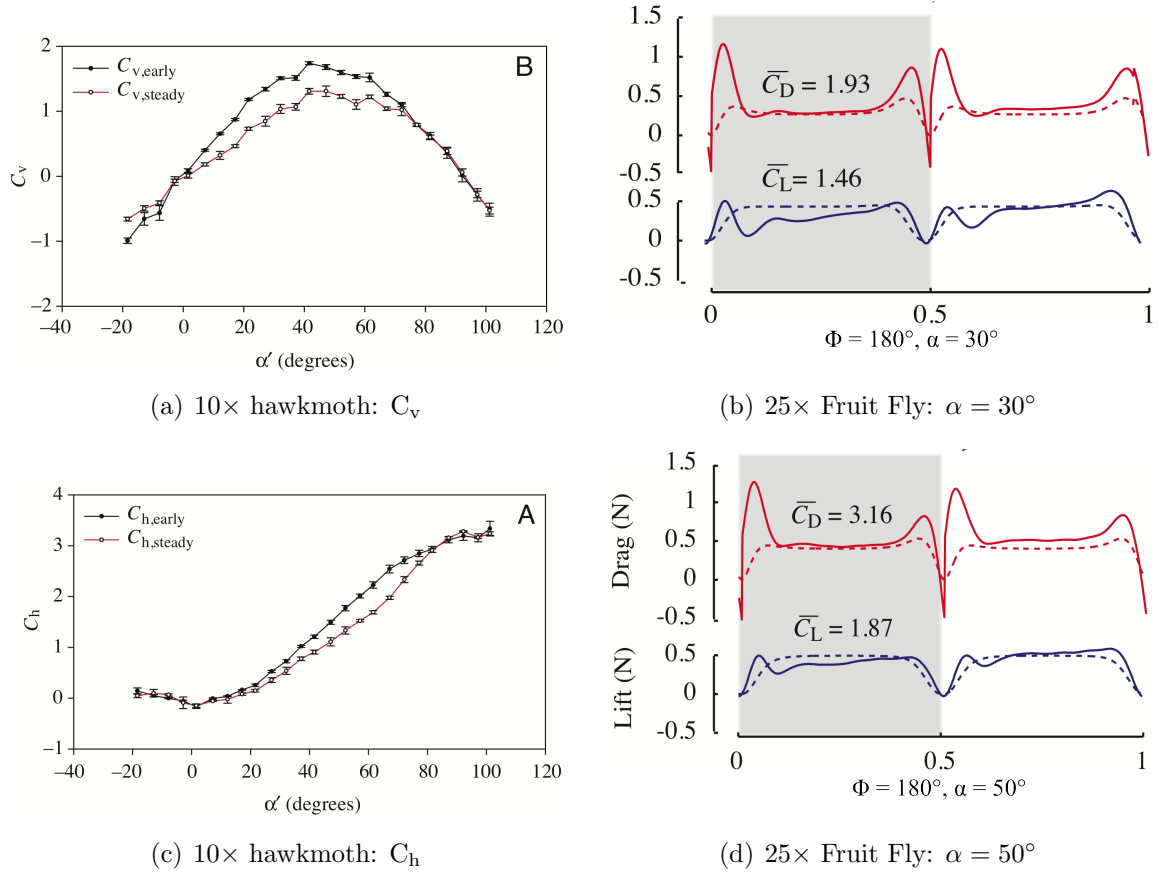
Figure 4.9: hawkmoth and Fruit Fly BEM predictions—modified from [73, 84].

Table 4.2 summarizes the mean aerodynamic coefficients illustrated in Figures 4.4-4.8 for the for the 30°, 45°, and 60° wings.

Table 4.2: Summary of Blade Element Model Mean Aerodynamic Coefficients

Parameter	30° wing	45° wing	60° wing
$\bar{\alpha}$	59.6°	49.7°	40.1°
$\bar{\Phi}$	88°	99°	107°
$\overline{C_L}$	0.5	0.8	1.0
$\overline{C_D}$	08	1.1	1.3
$\overline{L/D}$	0.4	0.5	0.6

4.5.2 Translational and Rotational Forces & Coefficients.

This section presents a refined model of lift and drag production by transforming the measured balance forces from wind axes to body aerodynamic forces and calculating a lift, drag, side force coefficient. The measured forces, F_x, F_y, and F_z were transformed to lift, drag, and side force in the body axes using Equation 4.5

$$
\begin{bmatrix} L_b \\ S_b \\ D_b \end{bmatrix} = \begin{bmatrix} F_z \sin(\alpha)\cos(\psi) - F_y \sin(\alpha)\sin(\psi) + F_x \cos(\alpha) \\ F_z \sin(\psi) + F_y \cos(\psi) \\ F_z \cos(\alpha)\cos(\psi) - F_y \sin(\psi)\cos(\alpha) - F_x \sin(\alpha) \end{bmatrix} \tag{4.5}
$$

where α is the pitch angle, defined here as the wing angle of attack during the stroke, and ψ is the yaw angle (ψ), the angle the wing makes with respect to the balance z-axis, and is assumed to be zero mounted in this configuration. Side force is defined positive along the wing span axis, lift is defined as remaining perpendicular to the wing reference angle of incidence, which is assumed to be coincident with the pitch angle, and drag is then the perpendicular vector bisector between the vertical force vector, F_x, and the lift vector, L.

The dimensionless force coefficients, C_L, C_D, and C_S were computed using Equation 2.46, which is given for a generalized force coefficient (C_{F_i}). Equation 2.46 is derived from a quasi-steady treatment of the wing during translation for a half-cycle, without regard to the direction of the resultant forces. The mean circulation around a wing element is given by Equation 4.6.

$$
\Gamma = \frac{1}{2} c U_r \overline{C_L} \tag{4.6}
$$

Substituting the flapping velocity, $r(d\hat{\phi}/d\hat{t})$, for the characteristic velocity, the circulation is then,

$$\Gamma = \frac{n\Phi\cos(\beta)}{8\cos(\beta_r)}\overline{C_L}\hat{c}\hat{r}(d\hat{\phi}/d\hat{t}) \tag{4.7}$$

and the dimensionless form is computed by dividing by the maximum circulation (Γ_{max}), which occurs at the maximum chord ($(\hat{c}\hat{r})_{max}$), and the maximum angular velocity ($(d\hat{\phi}/d\hat{t})_{max}$), yielding,

$$\hat{\Gamma} = \frac{\hat{c}\hat{r}\left(d\hat{\phi}/d\hat{t}\right)}{(\hat{c}\hat{r})_{max}\left(d\hat{\phi}/d\hat{t}\right)_{max}} \tag{4.8}$$

integrating the dimensionless circulation over the half cycle with respect to the circulatory vortex impulse created at the end of rotation, and the beginning of translation, gives the dimensionless impulse due to the mean circulation per unit span over the half cycle shown in Equation 4.9.

$$\hat{I}(\overline{C_L}) = \left((\hat{c}\hat{r})_{max}\left(d\hat{\phi}/d\hat{t}\right)_{max}\right)\int_{-1}^{1}\frac{d\hat{\phi}}{d\hat{t}}d\hat{\phi}\int_{0}^{1}\hat{c}\hat{r}^2 d\hat{r} \tag{4.9}$$

Assuming an invariant lift coefficient during the stroke and substituting half the root mean square of the dimensionless mean angular velocity for the first integral, and the dimensionless 2nd moment of wing area for the second integral, reduces and simplifies Equation 4.9 to a more compact numerical expression given by Equation 4.10.

$$\hat{I}(\overline{C_L}) = \frac{\hat{r}_2^2(S)\left(\overline{d\hat{\phi}/d\hat{t}}\right)^2}{2\,(\hat{c}\hat{r})_{max}\left(d\hat{\phi}/d\hat{t}\right)_{max}} \tag{4.10}$$

Ellington showed the mean aerodynamic force can be related to the dimensionless impulse of circulatory force, and the 2nd moment of wing area, by Equation 4.11.

$$\overline{F} = \frac{2\rho n\Phi R^2\hat{I}\cos\left(\beta\right)\Gamma_{max}}{\cos\left(\beta_r\right)} \tag{4.11}$$

164

Substituting Equations 4.7 and 4.10, and dividing through by the force coefficient, yields the general form of the coefficient result given previously in Equation 2.46, and repeated here below.

$$C_{Force_i} = \frac{8\rho_w \overline{\hat{F}}_i \cos^2(\beta_r)}{\rho n^2 \Phi^2 R^2 \hat{r}_2^2 (S) \left(\overline{d\hat{\phi}/d\hat{t}}\right)^2 \cos^2(\beta)} \tag{4.12}$$

This method of calculating the aerodynamic dimensionless force coefficients was applied to the cycle averaged Nano-17 forces, producing a coefficient value at every amplitude, and Φ, for each of the wings. The force coefficients were also calculated from the raw time history of the balance forces, which were separated into their positive and negative stroke cycles, and their coefficients were computed for the respective positive and negative half cycles of the wing stroke. The total force coefficients were calculated by averaging the coefficients from the positive and the absolute value of the negative phases of the wing stroke. Figure 4.10 shows the generalized force coefficients calculated from above, along with the cycle averaged values of C_L and C_D calculated using the BEM method shown in section 4.5.1 above. The BEM assumes zero side forces, and are not shown in subsequent illustrations. The BEM model is an extension of Prandtl's lifting line, or infinite wing theory, which is by definition a 2-D construct, and therefore does not have a mathematical treatment for root-to-tip developed forces.

165
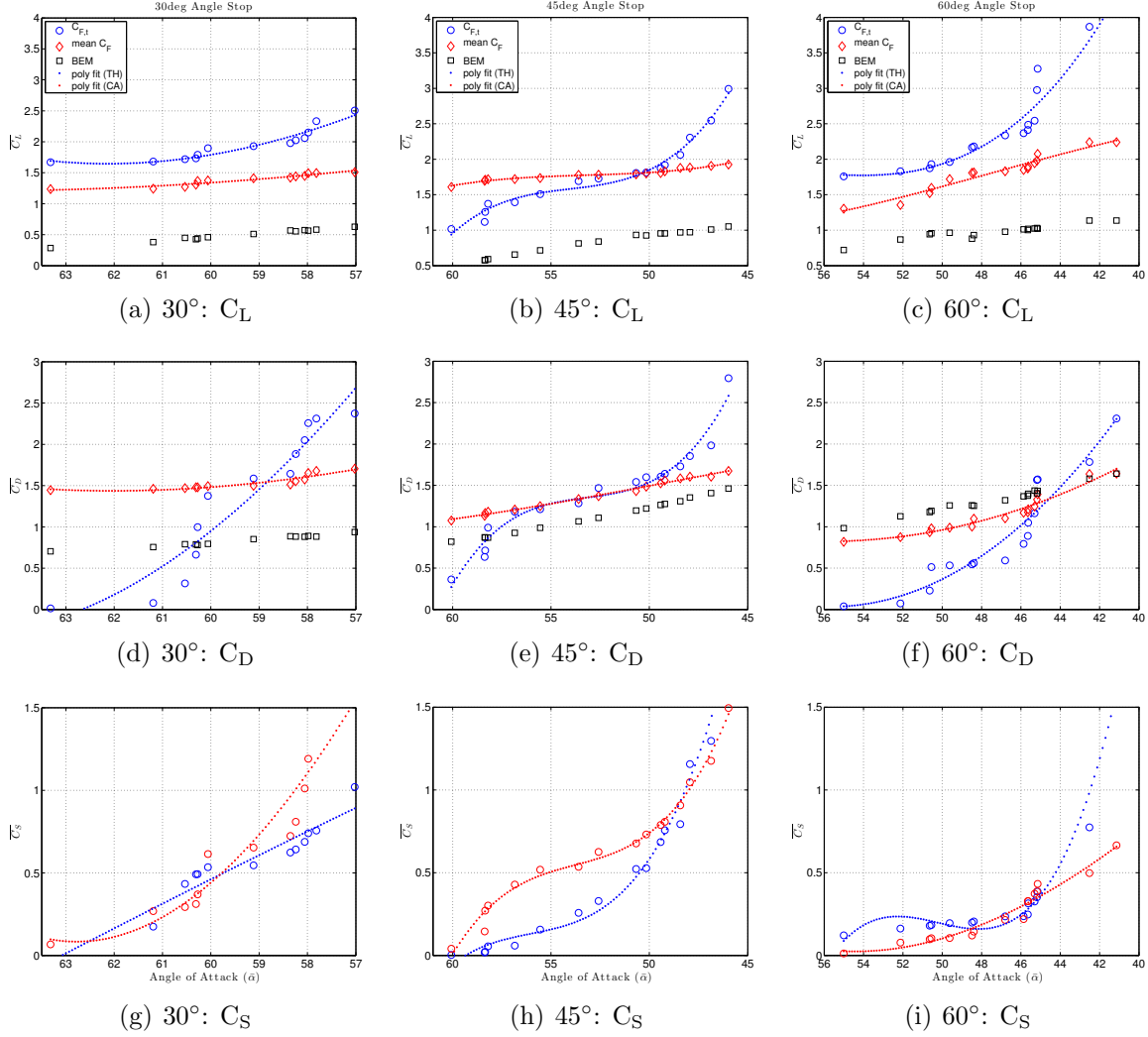
Figure 4.10: C_L, C_D, and C_S for the 30°, 45°, and 60° wings at the mean angle of attack ($\bar{\alpha}$) for each test point. *Red* markers are the coefficients calculated from the body axes forces using cycle averaged Nano-17 forces, *Blue* markers are the coefficients calculated from the time history of the body axes forces, separated into the positive and negative half cylces, then cycle averaged at each test point, *Black* markers are the cycle averaged BEM coefficients computed from the time history coefficients previously calculated in section 4.5.1. The blue and red dotted lines are 3$^{\text{rd}}$ order polynominals fit to the coefficients computed with the two different respective C_{Fi} methods—time history forces and mean cycle average forces.

For completeness, Equation 2.46, was applied to the cycle averaged measured Nano-17 balance forces, in the wind axes, to calculate the body axis force coefficients, vertical force coefficient (C_v), horizontal force coefficient (C_h), and the axial force coefficient (C_a). Figure 4.11 shows the body axes force coefficients for the 30°, 45°, and 60° wings at the mean angle of attack for each test point.

166

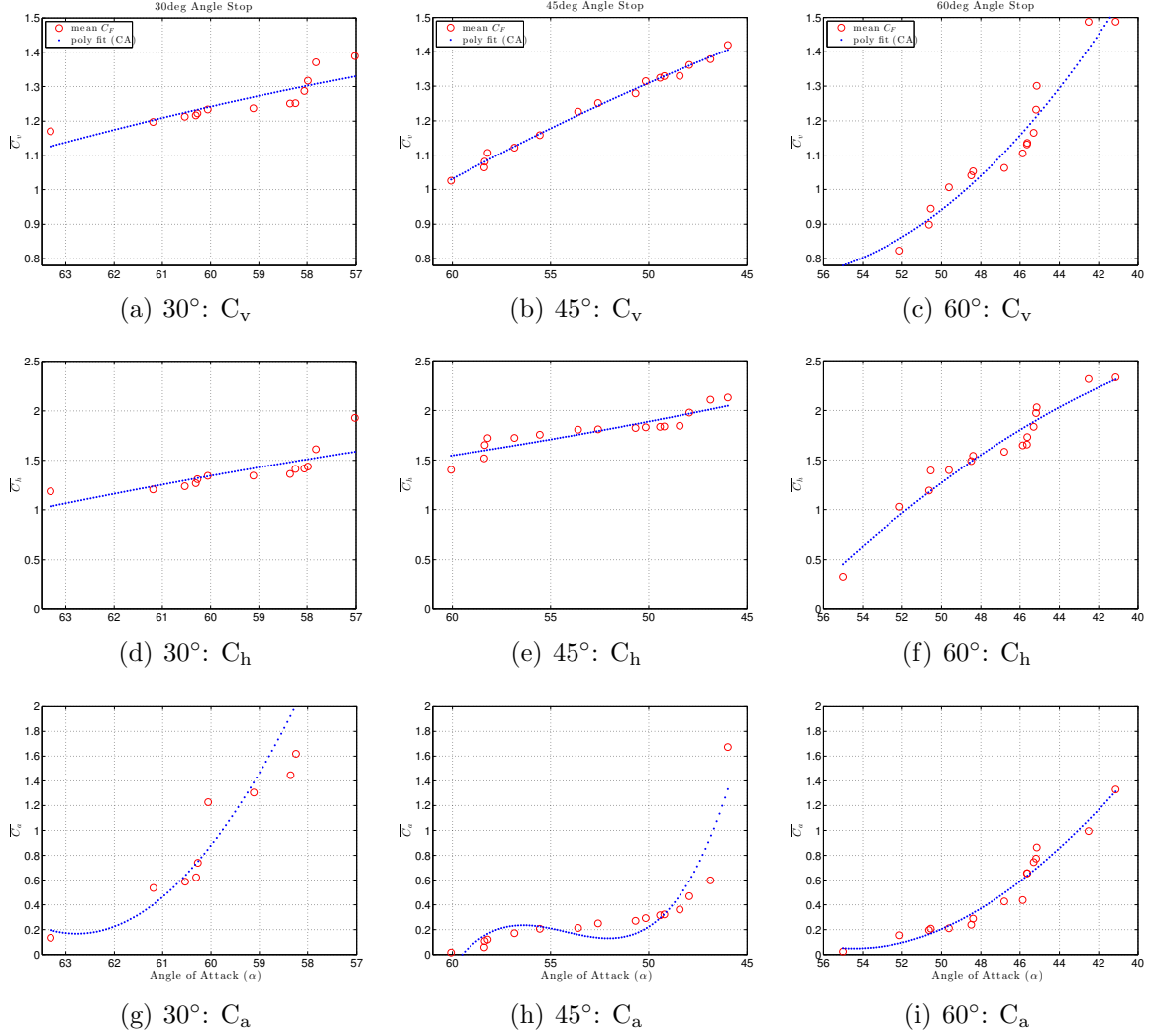**Figure 4.11:** C_v, C_h, and C_a for the 30°, 45°, and 60° wings at $\bar{\alpha}$ for each test point. *Red* markers are the coefficients calculated from the wind axes cycle averaged Nano-17 forces. The dotted lines are 3rd order polynominals fit to the C_{Fi} data.

Tables 4.3-4.5 summarize the 3-axis force coefficients calculated from the measured Nano-17 forces and Equation 2.46 for the 30°, 45°, and 60° wings.

Table 4.3: 30° 3-Axis Force Coefficients

A	Φ (deg)	$\bar{\alpha}$ (deg)	$\overline{C_L}$	$\overline{C_D}$	$\overline{C_S}$	$\overline{C_L/C_D}$	$\overline{C_v}$	$\overline{C_h}$	$\overline{C_a}$	$\overline{C_v/C_h}$
0.30	70.3	63.3	1.2	1.4	0.1	0.9	1.2	1.2	0.1	1.0
0.32	74.3	61.2	1.2	1.5	0.3	0.8	1.2	1.2	0.5	1.0
0.34	78.8	60.5	1.3	1.5	0.3	0.9	1.2	1.2	0.6	1.0
0.35	79.7	60.3	1.3	1.5	0.3	0.9	1.2	1.3	0.6	1.0
0.36	81.2	60.3	1.4	1.5	0.4	0.9	1.2	1.3	0.7	0.9
0.38	84.8	60.1	1.4	1.5	0.6	0.9	1.2	1.3	1.2	0.9
0.40	87.8	59.1	1.4	1.5	0.7	0.9	1.2	1.3	1.3	0.9
0.42	91.2	58.4	1.4	1.5	0.7	0.9	1.3	1.4	1.4	0.9
0.44	94.9	58.2	1.4	1.6	0.8	0.9	1.3	1.4	1.6	0.9
0.44	94.4	58.1	1.4	1.6	1.0	0.9	1.3	1.4	2.0	0.9
0.46	99.2	58.0	1.5	1.7	1.2	0.9	1.3	1.4	2.4	0.9
0.48	102.9	57.8	1.5	1.7	1.5	0.9	1.4	1.6	3.0	0.8
0.50	107.1	57.0	1.5	1.7	1.5	0.9	1.4	1.9	3.1	0.7

Table 4.4: 45° 3-Axis Force Coefficients

A	Φ (deg)	$\bar{\alpha}$ (deg)	$\overline{C_L}$	$\overline{C_D}$	$\overline{C_S}$	$\overline{C_L/C_D}$	$\overline{C_v}$	$\overline{C_h}$	$\overline{C_a}$	$\overline{C_v/C_h}$
0.30	69.6	60.1	1.6	1.1	0.0	1.5	1.0	1.4	0.0	0.7
0.32	72.8	58.4	1.7	1.1	0.1	1.5	1.1	1.5	0.1	0.7
0.34	76.3	58.3	1.7	1.2	0.3	1.5	1.1	1.7	0.1	0.7
0.36	78.5	58.2	1.7	1.2	0.3	1.5	1.1	1.7	0.1	0.6
0.38	83.1	56.8	1.7	1.2	0.4	1.4	1.1	1.7	0.2	0.7
0.40	88.4	55.5	1.7	1.2	0.5	1.4	1.2	1.8	0.2	0.7
0.42	92.7	53.6	1.8	1.3	0.5	1.3	1.2	1.8	0.2	0.7
0.44	97.6	52.6	1.8	1.4	0.6	1.3	1.3	1.8	0.3	0.7
0.46	101.8	50.7	1.8	1.4	0.7	1.2	1.3	1.8	0.3	0.7
0.48	106.1	50.2	1.8	1.5	0.7	1.2	1.3	1.8	0.3	0.7
0.50	112.1	49.4	1.8	1.5	0.8	1.2	1.3	1.8	0.3	0.7
0.52	115.1	49.2	1.8	1.6	0.8	1.2	1.3	1.8	0.3	0.7
0.54	118.2	48.4	1.9	1.6	0.9	1.2	1.3	1.8	0.4	0.7
0.56	121.7	47.9	1.9	1.6	1.0	1.2	1.4	2.0	0.5	0.7
0.58	123.3	46.9	1.9	1.6	1.2	1.2	1.4	2.1	0.6	0.7
0.60	125.1	46.0	1.9	1.7	1.5	1.1	1.4	2.1	1.7	0.7

Table 4.5: 60° 3-Axis Force Coefficients

A	Φ (deg)	$\bar{\alpha}$ (deg)	$\overline{C_L}$	$\overline{C_D}$	$\overline{C_S}$	$\overline{C_L/C_D}$	$\overline{C_v}$	$\overline{C_h}$	$\overline{C_a}$	$\overline{C_v/C_h}$
0.30	77.9	55.0	1.3	0.8	0.0	1.6	0.8	0.3	0.0	2.5
0.32	83.6	52.1	1.4	0.9	0.1	1.6	0.8	1.0	0.2	0.8
0.34	92.2	50.6	1.5	0.9	0.1	1.6	0.9	1.2	0.2	0.8
0.35	96.4	50.6	1.6	1.0	0.1	1.6	0.9	1.4	0.2	0.7
0.36	102.4	49.6	1.7	1.0	0.1	1.7	1.0	1.4	0.2	0.7
0.37	101.3	48.5	1.8	1.0	0.1	1.8	1.0	1.5	0.2	0.7
0.38	103.2	48.4	1.8	1.1	0.1	1.7	1.1	1.5	0.3	0.7
0.39	110.8	46.8	1.8	1.1	0.2	1.7	1.1	1.6	0.4	0.7
0.40	107.4	45.9	1.8	1.2	0.2	1.6	1.1	1.6	0.4	0.7
0.41	109.2	45.6	1.9	1.2	0.3	1.6	1.1	1.7	0.7	0.7
0.42	110.9	45.6	1.9	1.2	0.3	1.6	1.1	1.7	0.7	0.7
0.44	118.8	45.3	1.9	1.2	0.4	1.6	1.2	1.8	0.7	0.6
0.45	119.8	45.2	2.0	1.3	0.4	1.5	1.2	2.0	0.8	0.6
0.46	125.7	45.1	2.1	1.4	0.4	1.5	1.3	2.0	0.9	0.6
0.48	127.3	42.5	2.2	1.6	0.5	1.4	1.5	2.3	1.0	0.6
0.50	130.7	41.1	2.2	1.6	0.7	1.4	1.5	2.3	1.3	0.6

4.5.3 Improved Quasi-Steady Model.

The most critical force in predicting and modeling flight performance is the vertical force, or the lift force, if modeling control movements in the body centered axis frame. The magnitude of this vector at various flight conditions determines the payload capacity of future MAVs, hover characteristics, the flight performance envelope, and the control margins. Further analysis is applied to this force component in particular because of its ubiquitous relevance to the entire flight of future FWMAV design considerations. A refinement to the BEM is gained from further expansion of the application of quasi-steady principals to the main phases of the wing stroke cycle individually—*rotation* and *translation*—rather than on the entire stroke. A third component of this analysis is the effects of the virtual mass, which is modeled as a right circular cylinder about the wing span axis, where the semi-major axis is coincident with the *y*-axis, and the semi-minor axis is coincident with the *z*-axis. Argawal, Ellington, Khan, Userhwood and others summarized the virtual mass force about an infinitely thin wing remains normal to the wing's ventral surface throughout the stroke, resulting in no net force added to the total force vector, and can henceforth be exempted from the force balance equation [50, 71, 74, 84]. Using the definitions and equations for the morphological parameters defined in *Chapter* II, the mean translational force ($\overline{L_{trans}}$) is calculated using Equation 4.13 below.

$$\overline{L_{trans}} = \frac{\rho n^2 \Phi^2 R^2 S\left(\hat{r}_2^2(s)\right) \left(\overline{d\hat{\phi}\big/d\hat{t}}\right)^2 \cos^2(\beta)}{8\cos^2(\beta_r)}\overline{C_L} \tag{4.13}$$

The lift coefficient was calculated from the balance forces and Equation 2.46 [34, 35, 74].

Applying the definitions and equations for the morphological parameters defined in *Chapter* II, the rotational circulation (Γ_{rot}) can be defined similarly as the mean

translational circulation given above in Equation 4.6, as,

$$\Gamma_{rot} = \frac{\bar{\gamma}S\hat{c}^2\hat{\omega}}{\mathcal{R}}.$$ (4.14)

By definition, the maximum circulation occurs at the location of the maximum chord; therefore, the dimensionless rotational circulation is defined as $\hat{\Gamma}_{rot} = \hat{c}^2/\hat{c}^2_{max}$. The impulse due to the rotational circulation is given in Equation 4.15 below.

$$\hat{I}(\bar{\gamma}) = \left(\hat{c}^2\right)^{-1}_{max} \int\limits_{-1}^{1} d\hat{\phi} \int\limits_{0}^{1} \hat{c}^2 \hat{r} d\hat{r} = \frac{2\hat{v}\hat{r}_1(v)}{\hat{c}^2_{max}}$$ (4.15)

Substituting Equation 4.15 into the definition of the generic force expression given in Equation 4.11 yields the general form of the rotational force. The mean rotational force $(\overline{L_{rot}})$ is shown in Equation 4.16 below.

$$\overline{L_{rot}} = \frac{4\rho\bar{\gamma}n^2\hat{\omega}R^2\Phi S\left(\hat{r}_1(v)\right)\hat{v}\cos(\beta)}{\mathcal{R}\cos(\beta_r)}$$ (4.16)

where $\hat{v}$ is the nondimensional virtual mass $(\hat{v})$ given by Equation 4.19, $\hat{r}_1^1(v)$ is the nondimensional radius of 1st moment of virtual mass $(\hat{r}_1^1(v))$ given by Equation 4.21, $\hat{\omega}$ is the nondimensional angular velocity $(\hat{\omega})$, and is equal to $\hat{\dot{\phi}}/n$. The virtual mass per unit span (v') is equal to

$$v' = \frac{1}{4}\rho\pi c(r)^2$$ (4.17)

therefore, the total virtual mass (v_m) of a wing can be expressed as the integral sum of Equation 4.17

$$v = \int\limits_{0}^{R} v' dr = \frac{\rho\pi R^3}{\mathcal{R}^2} \int\limits_{0}^{1} \hat{c}^2 d\hat{r}$$ (4.18)

the nondimensional virtual mass $(\hat{v})$ is computed by diving v by a proportionality

170

constant equivalent to υ of a wing with span equal to 2R, and a chord length equal to $\bar{c}$, and is given by

$$\hat{\upsilon} = \frac{\upsilon \mathcal{R}^2}{2\rho\pi R^3} \tag{4.19}$$

with the dimensionless virtual mass defined, the k$^\text{th}$ moment of virtual mass (υ_k) can be expressed in terms of the dimensionless radius, $\hat{r}^k$, along the span, given by

$$\upsilon_k = \int_0^R \upsilon' r^k dr = \frac{\upsilon R^k}{\hat{\upsilon}} \int_0^1 \hat{c}^2 \hat{r}^k d\hat{r} \tag{4.20}$$

finally, the k$^\text{th}$ radii of virtual mass $(\hat{r}_k^k(\upsilon))$ can be computed with Equation 4.21.

$$\hat{r}_k^k(\upsilon) = \frac{\upsilon_k}{\upsilon R^k} = \frac{1}{\hat{\upsilon}} \int_0^1 \hat{c}^2 \hat{r}^k d\hat{r} \tag{4.21}$$

The mean rotational force coefficient $(\bar{\gamma})$, is a dimensionless representation of the approximate forces experienced during rotation between half cycles. $\bar{\gamma}$ is given by Equation 4.22 [34, 35].

$$\bar{\gamma} = \frac{\Phi \mathcal{R} \left(\hat{r}_2^2(s)\right) \left(\overline{d\hat{\phi}/d\hat{t}}\right)^2 \cos(\beta)}{32 \hat{\omega} \left(\hat{r}_1(\upsilon)\right) \hat{\upsilon} \cos(\beta_r)} \tag{4.22}$$

The morphological parameters shared amongst all three wings are as follows:

- $R = 50\text{mm}$
- $\bar{c} = 20\text{mm}$
- $S = 500\text{mm}^2$
- $\mathcal{R} = 5$
- $\rho = 1.2041\text{kg/m}^3$
- $\beta \approx 0$

- $\beta_r \approx 0$

- $\hat{v} = 1.0942$

- $\hat{r}_1(v) = 0.40648$

- $s_k^2 = 3.2045e - 07\mathrm{m}^4$

- $\hat{r}_2^2(s) = 0.50632$

Table 4.6 tabulates the litany of intermediate parameters calculated for the amplitude dependent values for all three wings tested.

These are empirically derived expressions for the rotational and translation portions of the stroke cycle, their intent is to improve on the 2-D BEM approximation of the actual vertical forces experienced by FWMAVs in flapping flight. Figure 4.12 shows a variety of approximations of force compared to the measured mean vertical force, $\overline{F_\mathrm{x}}$, in the wind axes, along with the mean body axis lift force, $\bar{L}$ for the 30°, 45°, and 60° wings.

Table 4.6: Intermediate Amplitude Dependent Morphological Parameters for 30°, 45°, 60° Angle Stop Wings.

30° wing							45° wing							60° wing						
A	n	Φ	$\frac{d\hat{\phi}}{dt}$	$\hat{\omega}$	$\bar{\gamma}$	$\overline{C_L}$	A	n	Φ	$\frac{d\hat{\phi}}{dt}$	$\hat{\omega}$	$\bar{\gamma}$	$\overline{C_L}$	A	n	Φ	$\frac{d\hat{\phi}}{dt}$	$\hat{\omega}$	$\bar{\gamma}$	$\overline{C_L}$
0.30	20	70.3	35.5	1.7	1.0	1.2	0.30	22	69.6	36.7	1.7	1.4	1.6	0.30	21	77.9	37.4	1.8	2.2	1.3
0.32	20	74.3	35.1	1.7	1.1	1.2	0.32	22	72.8	37.2	1.8	1.5	1.7	0.32	21	83.6	37.1	1.8	2.3	1.4
0.34	20	78.8	35.2	1.7	1.1	1.3	0.34	22	76.3	36.3	1.7	1.6	1.7	0.34	21	92.2	36.4	1.7	2.3	1.5
0.35	20	79.7	35.6	1.7	1.4	1.3	0.36	22	78.5	35.8	1.7	1.7	1.7	0.35	21	96.4	36.2	1.7	2.2	1.6
0.36	20	81.2	35.6	1.7	1.4	1.4	0.38	22	83.1	35.6	1.7	1.8	1.7	0.36	21	102.4	35.9	1.7	2.3	1.7
0.38	20	84.8	35.4	1.7	1.4	1.4	0.40	22	88.4	35.3	1.7	1.9	1.7	0.37	21	101.3	38.1	1.8	2.4	1.8
0.40	20	87.8	35.2	1.7	1.4	1.4	0.42	22	92.7	34.6	1.6	2.0	1.8	0.38	21	103.2	38.2	1.8	2.4	1.8
0.42	20	91.2	34.9	1.7	1.6	1.4	0.44	22	97.6	34.2	1.6	2.1	1.8	0.39	21	110.8	34.6	1.6	2.3	1.8
0.44	20	94.9	35.1	1.7	1.6	1.4	0.46	22	101.8	34.1	1.6	2.2	1.8	0.40	21	107.4	41.0	2.0	2.5	1.8
0.44	20	94.4	34.8	1.7	1.6	1.4	0.48	22	106.1	33.9	1.6	2.3	1.8	0.41	21	109.2	43.8	2.1	2.5	1.9
0.46	20	99.2	34.3	1.6	1.6	1.5	0.50	22	112.1	33.9	1.6	2.3	1.8	0.42	21	110.9	46.1	2.2	2.6	1.9
0.48	20	102.9	34.5	1.6	1.6	1.5	0.52	22	115.1	34.9	1.7	2.4	1.8	0.44	21	118.8	34.4	1.6	2.4	1.9
0.50	20	107.1	34.3	1.6	1.6	1.5	0.54	22	118.2	35.2	1.7	2.5	1.9	0.45	21	119.8	47.3	2.3	2.4	2.0
–	–	–	–	–	–	–	0.56	22	121.7	36.0	1.7	2.5	1.9	0.46	21	125.7	40.9	1.9	2.3	2.1
–	–	–	–	–	–	–	0.58	22	123.3	36.3	1.7	2.6	1.9	0.48	21	127.3	36.0	1.7	2.8	2.2
–	–	–	–	–	–	–	0.60	22	125.1	39.5	1.9	2.8	1.9	0.50	21	130.7	35.1	1.7	3.0	2.2

(a) 30°

(b) 45°

(c) 60°
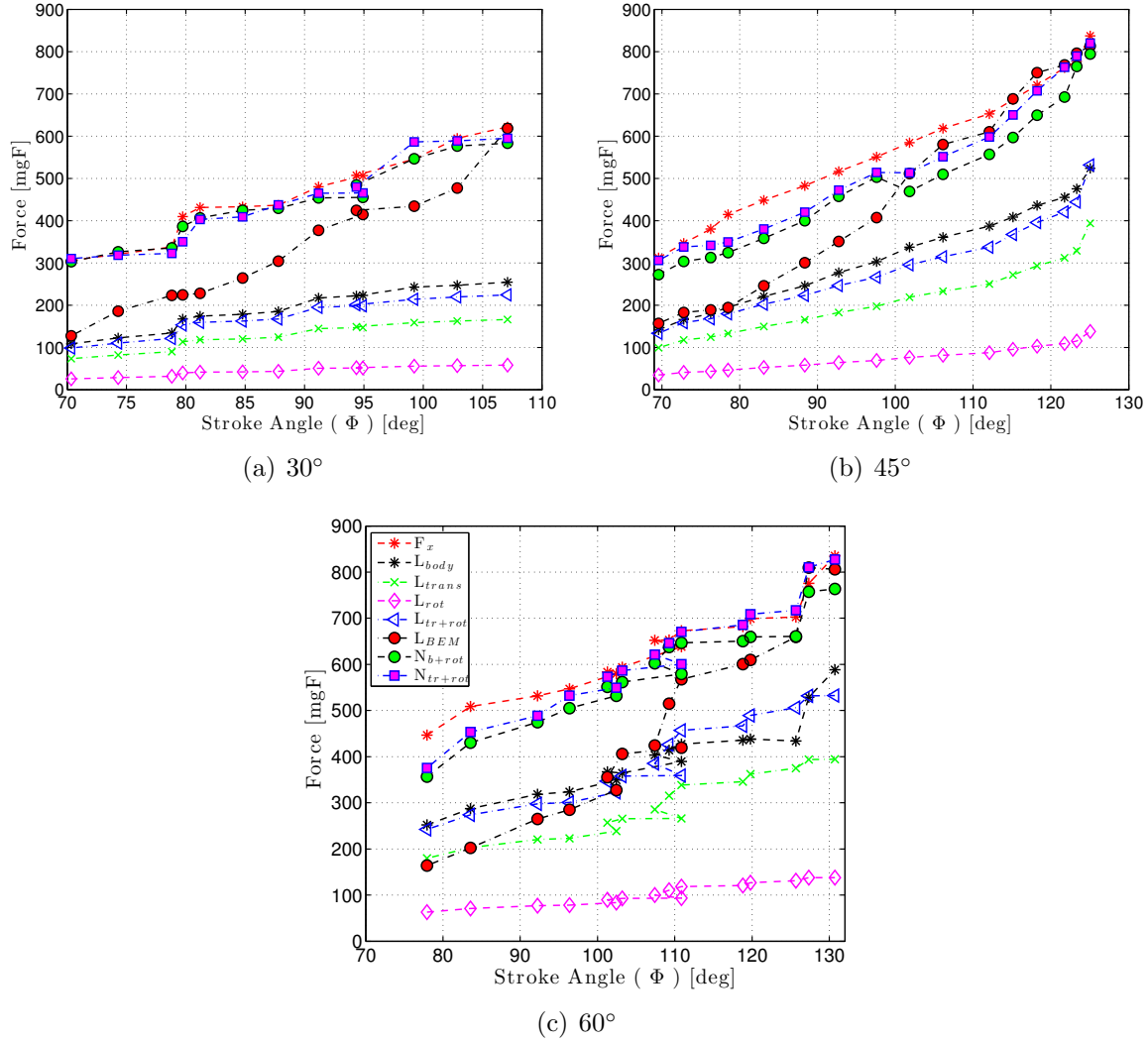
Figure 4.12: Vertical Force ($\mathbf{F_x}$) and Lift (L) for the **30°, 45°, and 60°** angle stop wings compared to the lifting-line BEM, the quasi-stready approximation, and an improved quasi-steady model. The *red* line is the measured vertical force from the **Nano-17**, the *black* is the lift in the body axis, the *green* is the translational lift, the *magenta* is the rotational lift, the *blue triangle* is an estimate of the total lift in the body axis from the sum of the translational and rotational lift components, the *red marker* is the cycle average lift estimate over the entire stroke obtained from the BEM, the *green marker* is a normal force (vertical) estimate from the sum of the body axis lift and the rotational lift, transferred back to the wind axes, and the *magenta marker* is a normal force (vertical) estimate from the sum of the translational and rotational lift, transferred back to the wind axes.

The plots in Figure 4.12 all show good agreement with the measured values presented. Tables 4.7-4.9 lists the improved force estimates and their mean error compared to the measured balance vertical force at each amplitude tested.

174

Table 4.7: 30° **Mean Improved Quasi-Steady Forces and % Error**

A	Lift (mgF)	L_{b+rot} (mgF)	err (%)	L_{tr+rot} (mgF)	err (%)	F_x (mgF)	L_{BEM} (mgF)	err (%)	N_{b+rot} (mgF)	err (%)	N_{tr+rot} (mgF)	err (%)
0.30	108	134	23.7	99	8.7	306	127	58.4	303	0.9	310	1.4
0.32	122	151	23.4	110	9.7	320	185	42.2	326	1.8	318	0.8
0.34	134	165	23.4	121	9.6	338	223	34.0	335	0.8	323	4.5
0.35	167	207	23.7	153	8.6	409	224	45.2	386	5.6	350	14.5
0.36	174	215	23.8	159	8.4	431	228	47.1	407	5.7	403	6.5
0.38	178	220	23.6	162	8.9	433	264	38.9	424	2.0	409	5.5
0.40	185	228	23.5	167	9.5	436	304	30.3	429	1.7	437	0.1
0.42	217	268	23.3	195	10.2	480	377	21.4	454	5.5	465	3.2
0.44	223	274	22.8	198	11.0	506	414	18.2	455	10.2	466	8.1
0.44	221	274	23.9	201	9.2	507	424	16.4	484	4.5	479	5.5
0.46	243	298	22.9	214	11.7	546	434	20.5	546	0.0	586	7.4
0.48	247	304	23.0	219	11.3	595	477	19.8	577	3.1	588	1.1
0.50	254	313	22.8	224	11.9	622	618	0.6	583	6.2	595	4.4
$\frac{1}{n}\sum$	–	–	23	–	10	–	–	30	–	4	–	5

Table 4.8: 45° **Mean Improved Quasi-Steady Forces and % Error**

A	Lift (mgF)	L_{b+rot} (mgF)	err (%)	L_{tr+rot} (mgF)	err (%)	F_x (mgF)	L_{BEM} (mgF)	err (%)	N_{b+rot} (mgF)	err (%)	N_{tr+rot} (mgF)	err (%)
0.30	142	176	24.5	134	5.6	312	157	49.8	272	12.8	306	2.1
0.32	166	207	24.8	158	4.4	346	182	47.3	303	12.4	337	2.5
0.34	180	223	24.2	168	6.7	380	188	50.4	313	17.8	342	10.2
0.36	195	242	23.9	180	7.9	414	194	53.1	324	21.7	350	15.6
0.38	220	273	23.8	202	8.4	448	246	45.2	358	20.1	380	15.2
0.40	246	303	23.5	223	9.3	482	300	37.8	400	17.1	420	12.9
0.42	277	341	23.0	246	11.1	516	351	32.1	457	11.4	472	8.6
0.44	303	372	22.8	266	12.2	550	407	26.1	502	8.7	514	6.6
0.46	337	414	22.7	295	12.4	584	511	12.5	469	19.7	513	12.2
0.48	361	442	22.6	314	12.9	618	580	6.1	510	17.6	551	10.9
0.50	387	474	22.6	337	12.8	652	610	6.5	557	14.6	598	8.3
0.52	408	504	23.3	367	10.2	686	688	0.3	597	13.1	650	5.3
0.54	436	539	23.5	395	9.4	720	750	4.1	650	9.8	707	1.8
0.56	455	564	24.0	421	7.5	762	768	0.8	693	9.1	763	0.1
0.58	475	590	24.2	444	6.6	777	796	2.4	765	1.6	790	1.6
0.60	524	661	26.3	531	1.5	837	806	3.6	794	5.1	820	2.0
$\frac{1}{n}\sum$	–	–	24	–	9	–	–	24	–	13	–	7

Table 4.9: 60° **Mean Improved Quasi-Steady Forces and % Error**

A	Lift (mgF)	L_{b+rot} (mgF)	err (%)	L_{tr+rot} (mgF)	err (%)	F_x (mgF)	L_{BEM} (mgF)	err (%)	N_{b+rot} (mgF)	err (%)	N_{tr+rot} (mgF)	err (%)
0.30	252	315	24.9	242	3.8	446	164	63.3	357	20.1	376	15.8
0.32	287	358	24.7	274	4.7	508	202	60.2	430	15.4	453	10.8
0.34	318	396	24.2	298	6.5	532	265	50.2	475	10.7	488	8.1
0.35	324	402	24.1	301	7.0	547	285	47.9	505	7.6	533	2.6
0.36	349	433	23.9	322	7.7	580	327	43.6	532	8.3	550	5.2
0.37	367	457	24.5	347	5.4	583	355	39.1	552	5.5	573	1.8
0.38	365	457	25.5	358	1.8	594	406	31.6	562	5.4	586	1.3
0.39	390	483	23.9	359	7.9	638	419	34.4	579	9.3	600	5.9
0.40	404	503	24.8	385	4.5	652	424	34.9	602	7.6	621	4.7
0.41	414	524	26.7	426	2.9	653	515	21.2	637	2.4	646	1.0
0.42	427	546	27.7	457	6.9	673	568	15.6	647	3.9	670	0.4
0.44	436	557	27.7	467	7.0	682	600	11.9	650	4.6	685	0.5
0.45	438	565	29.0	489	11.7	699	610	12.7	660	5.6	709	1.4
0.46	434	565	30.3	506	16.7	703	659	6.2	661	6.0	717	2.1
0.48	529	667	26.1	532	0.5	776	810	4.4	757	2.4	811	4.5
0.50	589	727	23.4	532	9.6	835	806	3.4	764	8.6	827	1.0
$\frac{1}{n}\sum$	–	–	26	–	7	–	–	30	–	8	–	4

The improved quasi-steady method using the sum of the translation and rotation forces most closely match the measured forces. As a companion to the graphical display of the empirical models presented in Figure 4.10, Equation 4.23 gives the form of the numerical model for C_L, C_D, and C_S as a function of α for the 30°, 45°, 60° angle stop wings.

$$C_{F_i} = A\alpha^3 + B\alpha^2 + C\alpha + D \quad \forall \quad \{\overline{\alpha}_{min} \leq \alpha_i \leq \overline{\alpha}_{max}\} \tag{4.23}$$

Table 4.10 gives the empirically determined A, B, C, D coefficients for C_L, C_D, and C_S for the 30°, 45°, 60° angle stop wings.

Table 4.10: Empirically Deteremined Polynominal Coefficients for C_L, C_D, and C_S

coeff	A	B	C	D
30° wing				
$C_{L,\alpha}$	9.957E-5	-0.0132	0.4557	-1.34E-6
$C_{D,\alpha}$	0.00019	-0.02367	0.7689	1.4E-6
$C_{S,\alpha}$	0.00077	-0.09686	3.042	3.48E-6
$C_{S,\phi}$	1.421E-6	0.000124	-0.0145	6.857E-5
45° wing				
$C_{L,\alpha}$	-0.0002795	0.04462	-2.383	44.35
$C_{D,\alpha}$	3.288E-5	-0.004797	0.1882	-0.03604
$C_{S,\alpha}$	-0.001412	0.2277	-12.27	221.6
$C_{S,\phi}$	2.303E-5	-0.006621	0.6409	-20.3
60° wing				
$C_{L,\alpha}$	9.87E-5	-0.01407	0.5918	-5.147
$C_{D,\alpha}$	- 1.006E-5	-0.005527	-0.5243	14.61
$C_{S,\alpha}$	4.771E-5	-0.003562	-0.03612	4.85
$C_{S,\phi}$	1.663E-6	-0.0003236	0.02308	-0.5935

While there is a clearly identified correlation between the change in α and the subsequent change in the lift and drag forces, and their corresponding dimensionless coefficients, the relationship between the change in side force and α is less clearly delineated. Therefore, a relationship between the side force and the total stroke angle at a specific amplitude was also developed, which provides an additional empirical model to estimate side force. A combined multi-variate α and ϕ relationship vs. C_S seems a plausible compromise; however, the change in α is directly correlated to the increase in Φ. As the driving amplitude increases, the total stroke angle, Φ linearly increases, imparting greater acceleration and deceleration forces on the wing at rotation, which increases the angular rate, resulting in greater total angular travel, and hence a lower angle of attack as measured from the horizontal. Figure 4.13 shows the 30°, 45°, 60° angle stop C_L and C_D data on single plots with a single unifying empirical polynomial curve fit to the combined data.
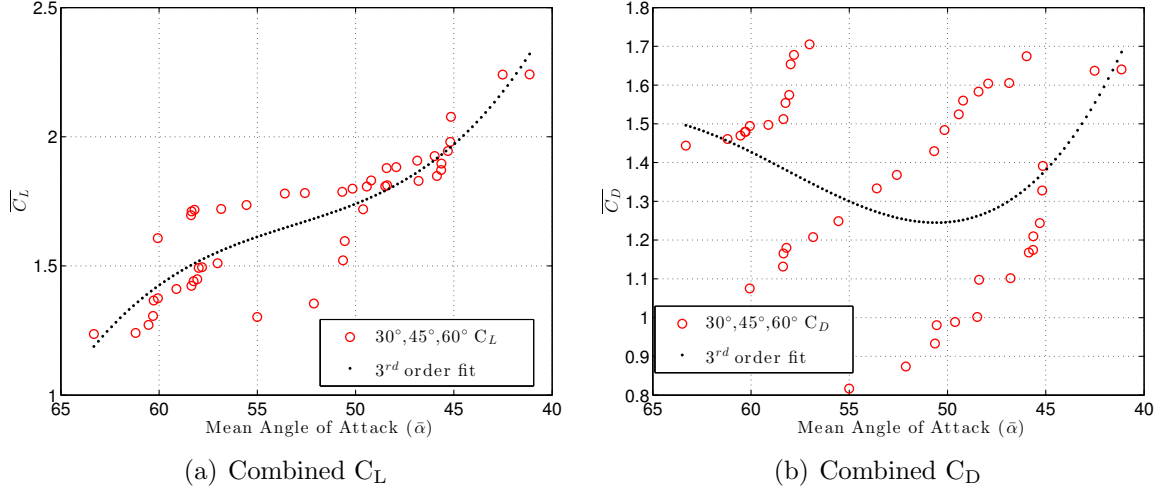
Figure 4.13: $30°$, $45°$, and $60°$ angle stop wings C_L and C_D coefficients combined on single plots with a single empirical 3rd order polynominal curve fit to each data set.

The empirically derived combined lift coefficient curve is instructive and suitable to apply to a wide region of angle stop combinations in future control law algorithm development. The combined drag coefficient curve is obviously not appropriate to apply across the design options of angle stop possibilities, and cannot be applied ubiquitously to any arbitrary angle stop, and must therefore be individually experimentally derived for each angle stop utilized in subsequent design models. The 3rd order polynomial fit to the combined $30°$, $45°$, and $60°$ lift coefficient curve fit is given below in Equation 4.24.

$$C_{L,\alpha} = -0.0002164\alpha^3 + 0.03452\alpha^2 - 1.859\alpha + 35.44 \quad \forall \quad \{65° \geq \alpha_i \geq 40°\} \quad (4.24)$$

4.6   Moments

Moment data in the x, y, z wind axis directions was also collected with the Nano-17 force/torque transducer. Using the balance coordinate axis system shown in Figure 3.14, the roll moment (M_z) is about the z-axis, the pitch moment (M_y) is about

178

the y-axis, and the yaw moment (M_x) is about the x-axis. This naming convention departs from standard aerodynamic moment treatments, where the roll, pitch, and yaw moments are designated l, m, and n respectively, and are taken about the x, y, z-axis, because the orientation of the Nano-17 places the x-axis vertically, and the z-axis horizontally in the test chamber, which is opposite from standard wind tunnel balance specific coordinate systems. The moments registered on the force balance were transferred to a common reference point on the flapper mounting structure where the linkage is attacked to the flapper body, shown in Figure 2.22, and was computed using Equations 3.10-3.11. The vector distance from the balance center to the pivot point is $r_{b-p} = [0, -10, 62.25]$mm, and was measured with digital calipers along each axis. Figure 4.14 shows M_x, M_y, and M_z on the same chart for the 30°, 45°, and 60° angle stop wings respectively.

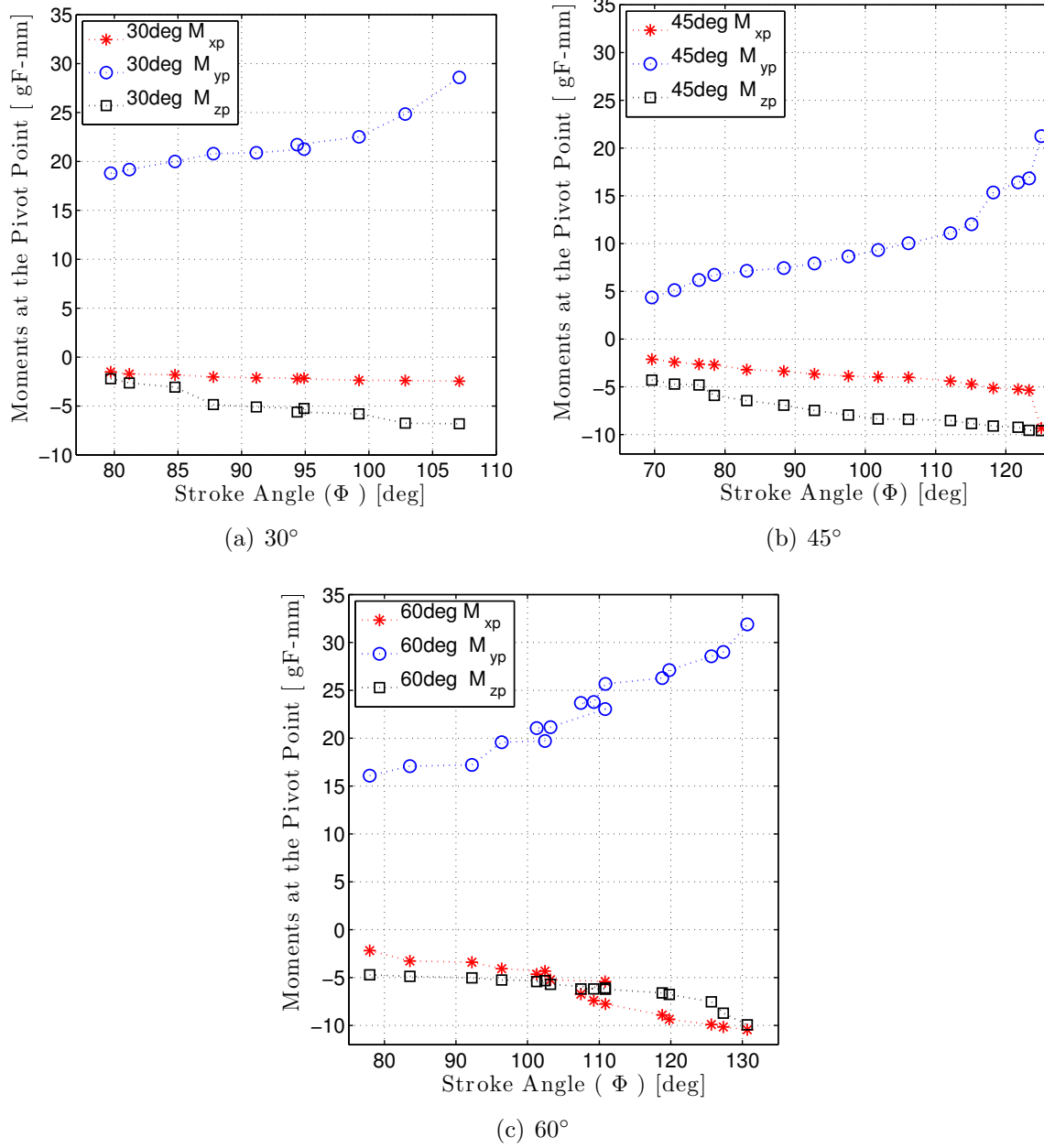(a) 30°

(b) 45°

(c) 60°

Figure 4.14: 30°, 45°, and 60° angle stop cycle average 3-axis moments vs. stroke angle, Φ. Moments are transferred from the balance center to the pivot point, located −10mm in the y-direction, and 62.25mm in the z-direction.

Figure 4.15 compares M_x, M_y, and M_z for the 30°, 45°, and 60° angle stop wings on three separate charts.
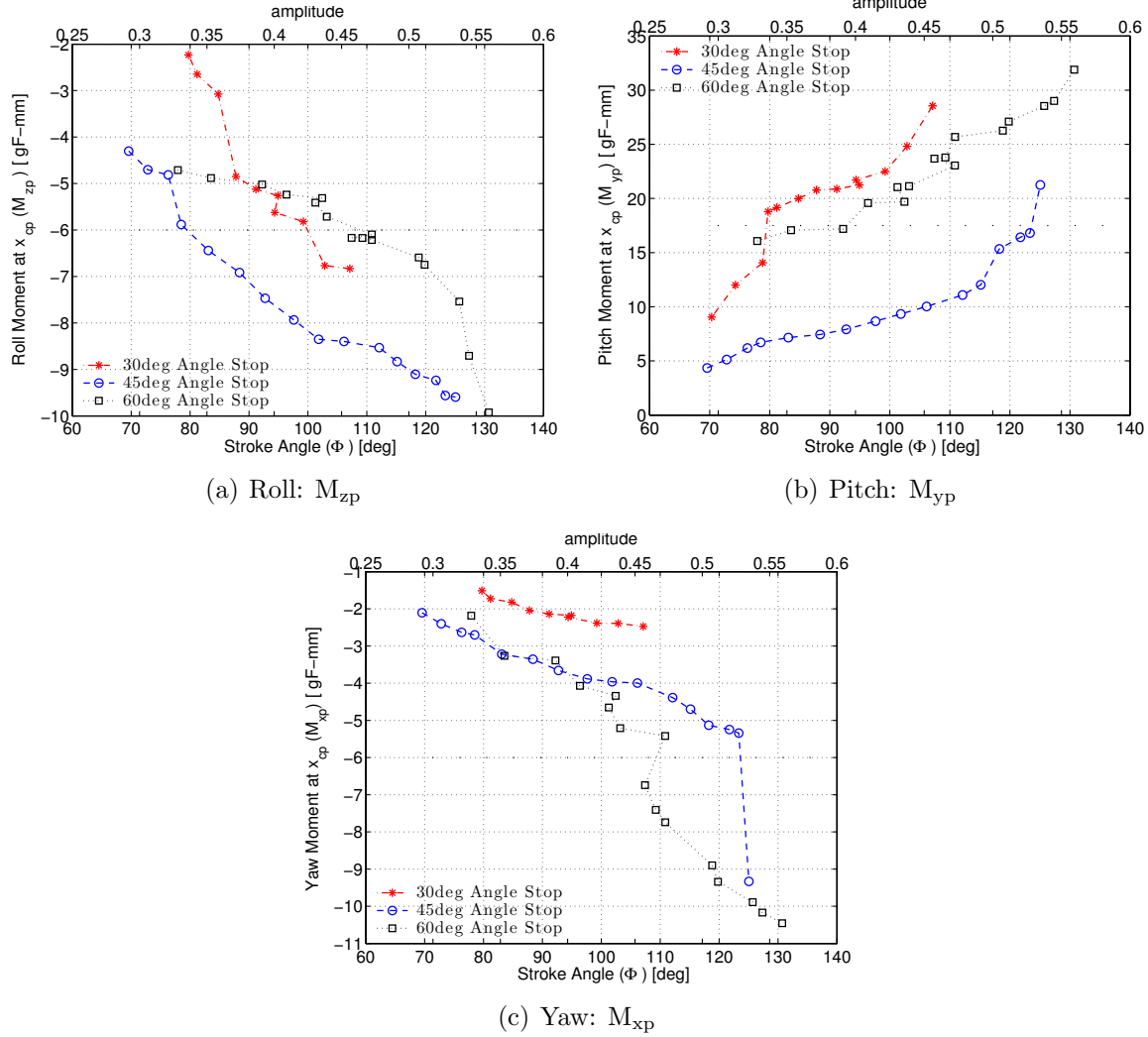
(a) Roll: M_{zp}

(b) Pitch: M_{yp}

(c) Yaw: M_{xp}

Figure 4.15: Comparison of the M_x, M_y, and M_z for all three angle stops. Moments are transferred from the balance center to the pivot point, located -10mm in the y-direction, and 62.25mm in the z-direction.

The results shown in Figures 4.14-4.15 confirm the transducer is capable of providing useful moment data, and shows expected aerodynamic torque trends about the MAC. Pitch moment about the wing's center of pressure increases as flap angle, and hence, vertical force increases. The roll and yaw moments are small, and slightly decrease in the negative direction as axial and vertical force increases with the increasing amplitude. DeLuca *et.al.* conducted research on the original flapper and hawkmoth wing design at a lower range of amplitudes, A=0.05 to A=0.35, for both trimmed and

untrimmed flapping, and the moment results followed the same general trends shown in Figures 4.14-4.15, although their magnitudes are less because their corresponding forces and stroke angles were correspondingly smaller [21].

4.7   Center of Pressure

Figure 4.16 shows the center of pressure (x_{cp}) location, $(in\ mm)$, as a function of drive signal amplitude, where the location of the x_{cp} is calculated by dividing the pitching moment at the pivot point (M_{yp}), by the vertical force, F_x. As expected, although there is some oscillation, especially at the lowest amplitude settings, where the forces and moments are smallest, and register near the balance's lower threshold, the center of pressure is nearly constant, within a few millimeters, as amplitude increases.
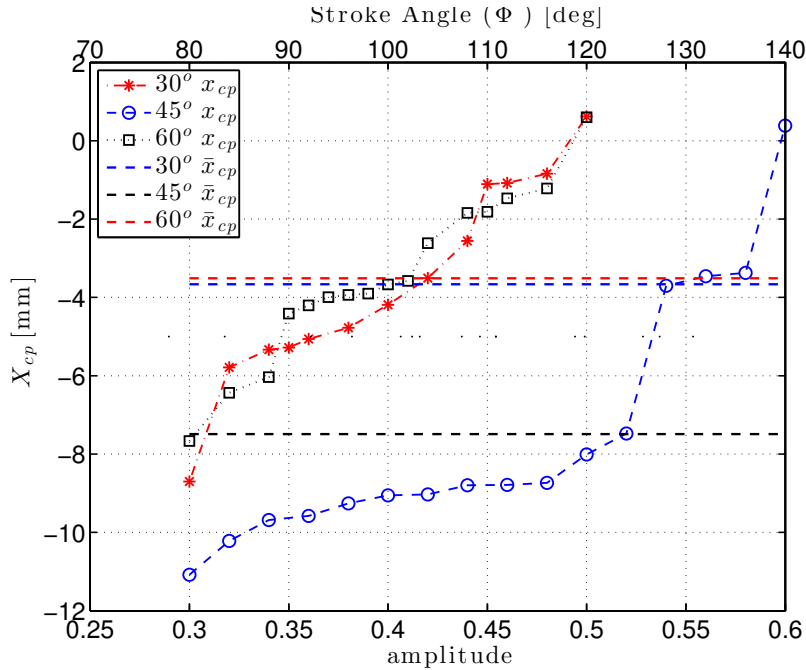
Figure 4.16: **30°, 45°, and 60° center of pressure location at the pivot point, x_{cp}, where $x_{cp} = {}^{M_{yp}}/_{F_x}$, as a function of drive amplitude and flap angle, Φ.**

The location of the mean center of pressure $(\overline{x_{cp}})$ for the 30°, 45°, and 60° wings are ≈ -3.7mm, -7mm, and -3.5mm respectively, which agrees well with the expected

location. The pivot point is ≈ -2mm behind the vertical force locus (toward the balance), and the result of $^{F_x}/_{M_{yp}}$ should be located a constant distance of -2mm behind the pivot point, but it is slightly aft of that (toward the balance) due to the influence of the data at the lower amplitude settings, which recorded forces near the lower bound of the balance threshold. The 45° data showed the most variability in the pitch moment and movement of x_{cp} as a function of increasing stroke angle. This is most likely due to the erratic wing behavior in the nonlinear regions of the operating envelope, where the wing and flapper were tested beyond their design parameters.

Previous testing on the original flapper and wing design investigated the change in the location of $\overline{x_{cp}}$ for both trimmed and untrimmed flapping [21, 23]. Symmetric wing flapping is defined as a trimmed flapping condition where the up and down-stroke angles are equivalent ($\phi_{min} = \phi_{max}$) measured from the zero motion point, perpendicular to the wing mount. An asymmetric wing flap angle is defined as an untrimmed flapping condition, characterized by an unequal up and downstroke angle, measured from rest, irrespective of the actual total flap angle achieved, Φ. Figure 4.17 illustrates the qualitative difference at a specific driving voltage.
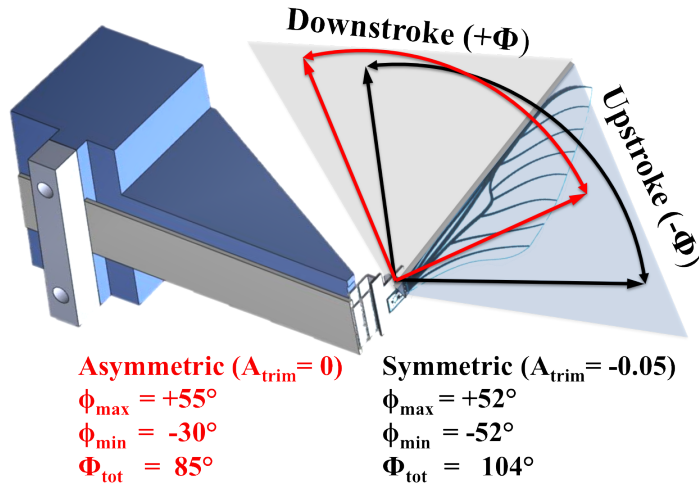
Figure 4.17: Example of trimmed (*symmetric*) and untrimmed (*asymmetric*) wing flap angles. The symmetric, trimmed wing angle is shown in black, and has a nearly equivalent up and downstroke angle, while the asymmetric, untrimmed wing flap angle is shown in red, which is predominated by the downstroke half of the flap cycle [21].

Although not conclusive, the mean values of $\overline{x_{cp}}$ shows the movement of the asymmetric center of pressure slightly in the direction of the asymmetry in the flap motion, which decreases the overall moment lever length, reducing the distance along the $z-$axis between the balance center and the locus of force. The mean location of $\overline{x_{cp}}$ is ≈ -19mm for the asymmetric tests, which is a shift in the center of pressure location of ≈ -14mm closer to the balance, shown together in Figure 4.18 below [21].
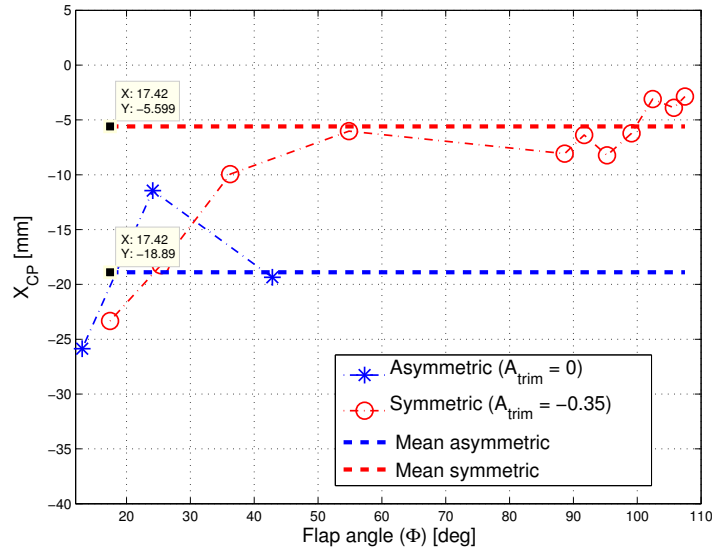
Figure 4.18: Trimmed (*symmetric*) and untrimmed (*asymmetric*) locations of center of pressure— from[21].

The goal of changing the wing flap symmetry through, the bias parameter, η, is to move the location of the x-direction center of pressure, x_{cp}, to motivate a change in control moment. A quantitative understanding of the differences between the aerodynamic forces and moments developed during symmetric and asymmetric flapping is crucial for design of control algorithms for future full-scale vehicle designs. It is necessary that asymmetric flapping produce a comparable, but not necessarily equal amount of vertical force as symmetric flapping, because in a full flight vehicle, control about the pitch axis is exclusively achieved through modulation of the stroke angle between two wings. Pitch control is achieved by precisely controlling the asymmetry in the wing's flap stroke; a larger downstroke angle during the flap cycle produces a nose down pitch, while a larger upstroke angle during the flap cycle yields a nose up pitch attitude. Roll is achieved by flapping one wing symmetrically at a higher amplitude, and the other wing flapping symmetrically at a lower amplitude.

185

4.8 Actuator Power

This section calculates the average power ($\bar{P}$) consumed by the PZT actuator as a function of drive amplitude, A, and stroke angle Φ. In addition, measurements of the the powered required per unit force are compared to the estimated or predicted necessary power. The consumed power is then nondimensionalized into the coefficient forms most recognizable in rotorcraft mechanics and flapping flight.

4.8.1 Cycle Average Power.

Because the drive signal is a time varying complex waveform, the standard electrical resistive relations, $V = IR$ and $P = I^2R = IV$, cannot be used to calculate the average PZT consumed power. Therefore, the most suitable relationship to compute PZT mean power consumption used in this research was one developed by NASA for PZT based structural health monitoring applications, and is given in Equation 4.25 below [46]

$$\bar{P} = \frac{1}{T} \sum_{t-T}^{t} V_{rms}(\omega, t) I_{rms}(\omega, t) \cos \vartheta_t \Delta t \tag{4.25}$$

where the root mean square voltage (V_{rms}) and the root mean square current (I_{rms}) are the root-mean-square of the drive voltage and current sampled off the amplifier before being sent to the PZT, and ϑ is the phase angle (ϑ_t) difference between the drive voltage and current. The voltage and current are recorded as inputs by the data acquisition box. The general form of the Alternating Current (AC) drive signal is :

$$y = a_p \cdot \sin(2\pi ft + \varphi) \tag{4.26}$$

where a_p is the signal peak amplitude (a_p), t is the time step (t), φ is the signal wave phase shift (φ) in $rads$, and f is the wave frequency (f), which is equal to the flap

cycle frequency (ω_f), in $[\text{rad}/\text{s}]$, divided by $2\pi \rightarrow f = \frac{\omega}{2\pi}$. Generally, rms values of a sample signal are computed by taking the root of the mean value, $\bar{x}$, squared, shown in Equation 4.27.

$$x_{rms} = \sqrt{\frac{1}{n} \sum_n \bar{x}^2(t)} \tag{4.27}$$

Where $\bar{x}$ is calculated per Equation 4.2 above. Since the AC current and voltage signals are time varying periodic signals, the average power can be calculated similarly to that of a constant source:

$$\bar{P} = \left\langle I\left(t\right)^2 R \right\rangle \tag{4.28}$$

where $\langle\rangle$ is the mean of a time varying function, and by definition of rms, $\left\langle I\left(t\right)^2 \right\rangle = (I_{rms})^2$. Since the resistance is time invariant, it can be factored out of the mean calculation, and substituting the relation $R = \frac{V}{I}$ for resistance, leaves the equation for $\bar{P}$:

$$\bar{P} = I_{rms} V_{rms} \tag{4.29}$$

Now substituting the general form of the AC signal, (using current, $I(t)$ as an example) into Equation 4.27, yields:

$$I_{rms} = \sqrt{\frac{1}{T_2 - T_1} \int_{T_1}^{T_2} (I_p \sin(\omega t))^2 \, dt} \tag{4.30}$$

Where I_p is the constant peak current value, T is the period of the wave form, and ω is the angular frequency defined as $\omega = 2\pi f = \frac{2\pi}{T}$. Factoring out I_p, and applying the trigonometric identity, $\sin^2(\omega t) = 1 - \cos^2(\omega t)$, will reduce the unpleasantness of integrating $\sin^2(\omega t)$, reducing Equation 4.30 to:

$$I_{rms} = I_p \sqrt{\frac{1}{T_2 - T_1} \int_{T_1}^{T_2} \frac{1 - \cos(2\omega t)}{2} \, dt} \qquad (4.31)$$

Equation 4.31 easily integrates to the form shown below in Equation 4.32:

$$I_{rms} = I_p \sqrt{\frac{1}{T_2 - T_1} \left[\frac{t}{2}\right]_{T_1}^{T_2}} = I_p \sqrt{\frac{1}{T_2 - T_1} \frac{T_2 - T_1}{2}} = \frac{I_p}{\sqrt{2}} \qquad (4.32)$$

The same analysis sequence used above, is applied to calculating V_{rms}, $V_{rms} = \frac{V_p}{\sqrt{2}}$. The peak values, I_p and V_p, are found by subsampling the raw current and voltage data, with the same algorithm used to subsample the force and moment data above, and then applying the same signal processing techniques detailed in section 3.2.2 of windowing, zero padding the data set to the closest power of 2, taking the FFT of the subsampled data set, and then removing data above one-half of the sampling frequency to prevent aliasing. The peak values are then the *maximum* value of the resulting subsampled frequency domain voltage and current data set. The phase angle, ϑ_t, for the current and voltage is calculated for the entire data set by breaking the signals into their complex components, $x + yi$, then $\vartheta_t = \tan^{-1}(\frac{y}{x})$, and the phase difference is calculated by taking the difference between their respective angles at each position in time, Δt.

Jordan *et. al.* stipulated a method to predict or model the amount of power required by an actuator based on an RC series circuit used to model piezoelectric wafers given in Equation 4.33 below

$$\bar{P} = 2\pi C f \tan(\delta) V_{rms}^2 \qquad (4.33)$$

where f is the operating frequency of the piezo, $\tan \delta \approx 0.3$, and is the loss tangent $(\tan(\delta))$, which was approximated from Figure 5 in [46], using $f = 25$Hz at $V_{peak} = 150$V. The Capacitance (C) of the piezo material was estimated to be equal to 0.01F

from Figure 2 in [46], using $f = 25\text{Hz}$ at $V_{\text{peak}} = 150\text{V}$. Finally, the V_{rms} was calculated from the actual amplifier data using Equation 4.32 above. Figure 4.19 shows the predicted power computed from Equation 4.33 at every amplitude compared to the measured cycle average power consumed, $\bar{P}$, for the 30°, 45°, and 60° angle stop wings as functions of both stroke angle and vertical force produced. Figure 4.20 shows all the wing angle stops plotted as force developed per unit power in $[^{\text{mgF}}/_{\text{mW}}]$ against flap angle. The jump in the 45° and 60° mean power vs. vertical force plot near the maximum force is most likely due to the wing exceeding its design stroke angle, exceeding the linear limits of the linkage design, resulting in heaving and binding at the stroke ends, overcoming these aeroelastic effects required substantially more power than when the wings operate within their linear bounds.
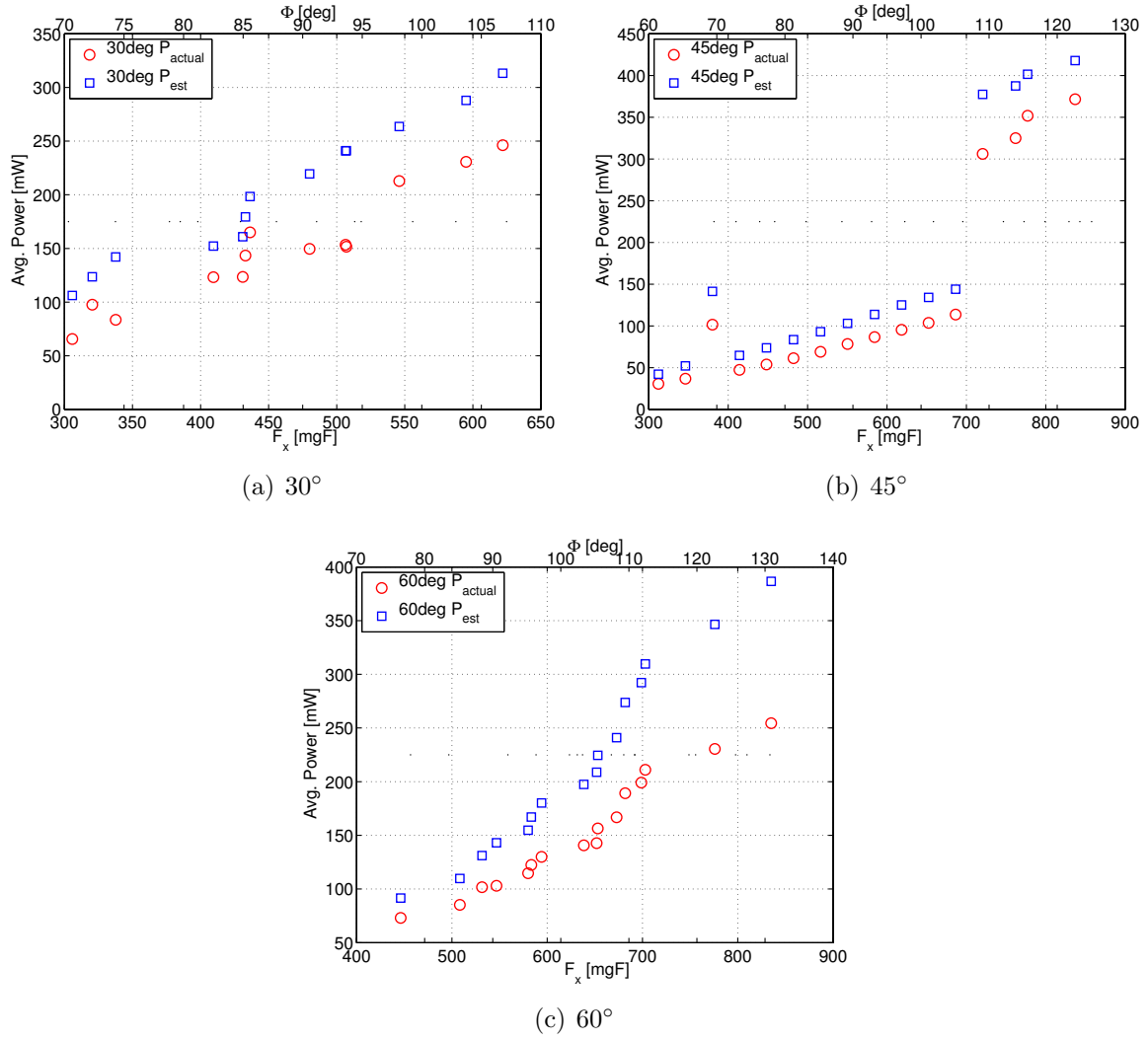
Figure 4.19: Cycle averaged actuator power plotted against the force developed during flapping at various driving amplitudes for 30°, 45°, and 60° angle stop wings. For reference the stroke angle in degrees required to produce the forces shown on the x-axis are shown as a secondary x-axis across the top of each plot.
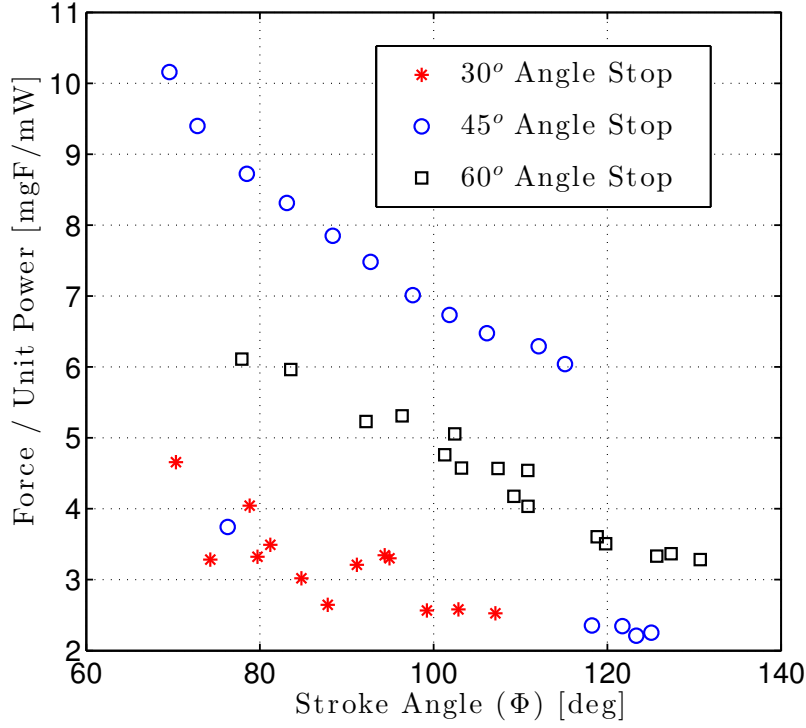
Figure 4.20: **Force per unit power required plotted against flap angle**

The results shown in Figure 4.20 are reasonable and follow expected trends that as drive amplitude increases, power consumption increases monotonically with force. The estimated power (P_{est}) was less than the actual power (P_{actual}) for all wing and test condition combinations. The average error between P_{est} and P_{actual} for the 30°, 45°, and 60° angle stop wings was $26.5\%, 12.3\%,$ and 28.5% respectively, and a good estimate for predicting the actual amount of power required to achieve a specific flap angle is add 23% to the value of P_{est}. This result combined with the error between Φ_{est} and $\Phi_{actual}, \approx 28\%$, gives designers considerable margin in matching wing performance and the appropriate corresponding power supply.

From Figure 4.19 the slope of the P_{actual} curve indicates the rate in the rise of power consumed directly effects an increase in drive amplitude, which is essentially the cost of producing more lift. The 60° angle stop wing has the lowest slope at 3.5, while the 45° angle stop wing has the largest slope at 6.1, and 30° angle stop wing has

a slope of 4.5. Therefore, the 60° angle stop wing subtends the largest stroke angle, and generates the largest vertical force for the amount of power drawn. The 45° angle stop wing showed a large increase in $\bar{P}$ after A=0.52 & $\Phi = 115°$, because the wing was operating beyond its design limits of $\Phi = 110°$, and was showing nonlinear responses in the linkage. The 60° angle stop wing reached its operating at its design limit after A=0.44 & $\Phi = 118°$, but a lower amplitude than the 45° angle stop wing. Because the 60° angle stop wing was allowed to rotate more at the rotation joint than the 45° wing, it exhibited less nonlinear behavior and required less power above the design limit. From Figure 4.20 it is evident all the angle stops become less efficient in terms of force developed per unit power as the amplitude is increased, and the flap angle increases. This is primarily due to the inertia developed in the wings and the amount of force necessary to overcome the added mass of air surrounding the wings. As the driving force increases, and the flap angle increases, the percentage of the inertial load compared to the aerodynamic force decreases, requiring more power to drive the wings to overcome induced wing drag.

Hollenbeck conducted extensive evaluation of the thoracic flight muscle system of the hawkmoth, *Manduca Sexta*. His experiments focused on the *tergum* Dorsoventral Muscles (DVM), and the *phragma* Dorsolongitudinal Muscles (DLM), which are the hawkmoth's primary flight actuation muscles. His experimental investigation assessed the static and dynamic loading on several fresh, and experimentally controlled desiccated specimens. He calculated the average power required to manually elevate the hawkmoth's wing in a flight attitude by integrating the load cell force necessary to move the tergum plate to actuate the DVM muscles from rest to a representative flight stroke angle, divided by the total time [42].

$$\bar{P} = \frac{\int_{x_1}^{x_2} F(x)dx}{\Delta t} \tag{4.34}$$

192

His results concluded the average power, $\bar{P}$, required to dynamically flap the wings, in a pseudo "natural" flapping motion, by applying a force to the flight musculature systems with a mechanical load cell, averaged over eight specimens, was ≈ 90mW [43]. The required power to drive the AFIT lab flapper in these preliminary experiments is in the same order of magnitude with Hollenbeck's DVM average power calculation. The average power required to drive the PZT actuator in trimmed flapping, at resonance, for the 30°, 45°, and 60° angle stop wings was 150mw, 140mW, and 151mW respectively.

4.8.2 Nondimensional Power Coefficients.

Another method used to compare rotorcraft mechanics and flapping wings across dissimilar wing and vehicle platforms is to use dimensionless representations of the power and force combination. These parameters are the Thrust Coefficient (C_T), Power Coefficient (C_P), and the Figure of Merit (FM). For rotorcraft applications, the FM is defined as the ratio of the ideal power of a rotor blade in hover to the actual power consumed in hover. Although originally developed to compare the relative performance of rotorcraft, the techniques are adapted here to fit into a flapping wing model for performance. The thrust coefficient is given by Equation 4.35

$$C_T = \frac{T_v}{\rho \omega^2 R^4} \tag{4.35}$$

where T_v is the vertical thrust measured in [N], taken here as the vertical component of the Nano-17 balance, F_x, and the remainder of the variables have been previously defined elsewhere in the text. The power coefficient is given by Equation 4.36

$$C_P = \frac{P_m}{\rho \omega^3 R^5} \tag{4.36}$$

where P_m is the power consumed by the motor, measured in [W], taken here as the average power, $\bar{P}$ consumed by the piezo during flapping. The Figure of Merit is the ratio of C_T and C_P given by Equation 4.37 [81].

$$\text{FM} = \frac{C_T^{3/2}}{\sqrt{2}\,C_P} \tag{4.37}$$

The expected trend is to see data points lie along the same line at fixed values of R, ρ, and ω, for a given amount of T_v. The flapping frequency, ω, is varying between the three different angle stop wings, which resulted in the separation in the linear data spread. Figure 4.21 shows C_T, C_P, and FM for the 30°, 45°, and 60° angle stop wings.

(a) Thrust Coefficient

(b) Power Coefficient
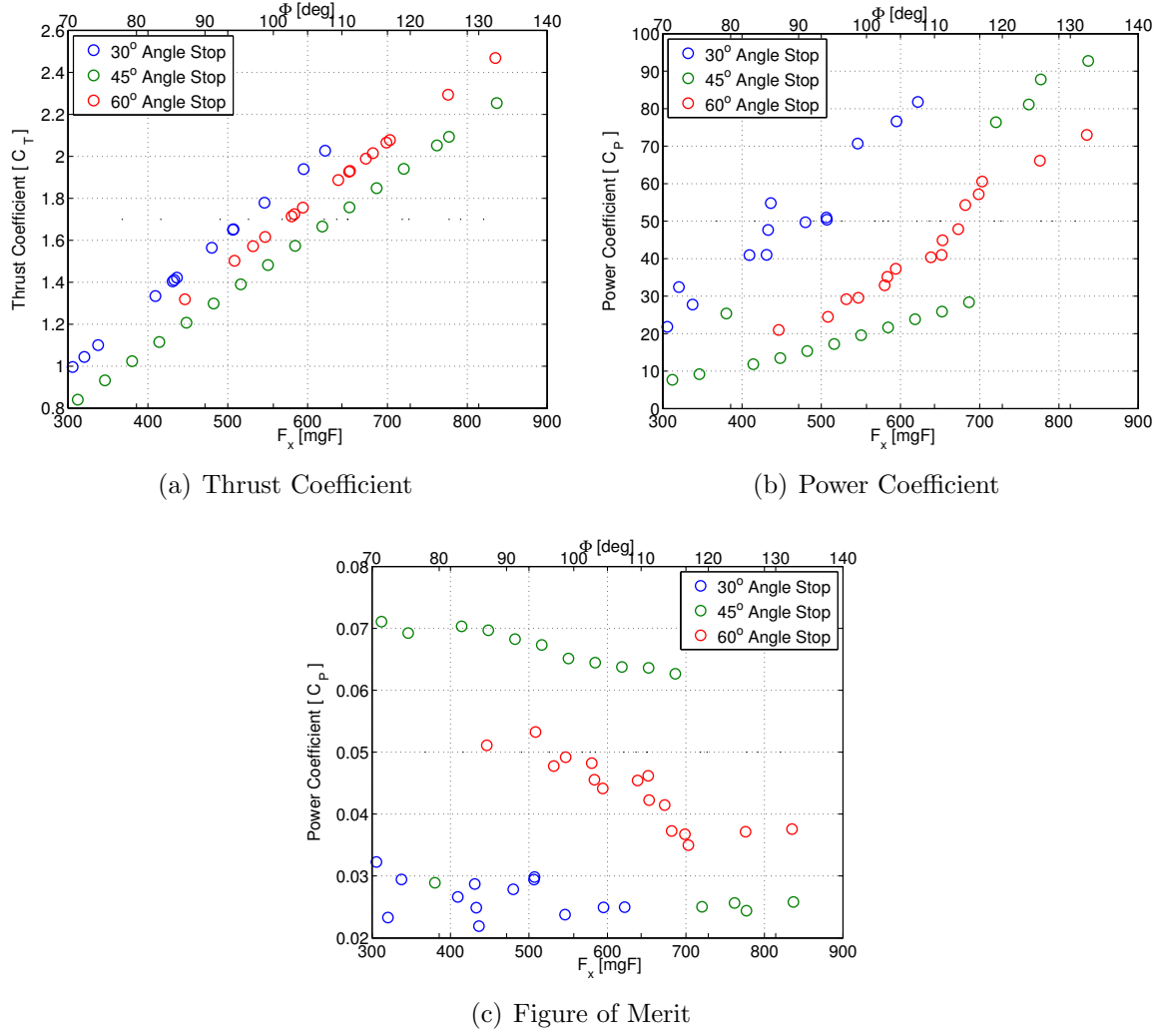
(c) Figure of Merit

Figure 4.21: Figure of Merit, Power, and Thrust Coefficients plotted against vertical force for 30°, 45°, and 60° angle stop wings. For reference the stroke angle in degrees required to produce the forces shown on the x-axis are shown as a secondary x-axis across the top of each plot.

At higher amplitudes, $A > 0.52$, the 45° angle stop wing exhibited non-linearities in the linkage and passive rotation joints, resulting in exponential increases in power consumption compared to only modest gains in force production, which is the culprit responsible for the discontinuity demonstrated in the coefficients plotted in Figure 4.21.

4.8.2.1 Comparison to AFIT's Previous Mechanical Flapper.

Svanberg and Curtis *et.al.* conducted similar testing with rectangular wings $5\times$ larger than *Manduca Sexta* comprised of mylar, aluminum, and carbon fiber, mounted on a mechanical gear driven flapper, utilizing prescribed wing kinematics (stroke angle and angle of attack), with a wing beat frequency of $\omega = 10 - 15\text{Hz}$ [13, 82]. Comparing that flapper and wing combination to the current piezo actuated flapper and passive rotation linkage together with the hawkmoth wing, C_T is $2\times$ orders of magnitude lower than the PZT actuated hawkmoth flapper, C_P is $1.5\times$ orders of magnitude smaller than the PZT actuated hawkmoth flapper, and the FM is $1\times$ order of magnitude smaller than the PZT actuated hawkmoth flapper [13, 82]. These results show the biomimetically designed hawkmoth wing and passive rotation linkage design is considerably more efficient in maximizing force production, and minimizing power consumption than the larger, bulkier, slower, mechanical gear driven flapper. The mean hawkmoth flapper FM is ≈ 0.05, while the FM for most standard rotorcraft is between 0.4 and 0.7 [81]. A rotor and blade combination optimized for hover will have a higher FM, and a wing rotor combination optimized for fast forward flight will have a lower FM. Insects and FWMAV's do not have rotors, and do not spend a lot of time in purely stationary motion like helicopters; therefore, it follows their FM is lower than the FM for rotorcraft.

V. PIV Results

5.1 Overview

P IV measurements were taken on the 30°, 45°, and 60° angle stop wings mounted horizontally in the test chamber, replicating the test configuration used in the force balance tests, and also mounted vertically with the wing span axis oriented along the balance x-axis. Three component velocity vector and contour plots are presented for a wide-range of test conditions and wing phases during the stroke cycle. In-plane velocity components are presented as traditional vector quivers, and the third component, out-of-plane and transverse to the laser sheet, is presented as a velocity contour map. 2-D v-velocity line plots taken at n-chords above and below the wing are derived from the velocity data, and presented to illustrate the vertical thrust developed during hover. 2-D u-velocity line plots are shown at several distances in front and behind the wing, and show the phases where the developed force is not restricted to vertical motion, but rather also contributes to horizontal forces, axially developed along the z-axis. Lastly, a *Rankine-Froude* axial disk actuator model, originally developed to estimate thrust from the transfer of momentum through a rotating propeller disk, was adapted to flapping wing flight to estimate the amount of vertical force developed, and was used to corroborate force balance results presented in *Chapter IV*.

5.2 Test Point Matrix

PIV testing was conducted on 30°, 45°, and 60° angle stop wings mounted vertically and horizontally in the test chamber. The horizontally mounted wings were tested with the laser sheet bisecting the wing at the mid-span, $0.5R$, at a single amplitude on all three wings. In addition to the mid-span location, the laser sheet

was moved across several span locations at $0.25R$, $0.75R$, and $1.0R$ on the 45° wing. Three different drive amplitudes were also tested on the 45° wing at the mid-span. PIV measurements were recorded for the same eight phases of the flap cycle at each test condition and laser location. The eight phases represent different times, and therefore wing locations in the stroke cycle. Phases 1-2 capture the wing from the mid downstroke to the end of the downstroke. Phase 3 is the start of the rotation to supination. Phase 4 is about midway through the upstroke. Phase 5 is the end of the upstroke, just at the onset of rotation to pronation. Phase 6 is just after pronation at the beginning of the next downstroke phase. Phase 7 is about 25% into the downstroke, and finally phase 8 completes the flap cycle at the mid downstroke. Figure 5.2 illustrates the wing position as acquired from the backscatter camera, camera 1, with the process $u - v$ velocity vector map overlaid during each phase of an example test condition. The bright reflection of the laser sheet off the mylar wing surface can be used to indicate wing position along the flap cycle, and its relative position in the test chamber.

The vertically mounted wings were tested with the laser sheet at approximately one half chord in front of the wing at a single amplitude. In this configuration at rest, the wing is oriented with the tip pointing skyward, and the root positioned at the bottom of the image plane, refer to Figure 5.1. In addition to a half chord in front of the wing, measurements on the 45° wing were taken with the laser sheet at one-and-a-half chords in front of the wing. The vertically mounted wing offers the advantage of having the entire *downward* pumping velocity component responsible for lift generation pass through the last sheet, which enables a complete estimate of the thrust produced during that phase. The horizontally mounted wings only provide detail on the vertical velocity component through a single slice at a single span location along the wing, which requires several assumptions and approximations

to estimate the net total vertical thrust produced at a specific phase. A subset of the force balance tests, representing the most stable forces and stroke angles correspond to PIV testing. Eight phases, with 50 image pairs collected per phase, at various amplitudes and laser sheet locations were recorded at each test condition. Tables 5.1-5.2 list the flapping test points along with the camera and laser settings used in the PIV tests, and Figure 5.1 shows a false color photo of an example of both the horizontal and vertical orientations.

(a) Horizontally Mounted Wing   (b) Vertically Mounted Wing
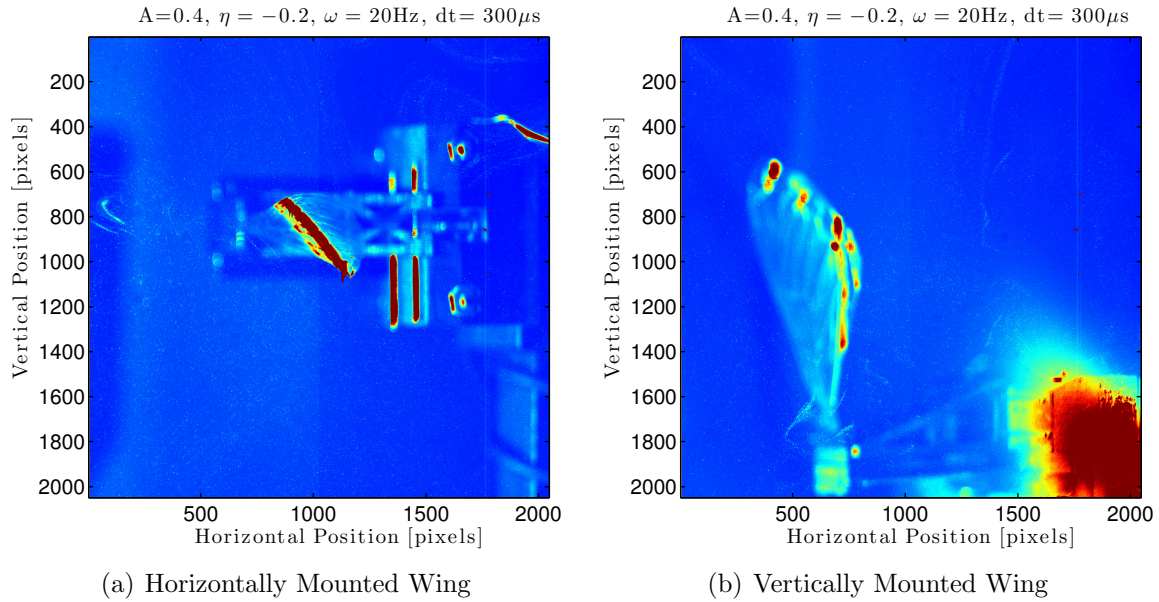
Figure 5.1: **False color capture of horizontal and vertical mounted wings in the seeded test chamber. Seed material is a 50 $^{L}/_{min}$ by volume dilution at 10psi of air and Rosco Smoke, atomized by a TSI 6-jet atomizer, with a nominal particle size $\approx$ 1-10μm, which is on order of $\approx$ 1-2 pixels, yielding a seeding density on order of $\approx$ 25-30 particles per 64$\times$64 pixel interrogation window.**

Table 5.1: Horizontal Wing—PIV Test Point Matrix

Orientation	A	Span Location (%R)	Test Time (s)	Pulse Δ t (μs)	Pulse Duration (μs)	# Bursts
30° wing						
Horizontal	0.40	0.5R	10	300	0.01	50
45° wing						
Horizontal	0.35	0.50R	10	300	0.01	50
Horizontal	0.35	0.75R	10	300	0.01	50
Horizontal	0.35	1.0R	10	300	0.01	50
Horizontal	0.40	0.25R	10	300	0.01	50
Horizontal	0.40	0.50R	10	300	0.01	50
Horizontal	0.40	0.75R	10	300	0.01	50
Horizontal	0.40	1.0R	10	300	0.01	50
Horizontal	0.45	0.50R	10	300	0.01	50
Horizontal	0.45	0.75R	10	300	0.01	50
Horizontal	0.45	1.0R	10	300	0.01	50
60° wing						
Horizontal	0.40	0.5R	10	300	0.01	50

Table 5.2: Vertical Wing—PIV Test Point Matrix

Orientation	A	Sheet Location (%c)	Test Time (s)	Pulse Δ t (μs)	Pulse Duration (μs)	# Bursts
30° wing						
Vertical	0.40	0.5c	10	300	0.01	50
45° wing						
Vertical	0.35	0.5c	10	300	0.01	50
Vertical	0.35	1.5c	10	300	0.01	50
Vertical	0.40	0.5c	10	300	0.01	50
Vertical	0.40	1.5c	10	300	0.01	50
Vertical	0.40	2.5c	10	300	0.01	50
Vertical	0.45	0.5c	10	300	0.01	50
60° wing						
Vertical	0.40	0.5c	10	300	0.01	50

5.3 PIV Results—*Horizontal Wing Orientation*

The PIV test procedures, methodology, calibration, set-up, and processing techniques were thoroughly discussed in section 3.4; therefore, this section will focus on

presenting the graphical flow visualization, and the velocity results from the tests conducted in Tables 5.1-5.2. The raw particle motion data was preprocessed with the Dantec DynamicStuido PIV software using a custom written script, combining several processing methodologies, and carefully selected options outlined in section 3.4.4 into a seamless processing recipe. This processing script produced a $\approx 14500 \times 12$ '.txt' file of u, v, w velocities in [m/s] across the two 2048×2048 2-D pixel image planes, mapped to a single 100mm $\times$ 90mm stereo image plane for every test point executed in Tables 5.1-5.2. A custom script was written in MATLAB® to further process the '.txt' files, which performed velocity line extractions, image processing and graphical overlays, thrust computations, produced stereo vector and velocity contour maps, and other analysis tasks required to translate the raw PIV data into usable processed FWMAV flow field data. The following sections contain extensive flow field depictions and linear velocity extractions across various spatial locations in the flow field, from which judgements of vorticity and the location, intensity, and transport of the LEV as an instrument of lift enhancement are proposed. To preface the results henceforth, it is instructive to illustrate qualitatively a complete eight phase test point through the flap cycle, which highlights both the wing position in each phase and what the appearance of vortical structures look like in relation to the entire flow field. Figure 5.2 shows a false color 2-D vector overlay of the u and v-velocity vectors from the stereo processed data projected on a false color image from the backscatter camera for the 60° wing at A=0.4.
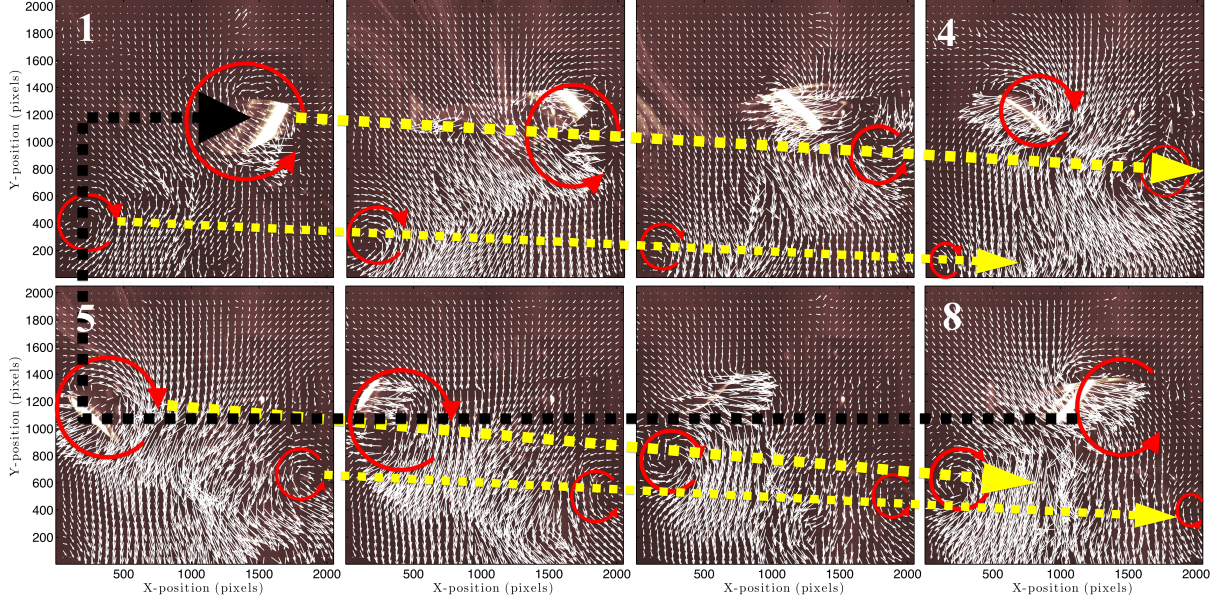
Figure 5.2: Graphic illustration of the progression of vortex generation through a single flap cycle. The flap cycle starts in the upper left with phase 1, and progress across the top to phase 4. The bottom row starts at the left end with phase 5, and progresses to the end of the flap cycle at phase 8, which is nearly coincident with phase 1. The LEV is highlighted in each image with a red ring, and a yellow connector tracks the linear translation from phase-to-phase of specific vorticial structures identifyed in the flow field.

Vortex cores with their rotation direction are shown in red, and the direction of their translation between phases are indicated with a yellow arrow. In phase 1, the wing is just past the mid-point of its downstroke cycle where two discrete vortex cores are observed in the vector field of view. One is the LEV, oriented such that it is on the LE suction side of the wing, increasing the dorsal-ventral surface pressure differential, increasing the wing's apparent camber and the net circulation around the wing, thereby augmenting and enhancing lift over the standard quasi-steady approximation. The second observed vortex core is detected near the lower left side of the image plane. The general motion of these vortices between subsequent phases is traceable with the yellow dashed lines. The overall motion, growth, and decay of these flow artifacts is down in the direction of the stroke. The wing begins to rotate through pronation and change direction to the upstroke half cycle in phases 3 and 4 and the larger vortex attached to the wing is quickly shed into the surrounding wake and substantially

202

reduced in diameter, while a new, but diminished vortex begins during the upstroke seen in phase 5. As the wing decelerates and begins the transition to supination and back to the downstroke, the growth of a new larger LEV is seen in phases 6 and 7, and finally at the last phase, mid-downstroke, the fully developed LEV is seen attached to the wing, and can be traced back to phase 1, and the start of a new flap cycle.

5.3.1   30°, 45°, 60° Comparison at A=0.4.

This section will show the graphical PIV results of the horizontally mounted 30°, 45°, and 60° wings at A=0.4, with the laser sheet intersecting the wings at 0.5R. Figure 5.3 is a multi-page illustration of the stereo u, v, w-velocity maps at every phase with their corresponding 1-D u and v-velocity line extractions. The top row of each subplot, a-c, is the stereo u, v, w-velocity map where the in-plane u and v-velocity is represented by the vector quivers, and the out-of-plane w-velocity component is represented by the color contour map. The second row, d-f of each subplot is the vertical v-velocity sampled at various cord positions above and below the wing. The third row, g-i of each subplot is the horizontal u-velocity sampled at various distances in front and behind the wing in motion. The 30° case corresponds with Figures 5.3(a),(d), and (g); the 45° case corresponds with Figures 5.3(b),(e), and (h); and the 60° case corresponds with Figures 5.3(c),(f), and (i). Note, the scales of the contour color bars and the velocity line extractions were purposely left to their native graduations. Setting uniform, but arbitrarily selected scales for presentation, obfuscates this data, blocks large portions of the flow field in particular phases, and excludes valid velocity points in the linear extractions in other cases. Furthermore, a single scale that is suitable across the disparate test regimes proved almost intractable; therefore, in the interest of representing each phase of each test condition most accurately, native scales were retained.
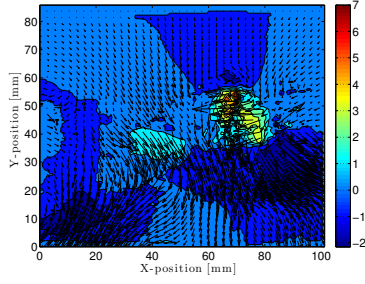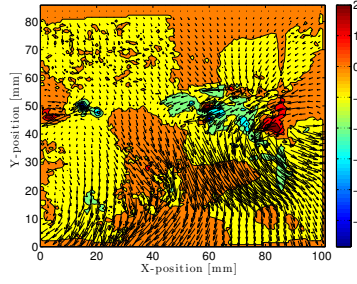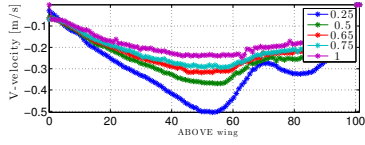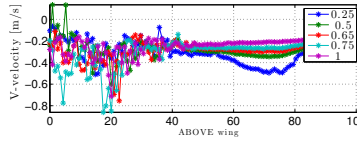
(a) (b) (c)

(d) (e) (f)

(g) 30° (h) 45° (i) 60°
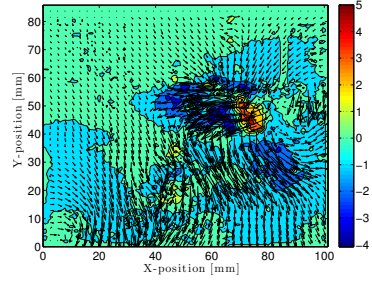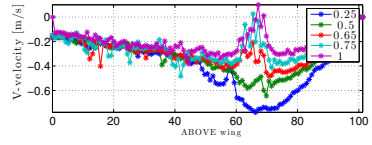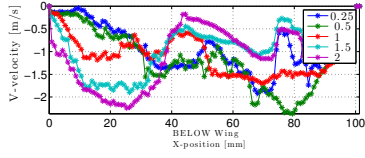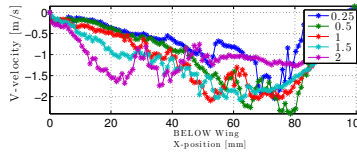
Figure 5.3: Phase 1

(a)

(b)

(c)

(d)

(e)

(f)

(g) 30°

(h) 45°

(i) 60°

Figure 5.3: Phase 2

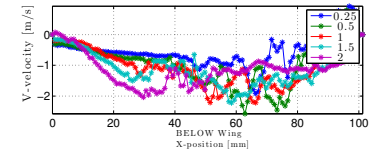(a)　　　　　　　　　　(b)　　　　　　　　　　(c)

(d)　　　　　　　　　　(e)　　　　　　　　　　(f)

(g) 30°　　　　　　　　(h) 45°　　　　　　　　(i) 60°

Figure 5.3: Phase 3

206

(a)   (b)   (c)

(d)   (e)   (f)

(g) 30°   (h) 45°   (i) 60°

Figure 5.3: Phase 4

(a)

(b)

(c)

(d)

(e)

(f)

(g) 30°

(h) 45°

(i) 60°

Figure 5.3: Phase 5

(a)   (b)   (c)

(d)   (e)   (f)

(g) 30°   (h) 45°   (i) 60°

Figure 5.3: Phase 6

209

(a) (b) (c)

(d) (e) (f)

(g) 30° (h) 45° (i) 60°
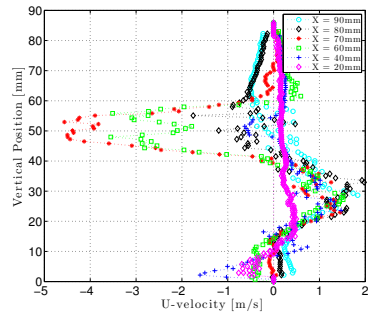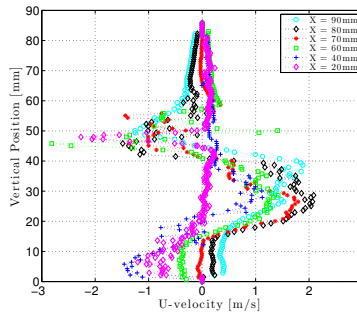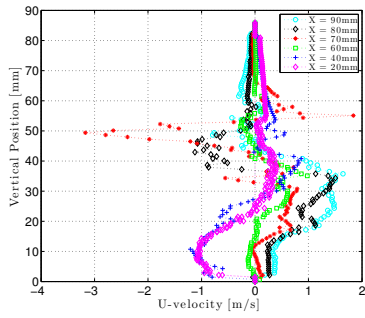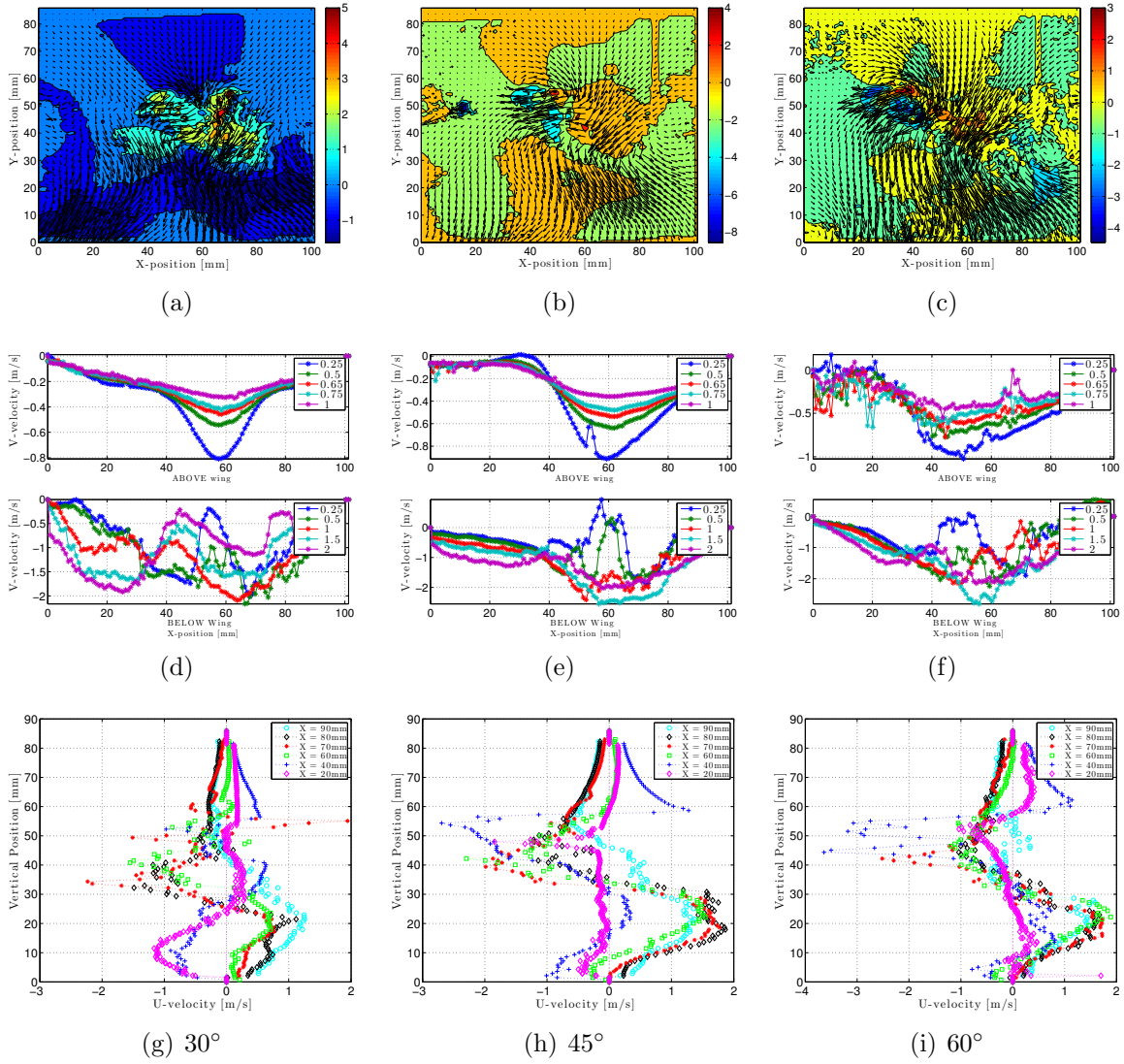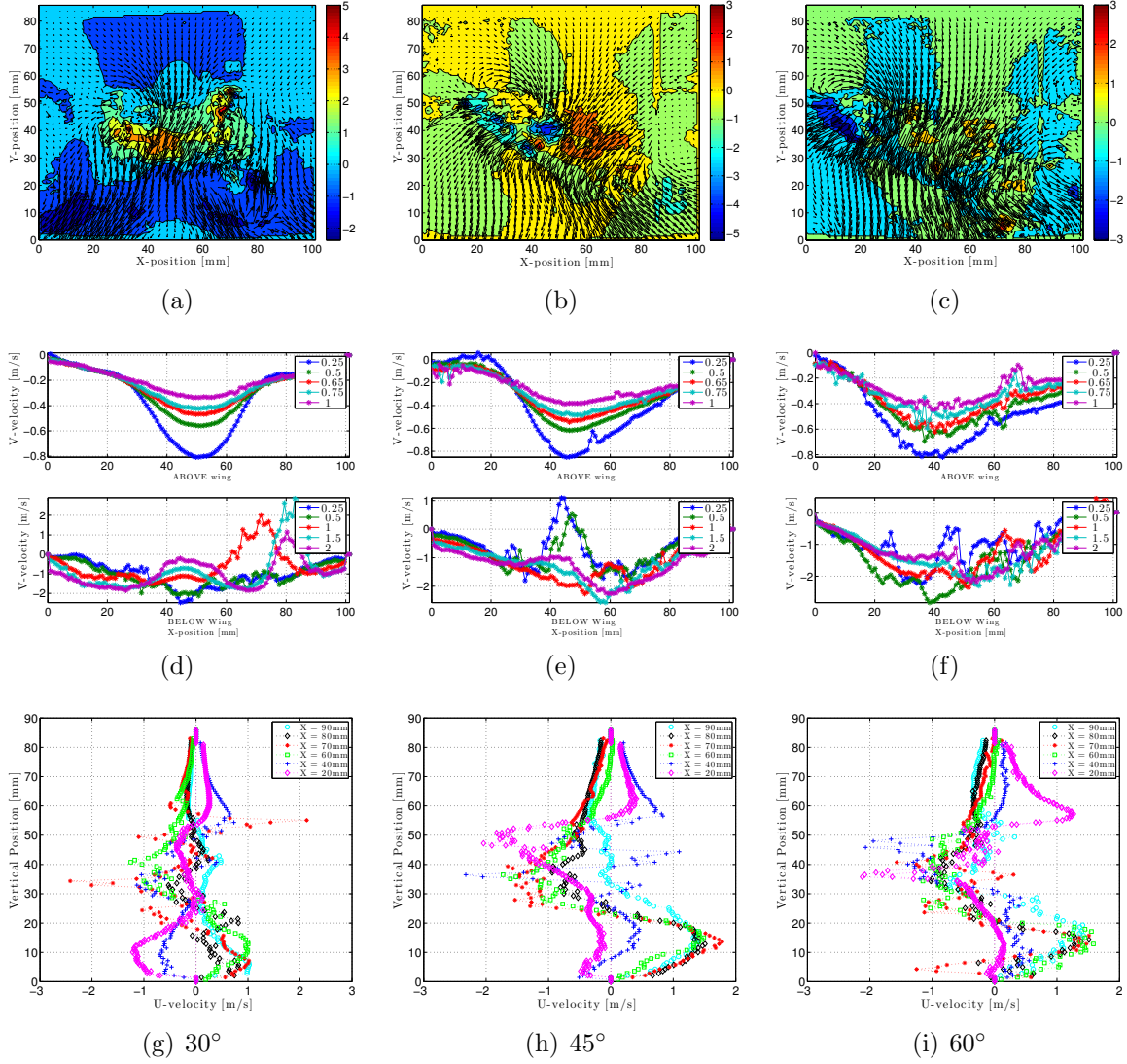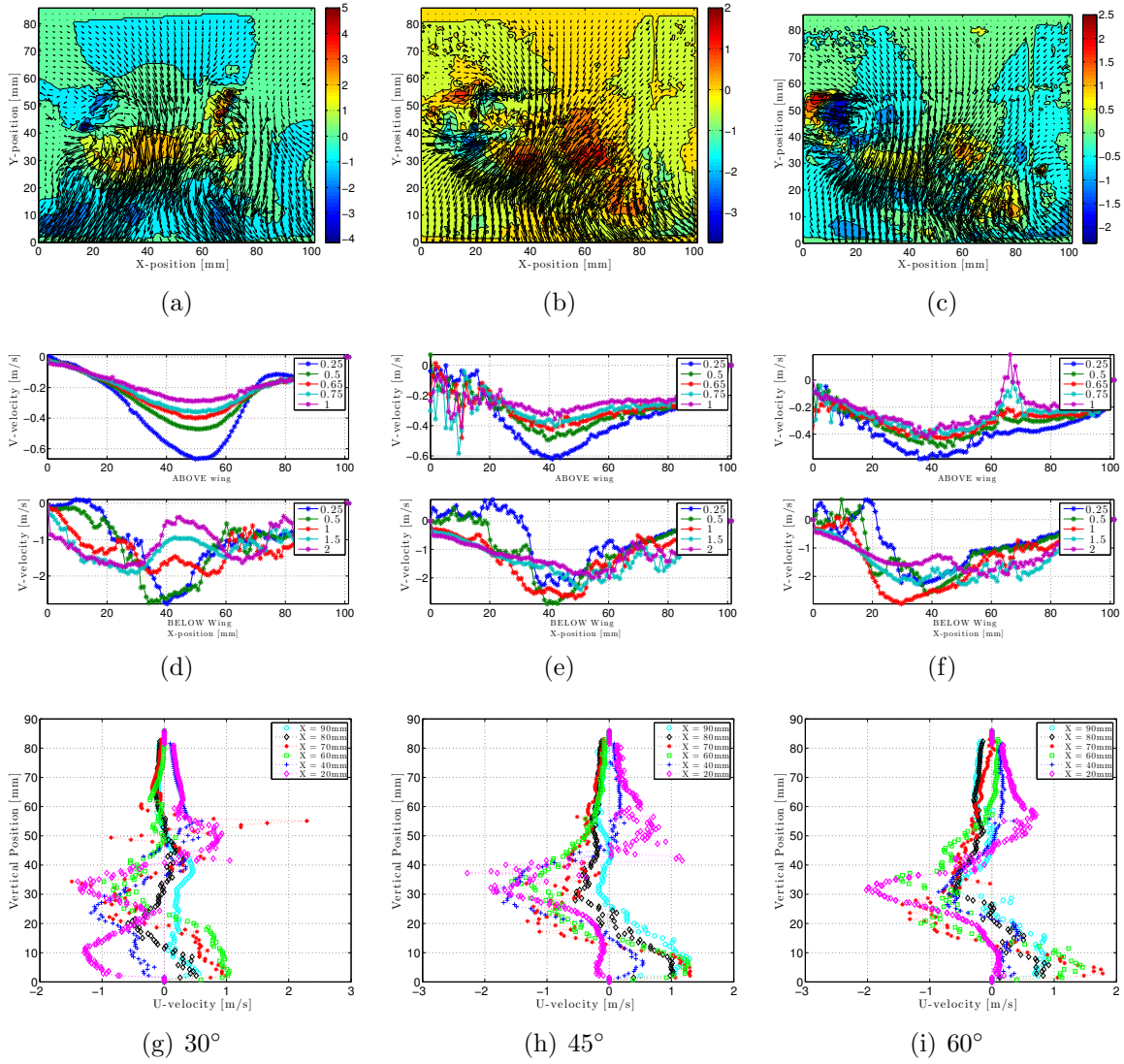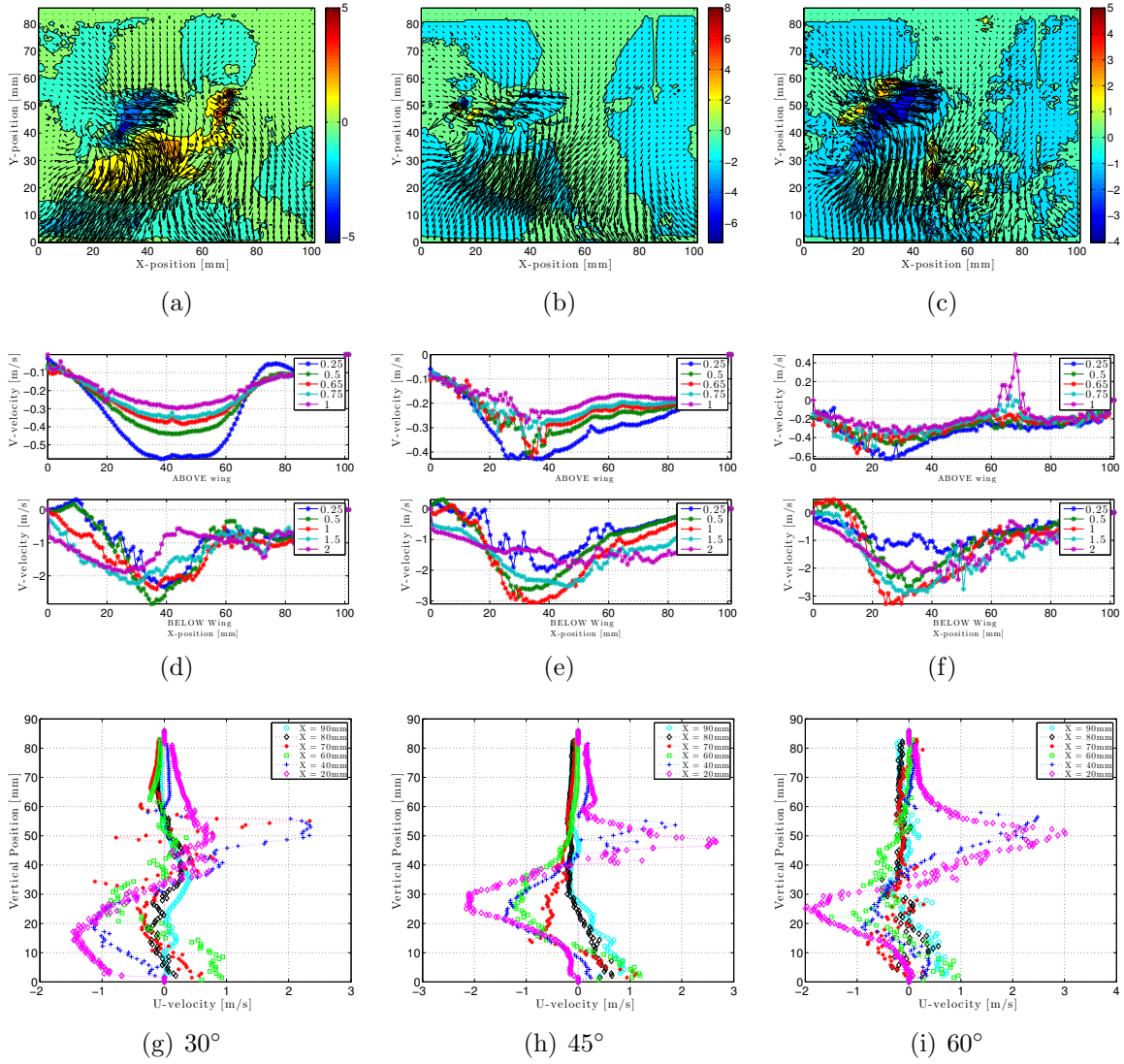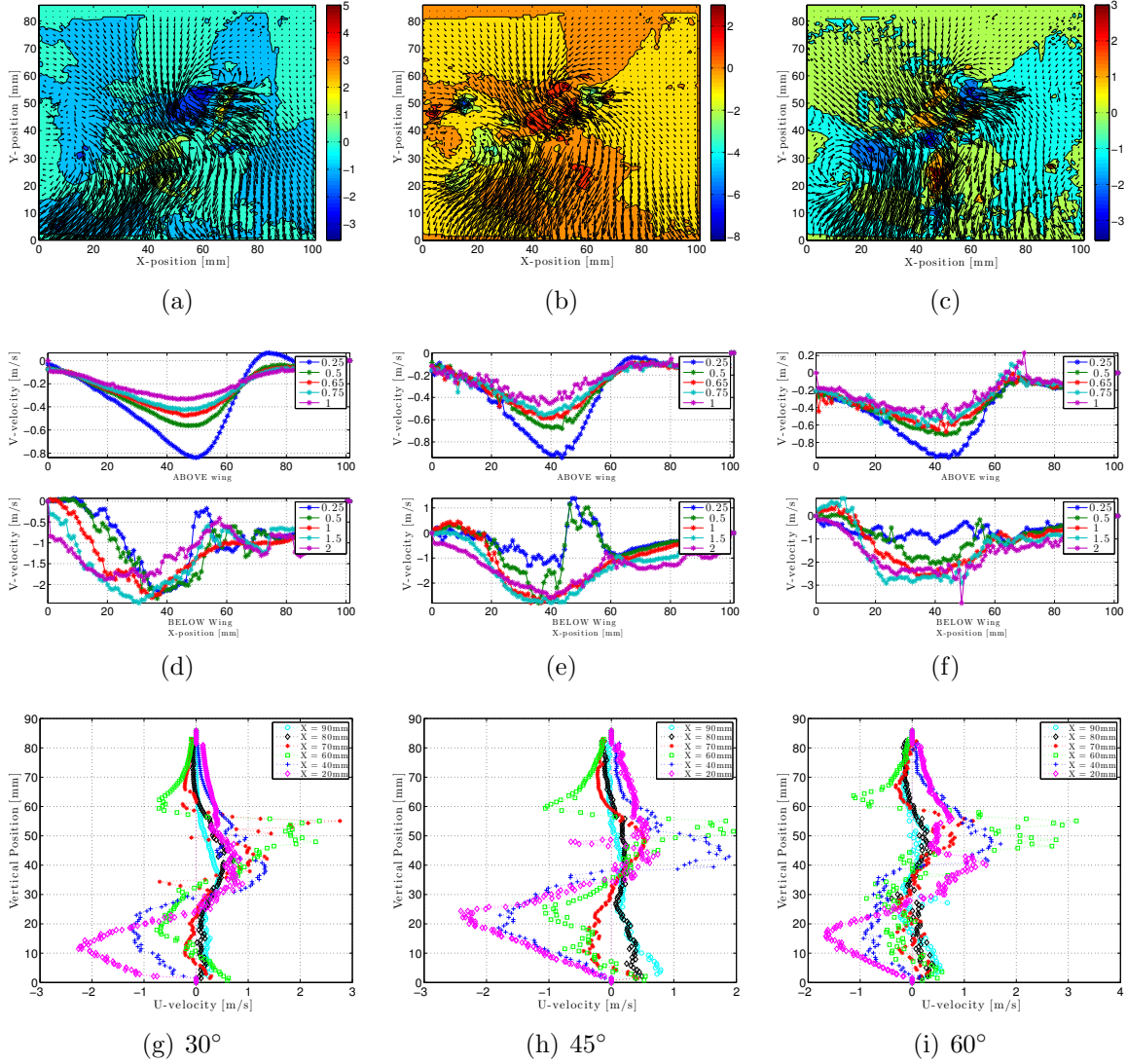
Figure 5.3: Phase 7

Figure 5.3: Phase 8

The velocity data is in good agreement with the force balance data. According to the results shown in Figures 5.3, the data shows the 60° wing produces the highest (−) velocities above and below the wing, resulting in the highest (−) total mean velocity across all eight phases. However, despite having the largest velocities above and below the wing, the 30° wing has a higher total (−) mean induced velocity. This is because the 30° wing has a much lower velocity above the wing, resulting in a larger difference between the above and below the wing velocities; however, the 60°

wing has higher mean velocities both above and below the wing, which means more air, and hence higher momentum flux transferred through the wing disk, producing more net vertical force. Table 5.3 shows the average velocities for the all three wings averaged from x=0mm to x=100mm. The higher the (−) vertical velocity, or more appropriately, the greater the induced velocity, which is the difference between the velocities above and below the wing, the greater the momentum flux through the wing disk, and the time rate of change of momentum over the stroke cycle equates to vertical force, *lift*, generation.

Table 5.3: **Horizontal Wing—30°, 45°, and 60° Wing PIV Velocity Summary**

Mean Velocity Component	Direction	Axis	30° [m/s]	45° [m/s]	60° [m/s]
v_{above} total	chordwise	(x)	-0.2343	-0.2643	-0.2845
v_{below} total	chordwise	(x)	-1.0382	-0.9579	-1.0397
v_{mean}	chordwise	(x)	-0.6351	-0.6744	-0.7618
$v_{induced}$	chordwise	(x)	-0.8038	-0.6935	-0.7552
u	axial	(z)	0.0180	-0.0279	0.0436
w	spanwise	(y)	0.0568	-0.0638	-0.0185

Figure 5.4 shows mean velocities plotted for the 30°, 45°, and 60° wings at A=0.4. The trace of the mean velocities for each phase match the general sinusoidal shape of the development of forces measured by the Nano-17 during a single wing flap cycle. Two interesting observations are evident about the secondary velocity components, u and w, first, the direction of the mean values are not consistent between the three different wings, despite being driven at the same voltage. The second is their magnitudes are an order of magnitude less than the primary v-velocity component in the lift generating direction. The difference in the sense of the u and w velocities, axial and spanwise, respectively, is indicative of vortex generation throughout the stroke cycle. The mean u and w velocities are calculated by taking the mean of the individual eight phases. The mean velocities of the eight phases are calculated by taking the mean of the stereo velocity field from the individual camera vector statistics. The

fact the u and w velocities are changing direction during each phase is indicative of vorticity being generated in vicinity of the wing during flapping. The presence of these vortical structures confirm the BEM approximation is limited when applied to flapping flight because it assumes zero spanwise and axial forces, and therefore, zero flow propagating in the y and z wind axes directions, which is clearly not proved in the flow physics shown.
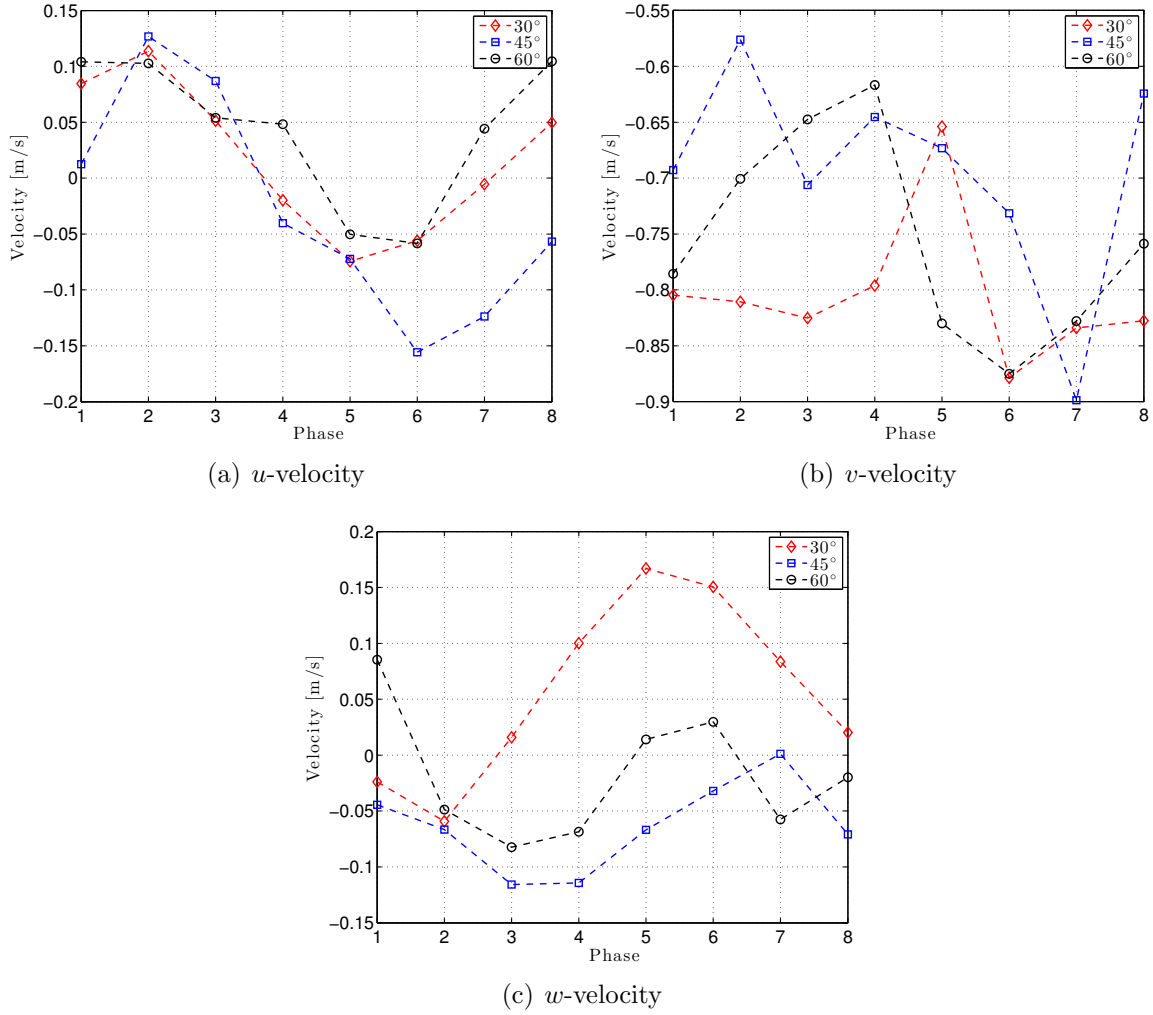

(a) u-velocity

(b) v-velocity

(c) w-velocity

Figure 5.4: 8-Phase mean velocities plotted per phase for the 30°, 45°, and 60° wings. Velocities follow the general trend of the Nano-17 force balance during a single wing stroke cycle.

Closer examination of a few phases reveal the extent of the development of vorticity in the wake of the flapping wing. Figure 5.5 shows a false color 2-D image of the

wing from the backscatter camera with the u and v-velocity vectors superimposed on the image for phases 1, 3, 5, and 8 during the flap cycle. The velocity vectors in all images are scaled-up 5× for presentation. The vectors come from the stereo velocity mapping, which is calculated from the separate 2-D vector statistics results. The vector map was de-warped using the wing's known chord and span length dimensions to resize the 100mm × 95mm rectangular vector map to a best fit of the square 2048 × 2048 pixel image map.
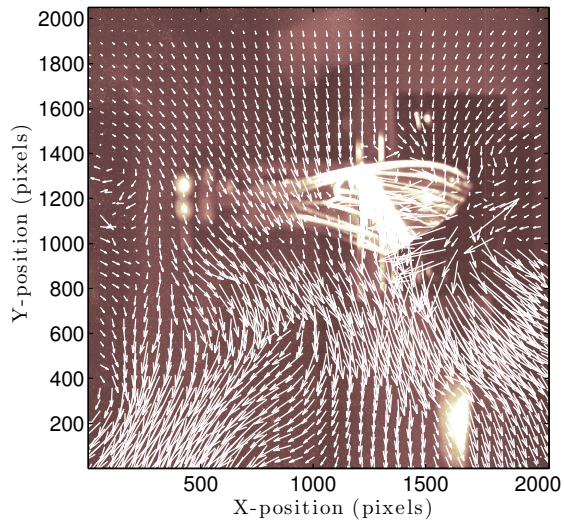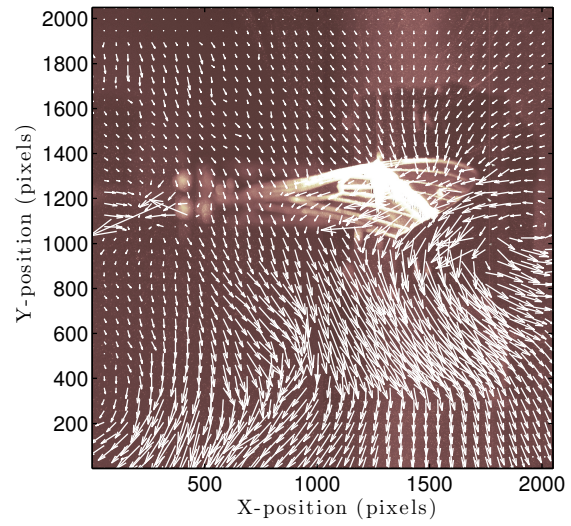

(a) 30°

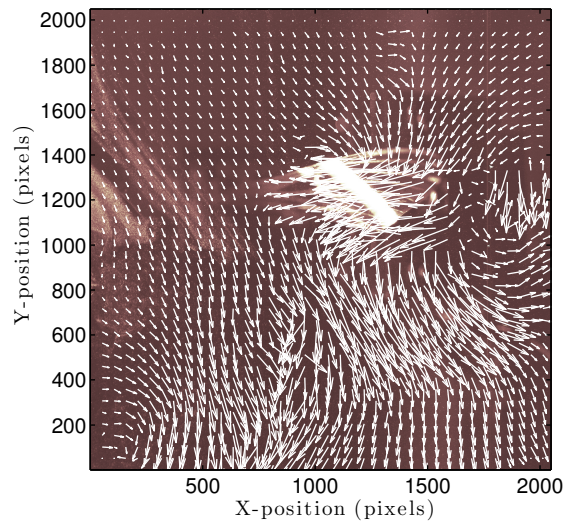(b) 45°
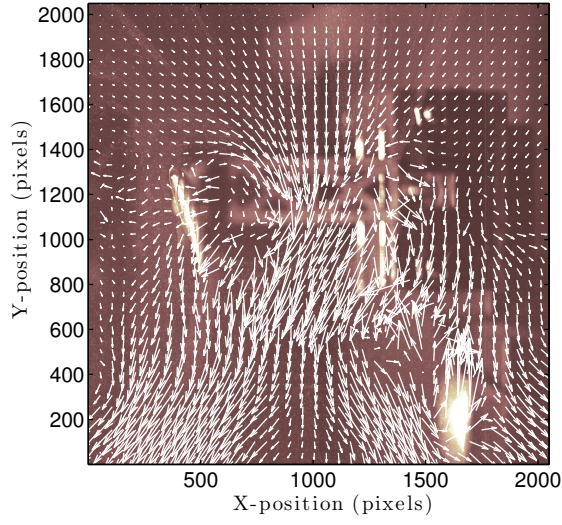
(c) 60°

Figure 5.5: Phase 1

214
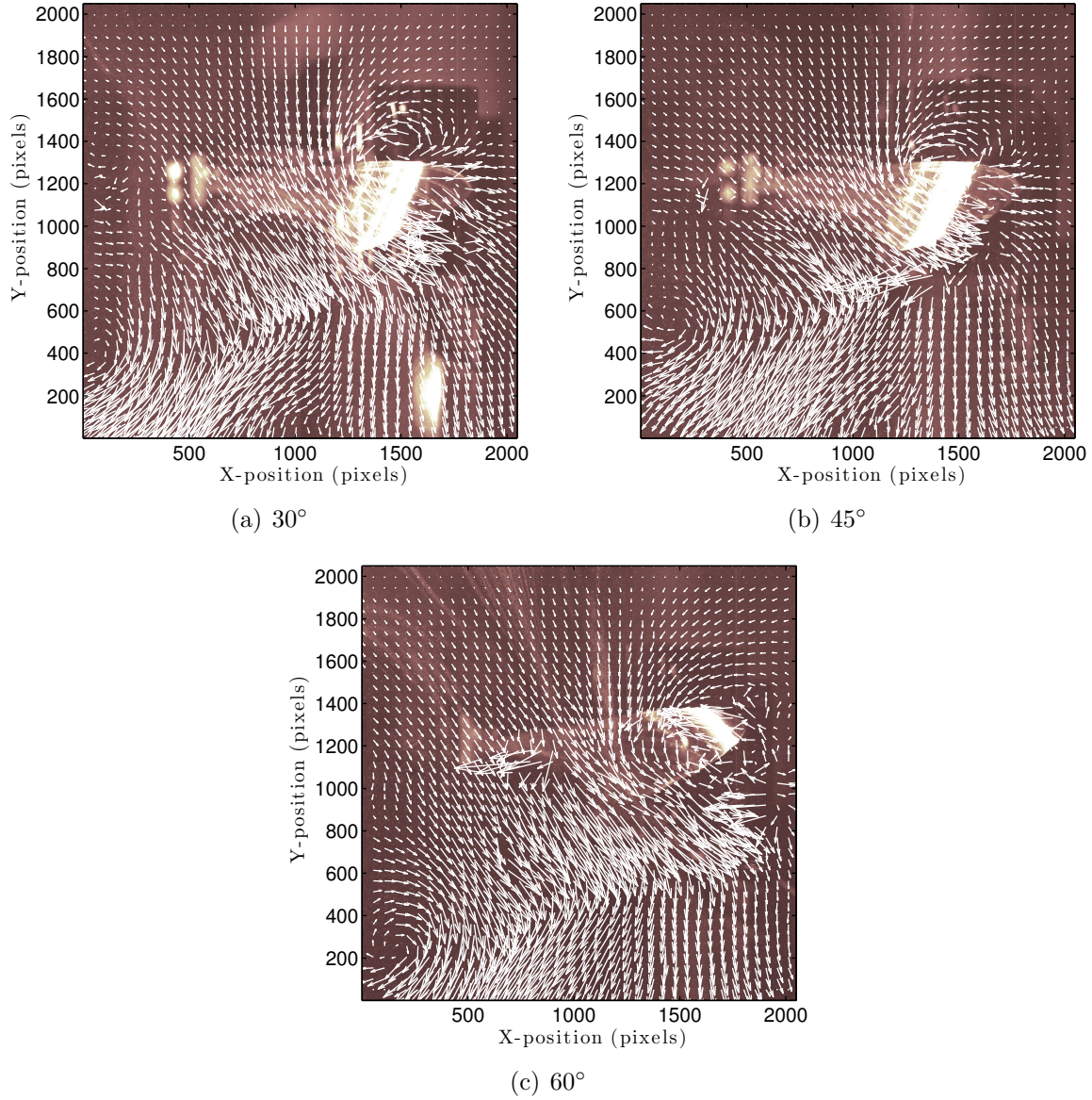
(d) 30°

(e) 45°

(f) 60°

Figure 5.5: Phase 3

215

(g) 30°

(h) 45°

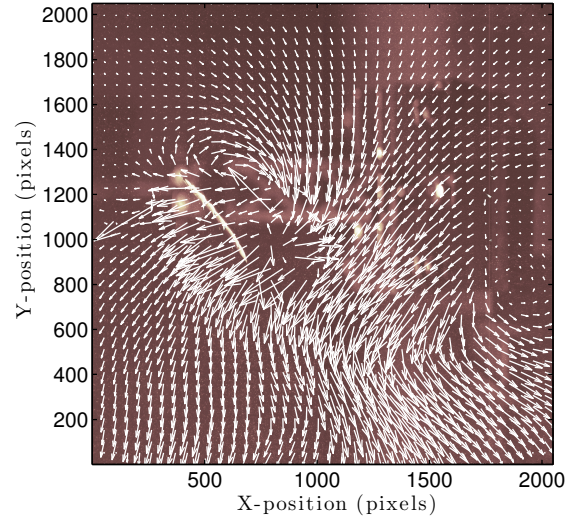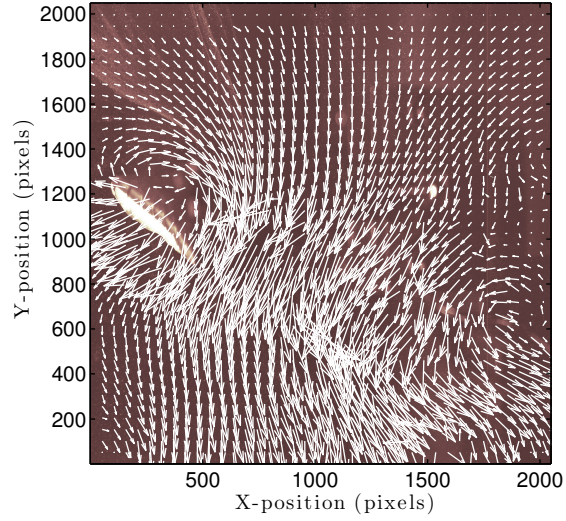(i) 60°

Figure 5.5: Phase 5
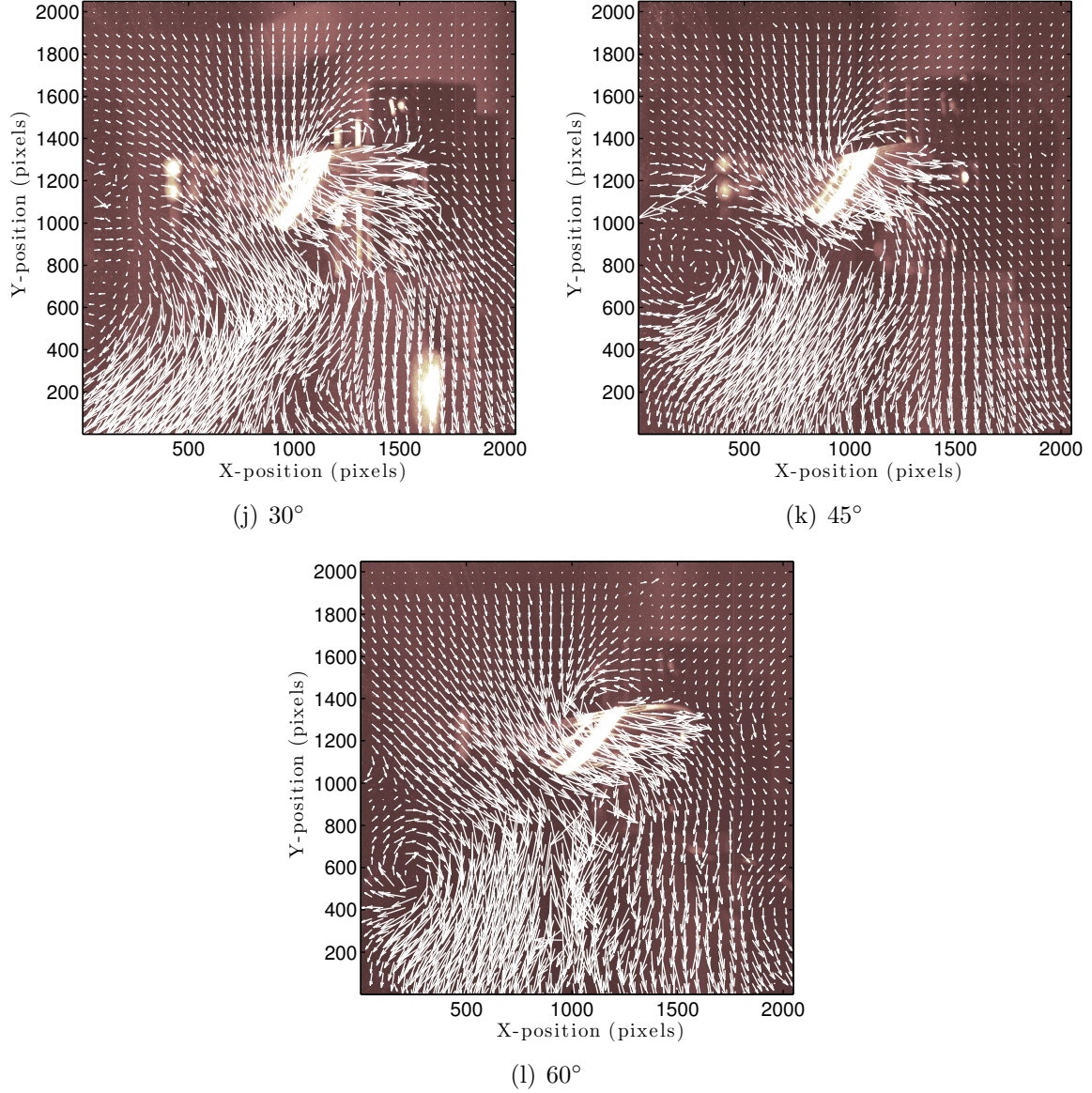
216

(j) 30°

(k) 45°

(l) 60°

Figure 5.5: Phase 8

Phase 1 shows the wing and the start-up vortex impulse begin as the wing motion and angular velocity increase on the downstroke. A counterclockwise rotation is evident around the wing, and referring to Figure 5.3(a)-(c), the direction of the spanwise w-velocity component makes physical sense with this rotation pattern. The w-velocity is (+), *coming out* of the page, to the left of the wing, and is (−), *going into* the page, on the right of the wing, which is consistent with a counterclockwise rotation.

Phase 3 is during supination, and rotation back to the upstroke phase. This phase shows the destruction of the wing tip vortex structures with little rotational motion, but still demonstrates a predominately downward flow motion of the air as it is being drawn into the rotating hemispherical disk, and accelerated through the disk below the wing, and the w-velocity component is generally (+) everywhere. Phase 5 is the start of pronation, and rotation back to the downstroke. This phase shows an interesting doublet of rotational velocity, and the influence of the vorticity from the previous stroke on the present stroke. The clockwise vorticity of the newly initiated downstroke is seen colliding with the counterclockwise wake of the previous stroke as the wing is passing through the wake of its predecessor. Again, the w-velocity component is generally positive, and does show a modest amount of spanwise shedding, especially in the 30° wing. Phase 8 is in the middle of the downstroke, and the previous wake structure has since dissipated and moved downstream of the wing, and the development of the purely counterclockwise rotation that dominated phase 1 is beginning to emerge. In the 45° and 60° wings, the clockwise vortex from the previous stroke is still visible at the lower left corner of the image, but has translated approximately two wing chords downstream. The intensity of the previous vortex core, estimated from the w-velocity component, is now approximately only half of the emerging counterclockwise vortex core, and will be completely ameliorated at the completion of the half cycle.

The differences observed in these three wings at the same phases is almost entirely due to the differences in the wing stop angles and the magnitude of the stroke angle, and the effect the different angle stops have on the angle of attack, which influences the wing dynamics, especially at the end of each half cycle between supination and pronation. The amount of angular rotation, and the angular rate have a considerable effect on the vortex core attached to the wing through translation. At the end of

the half stroke, the 30° wing hits the angle stop, and only rotates ≈ 30° over from the vertical (*recall this is the feather angle, ψ*), while the 60° wing rotates twice that amount. The combination of the additional rotation, and the higher wing stroke angle recorded by the 60° wing, ≈ 20° greater total feather angle travel than the 30° wing, have a dual effect of *i*) creating more vorticity at the ends of the half cycle, and *ii*) the higher stroke angle creates a larger torsional wave along the wing planform from root-to-tip once rotation is complete and the wing accelerates to the next translational half cycle. These two complementary mechanisms are the source of the enhanced lift often seen in flapping wing fliers. The torsional wave captures the LEV and maintains it along the LE of the wing, which enhances the projected wing area and effective camber of the wing during the half cycle. The addition of the trapped LEV along the wing's ventral surface is responsible for trapping and recirculating air around the the LE in a laminar bubble, increasing the wing's apparent camber, and increasing the leading edge pressure suction between the ventral and dorsal surfaces, inexorably leading to higher than postulated lift production. Figures 2.12-2.16 showed smoke visualization and CFD runs performed on a 10× scaled revolving mechanical Hawkmoth wing [86, 85, 93], and their results showed qualitatively what the PIV experiments performed here have shown quantitatively. Table 5.4 lists the velocities at each phase for all three wings at A=0.4.

Table 5.4: **Horizontal Wing—30°, 45°, and 60° Wing PIV Velocity By Phase at A=0.4 [m/s].**

Phase	30° wing			45° wing			60° wing		
	v_{ind}	u	w	v_{ind}	u	w	v_{ind}	u	w
1	-0.8048	0.0846	-0.0238	-0.6928	0.0124	-0.0445	-0.7856	0.1041	0.0854
2	-0.8106	0.1136	-0.0591	-0.5762	0.1267	-0.0666	-0.7006	0.1026	-0.0487
3	-0.8252	0.0514	0.0159	-0.7061	0.0869	-0.1158	-0.6475	0.0540	-0.0823
4	-0.7960	-0.0197	0.1001	-0.6453	-0.0404	-0.1144	-0.6166	0.0483	-0.0684
5	-0.6540	-0.0743	0.1670	-0.6733	-0.0723	-0.0668	-0.8300	-0.0503	0.0140
6	-0.8786	-0.0559	0.1504	-0.7315	-0.1558	-0.0321	-0.8750	-0.0584	0.0298
7	-0.8341	-0.0054	0.0837	-0.8986	-0.1237	0.0012	-0.8278	0.0441	-0.0576
8	-0.8275	0.0496	0.0203	-0.6244	-0.0568	-0.0710	-0.7585	0.1045	-0.0199

5.3.2   45° Wing Comparison at A=0.35, 0.40, and 0.45.

The previous section compared the PIV results across the three different angle stop wings at a constant driving amplitude and laser sheet location. This section compares the effect of changing the drive amplitude on the 45° wing at a single laser sheet location. PIV data was collected at A=0.35, 0.4, and 0.45 at the midspan, 0.5R. Figure 5.6 shows the stereo velocity contour map at phases 1, 3, 5, and 8 for A=0.35, 0.40, and 0.45 for the 45° wing.
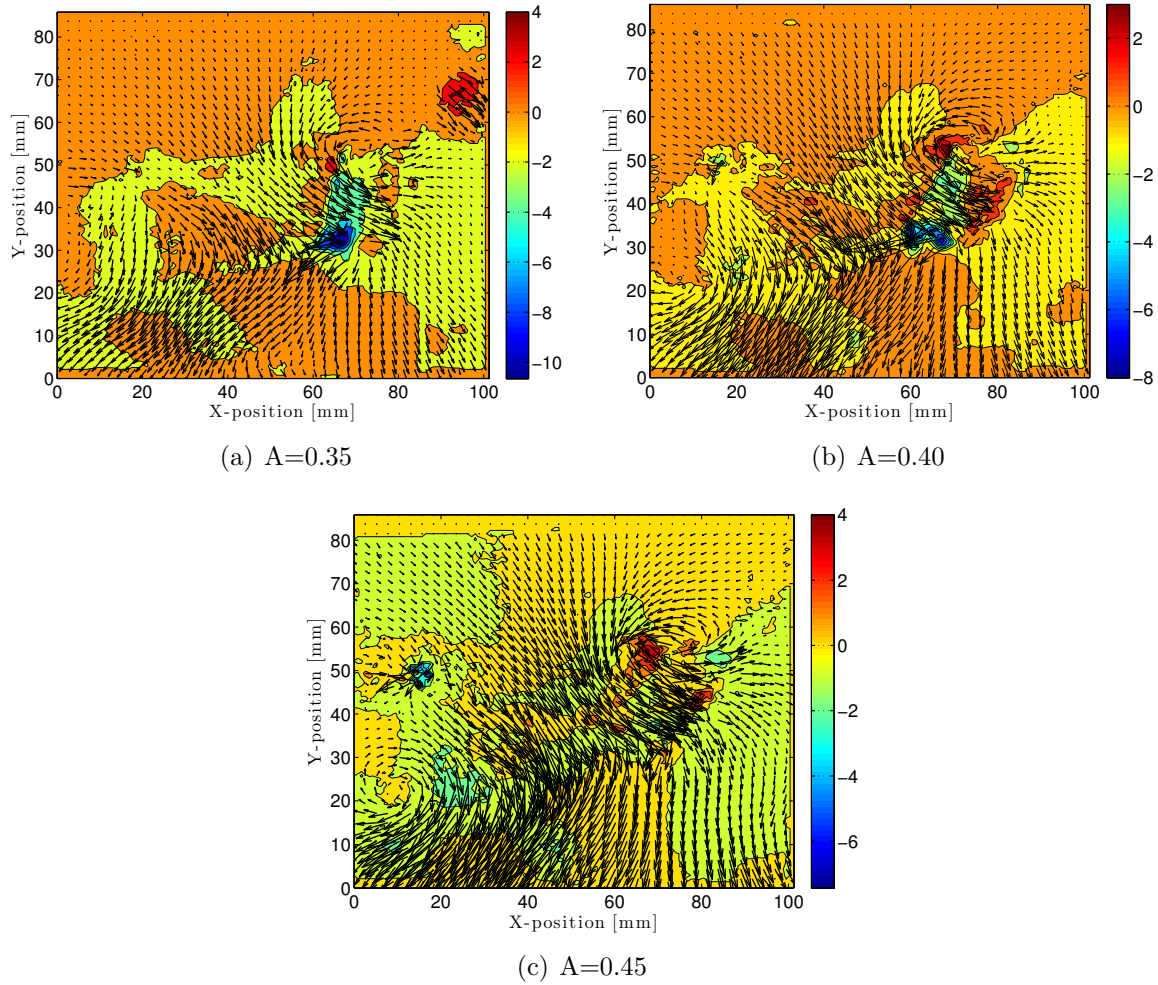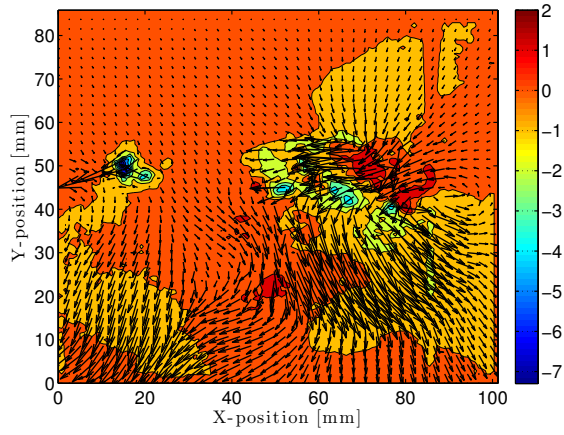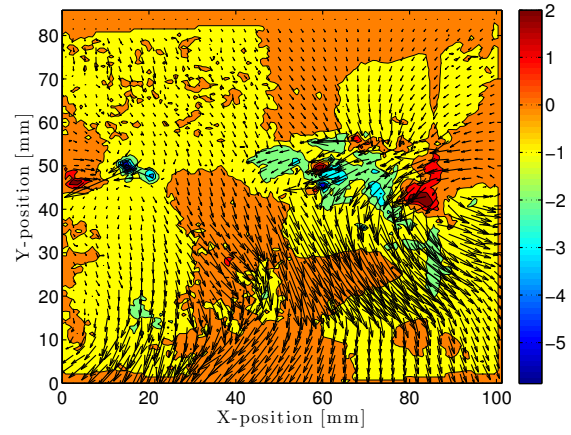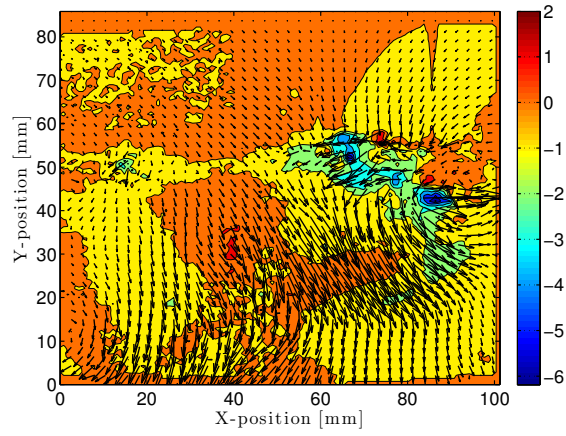

(a) A=0.35

(b) A=0.40

(c) A=0.45
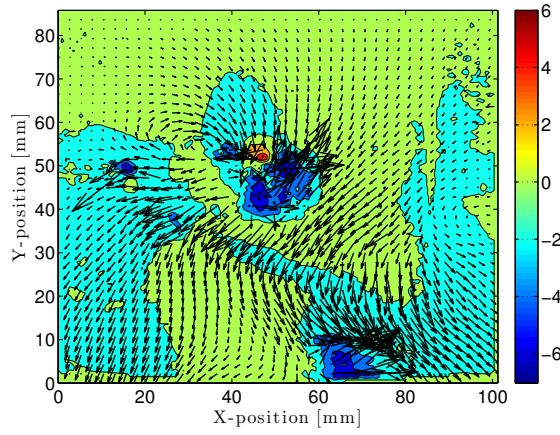
Figure 5.6: **Phase 1**

(d) A=0.35

(e) A=0.40

(f) A=0.45

Figure 5.6: Phase 3

(g) A=0.35
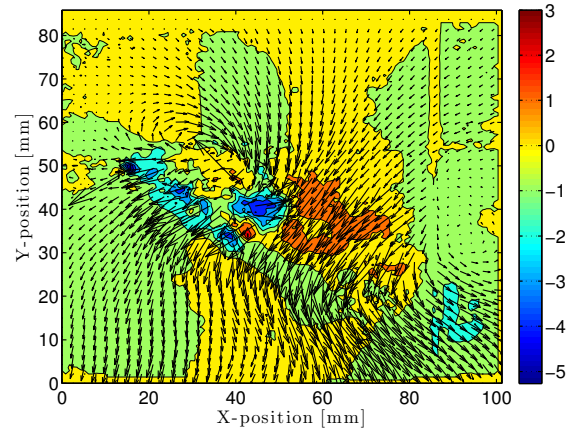
(h) A=0.40

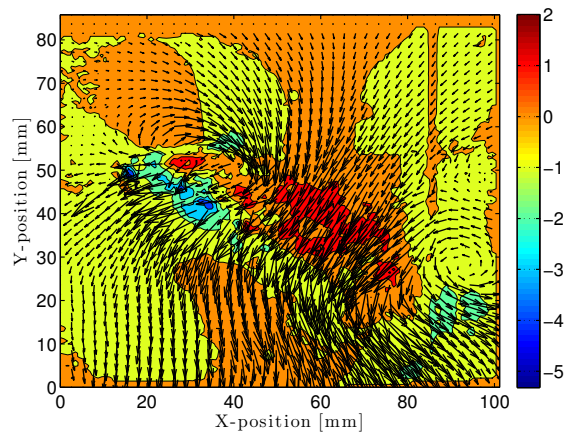

(i) A=0.45

Figure 5.6: Phase 5

(j) A=0.35

(k) A=0.40

(l) A=0.45
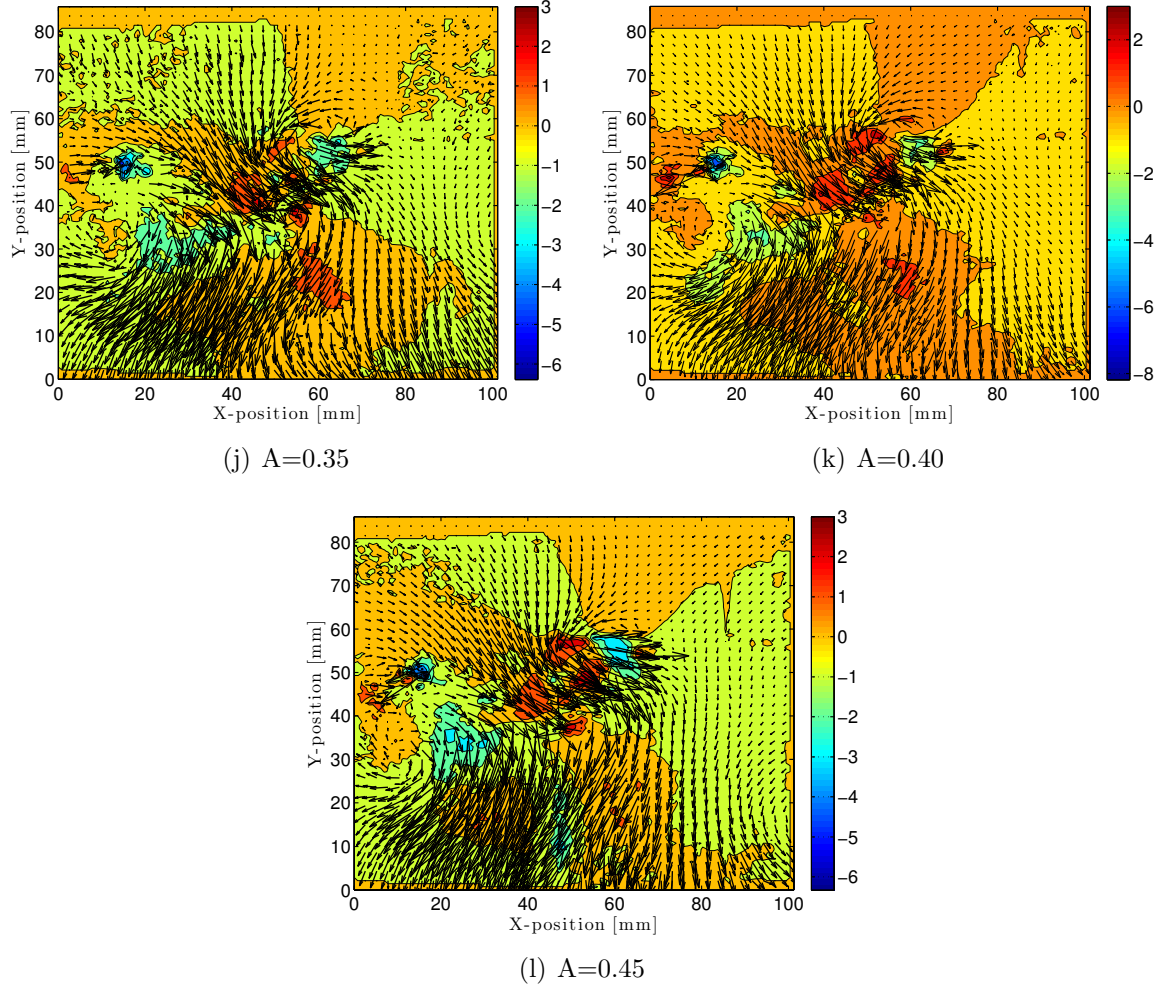
Figure 5.6: Phase 8

The velocity contour plots generally show expected trends. As the drive amplitude increased, so did the magnitude and intensity of the u and v-velocity quivers. For reference to the magnitude of the increase in wing kinematics between A=0.35 and A=0.45, Table 4.4 lists for A=0.35: $\Phi = 77°$, $\alpha = 57°$, for A=0.40: $\Phi = 88°$, $\alpha = 55.5°$, and for A=0.45: $\Phi = 88°$, $\alpha = 50.5°$. The general pattern and direction of the velocity quivers remained consistent between amplitudes. Figure 5.6(a)-(c) shows an increase in vorticity just to the right of the wing, which is matched with a corresponding increase in spanwise flow in and out of the page. Phases 5 and 8 show the characteristic clockwise and counterclockwise vortices, increasing in velocity with

223

increasing amplitude, as the wing begins to translate and starts the return downstroke through the wake from the previous upstroke phase. Figures 5.7-5.9 shows the velocity contour plots at $0.25\times, 1.0\times,$ and $2.0\times$ chords below the wing for all three amplitudes tested.

(a) A=0.35

(b) A=0.40

(c) A=0.45

Figure 5.7: Vertical velocity profiles for all eight phases at A=0.35, 0.40, and 0.45 at $0.25\times$ chords below the wing.

(a) A=0.35
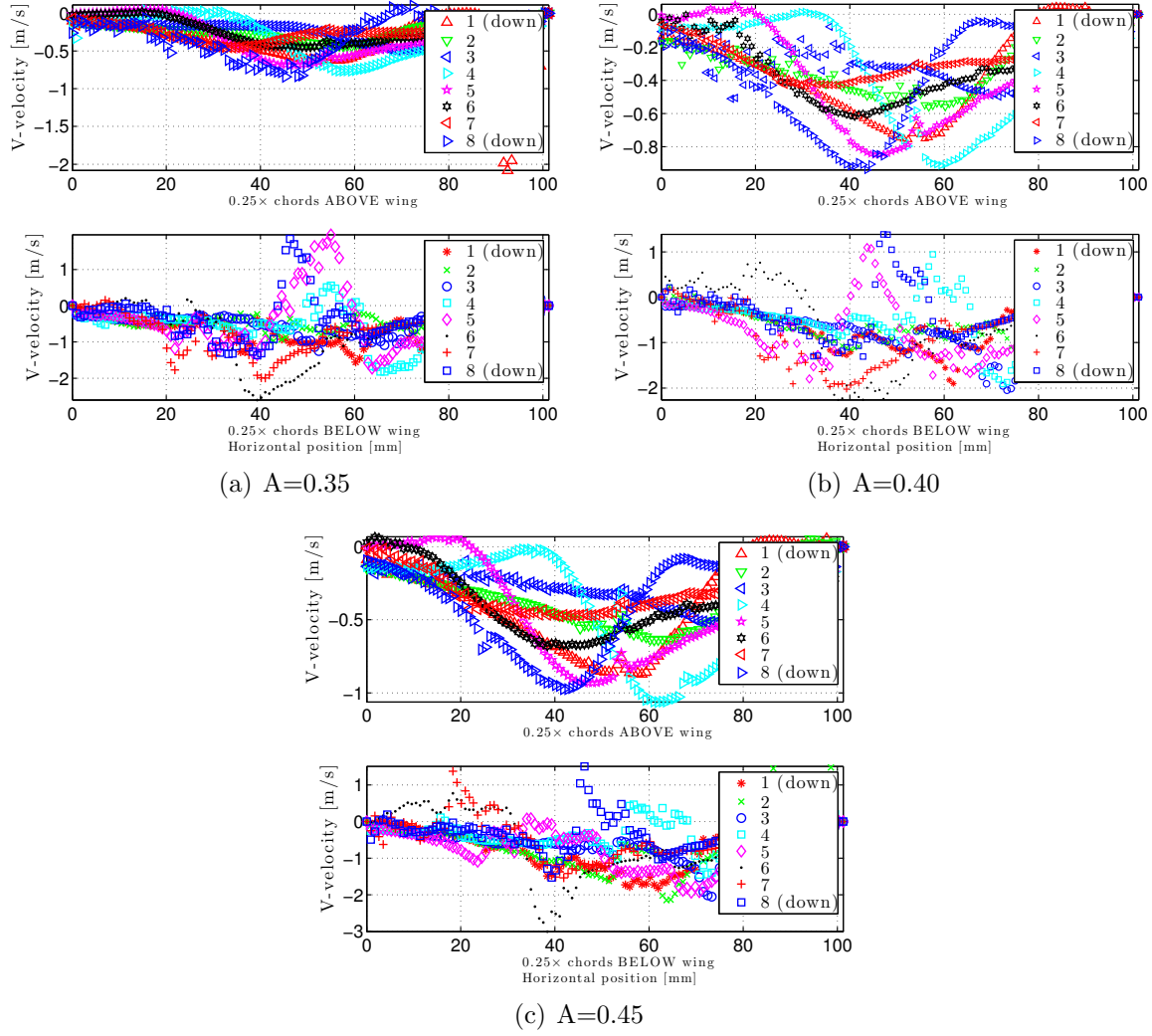
(b) A=0.40

(c) A=0.45
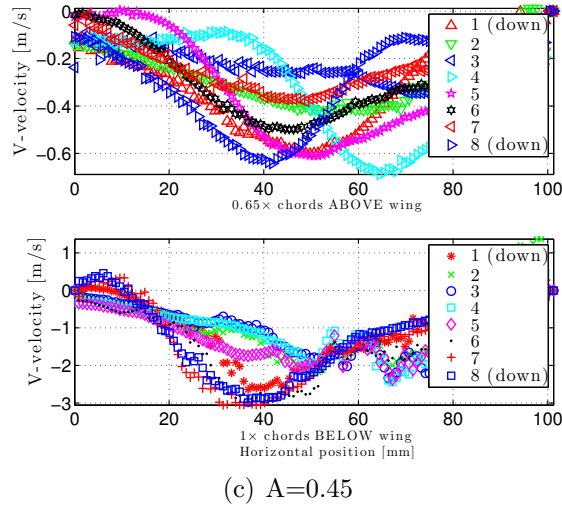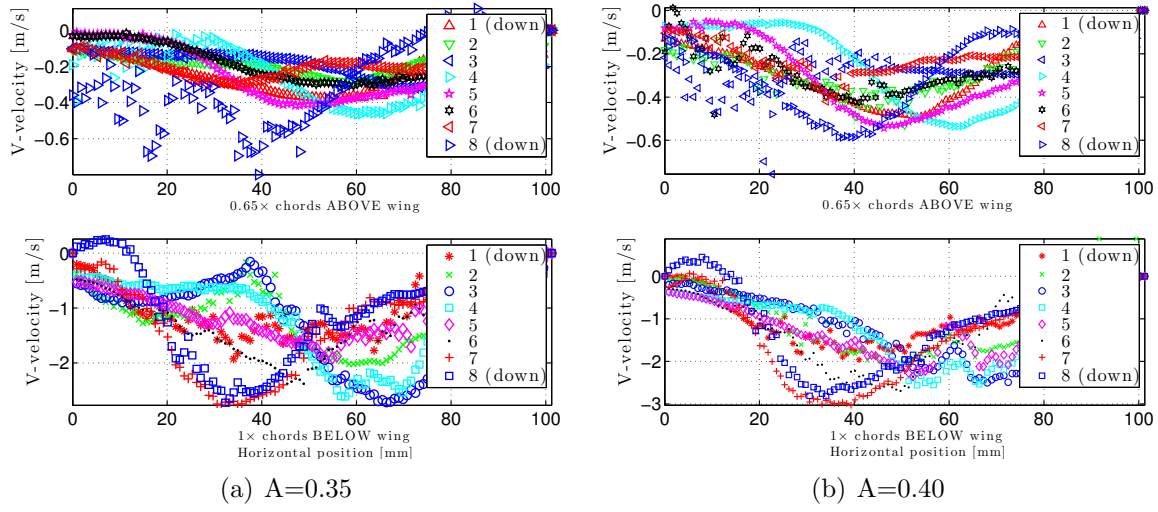
Figure 5.8: Vertical velocity profiles for all eight phases at A=0.35, 0.40, and 0.45 at $1.0\times$ chords below the wing.
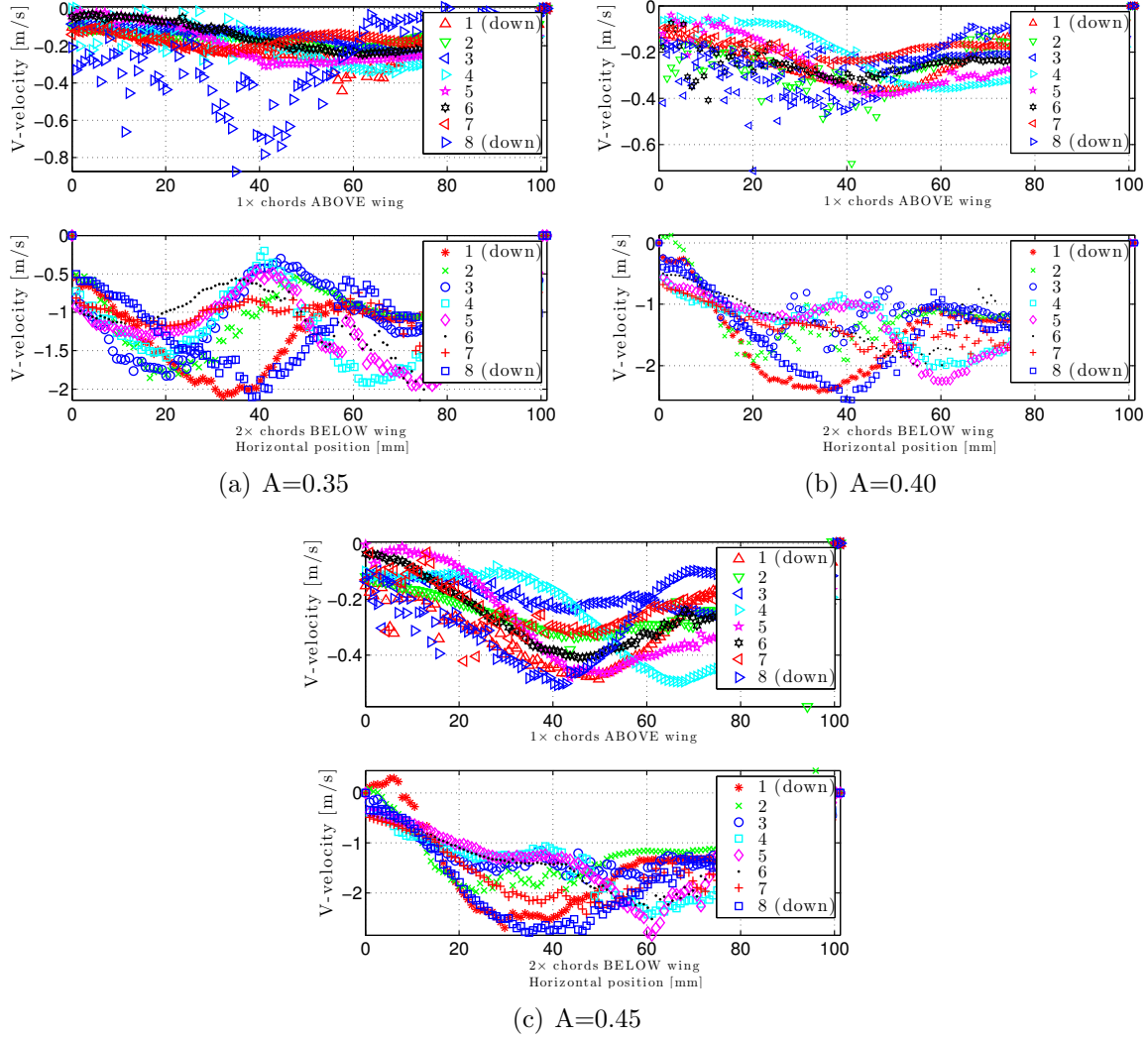
Figure 5.9: Vertical velocity profiles for all eight phases at A=0.35, 0.40, and 0.45 at $2.0\times$ chords below the wing.

For all amplitudes, at $0.25\times$ chords below the wing, there is an interesting positive v-velocity component in phases 5 and 8 near the 50mm position, and to a lesser extent phase 4, where there flow is attached just below the leading edge of wing, and is actually being pumped up and over the wing. By deduction, this flow phenomenon inextricably leads to the conclusion that during the translational portions of the stroke, air just below the wing surface remains attached to the wing as it is being drawn up-and-over the wing from the mid-span to the tip in a LEV, which increases its apparent camber. During the purely translational downstroke phases—1, 2, 6, and

7—the velocity is mostly negative and in the down direction, indicating stable flow during that portion of the stroke. At 0.25× chords above the wing, the suction into the actuator disk is sinusoidal as a function of phase where the peak suction moves left to right as the phases progress from 1-8. At one chord below the wing, the velocity profiles are all more stable and are mostly negative for all phases. At A=0.35, the velocity below the wing showed some oscillation with phase at all horizontal slices below the wing, which would result in a corresponding oscillation in vertical thrust. A 0.65× chords above the wing, the suction remains sinusoidal with phase across all phases. Velocity at two chords below the wing begins to dissipate and shows an overall decrease in maximal values from the one chord below values, indicating the maximum induced flow occurs at roughly 0.25× chords above the wing to about 1.0× chords below the wing. Table 5.5 shows the mean u, v, and w-velocities averaged across the RoI from x=0mm to x=100mm for all three amplitudes.

Table 5.5: Horizontal Wing—45° Wing PIV Velocity Summary At A=0.35, 0.40, & 0.45

Mean Velocity Component	Direction	Axis	A=0.35 [m/s]	A=0.40 [m/s]	A=0.45 (m/s)
v_{above}	chordwise	(x)	-0.2250	-0.2473	-0.2912
v_{below}	chordwise	(x)	-0.9333	-0.9579	-1.0039
v_{mean}	chordwise	(x)	-0.5916	-0.6744	-0.7358
$v_{induced}$	chordwise	(x)	-0.7083	-0.7106	-0.7127
u	axial	(z)	-0.0371	-0.0279	-0.0195
w	spanwise	(y)	-0.0119	-0.0638	-0.0633

Figure 5.10 shows the progression of the cartesian velocity components over the stroke cycle. The phase averaged velocities follow the same general progression of the vertical force, F_x, on the Nano-17 force balance over the stroke cycle. The negative downward velocity, associated with hover force, peaks during the downstroke translation parts of the stroke cycle, begins to decrease in magnitude during rotation, and then decreases significantly in magnitude during the upstroke portion of the stroke cycle.

(a) *u*-velocity

(b) *v*-velocity

(c) *w*-velocity
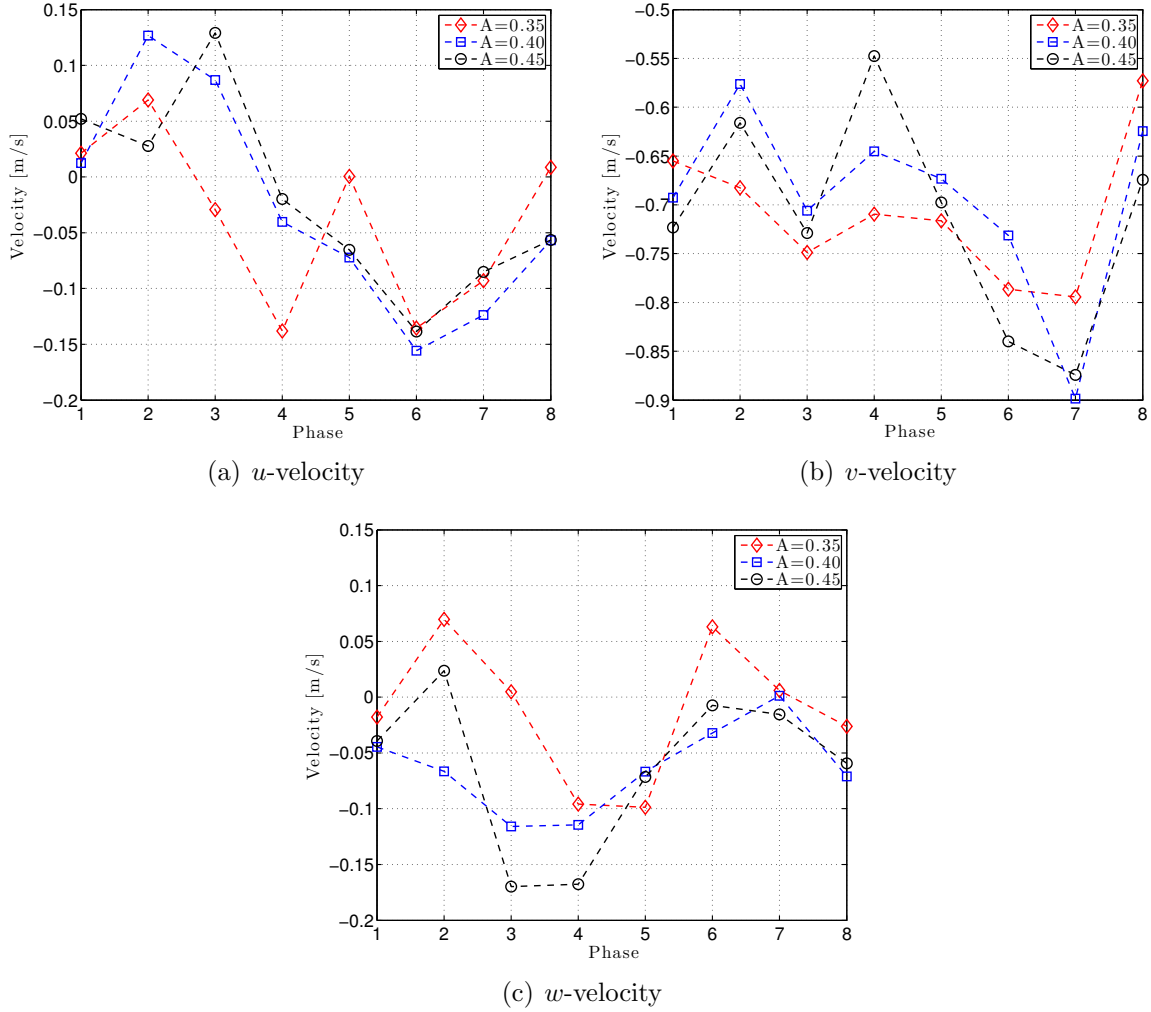
Figure 5.10: 8-Phase mean velocities plotted per phase for the 45° wing at A=0.35, 0.40, and 0.45. Velocities follow the general trend of the Nano-17 force balance during a single wing stroke cycle.

5.3.3   45° Wing Comparison at 0.25R, 0.5R, 0.75R, and 1.0R.

The previous section compared the effect of changing the drive amplitude on the 45° wing at a single laser sheet location. This section compares the flow field on the 45° wing at various locations along the wing span at a fixed amplitude. PIV data was collected at an amplitude of A=0.4 at 0.25R, 0.5R, 0.75R, and 1.0R span locations. In previous sections, comparisons were shown at phases 1, 3, 5, and 8, which showed the mid downstroke, rotation to the upstroke, rotation to the downstroke, and back

to the mid downstroke cycles; however, for the different span location comparisons, it is more instructive to show the the mid-stroke phases 2, 4, 6, and 7 which will provide insight into flow physics during translation along the entire span. Figure 5.11 shows the stereo velocity contour map at phases 2, 4, 6, and 7 for A=0.4 at 0.25R, 0.5R, 0.75R, and 1.0R for the 45° wing.

(a) 0.25R

(b) 0.50R

(c) 0.75R

(d) 1.0R
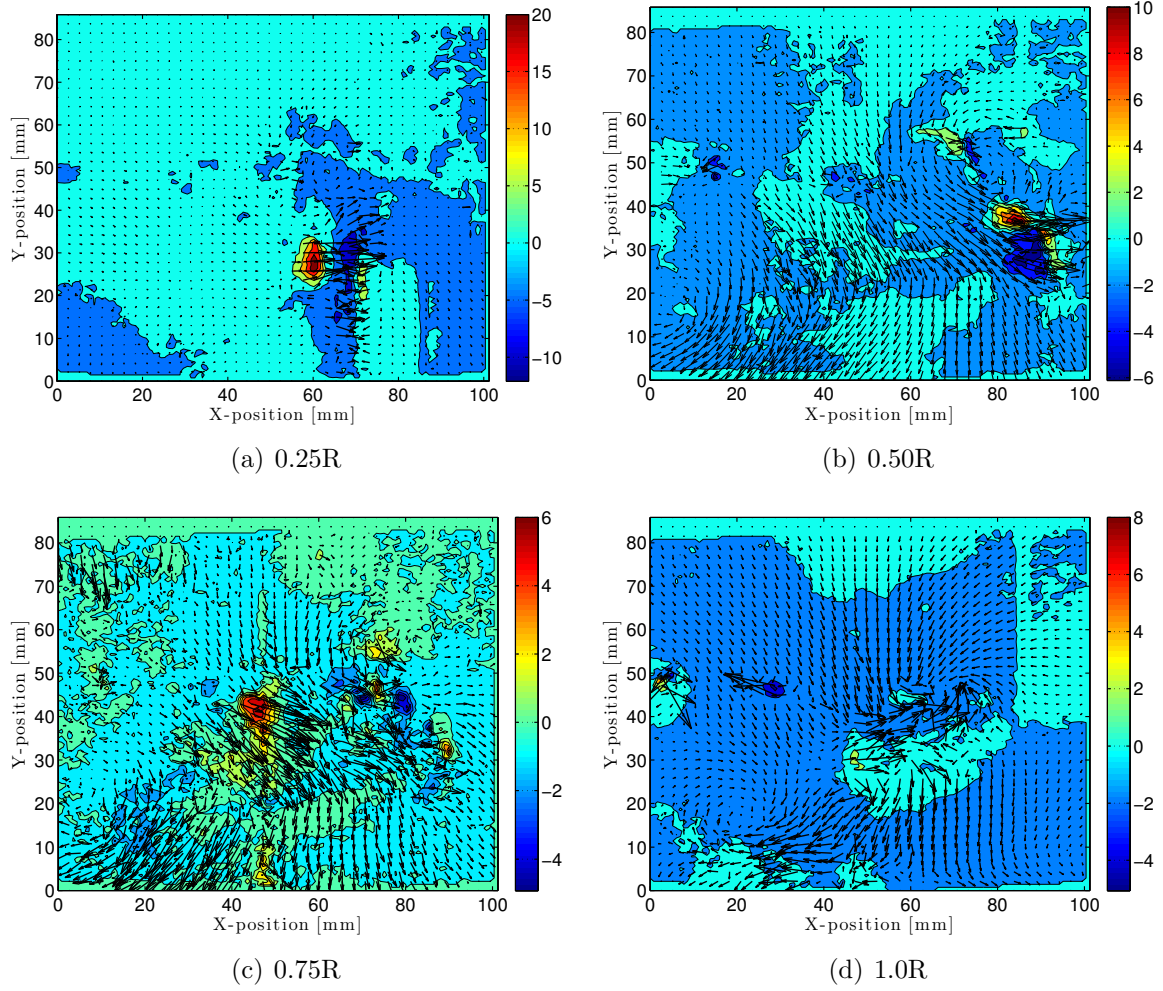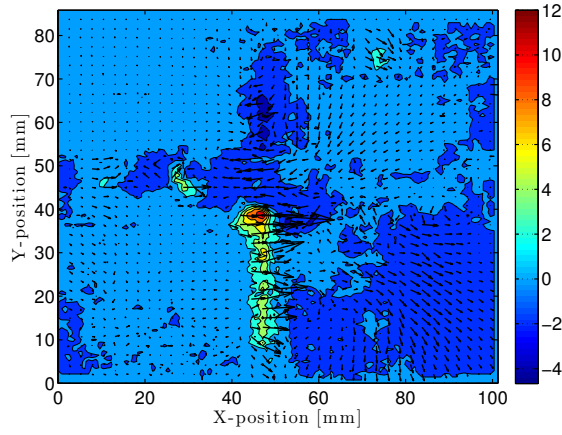
Figure 5.11: Phase 2

(e) 0.25R
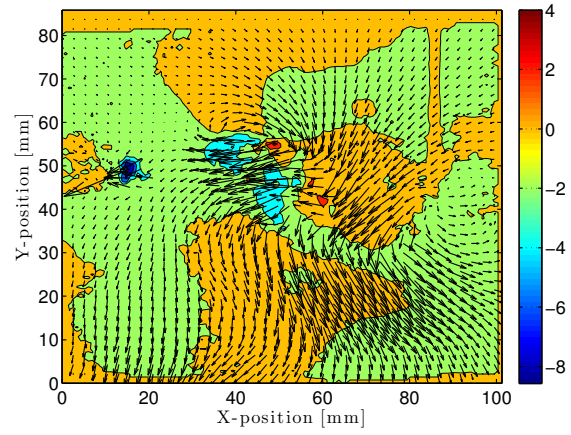
(f) 0.50R
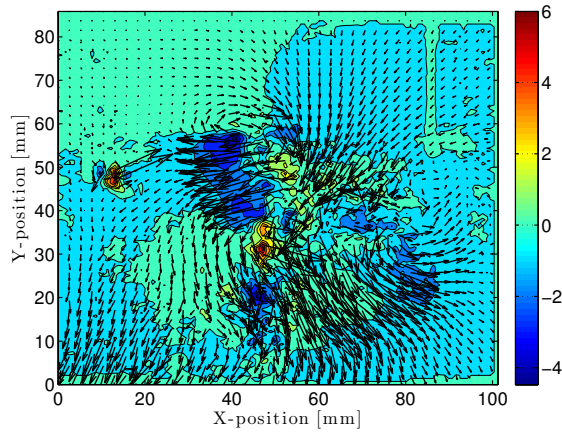
(g) 0.75R
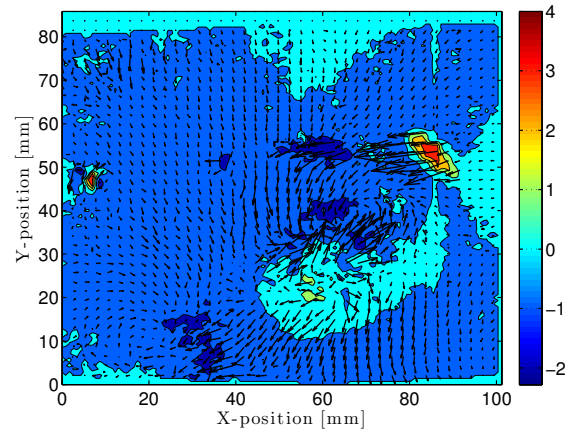
(h) 1.0R

Figure 5.11: Phase 4
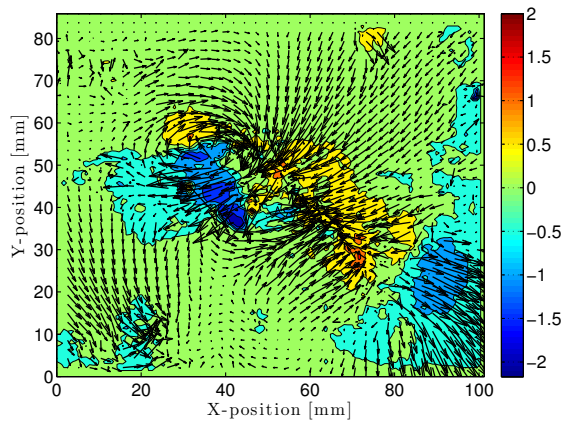
(i) 0.25R
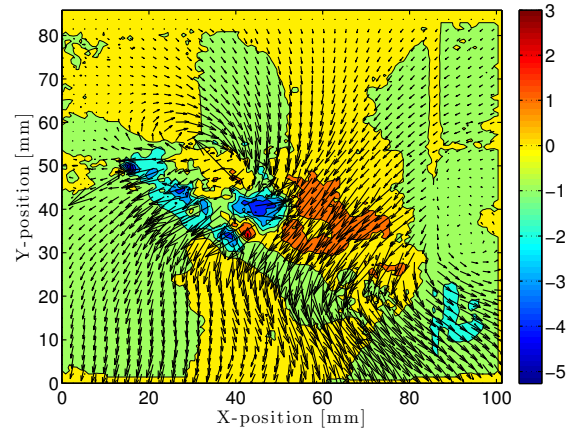
(j) 0.50R
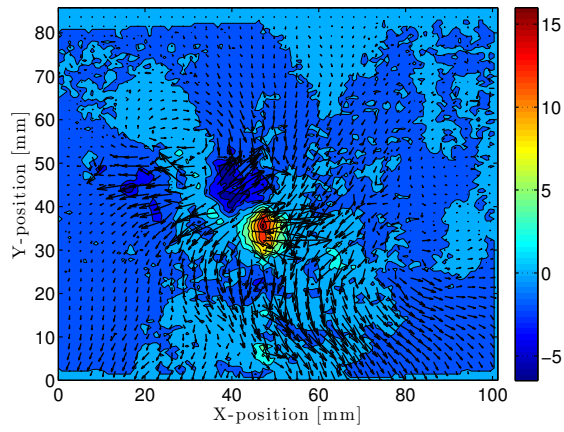
(k) 0.75R
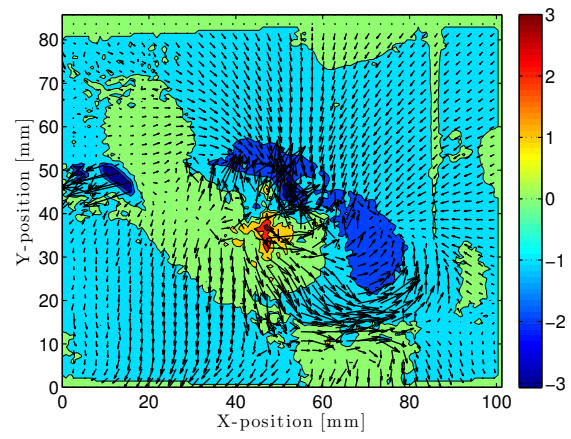
(l) 1.0R

Figure 5.11: Phase 6

(m) 0.25R

(n) 0.50R

(o) 0.75R

(p) 1.0R
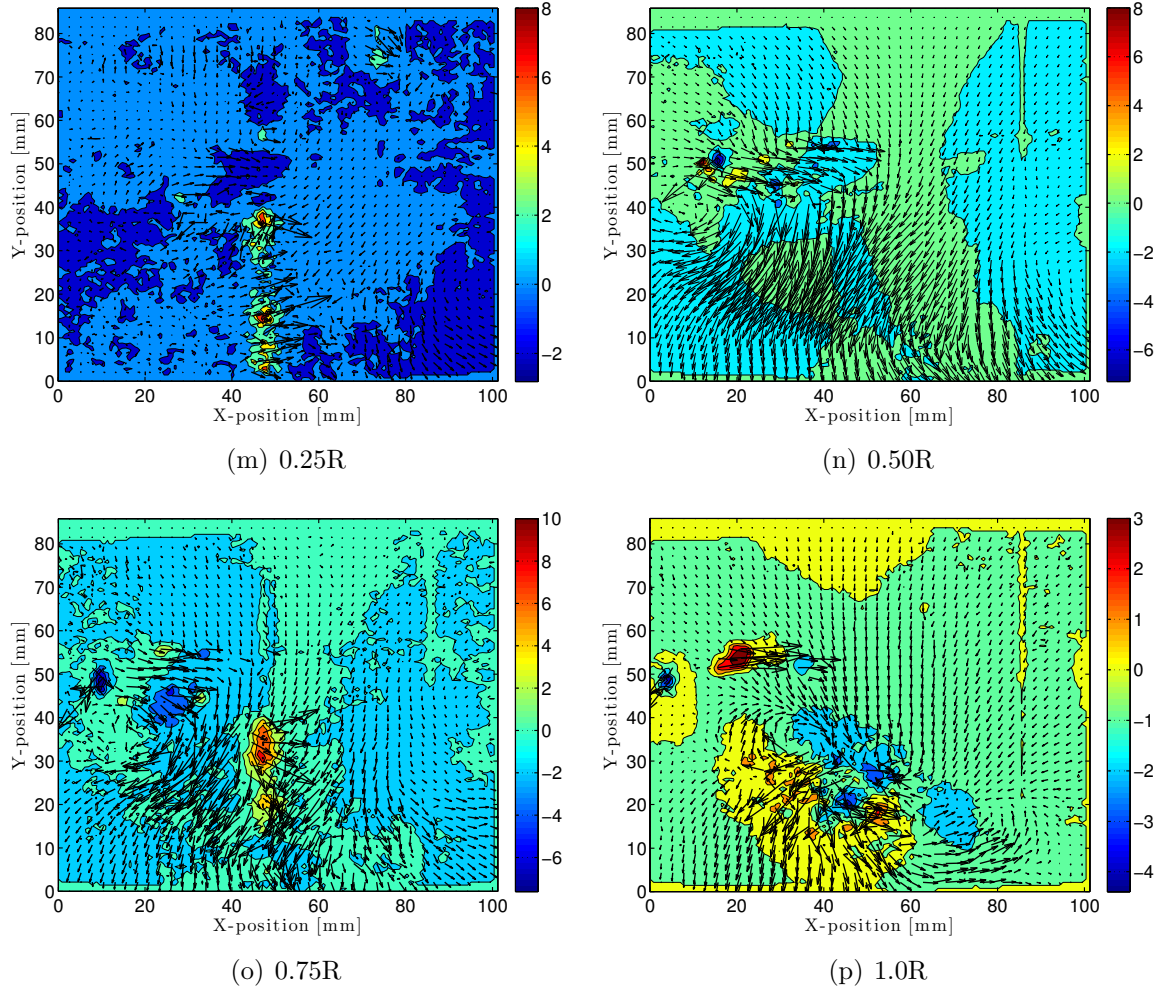
Figure 5.11: Phase 7

The velocity contours do show an interesting evolution of the flow field as it progress along the span. The spanwise flow, and the LEV coalesce with the tip vortex to form a continuous vortical structure that extends along the length of the wing from near the wing root until it is shed into the wake along the path of the wing tip. The vortex wake produced by the LEV tip vortex, and the combined SS vortices form a vortex ring. When the phase and orientation of the vortical structures align, the vortex ring produces a linear momentum jet, which provides the thrust necessary for sustained hovering. This LEV is stable for the duration of the flap half-cycle. In addition to circulatory aerodynamic phenomena, there are

aerodynamic forces associated with the rapid acceleration and deceleration of the volume of entrained air in the immediate vicinity of the wing, attributable to viscous effects, as the wing flips and changes its direction of motion at the end of each half cycle, maintaining the wing's LE into the direction of the relative wind. This non-circulatory phenomenon influences the pressure distribution along the wing surface as well as the pressure and velocity field about the wing. The circulatory and non-circulatory aerodynamic phenomena each produce localized wake structures. These local wake structures interact to form the complex wake structures observed in the PIV progression from phase to phase through the stroke cycle.

Sustained flight is achieved when the vortical wake structures align in space and time to form a coherent momentum jet of air normal to the direction of travel; which in hover, is vertical towards the earth. A coherent attached LEV with spanwise flow during up and downstroke translation forms a negative pressure region around the the wing, producing a leading edge suction, and hence, is responsible for enhancing lift production. At wing beat velocities equitable to static hover, the downstroke wake is a small diameter, high gradient, and stable LEV with a strong root-to-tip w-velocity component, increasing in diameter from wing base to tip, separating from the wing at approximately 0.75R during the 2nd half of the downstroke, and merging with a large tip vortex from the previous half cycle with a nonuniform core, which connects to a combined SS vortex generated by pronation. Figure 5.11(a)-(c) shows the LEV being shed out of the page. The tightly wound pulsed circles at 0.25R and 0.75R show the LEV being shed into the wake, and Figure 5.11(d) corresponds closely to the findings published by Van Den Berg on the Cambridge 10$\times$ mechanical Hawkmoth flapper that the well behaved, tightly wound LEV breaks down at 0.75R, see Figure 2.12 [85]. Figure 5.11(e)-(g) shows the same vortex progression along the span during the mid upstroke, but it appears to break down a bit earlier than 0.75R. Although the

LEV structure is still clearly present in phase 4, Figure 5.11(g), its shape is not as clearly delineated, and it appears to have begun to be tangled by the formation of the clockwise vortex that is encircling the wing and the remnant of the counterclockwise vortex from the previous half cycle just to the right of the wing, as it begins to be convected down stream of the translation. At the end of pronation and the beginning of the next downstroke phase, the LEV is weak and has yet to fully form, shown by Figure 5.11(i)-(k). By the time the wing has reached the mid-stroke of the next phase, the LEV has regained its strength, and the pulsed nature of the characteristic spanwise shedding is evident in Figures 5.11(m)-(o).

In all phases depicted, the presence of any LEV shown by pulsed shedding of the w-velocity component, or u, v velocity circulation, has largely dissipated at the wing tip, 1.0R. Another good graphic illustration of the progression of the flow is to look at the wing itself in a false color vector overlay at these four span locations during a single phase. Figure 5.12 shows the 45° wing at the last phase in the test sequence, phase 8, at 0.25R, 0.5R, 0.75R, and 1.0R.

(a) 0.25R

(b) 0.50R

(c) 0.75R
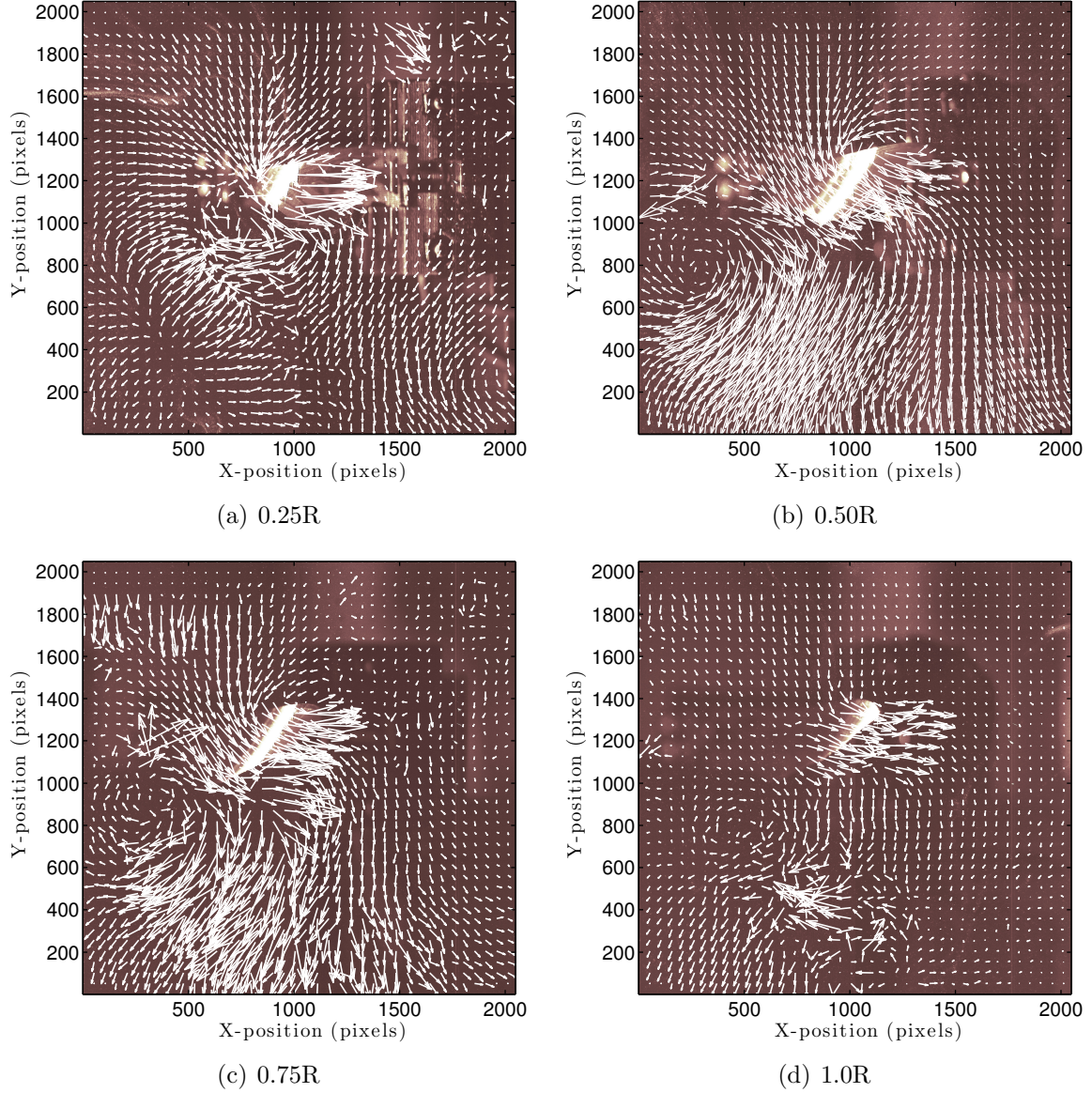
(d) 1.0R

Figure 5.12: Phase 8 false color image vector overlay of the 45° wing at 0.25R, 0.5R, 0.75R, and 1.0R at A=0.4 during the downstroke.

This depiction is particularly useful in illustrating the contextual framework of the depth of the flow structures around the wing. The matriculation of the two visible vortexes are evident in the progression down the span from root-to-tip. The fully developed vortex structures are clearly visible at 0.5R and 0.75R; the clockwise vortex from the upstroke is visible in the lower left corner, and the counterclockwise vortex from the current half stroke is visible around the wing. At 0.25R the ingredient of

235

the rotational patterns manifest near the wing root as air is being draw into the wing from above, and being expelled below. Further, the demarcation marking the collision with the previous upstroke vortex begin to form, and the opposing velocity gradients intersect forming counter-rotating flow patterns. At the wing tip, 1.0R, the counterclockwise vortex attached to the wing has dissipated and the remaining vestige is purely translational u-velocity that is created from the simple linear motion of the wing pushing the air along its path. The clockwise vortex is barely visible, and has also essentially dissipated its strength at 1.0R. Figure 5.13 shows the vertical velocity at $1\times$ chords below the wing for all four span locations illustrating how the vertical velocity below the wing changes as a function of span location.
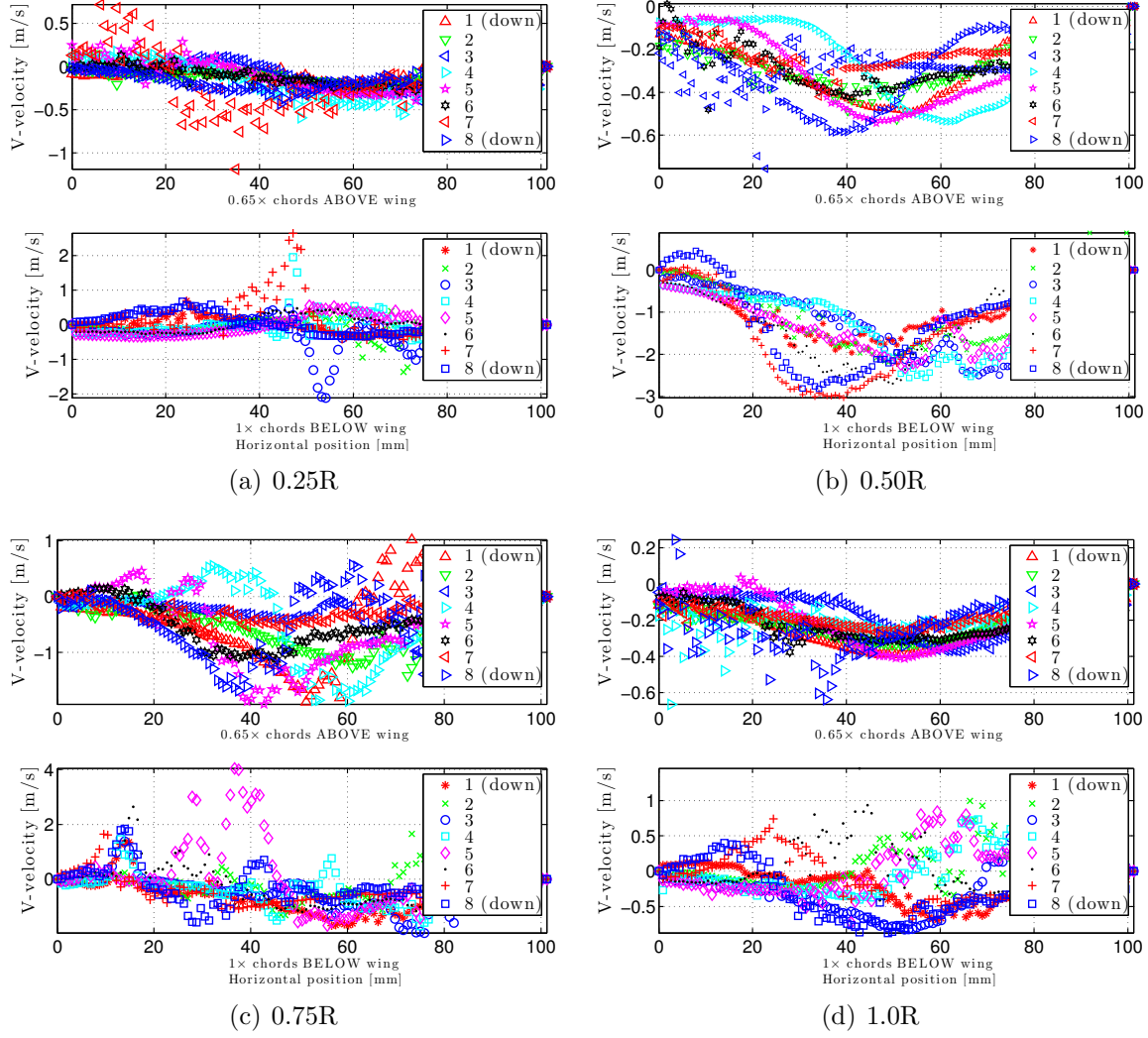
Figure 5.13: 8 phase vertical velocity profiles at 1× chords below the 45° wing at 0.25R, 0.5R, 0.75R, and 1.0R at A=0.4.

The velocity below the wing increases from 0.25R to a maximum at 0.50R, and then begins to decrease again through to the end of the wing at 1.0R. Figure 5.14 shows a plot of the mean velocities calculated for various chord locations below the wing at each phase.

(a) 0.5× chords below   (b) 1.0× chords below

(c) 1.5× chords below   (d) 2.0× chords below
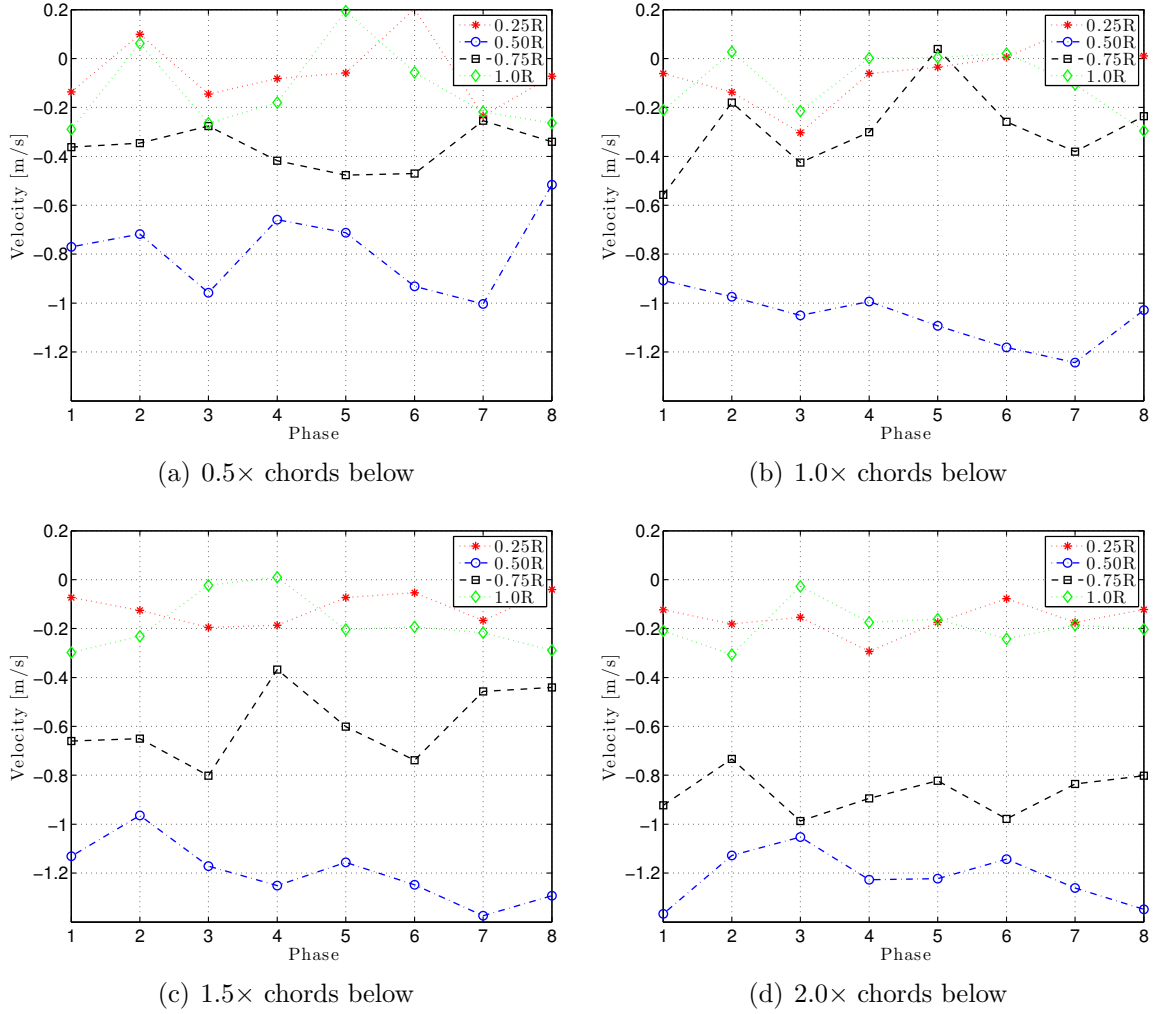
Figure 5.14: 8 phase mean vertical velocity at various chord lengths below the wing at 0.25R, 0.5R, 0.75R, and 1.0R.

The max velocity, and therefore the maximum lift production, occurs for the laser plane corresponding to the mid-span, 0.5R, which is also coincident with the location of the maximum chord, $\bar{c} = 20$mm. This makes intuitive sense since the location of the maximum chord is also near the location of the mean aerodynamic center (MAC) of the wing, and the center of pressure (CoP). If the locus of all force points across the wing surface were reduced to a single force vector it would be affixed to the CoP Therefore, the maximum velocity below the wing should occur in a planar slice through the mid-span, which contains $\bar{c}$, MAC, and CoP. Because the wing bends and

slightly twists during deceleration to rotation, the effective span decreases slightly, temporarily moving the mid-span closer to the tip.

5.3.4   Thrust From Vertical Velocity.

The mean velocities above and below the wing are used to calculate the induced velocity (ν_i), which is assumed equal to the velocity the volume of air in a given stream tube reaches as it is accelerated through a hypothetical actuator propeller disk. The mean forces developed during a flap cycle are approximated using a modification of the *Rankine-Froude* axial actuator disk model, more commonly known as disk momentum theory. The model stipulates purely axial flow through a fixed rotating disk, assuming an ideal, incompressible fluid operating medium. The rotating disk imparts a velocity to the fluid, and a resulting pressure differential ensues between the upper and lower surfaces of the actuator disk [81]. Figure 5.15 shows a graphic of an idealized actuator disk.
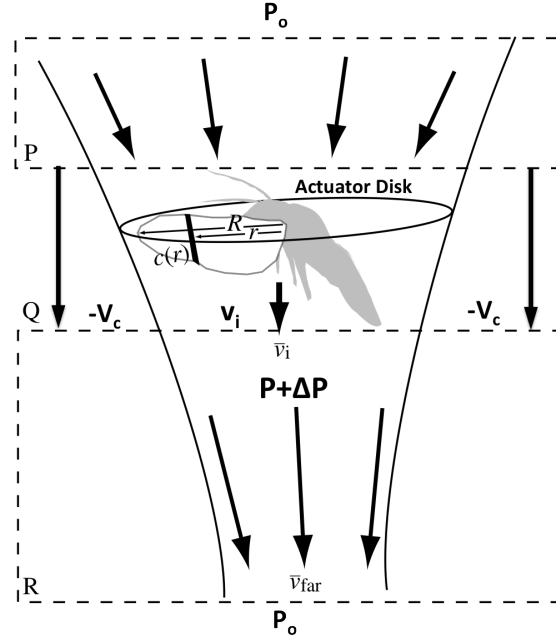
Figure 5.15: **Graphical example of a *Rankine-Froude* pulsed actuator disk model used in axial force momentum calculations. (P) is the location of the the far-field in-flow. (Q) is the near-field location in vicinity of the actuator disk. (R) is the location of the far-field out-flow. (ν_i) is the induced flow velocity at the disk. (ν_{far}) is the induced velocity in the far-field—(*adapted with permission from JEB*) [72, 75, 81].**

Referring to the Figure 5.15, the pressure inside the arc of the pulsed actuator disk is greater than the pressure above the disk, leaving a discontinuity in the pressure field. Unlike solving for velocity and pressure through a pitot static tube, where the functions are continuous, and Bernoulli's equations for an incompressible, inviscid flow, can be used to solve for the velocity and pressure conditions downstream of the inlet flow conditions, the discontinuity in the actuator disk field requires independent application of Bernoulli's equations above and below the disk [81]. The total hydraulic head (H_o), the sum of the elevation head and static pressure head, for the upstream hydraulic head (H_{us}), section is equivalent to Equation 5.1

$$H_{us} = P_o + \rho\frac{V_c^2}{2} = P + \rho\frac{(V_c + \nu_i)^2}{2} \tag{5.1}$$

where V_c is the outside free stream velocity (V_c), ρ is the air density (ρ), ν_i is the averaged induced velocity over the entire disk, $\bar{P}$ is the mean pressure ($\bar{P}$), and the

total pressure (P_o) (*far-field*) and is equal to the sum of the static and dynamic pressures [59, 81]. The downstream total head can then be represented similarly by Equation 5.2

$$H_{ds} = P_o + \rho\frac{(V_c + \nu_i)^2}{2} = P + \Delta P + \rho\frac{(V_c + \nu_i)^2}{2} \tag{5.2}$$

where the only difference is the term $P + \Delta P$, which is the pressure differential below the disk as a result of the force imparted to the fluid by the actuator disk [59, 81]. Manipulating the above expressions for the upstream and downstream head, and equating like terms, leaves a single expression in terms of the pressure differential, ΔP, shown by Equation 5.3 [59, 81].

$$\Delta P = \rho \left(V_c + \frac{\nu_i}{2} \right) \nu_i \tag{5.3}$$

Equating the flow at the far field and at the disk:

$$P + \frac{mg}{A_d} + \rho\frac{\nu_i^2}{2} = P_o + \rho\frac{\nu_{far}^2}{2} \tag{5.4}$$

where mg is opposed by the mean vertical force (*or thrust*), F_v, and ν_{far} is:

$$\nu_{far} = \sqrt{\frac{2mg}{\rho A_d}} \tag{5.5}$$

arranging the weight terms on the left and the momentum flux terms on the right:

$$mg = \frac{\rho \nu_{far}^2 A_d}{2} \tag{5.6}$$

rearranging and substituting $\nu_{far} = 2\nu_i$:

$$mg = 2\rho\nu_i^2 A_d \tag{5.7}$$

Preserving continuity, as the area entrained by the net momentum flux, *stream tube of flow*, narrows in the far-field, the area necessarily varies inversely with the induced velocity, and the far-field area is thus, $A_{far} = \frac{A_d}{2}$. This is the standard result shown by [35, 72, 81]. A straightforward application of Newton's 2nd law leaves a force balance expression in terms of the total average thrust $(\bar{T})$, produced as a function of the actuator disk radius (R_d), given in Equation 5.8 [81, 59].

$$F_v \equiv -\bar{T} = mg = \pi R_d^2 \rho \left(V_c + \nu_i\right)^2 = 2A_d \rho \left(V_c + \nu_i\right) \nu_i \qquad (5.8)$$

where A_d is the generalized actuator disk area (A_d); and for flapping wing applications, A_d is twice the swept area of a single wing. The resultant direction of $\bar{T}$ is opposite the direction of ν_i, and in a hover condition, ν_i is assumed vertically down (*towards the earth*), and $\bar{T}$ is pointing vertically up (*towards the sky*). In hover, or any static condition where the free stream velocity is zero, $V_c = 0$, and Equation 5.8 is reduced to the form shown in Equation 5.9 below [35, 59, 81].

$$F_v \equiv \bar{T} = 2A_d \rho \nu_i^2 \qquad (5.9)$$

Equation 5.9 can be applied to the AFIT FWMAV to calculate the peak thrust at the wing tip for a specified set of flapping parameters. The equation requires slight modification, where ν_i is replaced by the average tip velocity, $\overline{U_t}$, given in Equation 3.13, and the actuator blade disk area, $A_d = \pi r^2$, is replaced by the swept area of a single AFIT flapper wing, which is approximated by the area of a circular arc, $A_{arc} = \frac{r^2 \Phi}{2}$, where the radius of the arc segment, r, is equal to the wing length from tip to root, R, and Φ is the actual swept angle in radians from the optical tracking results in tabulated in Table3.2. Substituting the above modifications into Equation 5.8 results in an expression for the maximum expected thrust (T_{max}), applied to a

flapping wing specimen, given below in Equation 5.10.

$$F_{v_{max}} \equiv T_{max} = 4\rho\omega^2\Phi^3 R^4 \tag{5.10}$$

After substituting the actual values of the wing and the test conditions used in these experiments into Equation 5.10, the theoretical maximum thrust, T_{max} for the PIV experiments conducted heretofore are catalogued in Table 5.6.

Table 5.6: Horizontal Wing—Maximum Expected Thrust

Angle Stop	A	Φ [deg]	ω [Hz]	T_{max} [mgF]
30°	0.40	87.8	20	445
45°	0.35	77.5	22	368
45°	0.40	88.5	22	546
45°	0.45	99.7	22	790
60°	0.40	107.5	22	968

This derivation assumes an idealized scenario, where the assumption of an ideal, incompressible, inviscid fluid does not accurately represent the actual operating conditions. Therefore, any periodicity in the pulsed momentum flux as a result of cyclic wing flapping, versus uniform rotor rotation, is ameliorated by the presence of viscous forces in the far field, meaning ν_{far} will vary only slightly from the strictly uniform rotor blade disk analysis. Ellington stipulated in his treatise on the development of a comprehensive vortex theory of animal flight that although accounting for the periodicity of far field wake is a more satisfying physical description of flapping flight phenomenon, his experimental findings of insects with a *horizontal* stroke plane, i.e. the *Manduca Sexta*, resulted in less than a 20% difference in the induced power and induced velocity, as compared to those calculated from an application of the exceedingly more simplistic *Rankine-Froude* momentum disk theory [35].

The average 8-phase induced velocities derived from the PIV results shown in the preceding sections, can be substituted in Equation 5.9 to calculate the average

sectional thrust, *vertical force*, produced by the flapping wing PIV experiments. The mean thrust, calculated from the vertical velocity profiles above and below the wing, are substantially lower than both the maximum expected thrust at the wing tip, and the average vertical force recorded by the Nano-17 force balance. The velocity profiles are measured across a differential arc area (dA_{arc}), of the wing, spanned by the 4mm thick laser sheet.

In the limit, as the number of cross sectional measurements taken approach infinity, the three dimensional nature of the flow would become more evident—the same *u-shaped* velocity profile will grow in depth as the laser sheet progresses from the wing base to the wing tip. An infinite number of PIV measurements summed along the span is necessary to numerically calculate the exact thrust produced from the induced velocity field below the wing. Armed with measurements from only a few span locations, a coarse function of ν_i in terms of the wing span, R, was developed to integrate across the span to calculate an estimate of the expected thrust from the induced velocity across the entire span. A first order, linear equation was fit to a three point line plot of the the induced velocity and span location. The coordinate pairs were: *i*) at the root, where R=0mm and $\nu_i = 0$. The value of $\nu_i = 0$, at R=0, is assumed because of the no-slip condition, and zero motion was assumed at the wing root/linkage connection point, *ii*) at the mid-span where $R = 25$mm and $\nu_i =$ the mean induced velocity calculated from the 8-phase PIV 2-D velocity line extractions at each test point, and *iii*) at the tip where $R = 50$mm and $\nu_i = U_t$, the average tip velocity, U_t, was chosen for the value of ν_i at $R = 50$mm. The linear fit to the plot of ν_i vs. R is of the form $\nu_i(r) = ar + b$, where the wing location, r, is in mm, and the coefficients, a and b, for each test configuration are listed in Table 5.7 below.

Angle Stop	A	Φ [deg]	(a)	(b)
30°	0.40	87.8	0.0614	-0.8575
45°	0.35	77.5	0.0594	-0.8064
45°	0.40	88.5	0.0679	-0.8852
45°	0.45	99.7	0.0768	-0.9778
60°	0.40	107.5	0.0825	-1.03

Table 5.7: Coefficients, a & b, For $\nu_i(\mathrm{r}) = ar + b$

The function for ν_i was integrated across the area of a circular arc, which is invariant, given by Equation 5.11 below.

$$F_x \equiv \bar{T} = \int_0^{\mathrm{R}} \int_0^{\Phi} 2\rho\nu_i^2 dA$$

where:

$$dA = r\mathrm{d}\Phi\mathrm{dr}$$

substituting:

$$T = \int_0^{\mathrm{R}} \left(\int_0^{\Phi} 2\rho\nu_i^2 r d\Phi \right) \mathrm{dr}$$
$$= (2\rho) \int_0^{\mathrm{R}} \left(r\nu_i^2 \int_0^{\Phi} d\Phi \right) \mathrm{dr} \tag{5.11}$$
$$= (2\rho\Phi) \int_0^{\mathrm{R}} r\nu_i^2 \mathrm{dr}$$

and:

$$\nu_i(\mathrm{r}) = -ar + b \qquad (\text{with } r \text{ in mm})$$

substituting:

$$\bar{T} = (2\rho\Phi) \int_0^{\mathrm{R}} r\left(-ar + b\right)^2 \mathrm{dr}$$

The resultant expression for $\bar{T}$ is a function of the spanwise location, r, along the wing. Figure 5.16 shows a 3-D illustration of the differential area element $(rdrd\phi)$ with respect to the total angle subtended by the flap arc, Φ.
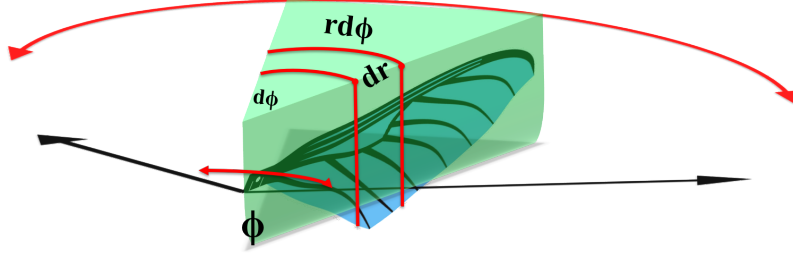
Figure 5.16: Illustration of the differential arc area used to calculate the projected thrust along the entire span from the single PIV data location at mid-span.

Figure 5.17 shows $\bar{T}$ for the 30°, 45°, and 60° angle stop wings calculated for each phase using Equation 5.9, and the mean induced velocity calculated for each phase plotted against a normalized flap cycle of the vertical force balance data recorded during each PIV test.
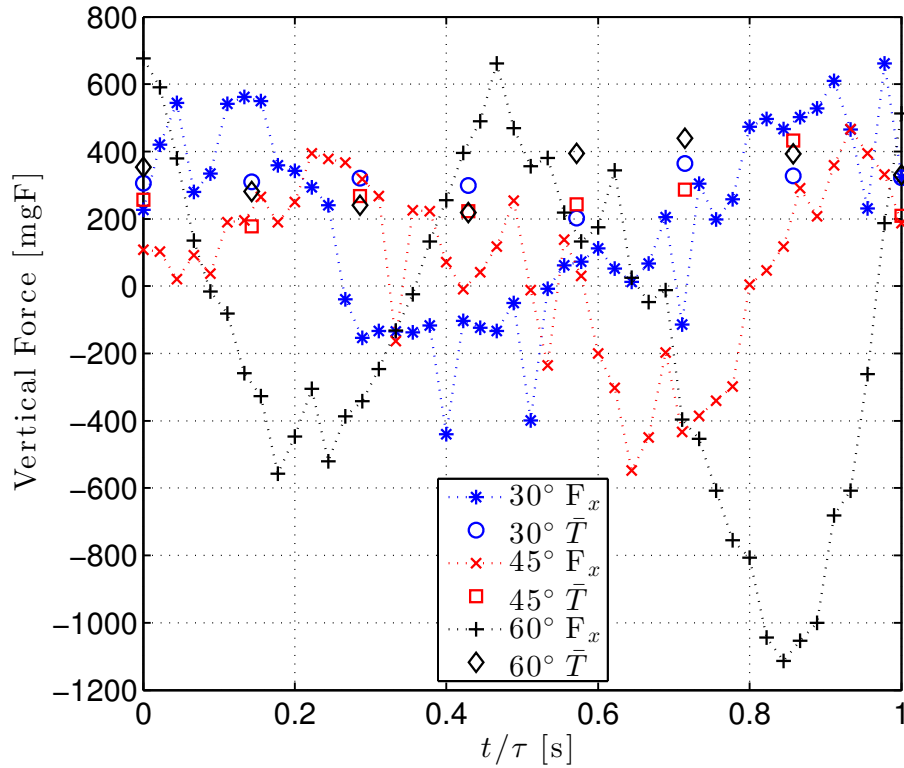
Figure 5.17: 30°, 45°, and 60° wing mean thrust per phase, $\bar{T}$, using the mean induced velocity calculated per phase from the velocity above and below the wing at 1× chord plotted against the vertical force, F_x, measured by the Nano-17, for a normalized flap cycle t/τ.

The vertical force balance data shows considerable more fluctuation during the flap cycle than do the thrust numbers calculated from the vertical component of the PIV velocity flow field. The wing is mounted to the force balance 63mm in front $(+z)$, and 10mm to the left $(-y)$ of the balance centroid, and the locus of the vertical force concentration at the CoP is another 20-25mm left $(-y)$ of the balance center. This offset contributes to the magnitude of the local oscillation during a flap cycle. Table 5.8 shows the phase averaged thrust, the total cycle thrust calculated from the first order coefficients in Table 5.7 and the mean of the integrated approximation derived in Equation 5.11, and the average vertical force, F_x, recorded by the Nano-17 balance for the tests conducted at the mid-span, 0.5R.

Table 5.8: **Thrust & Mean Vertical Force For Horizontally Mounted 30°, 45°, and 60° Wings.**

Angle Stop	A	$\bar{T}_1$	$\bar{T}_2$	$\bar{T}_3$	$\bar{T}_4$	$\bar{T}_5$	$\bar{T}_6$	$\bar{T}_7$	$\bar{T}_8$	$\bar{T}_{tot}$	F_x	$\Delta\%$
30°	0.40	305.3	309.8	321.0	298.7	201.6	363.9	328.0	322.8	375.0	449	-16
45°	0.35	229.9	249.7	300.4	269.7	274.9	331.4	338.1	175.8	523.0	443	+18
45°	0.40	257.1	177.9	267.1	223.1	242.9	286.6	432.6	208.9	532.0	584	-9
45°	0.45	280.1	203.3	284.7	160.6	260.6	378.0	409.4	243.7	549.0	700	-21
60°	0.40	353.8	281.4	240.3	218.0	394.9	438.9	392.8	329.8	658.0	813	-19

The integrated first order approximation renders a good estimate of the vertical force produced, especially since it only requires a single measurement at the mid span of the wing. The errors between the force balance measurement and the PIV velocity model was approximately 20%. Figure 5.18 show the curves of the integrated functions plotted across a linearly spaced vector from 0-50mm, graphically illustrating the predicted thrust per unit span with the mean Nano-17 vertical force values for reference.

(a) Varying Wing Angle

(b) Varying Amplitude

(c) Varying Span Location
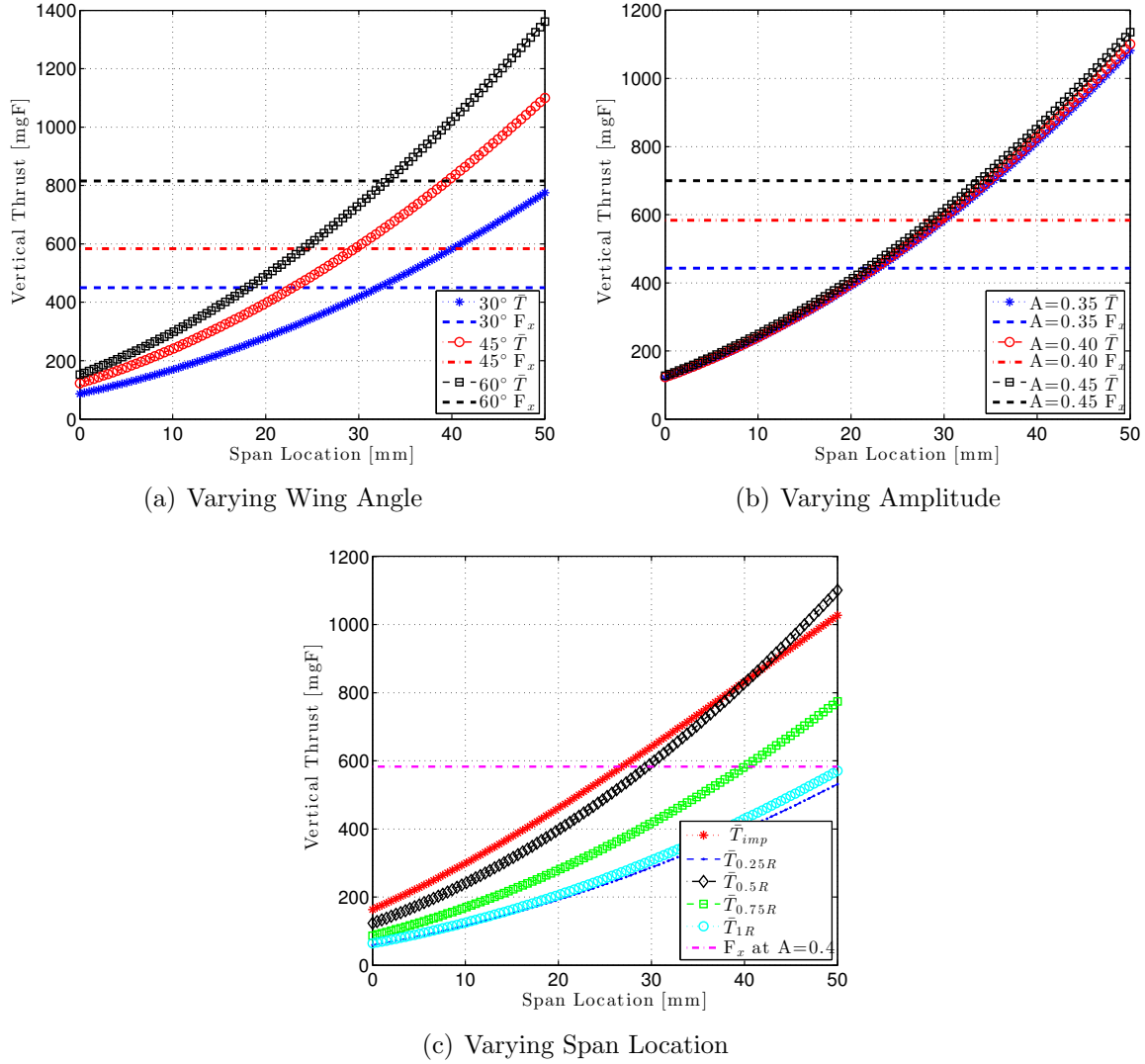
Figure 5.18: Curves of the integrated thrust/unit span functions plotted from 0-50mm along the span, which were derived from integrating the equations for the induced velocity as a function of span location, $v_i(\mathbf{r})$, over the differential swept area $r dr d\theta$. The estimate of the total thrust is the area from 0mm$< x <$50mm under each curve. The dashed lines of constant force represent the mean vertical force, $\overline{F_x}$, measured by the force balance.

Referring to Figure 5.18, in all cases, curves from the resulting polynomial thrust equations over predicted the thrust moving towards the wing tip; however, the average thrust calculated from the area under the curves were all predominately about 20% below the measured Nano-17 balance data. The primary reason for characterizing this momentum flux technique as a *coarse* method of approximating vertical forces from velocity is the reliance on a single empirical measurement between the

248

root and tip, and because the chord varies constantly along the span. To examine the postulate that increasing the number of PIV measurements along the span will increase the fidelity of the thrust prediction, measurements were taken at the following span locations: 0.25R, 0.5R, 0.75R, and 1.0R at A=0.4. The induced velocity was calculated at each span location, and the equation to the fit of induced velocity vs. span location was expanded from a linear fit to a second order polynomial. The new (ν_i, r) coordinate pairs are $\nu_i = [0, -0.0841, -0.9579, -0.4956, -0.1555]$m/s and $r = [0, 12.5, 25, 37.5, 50]$mm. Figure 5.18(c) shows the thrust curves for all the individual span locations and the *improved* curve utilizing multiple span locations to develop the polynomial approximation. At this drive amplitude (A=0.4) and stroke angle ($\Phi = 88.5°$), Table 5.9 lists the mean thrust calculated at each individual span location, and the improved multi-point mean thrust, using the induced velocity at all four span locations to compute a 2nd order polynomial function of $\nu_i(r)$, integrated across the span to calculate the mean thrust, compared to the measured value of the vertical force, F_x, on the Nano-17.

Table 5.9: Vertical Thrust At 0.25R, 0.5R, 0.75R, & 1.0R vs. F_x For The 45° Wing.

Span Location	A	Φ [deg]	$\bar{T}$ [mgF]	F_x [mgF]	$\Delta\%$
0.25R	0.40	88.5°	258	583	-55.7
0.50R	0.40	88.5°	532	583	-8.8
0.75R	0.40	88.5°	375	583	-35.7
1.0R	0.40	88.5°	276	583	-52.7
Multi-Point	0.40	88.5°	565	583	-3.1

The multi-point thrust calculation is the best approximation to the actual measured force values. However, the difference between the improved multi-point vertical thrust approximation and the single point predictor is only 5%. Taking into consideration the amount of effort, data storage, and processing overhead required to take subsequent PIV measurements, the single point measurement at the mid-span is sufficient for estimating vertical force in future design iterations. Regardless of

249

the number of measurements taken along the span, using this method will always require interpolating or estimating the flow behavior, i.e. the induced velocity between measurements, which introduces error and uncertainty in the resulting thrust calculation. A more comprehensive approach, less susceptible to error and uncertainty, is to measure the entire vertical flow field across the stroke simultaneously. Recording the velocity at all points above and below the wing simultaneously will permit calculating the total vertical thrust produced by the wing in a single measurement. The next section will detail a series of PIV tests with the wing mounted vertically in the test chamber.

5.4 PIV Results—*Vertical Wing Orientation*

Testing was conducted on the 30°, 45°, and 60° wings mounted vertically in the test chamber. The entire wing and force balance mounting structure was rotated 90° about the wing's spanwise axis, orienting the wing vertically in the test chamber with the TE facing the stereo cameras, while also ensuring the laser sheet was not moved from the horizontal testing configuration to preserve the calibration, which positioned the laser sheet between the wing and the cameras. The primary goal of this unorthodox test configuration was to capture the entire vertical flow field as it was expelled through the laser sheet. In this orientation, the vertical velocity component responsible for lift generation, is now the out-of-plane horizontal stereo w-velocity component. Capturing the entire velocity field through the laser sheet permitted direction calculation of the total thrust produced over the entire swept area of the wing, and yield new insight into the flow physics.

A secondary goal of the vertically mounted wing configuration is data verification. The vertical testing was conducted with the wing placed at various chord positions in front of the laser sheet, while during the horizontal testing, the laser sheet intersected

the wing at specific span locations, and the 2-D vertical velocity profiles were extracted along lines of constant y-coordinate at specific chord distances above and below the wing. Comparing the intersection of any of these two measurement planes should reveal similar 2-D velocity profiles. The horizontal v-velocity profile at specific chord distances beneath the wing were compared to the the $(-)w$-velocity profile from the vertically mounted wing at the same chord distance behind the laser sheet to verify the veracity and fidelity of the flow field data.

5.4.1   Horizontal & Vertical Plane Intersection.

Plotting the velocity profile at the intersection of the horizontal and vertical planes is used to verify data integrity, and to confirm the flow field is characterizing actual fluid physics, and not capturing testing anomalies, reflections in the test chamber, or camera artifacts. This research effort is not an investigation in numerical aerodynamic methods or PIV testing procedures; therefore, the intersection of a few sample test points are shown to satisfy the determination of data fidelity, and confirm the reality of the flow physics depicted. Phase 6 for the 30°, 45°, and 60° wings was selected in both the horizontal and vertical data files, and the LE and TE were selected from the image where the wing was most parallel to the camera in the horizontal test, and the most vertical in the vertical test with a built-in MATLAB® screen capture tool. The vertical file was selected that was 1× chord away from the laser sheet, and a w-velocity profile, normal to the flapping plane, at several locations around the mid-span was extracted and stored in an array. The horizontal file was selected with the laser sheet at the mid-span, 0.5R, and a v-velocity profile at 1× chord below the wing was extracted and stored in the same array as the vertical w-velocity profile. Figure 5.19 shows the phase 6 vertical v-velocity component, also normal to the flapping plane, at approximately 1× chords below the wing at 0.5R for the 30°, 45°, and 60°
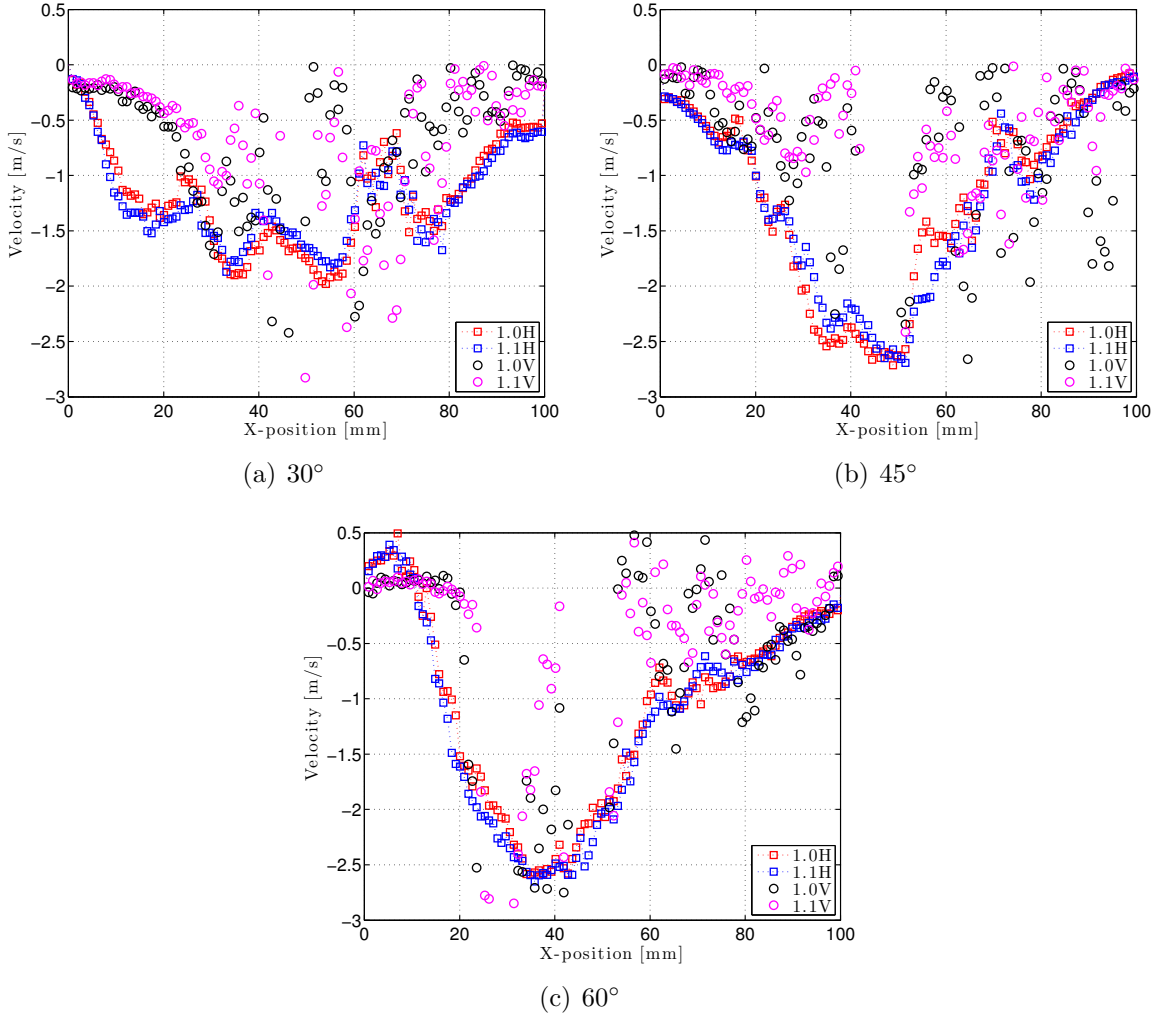
wings at A=0.4.

(a) 30°

(b) 45°

(c) 60°

Figure 5.19: Horizontal and vertical wing v and w-velocity plane interesection at phase 6 at approximately $1\times$ chords below the wing, measured at the mid-span, at **A=0.4.** Lines at $1.1\times$ chords below the wing are also shown to account for the coarseness in measuring the LE and TE on the vertical wing since it is located behind the focal plane of the camera and barely in view.

The velocity profiles at the plane intersection of the mid-span and $1\times$ chord below the wing are not exact matches, but they do follow the same general trend, and more importantly, their magnitudes are very close, confirming the data depicted represents physical phenomena in the flow field. The w-velocity measurement from the vertical wing contains considerable oscillation, and is more noisy than the v-velocity from the horizontal wing. However, the w-velocity is not a direct measurement, but rather it is

a derived measurement from the two stereo cameras, while the v-velocity vector field results from direct camera particle displacement measurements. With the fidelity of the data satisfied, the next section will show a sample of the vertical PIV tests.

5.4.2   30°, 45°, 60° Comparison at A=0.4.

Testing was conducted on the 30°, 45°, 60° vertically mounted wings at A=0.4. Since the wing is vertically mounted in a non-flight orientation, the stereo velocity contour plots are not as instructive into the flow field physics as the horizontal wing; however, the total vertical v-velocity field responsible for lift production, is now oriented horizontally, expelled through the laser sheet, and can be computed across the entire stroke cycle as the stereo w-velocity component. The goal of the vertically mounted wing testing is to capture the total vertical thrust produced by the wing simultaneously without necessitating splicing together multiple spanwise slices across multiple phases. The reference coordinate system used by the Nano-17 balance and the PIV system remains fixed. The force balance and the wing mounting interface remained constant, rotated 90°; therefore, the sense and direction of the forces do not change. The PIV system measures velocity in the same three planes, but the velocity components produced by the wing it is measuring is different from the horizontal testing. The vertical velocity component was (v) measured in the horizontal plane, and is now ($-w$) measured in the vertical plane; the spanwise component was (w) measured in the horizontal plane, and is now ($+v$) measured in the vertical plane, and finally the horizontal, or axial, velocity component remains (u) in both measurement planes. Figure 5.20 shows the stereo velocity vector contour plots for the vertically mounted 30°, 45°, 60° wings at A=0.4, and w-velocity profiles, normal to the flapping plane, at ± 10% of the mid-span, corresponding to y=20mm to y=30mm for all eight phases. The wing is oriented with the tip pointing skyward, so phases 1 and 8 correspond

with the wing near the top-right corner of the image plane, while the wing position in phases 4 and 5 correspond with the wing tip near the top-left corner of the image plane.
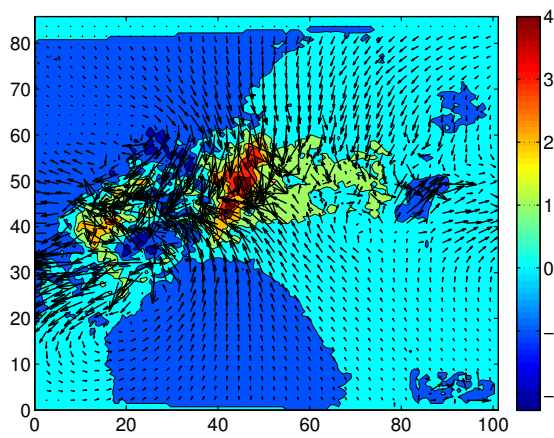
(a) 30°
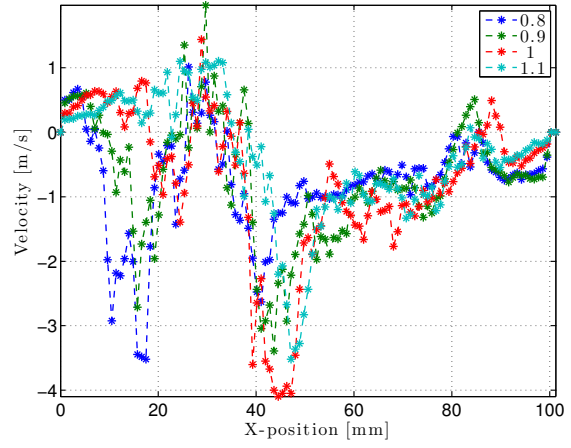
(b) 30°

(c) 45°

(d) 45°

(e) 60°

(f) 60°

Figure 5.20: Phase 1

255

(a) 30°

(b) 30°

(c) 45°

(d) 45°

(e) 60°

(f) 60°

Figure 5.20: Phase 2

256

(a) 30°

(b) 30°

(c) 45°

(d) 45°

(e) 60°

(f) 60°
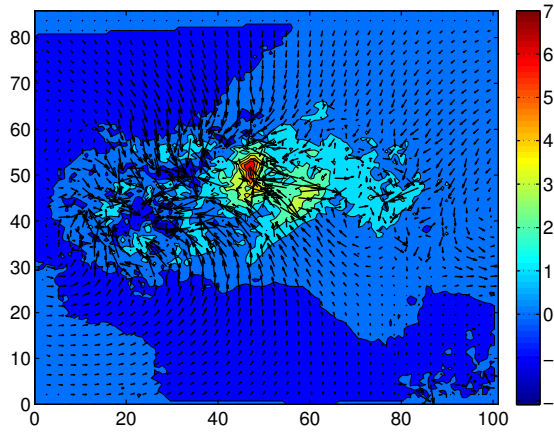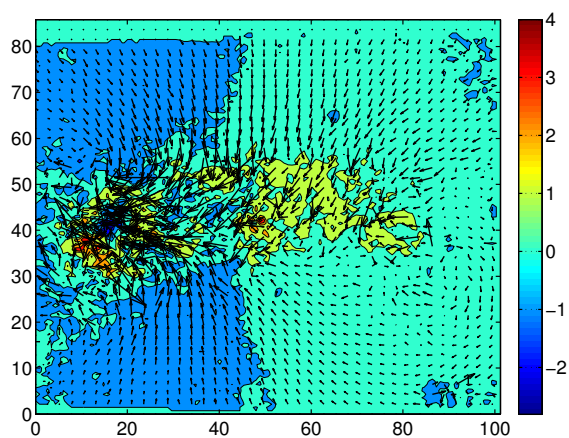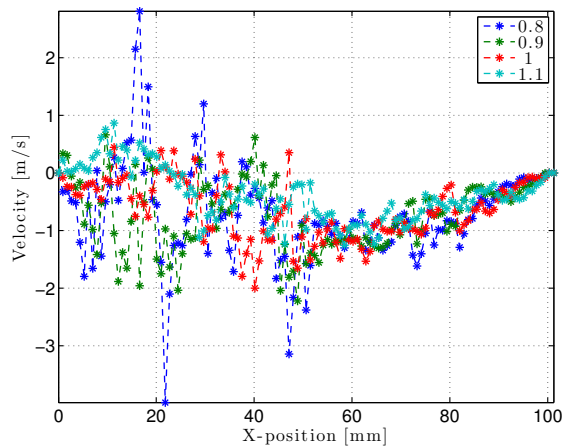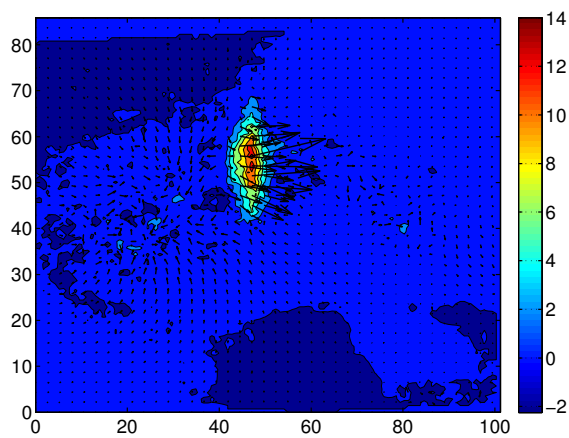
Figure 5.20: Phase 3

(a) 30°

(b) 30°
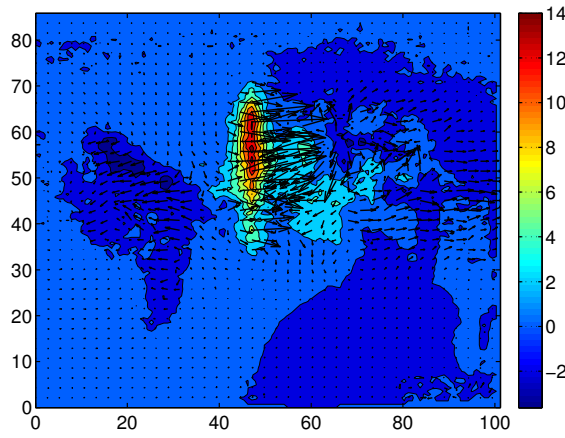
(c) 45°
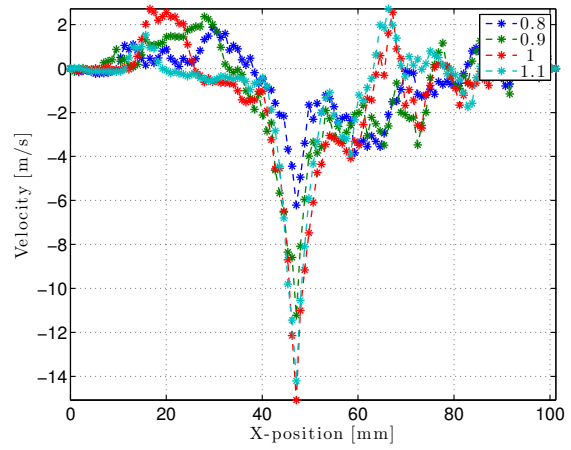
(d) 45°
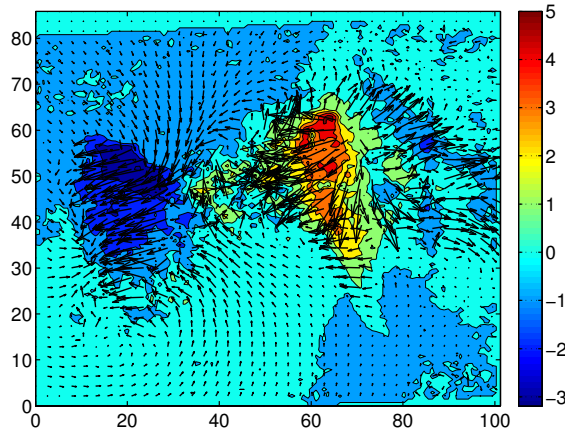
(e) 60°
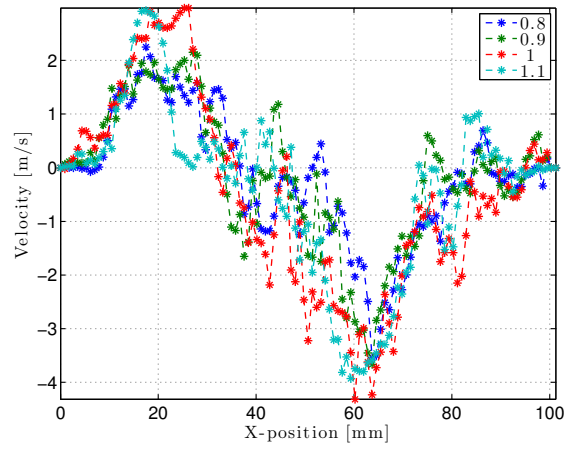
(f) 60°

Figure 5.20: Phase 4
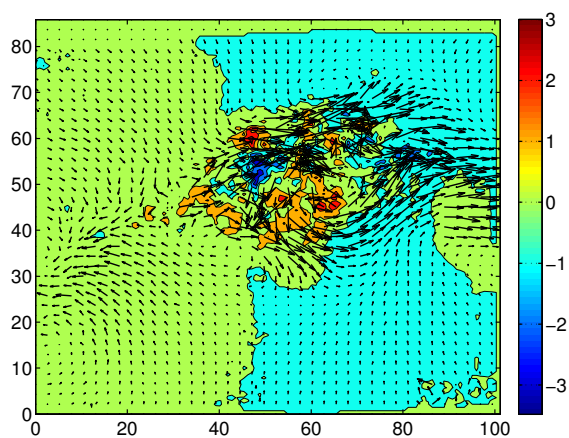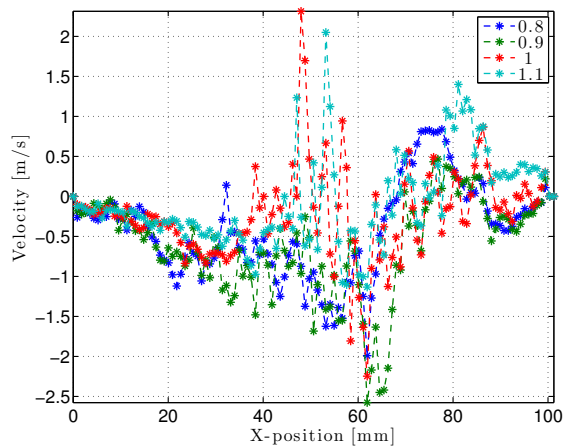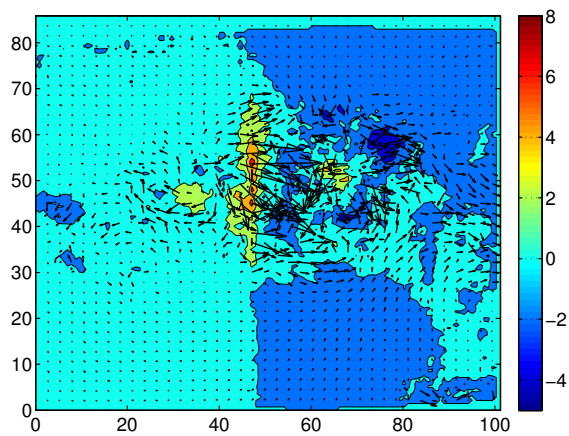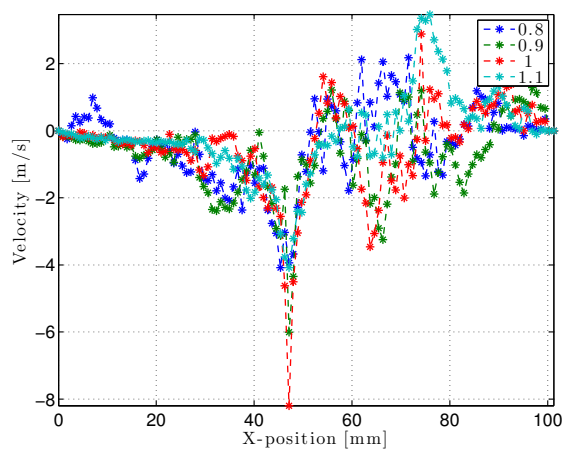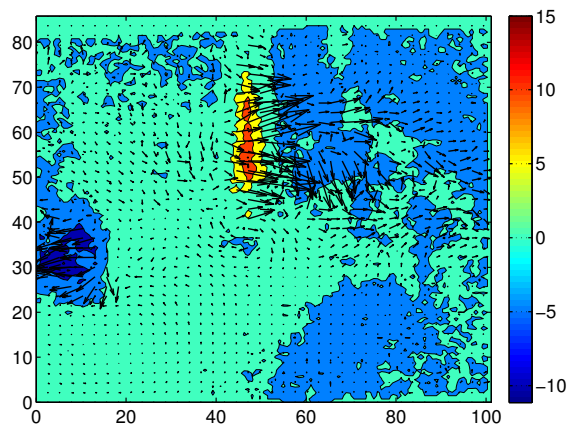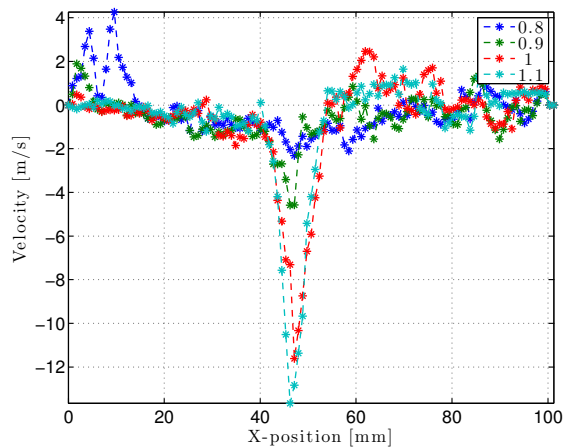
258

(a) 30°

(b) 30°

(c) 45°

(d) 45°

(e) 60°

(f) 60°

Figure 5.20: Phase 5

259

(a) 30°

(b) 30°

(c) 45°

(d) 45°

(e) 60°

(f) 60°

Figure 5.20: Phase 6

260

(a) 30°

(b) 30°

(c) 45°

(d) 45°

(e) 60°

(f) 60°

Figure 5.20: Phase 7

261

(a) 30°

(b) 30°

(c) 45°

(d) 45°

(e) 60°
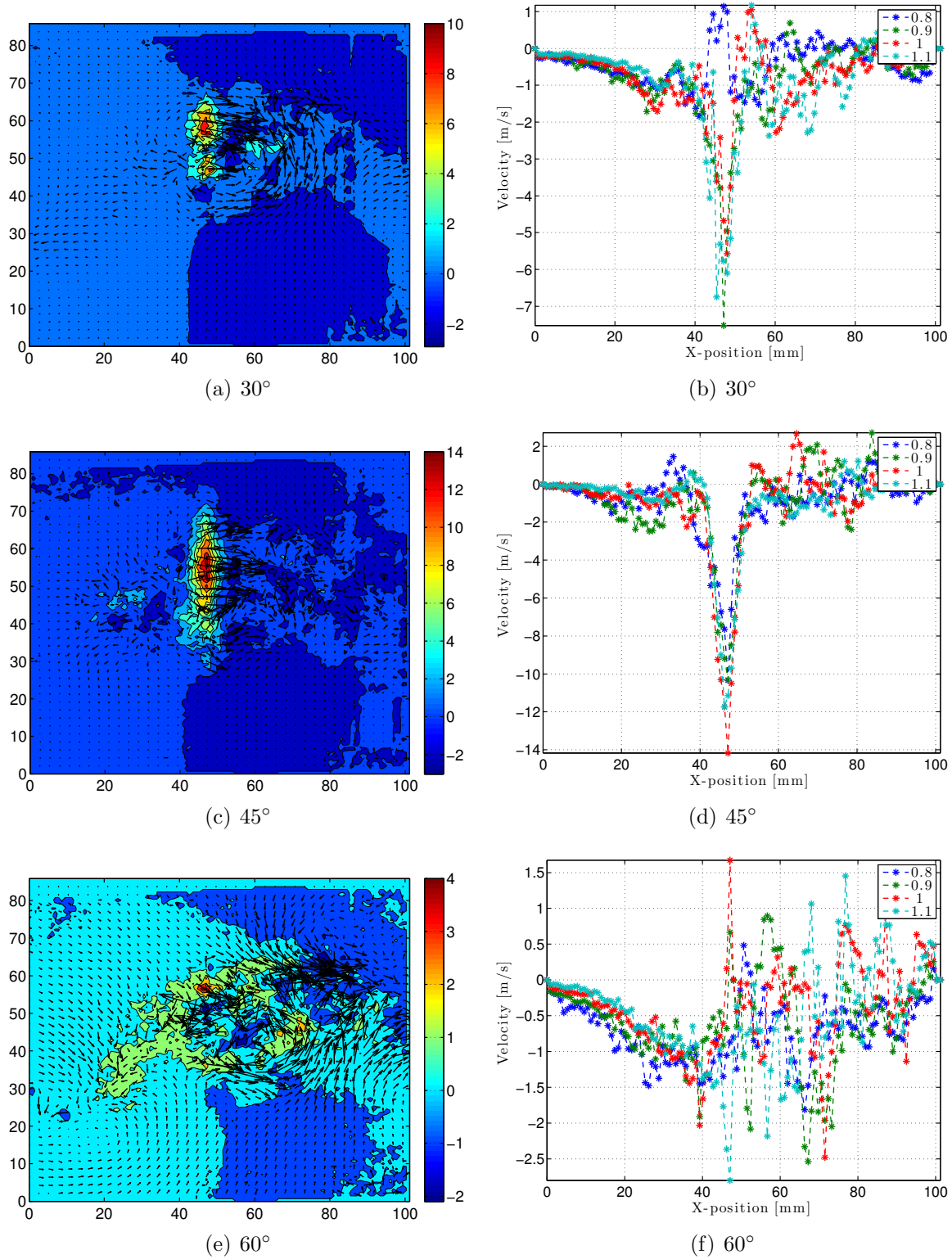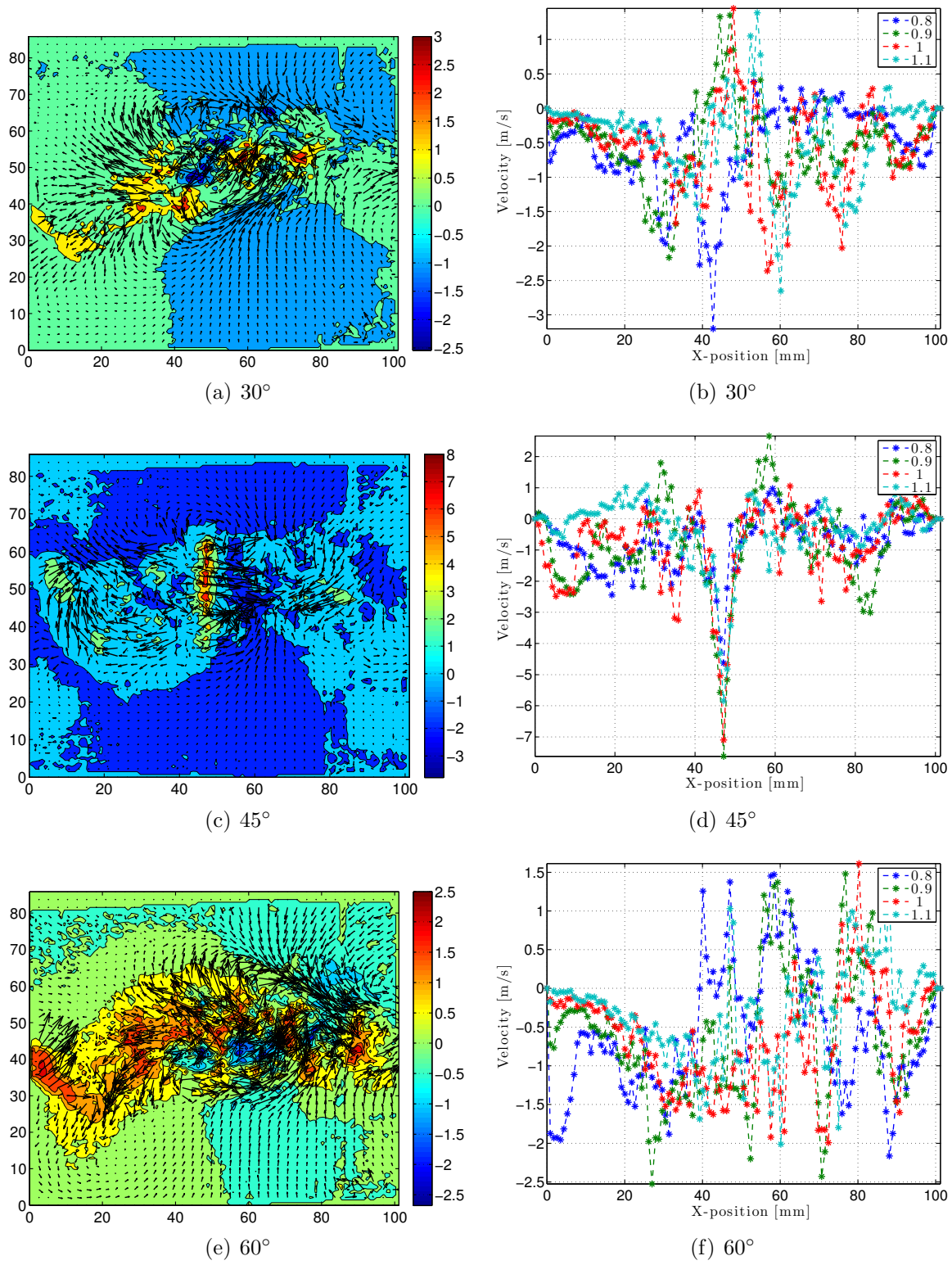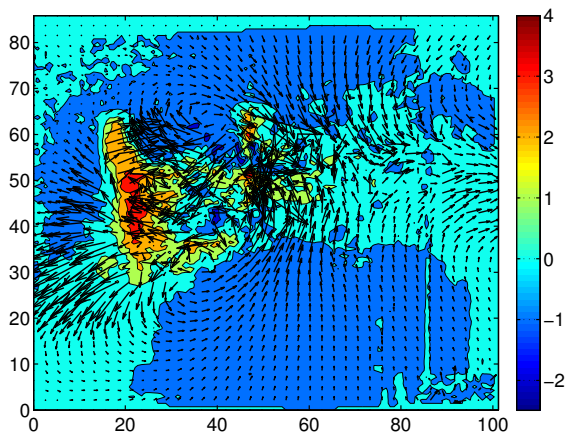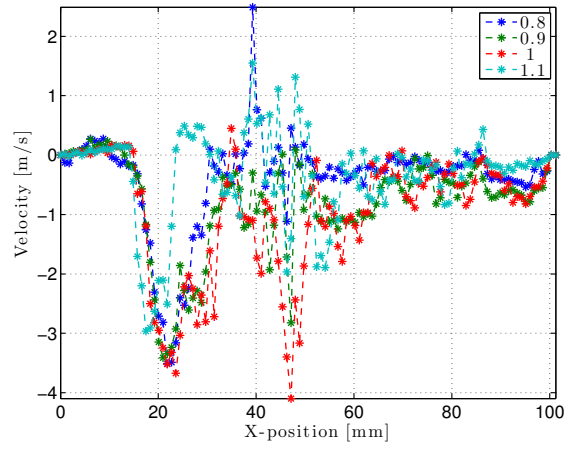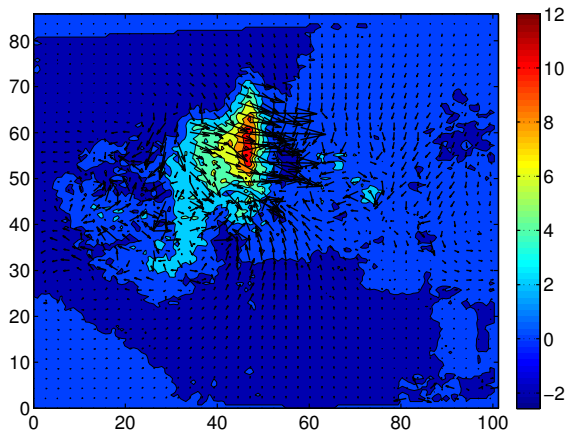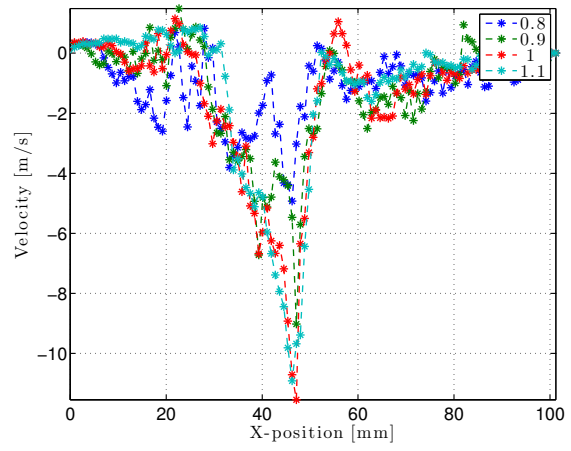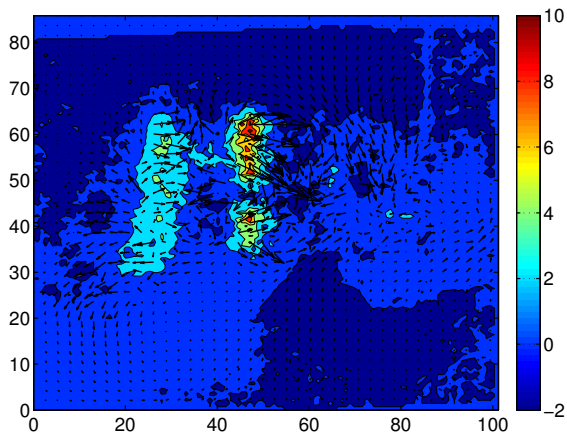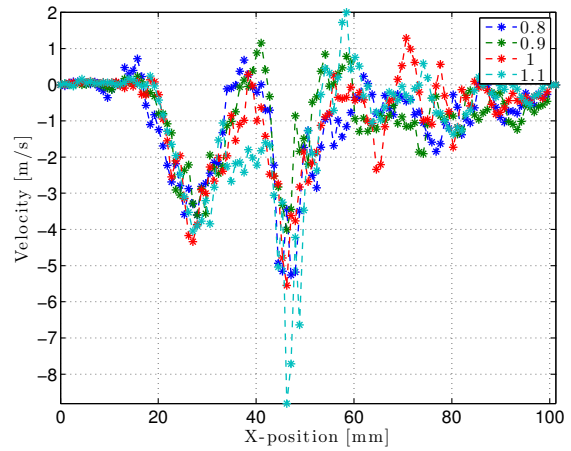
(f) 60°

Figure 5.20: Phase 8

262

The w-velocity component, responsible for lift generation, is clearly evident through-out the stroke cycle. On the far left of the images in phase 4, and to a lesser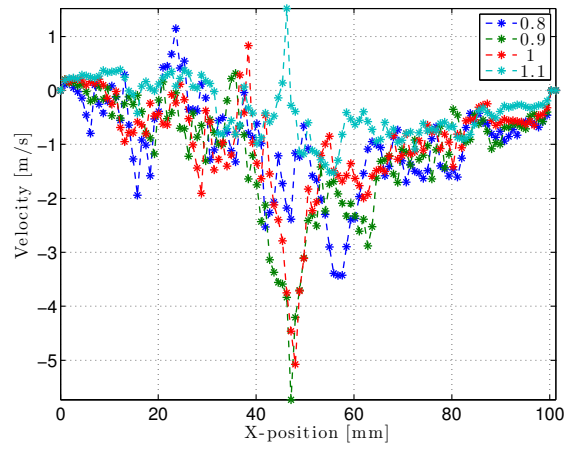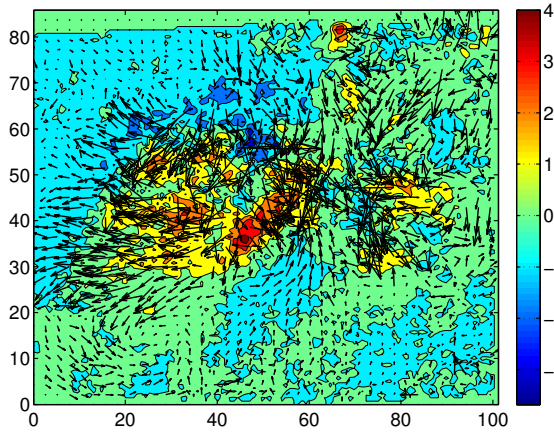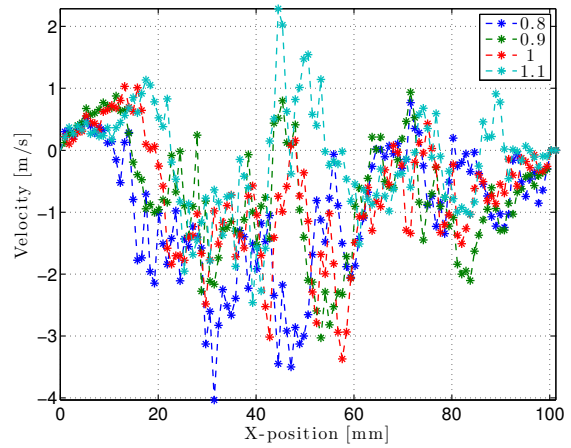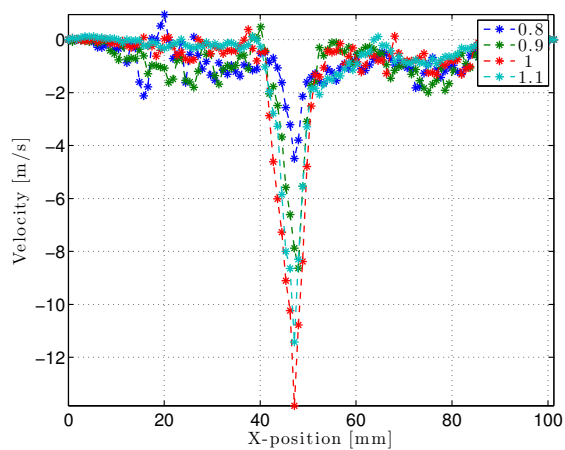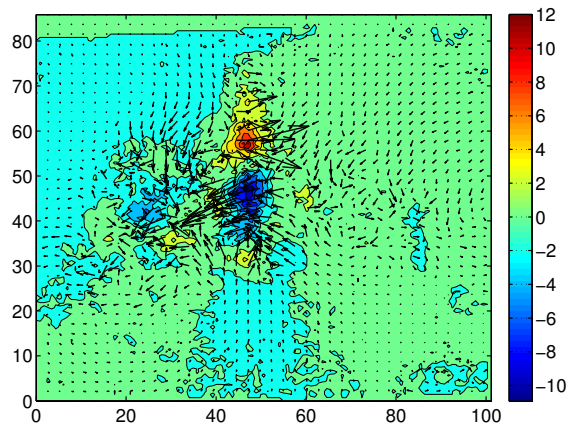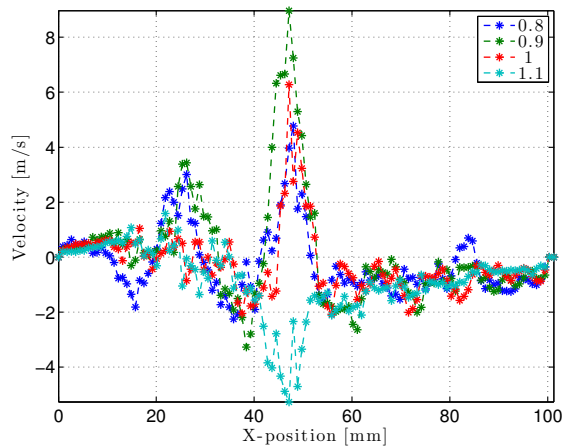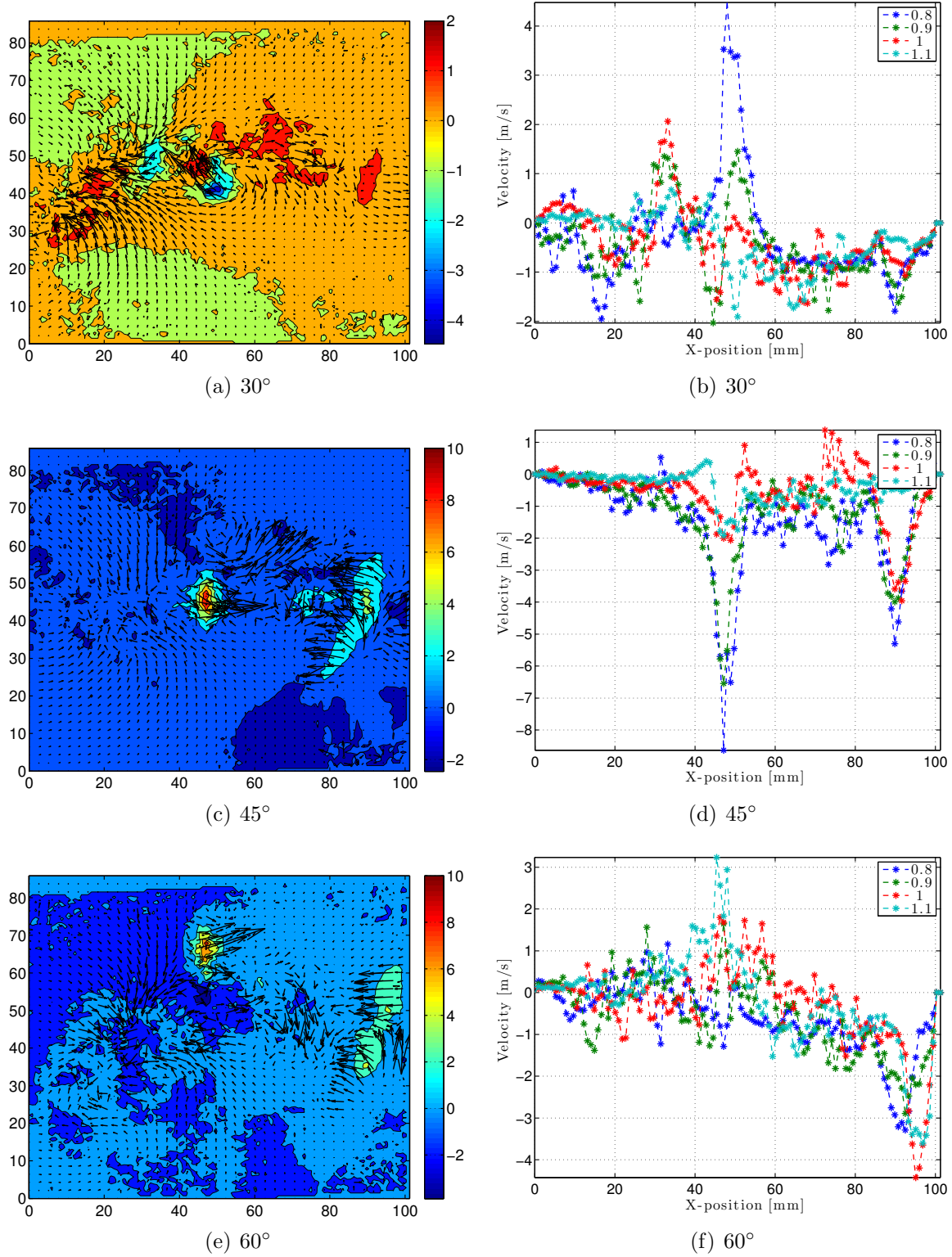 extent, phase 8, and on the far right edge of phase 3, there are some non-physical artifacts in the velocity map from the presence of the wing in the background. The u and v-velocity quivers represent flow transported axially along the spanwsie wing axis. The wing is in front of the laser sheet; therefore, the 2-D vector quivers represent the transport of axial momentum traveling along the wing span, which is the horizontal component of the the LEV at $1\times$ chords away from the wing. The w-velocity contours depict a linear momentum jet expelled through the laser sheet, concentrated about the midspan, between the root and tip. Phases 2-8 in Figure 5.20 show the concentrated and semi-concentric w-velocity momentum jet produced by the flapping wing, comprising one-half of an axial actuator disk, which is most discernible in the 45° test points. The w-velocity profiles extracted at $\pm10\%$ of the mid-span are quantitative representations of the velocity jet generated by the wing. There is some oscillation in the velocity profile, mainly on the upstroke side of the wing, generated by the translational u-velocity of the wing, mixing and stirring the out-of-plane w-velocity component as it is being expelled through the laser sheet, trapping fluid near the wing itself, drawing it rearward and over the wing surface, which is the ingredient of vorticity creation.

The mean thrust, $\bar{T}$, generated by the wing was calculated using a modified form of Equation 5.9 applied over the entire stroke plane, which spanned the entire RoI, from x=0mm to x=100mm and y=0mm to y=85mm. The laser sheet is oriented in front of the wing and the measurements capture the velocity expelled through the actuator disk, but they do not measure the entrained velocity above the actuator disk. Therefore, the thrust computations from the vertically mounted wing are not based on the differential induced velocity. Although a noted limitation of this method, it is still

a valid mathematical numerical method because of the relative magnitude difference between the velocities above and below the rotating wing. The velocities above the wing go to zero at just a few millimeters ($\approx 0.75 - 1.0\times$ chords) above the wing, while the velocities below the wing are nearly an order of magnitude higher and do not deteriorate to zero to well beyond $\approx 2\times$ chords beneath the wing. Equation 5.12 gives the modified form of the equation used to calculate the mean thrust generated through the flap cycle.

$$\bar{T} = \frac{2\rho}{kmn} \left(\sum_{k=1}^{k} \left(\sum_{i=1,j=1}^{i=m,j=n} w_{ij}^2 dx_i dy_j \right)_k \right) \tag{5.12}$$

The area of the swept arc is replaced with a differential grid area $(dxdy)$ determined by the spatial resolution of the PIV camera set-up, where $dx = 0.87248$mm and $dy = 0.71521$mm. The w-velocity at each x, y coordinate location is squared and multiplied by the differential grid area, and summed over the entire interrogation region, which is $m \times n$. The mean thrust is calculated for each phase, and the mean thrust for a single stroke cycle is computed from the phase averaged thrust values for $k = 8$ phases. Figure 5.21 shows the differential grid used to compute the velocity over the swept area of the wing.
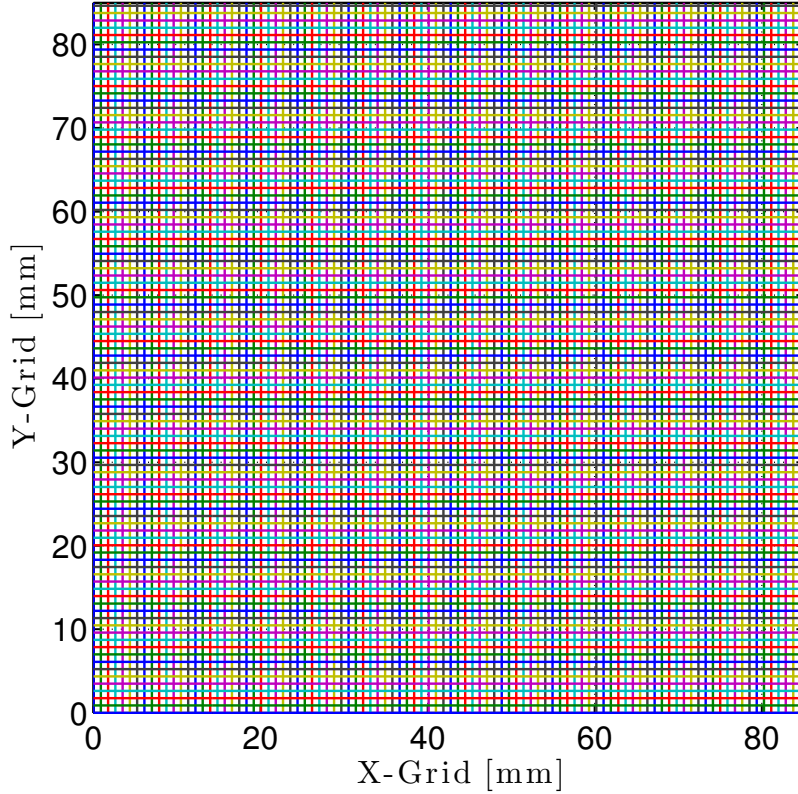
Figure 5.21: $x - y$ grid of the actual differential area, $dxdy$, used to compute the thrust from the PIV vertical measurements. The matrix is a rectangular grid 121×117 points, dx=**0.87248mm**, dy=**0.71521mm**.

The utility in determining which method produces more repeatable, accurate, and reliable thrust numbers is ultimately to aid in the modeling of future full vehicle design iterations. Using the PIV thrust computation method most closely matching the measured Nano-17 force balance data, the next step is ostensibly to use the vertical force values obtained from the PIV testing to calculate dimensionless vertical force coefficients, C_v, for each of the wing angle stops, and then compare to those same coefficients calculated from the measured balance data. Given a measured force parameter, C_{Fi}, Equation 5.13 was utilized to compute the corresponding force coefficient, C_v.

$$C_{\mathrm{v}} = \frac{8\bar{T}\mathcal{R}}{\rho n^2 \Phi^2 R^4 \left(\hat{r}_2^2\left(S\right)\right)\left(\overline{d\hat{\phi}\big/d\hat{t}}\right)^2} \tag{5.13}$$

Table 5.10 shows the mean phase averaged thrust calculated for the 30°, 45°, 60° vertically mounted wings at 1.0× chords behind the laser sheet, and the values of C_{v} calculated from the mean phase averaged vertical thrust, alongside the mean vertical force coefficient values calculated with the quasi-steady model, $C_{\mathrm{v,m}}$, from Tables 4.3-4.5, reported previously in *Chapter* IV. Additionally, vertical PIV data was collected on the 45° wing at at A=0.35, A=0.40 and A=0.45, at 1.5× chords behind the laser sheet, and at a single untrimmed case, A_{trim}=0, at A=0.4, also at 1.5× chords behind the laser sheet, and their thrust results are also catalogued in Table 5.10 below.

Table 5.10: **Thrust & Mean Vertical Forces For Vertically Mounted 30°, 45°, and 60° Wings.**

Angle Stop	A	$\bar{T}_1$	$\bar{T}_2$	$\bar{T}_3$	$\bar{T}_4$	$\bar{T}_5$	$\bar{T}_6$	$\bar{T}_7$	$\bar{T}_8$	$\bar{T}_{\mathbf{tot}}$	$\mathbf{F_x}$	$\mathbf{C_v}$	$\mathbf{C_{v,m}}$
					1.0× Chords Behind The Laser Sheet								
30°	0.40	502.4	368.4	261.7	508.6	246.9	804.7	310.8	474.9	434.8	449	1.33	1.2
45°	0.40	551.1	1239	799.7	235.1	643.1	201	754.2	189.7	576.6	584	1.43	1.2
60°	0.40	533.7	972.8	622.4	719.2	2252	299.5	314.1	1158	859.0	813	1.25	1.1
					1.5× Chords Behind The Laser Sheet								
45°	0.35	767.7	991.3	135.3	139.4	572.6	212.1	1014	334.7	520.9	443	1.70	1.1
45°	0.40	798.8	619.4	263.2	889.8	230.6	784.4	325.9	948.7	607.6	584	1.51	1.2
45°	0.45	181.7	965.0	248.0	537.7	273.1	986.7	1421	523.8	642.2	700	1.25	1.3
				$A_{\mathbf{trim}}$=0, 1.5× Chords Behind The Laser Sheet									
45°	0.40	260.9	574.7	211.7	1048	222.1	1196	314.4	354.7	523.0	561	–	–

The vertical force coefficients, C_{v}, calculated by substituting the values from the vertically mounted wing mean thrust into the quasi-steady force equation, are higher than the coefficients, $C_{\mathrm{v,m}}$, computed using the mean force balance data. Figure 5.22 traces the mean thrust developed over the stroke for the data listed in Table 5.10 above.
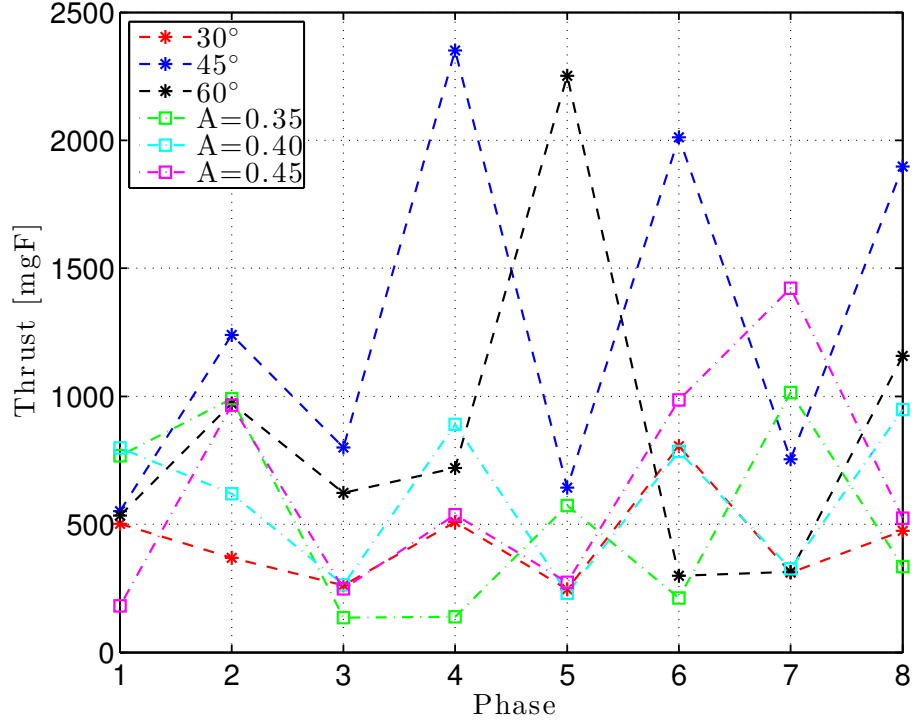
Figure 5.22: Mean thrust, $\bar{T}$, from vertical PIV runs plotted over the stroke cycle for the 30°, 45°, and 60° wings at A=0.4; and for the 45° wing at A=0.35, A=0.40, and A=0.45.

5.4.3 Vertical PIV Summary.

The goal of the vertical PIV testing was achieved. The vertical PIV thrust calculation is less cumbersome, and less reliant on assumptions and approximations, than the horizontal PIV calculations. Computing the complete mean phase averaged thrust is possible with a single test condition run at several phases along the stroke cycle. In addition to requiring fewer data points than the horizontal tests, the thrust results computed from the vertical PIV testing was closer to the measured vertical force, F_x, recorded off the Nano-17 force balance. Table 5.11 shows the percent error between the vertical and horizontal PIV thrust results and their respective vertical forces measured with the Nano-17 balance.

Table 5.11: % Error Between Vertical & Horizontal PIV Thrust Calculation & Measured F_x

Angle Stop	A	F_x [mgF]	Vertical (Δ%)	Horizontal (Δ%)
30°	0.40	449	-3.1%	-16%
45°	0.35	443	+15%	+18%
45°	0.40	584	-1.2%	-9%
45°	0.45	700	-7.8%	-21%
60°	0.40	813	+5.4%	-19%

VI. Conclusions

6.1 Summary

CONSIDERABLE research and investigation has been conducted on the aerodynamic performance and the predominate flow physics of the *Manduca Sexta* size of biomimetically designed and fabricated wings as part of the AFIT FWMAV design project. The work described in this document represents a significant research effort towards advancing the knowledge of the flow physics of FWMAV's, and in particular, the *Manduca Sexta* class of biomimetically designed wings. The stated goal of the research was to evaluate the thesis statement: *A robust analysis of the forces and moments on AFIT's* Manduca Sexta *class, bio-inspired, designed and fabricated engineered wings and PZT drive mechanism, coupled with an experimental fluid dynamics investigation through stereoscopic flow visualization methods, will: i) enhance understanding of the complex three-dimensional fluid/structure interactions in hover, and further elucidate the sometimes nebulous aerodynamic principles, which will facilitate development of an enhanced quasi-steady aerodynamic model as a function of kinematic parameters such as stroke angle, angle of attack, and elevation angle; and ii) aid in the design and development of future refinements including those related to the wing and linkage design, as well as stabiliy and control, supporting the evolution towards a fully functional, air vehicle platform.* The research plan devised and executed to explore this hypothesis consisted of several phases of research, which encompassed: *i*) thorough review of published research to evaluate the merits of previously proposed flapping wing aerodynamic flight theories *ii*) AFIT wing, power plant, and drive mechanism operationalization, and custom software development; *iii*) wing modal response characterization and custom wing and flapper tuning software development; *iv*) PIV baseline testing, and implementation of a custom laser

269

phase synchronization routine written into the flapper drive signal, which permitted ubiquitous control of the phase capture sequence, over any number of phases, at any flapping frequency and sample rate, without the use of external photodiode cells, strobes, or any other physical marking aid; *v*) determining the wing's three kinematic angles through a novel optical tracking algorithm, which uses a compendium of OpenCV libraries and custom written software routines to obtain an accurate kinematic time history; *vi*) investigation into the optimal wing passive rotation joint angle was conducted on 30°, 45°, and 60° passive rotation angle stops. These wing and angle stop combinations were used in a variety of flapping conditions and forces and moments, center of pressure, dimensionless aerodynamic coefficients, wing kinematic angles, power consumption, and an overall Figure of Merit were determined. *vii*) Extensive aerodynamic analysis was conducted on the three wings. Lift, drag, and side force coefficients were calculated from the kinematic angles and force balance data. Quasi-steady models were tested and compared to the force balance data, and a hybrid model was utilized, which included the translational and rotational phases of the half cycle, to enhance the force coefficient model; and *viii*) Stereoscopic PIV data was collected on all three wing models. Three component, u, v, and w-velocity data was collected on wings mounted horizontally and vertically in the test chamber. Flow physics were explored and annotated in velocity vector contour diagrams. The transfer of momentum flux through an approximate rotating semi-disk was calculated to determine the mean velocity above and below the wing stroke plane. The induced velocity was used in a quasi-steady analysis, which implemented a modified *Rankine-Froude* actuator disk to calculated the vertical thrust produced by the wing. The research questions answered and the conclusions inferred from deep exploration into the methods, techniques, and procedures utilized to address these questions are summarized in the next section, followed by an outline of the research contributions

270

added to this field of science in the subsequent section.

6.2 Research Conclusions

Successful completion of this research tasks summarized in Section 6.1 provided the data necessary to address the research hypothesis. The conclusions and detailed insights learned during the course of this research will be articulated.

1. **Anderson postulated using a $45°$ wing passive rotation angle stop based on the assumptions obtained from using a BEM of wing aerodynamics. Is there an optimal translational AoA and passive rotation angle stop for vertical force production?**

Strict wing angle stop optimization was *not* the stated goal of this research; however, in the context of this research, the 45° wing angle stop did not produce optimal wing aerodynamic performance. Of the 30°, 45°, and 60° angle stop wings tested, the 60° stop was empirically the superior performing wing at a specific amplitude. The 60° angle stop wing obtained the maximum designed linkage stroke angle of 110° at A=0.41, while the 45° angle stop wing did not reach the maximal design stroke angle until A=0.50, and the 30° angle stop wing never obtained the maximal design stroke angle in this testing. In terms of power and efficiency, the 45° and 60° angle stop wings performance were closely matched. The 45° angle stop wing consumed an average of 140mW, produced an average of 568mgF of vertical force, had a mean FM of 0.054, and its mean force/power ratio was 4.07. The 60° wing angle stop wing consumed an average of 151mW, produced an average of 631mgF of vertical force, had a mean FM of 0.045, and its mean force/power ratio was 4.2. However, to achieve those force and stroke angle magnitudes, the 45° angle stop wing had to be driven to an amplitude of A=0.6, while the 60° angle stop wing was only driven to an amplitude of A=0.5. Further optimization with finer granularity above and below 60° angle stop wing is

necessary to determine the absolute maximum wing performance for the minimal power expenditure. To realize the maximum benefit of using the 60° angle stop wing in future FWMAV vehicle designs it is necessary to redesign the linkage and passive rotation joint for optimum stroke performance. The current design's $\pm\phi$ limits are too restrictive, and are obtained at low driving voltages. To realize the full potential of the this wing, linkage must be able to translate through at least 150° of stroke angle within the linear kinematic region and without binding. A redesigned linkage that remains within the linear performance limits will produce greater stroke angles and generate higher lift forces, while only consuming moderately more power. The passive rotation joint itself is the weak link in the drive train. It experienced numerous shear failures during the course of this research, and is definitively not a flight worthy component. The joint is too wide and too flexible. Repeated high frequency bending caused early life cycle fatigue failures making it unsuitable for future robust flight vehicle designs.

2. **AFRL researchers, Doman *et.al.*, based on the conservative *quasi-steady* aerodynamic assumption, assumed negligible side force contribution in their non-harmonic, non-resonant, piece-wise, Split-Cycle Constant-Period Frequency Modulation (SCCPFM) control model [26]. Experimental results from Anderson's bi-harmonic, resonant, continuous, 5-DoF BABM control algorithm implementation partially contradicts Doman *et.al.*'s. zero-side force assumption, and provided a few experimental examples of the presence of coupled side forces tied to asymmetric amplitude modulation, which he speculated resulted from the development and sustainment of spanwise flow through the half stroke [2]. Therefore, under what conditions, if any, is a side-force generated during symmetric wing flapping, and**

can it be measured and accurately added to existing aerodynamic models?

Side forces were generated during all testing. However, the cycle averaged side forces were small, and oscillated between $\approx \pm 5$mgF and 100mgF with amplitude, which was an order of magnitude less than the vertical forces, which ranged between 350mgF and 900mgF. The 30°, 45°, and 60° angle stop mean side forces averaged over all amplitudes was 22mgF, 21mgF, and 32mgF respectively. The mean side force coefficient, $C_S \approx 0.5$, in the body axis, and the mean spanwise force coefficient, $C_a \approx 0.7$, in the balance axis, across all wing angle stops and amplitudes. The presence of spanwise flow emanating from wing root to wing tip is confirmed in the PIV flow visualizations for all three wing angle stops. The varying span location PIV testing show the emergence, growth, propagation, and eventual unwinding and dispersion of the LEV as a function of span. This vortex motion indicates the presence of spanwise flow, and therefore, side forces. The growth, translation, and decay of LEV are clearly observed and delineated in the phase averaged PIV vector contour plots, which confirm the assertion that the BEM's zero side force assumption, though a reasonable first order approximation, does not completely and accurately model the physical flow phenomenon observed in flapping wing flight.

3. **What occurs within the fluid medium that corresponds to differences in force production over classical BEM theory, and can stereoscopic PIV provide useful insights into the three-dimensional unsteady nature of the flow generated by flapping wings in a horizontal stroke plane?**

The combination of simultaneous stereoscopic PIV and 6-DoF force measurements were used to develop an improvement to the quasi-steady-state model. The verification of a side force coefficient in the force measurements, and the confirmation of

the development and sustainment of a LEV through the flap cycle offer necessary and sufficient explanation of the enhanced force production seen in flapping wing flight. The adaptation of the actuator disk model construct to the flapping wing PIV measurements is to quantitatively model the aerodynamic effects of flapping flight by computing the induced velocity created by the transport of vertical momentum produced by the flapping wing. The pressure applied to the surrounding air by the wings is a direct result of the total circulation (Γ_t) around them, which caused a pulsed sheet of vorticity shed into the wake. The unsteady nature of the wing's planform through the half cycle seen in the PIV images results in the LEV adhering to the wing during the stroke. At the rotation transition, the LEV is immediately shed into the surrounding wake off the tip, and a new LEV almost instantly reforms during the subsequent translation. As the wing passes through its previous wake, the LEV grows and entrains air into a form of a laminar bubble extending across the wing surface, which acts to increase the apparent camber, increasing the LE suction peak of the wing, thereby increasing lift. Furthermore, because the kinematic motion of the wake itself is a function of the induced velocity created by the downward axial momentum transfer, the pressure exerted by the flapping wings can be directly related to the induced velocity, and the power required to maintain this momentum transfer—*i.e. sustained hover*. PIV vertical velocity measurements taken normal and parallel to the laser sheet verified the vertical force balance measurements within 7% and 15% respectively.

4. **Can an improved aero model be expressed as a function of similarity parameters and / or relevant wing design parameters that can be manipulated within the available degrees of freedom of the AFIT PZT driven flapper?**

274

The result of the force balance testing is the derivation of the dimensionless coefficients that can be used in control models for vehicle design analysis. A companion to the force coefficient figures presented in *Chapter* IV is an empirical model based on the coefficient data calculated as a function of amplitude and wing angle of attack. An empirical model fit to the coefficients and their corresponding angle of attack for the AFIT engineered wings was presented in *Chapter* IV.

6.3 Significant Contributions

In the course of this work, several contributions, presented in chronological order, have been made to the field of FWMAV aerodynamics which are significant:

1. Developed a self-contained menu driven GUI to control all aspects of subsequent FWMAV testing. This interface provides self explanatory access to wing structural ID tools to perform modal analysis on new wing designs. The software interface offers menu driven access providing flapper drive signal customization of numerous combinations of flapping parameters. This is the core function of the GUI, which drives the flapper, stores and catalogues force and moment data in user specified files organized by date, and has numerous built-in plotting features. The software allows the user to perform a custom auto-tuning of the flapper, which provides an 'engine map' of the amplitude and A_{trim} settings required to achieve symmetric up and downstroke flapping across the user specified amplitude range, spacing density, and error tolerance. The flapping software has built-in TTL functionality to simultaneously trigger up to three high-speed cameras or to trigger the stereo PIV laser system at a user specified number of phases.

2. Developed and executed the first simultaneous integrated 6-DoF force balance and stereo PIV measurement system. This system is capable of collecting force

and moment data while also calculating three component velocity phase averaged PIV measurements. The ability to phase lock the PIV image at any part of the wing stroke is a truly novel accomplishment. Previous flapping wing PIV research either utilized a constant laser light source and a video camera that recorded blocks of flapping time, and then later parsed through several thousands of images to collate images from the same wing position temporally based on time markers, or phased averaged PIV data was collected using either external photodiodes or a strobe to trigger an external TTL signal to trigger the laser, or something attached to the flapping mechanism itself to trigger the laser to fire. A fully integrated solution was developed to implement the laser TTL signal with the flapper drive signal as an integrated signal sent through the data acquisition box to the flapper's piezo, and the PIV laser and data acquisition system simultaneously.

3. Developed an improved force coefficient model. Previous researchers Sane, Doman *et.al.*, and Anderson all have relied on an approximate 2-D BEM force approximation based on C_L and C_D coefficients derived from empirical curve fits to a revolving $25\times$ fruit fly wing. This research has produced an improved quasi-steady model that incorporates the side force coefficient that accounted for the translation and the rotational phases of the stroke cycle. A contribution specifically related to the AFIT FWMAV program, is the development of aerodynamic performance data for biomimetic hawkmoth wings. This supports AFIT's self-appointed niche in the ever crowded field of flapping wing research. The decision to settle on this particular size envelope, restricted to the *Manduca Sexta* form factor, is with the intention that this size insect presents the smallest practical airframe suited for an actual flapping ISR platform.

4. Performed the first nonintrusive complete wing time history kinematic angle

tracking of a passively controlled flapping wing. Previous research was able to track the mean value of a single kinematic angle, usually the stroke angle, and then mathematically derive the remaining angles based on dynamic models of the wing and drive mechanism. A second method cited in the literature to track the wing position was adding external tracking devices, or contrasting dots, to the wing or flapping apparatus, which altered the wing dynamic response, to provide tracking fiducial points that were used in a basic point cloud routine to track those specific points. This research led to novel real-time optical tracking of the entire wing surface to calculate all three kinematic angles at every instant in time, without adding anything to the wings or flapping mechanism.

5. Performed the first comprehensive stereo u, v, w-velocity PIV assessment of multiple wing AoA's, amplitudes, stroke angles, span locations and wing orientations. This research successfully executed rarely seen, if ever on a flapping wing specimen of this size envelope, vertical wing orientation PIV testing, and verified that thrust production calculations were possible, and more accurate than with the standard horizontal wing configuration. The PIV tests reported the intersection of velocity from different planes conducted on a flapping wing specimen, adding an additional level of fidelity and data veracity scarcely seen in the literature, especially on a direct scale flapping wing. The PIV testing also empirically confirmed the presence of LEV development, which was previously theorized, and anecdotally represented by a very large $10\times$ mechanical hawkmoth wing with a brass smoke rake attached to the wing LE [84]. The quantitative discovery of the flow physics responsible for enhanced lift is a significant contribution to the field of flapping wing aerodynamics, which was occupied previously by conjecture from the biological community based on hard-to-duplicate experiments, performed on live insects, where the researches had a

priori confirmation of actual flight.

6. This research was the first to adapt and modify the rotorcraft mechanics quasi-steady *Rankine-Froude* actuator model to a single flapping wing experiment, which was used to calculate vertical force from the transport of vertical momentum. The net momentum flux was obtained from the induced velocity, which was computed from the difference between the velocity of the air drawn into the annulus and the velocity of the air expelled through the semi-disk. The horizontal PIV experiments confirmed the maximum induced velocity, and hence, the maximum lift is generated at the mid-span, which is the location of the mean chord and the mean aerodynamic center of the wing. A novel first-order model was developed to calculate the thrust produced across the entire span from discrete velocity measurement planes taken transverse to the wing on a horizontally mounted wing. The model integrated the relationship between the span location of the induced velocity at a few locations across a differential wing arc element, and was able to calculate the expected thrust produced by the entire wing within 20% of the measured force balance data.

7. The polynomial model developed to compute the mean thrust across the span of a horizontally mounted wing is a reasonable method to estimate the vertical force generated by the wing. However, a more accurate force estimation method was developed using a vertically mounted wing, which measured the vertical velocity over the entire swept region below the wing. This method computed the mean thrust by taking the mean of the sum of the thrust at every point in the xy measurement grid. The thrust calculation method using a vertically mounted wing was accurate to within 8% of the measured force balance data, and was 10% more accurate than the mean thrust calculated from a horizontally mounted wing.

VII. Recommendations for Future Research

7.1   Overview

THIS chapter presents opportunities for future work, identifies where deeper investigation is warranted, and specifies areas that were outside the scope of this research effort.

7.2   Future Research Opportunities

This section lists various test parameters that should be studied as part of a greater research effort into completing the aerodynamic analysis of the AFIT FW-MAV wing. The recommendations are shown in a 'test card' manner, similar to the format presented in a Test Readiness Review (TRR), before a test flight, which shows an incremental 'build-up' test method strategy for isolating specific wing parameters, while fixing others constant, and assessing the affect those changes impart to the aerodynamic response of the system under test. The analogy used in the test community is aptly applied here—*crawl, walk, run.*

7.2.1   Vacuum Chamber.

Table 7.1 lists recommended air density vacuum tests. These tests can be conducted in the AFIT vacuum chamber using specially designed connectors for the Nano-17 Titanium force balance and the Opto NCDT1700 displacement sensor. These tests would assist in determining the inertial forces and power required to accelerate and decelerate the wing between the up and downstroke flap cycles without the additional burden of the virtual air mass enveloping the wing during flight. In addition to providing the inertial forces in a pure vacuum, the effect of Reynolds number scaling can be accomplished by changing the fluid density through varying the pressure from

279

Table 7.1: **Test Point Matrix—Varying Atmospheric Pressure Tests**

VARIABLE CHANGE: ATMOSPHERIC PRESSURE							
Passive Rotation Angle *(deg)*	Flapping Frequency *(ω)*	Pressure (% atmospheric)	Stroke Bias *(η)*	Asymmetric Flapping	Symmetric Flapping	Planform Area *(mm²)*	Aspect Ratio *(Æ)* R^2/S
30	resonance	atmospheric	0	✕	✓	513	4.9
30	resonance	-25%	0	✕	✓	513	4.9
30	resonance	-50%	0	✕	✓	513	4.9
30	resonance	-75%	0	✕	✓	513	4.9
30	resonance	-85%	0	✕	✓	513	4.9
30	resonance	-95%	0	✕	✓	513	4.9
45	resonance	atmospheric	0	✕	✓	513	4.9
45	resonance	-25%	0	✕	✓	513	4.9
45	resonance	-50%	0	✕	✓	513	4.9
45	resonance	-75%	0	✕	✓	513	4.9
45	resonance	-85%	0	✕	✓	513	4.9
45	resonance	-95%	0	✕	✓	513	4.9
45	resonance	atmospheric	0	✓	✕	513	4.9
45	resonance	-25%	0	✓	✕	513	4.9
45	resonance	-50%	0	✓	✕	513	4.9
45	resonance	-75%	0	✓	✕	513	4.9
45	resonance	-85%	0	✓	✕	513	4.9
45	resonance	-95%	0	✓	✕	513	4.9
60	resonance	atmospheric	0	✓	✕	513	4.9
60	resonance	-25%	0	✓	✕	513	4.9
60	resonance	-50%	0	✓	✕	513	4.9
60	resonance	-75%	0	✓	✕	513	4.9
60	resonance	-85%	0	✓	✕	513	4.9
60	resonance	-95%	0	✓	✕	513	4.9
65	resonance	atmospheric	0	✓	✕	513	4.9
65	resonance	-25%	0	✓	✕	513	4.9
65	resonance	-50%	0	✓	✕	513	4.9
65	resonance	-75%	0	✓	✕	513	4.9
65	resonance	-85%	0	✓	✕	513	4.9
65	resonance	-95%	0	✓	✕	513	4.9

7.2.2   Passive Rotation.

Table 7.2 lists additional passive rotation joint stop tests that might be considered to further optimize the most suitable wing rotation stop angle, which will maximize stroke angle travel, and hence vertical force, while also minimizing PZT power consumption. The kinematic and force results for the three passive rotation wing angle stops presented in *Chapter* IV represent very coarse angular graduations. Future testing should concentrate on finer granularity rotation joints around the 60° angle stop tests conducted in the present research. These tests should vary the physical passive rotation joint stop, shown in Figure 2.26, and hold all other design parameters constant. When the symmetric column is checked, the goal is to achieve symmetric flapping, equal up and downstroke travel, and the $^{up}/_{down}$ stroke bias (η) percentage

is 0 meaning, the wing trim parameter, A_{trim}, is set by the auto-tune mapping to achieve $\phi_{max} = \phi_{min}$, so it is not biased in either direction of the flap cycle.

Table 7.2: Test Point Matrix—Passive Rotation Angle Stop Change

				VARIABLE CHANGE: PASSIVE ROTATION JOINT ANGLE				
Passive Rotation Angle *(deg)*	Flapping Frequency *(ω)*	Amplitude	Stroke Bias *(η)*	BABM	Symmetric Flapping	Camber (% ± std thickness)	Planform Area *(mm²)*	Aspect Ratio *(Æ)* R^2/S
52	resonance	± 1mm (max deflection)	0	×	✓	0	513	4.9
54	resonance	± 1mm (max deflection)	0	×	✓	0	513	4.9
56	resonance	± 1mm (max deflection)	0	×	✓	0	513	4.9
58	resonance	± 1mm (max deflection)	0	×	✓	0	513	4.9
60	resonance	± 1mm (max deflection)	0	×	✓	0	513	4.9
62	resonance	± 1mm (max deflection)	0	×	✓	0	513	4.9
64	resonance	± 1mm (max deflection)	0	×	✓	0	513	4.9
66	resonance	± 1mm (max deflection)	0	×	✓	0	513	4.9
68	resonance	± 1mm (max deflection)	0	×	✓	0	513	4.9

7.2.3 Stroke Bias.

Table 7.3 lists a recommended set of stroke bias offset tests. The sign of the stroke bias parameter, η, determines which portion of the drive signal, hence, which half of the flap cycle, *up or downstroke*, is biased, or weighted. $+\eta$ is biased toward the *up* stroke, and $-\eta$ is biased toward the *down* stroke. It is imperative asymmetric flapping produces a comparable, but not necessarily equal amount of vertical force as symmetric flapping, because in a full flight vehicle, control about the pitch axis is exclusively achieved through modulation of the stroke angle between two wings. Pitch control is achieved by precisely controlling the asymmetry in the wing's flap stroke; a larger downstroke angle during the flap cycle produces a nose down pitch, while a larger upstroke angle during the flap cycle yields a nose up pitch attitude. Roll is achieved by flapping one wing symmetrically at a higher amplitude, and the other wing flapping symmetrically at a lower amplitude. Purposeful stroke angle asymmetry is achieved through differential application of η to one or both wings. The intent is to determine the forces generated by varying η, which can be used to

create a look-up table for future vehicle designs to determine control inputs necessary for maneuver.

Table 7.3: Test Point Matrix—Bias Offset

				VARIABLE CHANGE: UP-to-downstroke BIAS OFFSET				
Passive Rotation Angle(deg)	Flapping Frequency(ω)	Amplitude	Stroke Bias(η)	BABM	Symmetric Flapping	Camber (% ± std thickness)	Planform Area (mm²)	Aspect Ratio (Æ) R²/S
20	resonance	± 1mm	−10% down	×	×	0	513	4.9
30	resonance	± 1mm	−20% down	×	×	0	513	4.9
45	resonance	± 1mm	−30% down	×	×	0	513	4.9
60	resonance	± 1mm	−40% down	×	×	0	513	4.9
20	resonance	± 1mm	+10% up	×	×	0	513	4.9
30	resonance	± 1mm	+20% up	×	×	0	513	4.9
45	resonance	± 1mm	+30% up	×	×	0	513	4.9
60	resonance	± 1mm	+40% up	×	×	0	513	4.9

7.2.4 Intra-Stroke Rate.

Table 7.4 lists a recommended set of BABM test points, which are accomplished by varying the split-cycle parameter (τ_s). The BABM modulated flap drive signal was developed by Anderson as a modification of the SCCPFM control algorithm developed by Doman *et.al.* at the Air Force Research Laboratory (AFRL), which both essentially control the flapping rate, or *frequency* with which either the *up* or *down* stroke half cycles are completed, independent of the other half cycle, without changing the overall flapping period (τ) [2, 11, 27].

Table 7.4: Test Point Matrix—Intra-Stroke Rate Change

				VARIABLE CHANGE: UP-to-downstroke RATE CHANGE				
Passive Rotation Angle(deg)	Flapping Frequency(ω)	Amplitude	Stroke Bias(η)	BABM (τ_s)	Symmetric Flapping	Camber (% ± std thickness)	Planform Area (mm²)	Aspect Ratio (Æ) R²/S
20	resonance	± 1mm	0	$0 - \pm 0.15$	×	0	513	4.9
30	resonance	± 1mm	0	$0 - \pm 0.15$	×	0	513	4.9
45	resonance	± 1mm	0	$0 - \pm 0.15$	×	0	513	4.9
60	resonance	± 1mm	0	$0 - \pm 0.15$	×	0	513	4.9

7.2.5 Differential Amplitude.

Table 7.5 lists recommended tests for differential amplitude control between two separate wings. The AFIT FWMAV test bench has the ability to drive two wings with two separate PZT actuators. Anderson verified a method to control roll rate

$(\dot{C}_\ell)$, by asymmetrically controlling the amplitude of the drive actuators attached to each wing separately. The aerodynamic model did not include provision for the difference in side force generated from the different flapping amplitudes between the two wings; therefore, a series of tests are proposed to measure the amount of net side force generated due to differential amplitude modulation between a double wing, dual PZT driven flapper assembly [2].

Table 7.5: **Test Point Matrix—Differential Actuator Amplitude**

VARIABLE CHANGE: LEFT-to-RIGHT WING AMPLITUDE CHANGE							
Passive Rotation Angle*(deg)*	Flapping Frequency*(ω)*	Left Amplitude	Right Amplitude	BABM	Camber (% ± std thickness)	Planform Area *(mm²)*	Aspect Ratio *(Æ)* R^2/S
45	resonance	0.3	0.1	×	0	513	4.9
45	resonance	0.4	0.1	×	0	513	4.9
45	resonance	0.5	0.1	×	0	513	4.9
45	resonance	0.1	0.5	×	0	513	4.9
45	resonance	0.1	0.4	×	0	513	4.9
45	resonance	0.1	0.3	×	0	513	4.9
45	resonance	0.4	0.3	×	0	513	4.9
45	resonance	0.3	0.4	×	0	513	4.9

7.2.6   Camber.

Table 7.6 lists the tests where the wing camber is altered by changing the stiffness of the wing through changing the venation thickness of the trailing edge carbon fiber spars. Varying the wing stiffness changes the ratio of bending to torsion modes, which changes the onset, duration, and intensity of wing folding and furrowing at the ends of the half cycle, thereby altering the rotational dynamics of the wing, which changes the mode of leading edge vortex propagation, shedding, and subsequent flow recapture [65]. Wing camber is achieved by varying the depth of the molds used to set the carbon fiber venation pattern during the manufacturing process, and is measured by the overall change in carbon fiber vein deflection from wing root to wing tip.

Table 7.6: Test Point Matrix—Camber Change

VARIABLE CHANGE: AIRFOIL CAMBER BY CHANGING VENATION THICKNESS								
Passive Rotation Angle (deg)	Flapping Frequency (ω)	Amplitude	Stroke Bias (η)	BABM	Symmetric Flapping	Camber (% ± std thickness)	Planform Area (mm^2)	Aspect Ratio $(\mathcal{R})$ R^2/S
20	resonance	± 1mm	0	×	✓	+10%	513	4.9
30	resonance	± 1mm	0	×	✓	+10%	513	4.9
45	resonance	± 1mm	0	×	✓	+10%	513	4.9
60	resonance	± 1mm	0	×	✓	+10%	513	4.9
20	resonance	± 1mm	0	×	✓	−10%	513	4.9
30	resonance	± 1mm	0	×	✓	−10%	513	4.9
45	resonance	± 1mm	0	×	✓	−10%	513	4.9
60	resonance	± 1mm	0	×	✓	−10%	513	4.9

7.2.7 Aspect Ratio.

Table 7.7 is essentially a repeat of the tests listed in Tables 7.2 and 7.6 with a different aspect ratio, $\mathcal{R}$. The $\mathcal{R}$ is changed by altering the planform shape of the wing, making it more triangular in shape, while retaining the overall wing length, R, at $50mm$. The new planform shape reduces wing *slenderness*, nearly doubles the wing area, S, and decreases the $\mathcal{R}$ by half. Changing the $\mathcal{R}$ of the wings will permit investigation into the flap dynamics of the torsion wave, which is materially affected by the slenderness ratio of the wing. The more slender the wing, the less wing surface there is for the wave to dissipate across. A decrease in wing surface area will increase the speed of wave propagation across the wing, altering the rotation at the ends of the half cycle between supination and pronation, which affects the angular rate dynamics and influences the wing's rotational lift characteristics.

Table 7.7: Test Point Matrix—Planform and Aspect Ratio

VARIABLE CHANGE: AIRFOIL PLANFORM AND ASPECT RATIO								
Passive Rotation Angle *(deg)*	**Flapping Frequency** (ω)	**Amplitude**	**Stroke Bias** (η)	**BABM**	**Symmetric Flapping**	**Camber** (% ± std thickness)	**Planform Area** (mm^2)	**Aspect Ratio** $(\mathcal{R})$ R^2/S
0 (free)	resonance	± 1mm	0	×	✓	0	1022	2.45
5	resonance	± 1mm	0	×	✓	0	1022	2.45
10	resonance	± 1mm	0	×	✓	0	1022	2.45
20	resonance	± 1mm	0	×	✓	0	1022	2.45
30	resonance	± 1mm	0	×	✓	0	1022	2.45
45	resonance	± 1mm	0	×	✓	0	1022	2.45
60	resonance	± 1mm	0	×	✓	0	1022	2.45
75	resonance	± 1mm	0	×	✓	0	1022	2.45
90 (clamped)	resonance	± 1mm	0	×	✓	0	1022	2.45
20	resonance	± 1mm	0	×	✓	+10%	1022	2.45
30	resonance	± 1mm	0	×	✓	+10%	1022	2.45
45	resonance	± 1mm	0	×	✓	+10%	1022	2.45
60	resonance	± 1mm	0	×	✓	+10%	1022	2.45
20	resonance	± 1mm	0	×	✓	−10%	1022	2.45
30	resonance	± 1mm	0	×	✓	−10%	1022	2.45
45	resonance	± 1mm	0	×	✓	−10%	1022	2.45
60	resonance	± 1mm	0	×	✓	−10%	1022	2.45

Bibliography

[1] Air Armament Center. *Weapons File.* Air Armament Center (AAC/XR), 207 West Avenue D, Suite 300, Eglin AFB, Fl 32542-6844, 12th edition, July 2009.

[2] Anderson, Michael L. *Design and Control of Flapping Wing Micro Air Vehicles.* Dissertation, Air Force Institute of Technology, 2950 Hobson Way, WPAFB, OH 45433, September 2011.

[3] ATI Technology Applications. *Network Force/Torque Sensor System.* ATI Industrial Automation, Pinnacle Park, 1031 Goodwirth Drive, Apex, NC 27539, August 2010.

[4] Avadhanula, S. and R.S. Fearing. "Flexure Design Rules for Carbon Fiber Micro-robotic Mechanisms". *Robotics and Automation, 2005. ICRA 2005. Proceedings of the 2005 IEEE International Conference on*, 1579 – 1584. april 2005.

[5] Avadhanula, S., R. J. Wood, D. Campolo, and R. S. Fearing. "Dynamically Tuned Design of the MFI Thorax". *Proceedings of the 2002 IEEE International Conference on Robotics and Automation, Washington, DC,*, May 2002.

[6] Baek, Stanley S., Kevin Y. Ma, and Ronald S. Fearing. "Efficient resonant drive of flapping-wing robots". *Proceedings of the 2009 IEEE/RSJ international conference on Intelligent robots and systems*, IROS'09, 2854–2860. IEEE Press, Piscataway, NJ, USA, 2009. ISBN 978-1-4244-3803-7. URL `http://dl.acm.org/citation.cfm?id=1733023.1733205`.

[7] Barlow, Jewel B., William H. Rae, and Alan Pope. *Low-Speed Wind Tunnel Testing.* A Wiley-Interscience Publication. John Wiley and Sons, Inc., 3rd edition, 1999.

[8] Birch, James M. and Michael H. Dickinson. "The influence of wing–wake interactions on the production of aerodynamic forces in flapping flight". *Journal of Experimental Biology*, 206(13):2257–2272, 07 2003. URL `http://jeb.biologists.org/content/206/13/2257.abstract`.

[9] Birch, James M., William B. Dickson, and Michael H. Dickinson. "Force production and flow structure of the leading edge vortex on flapping wings at high and low Reynolds numbers". *Journal of Experimental Biology*, 207(7):1063–1072, 03 2004. URL `http://jeb.biologists.org/content/207/7/1063.abstract`.

[10] Brendley, Keith W. and Randall Steeb. *Military Applications of Microelectromechanical Systems.* Rand Report No: MR-175-OSD/AF/A, RAND Corporation, Santa Monica, CA, 1993, pp 16-30.

[11] Carl, Justin R. *Power Requirements for Bi-Harmonic Amplitude and Bias Modulation Control of a Flapping Wing Micro Air Vehicle.* Master's thesis, Air Force Institute of Technology, 2950 Hobson Way, WPAFB, OH 45433, March 2013.

[12] Conn, A T, S C Burgess, and C S Ling. "Design of a parallel crank-rocker flapping mechanism for insect-inspired micro air vehicles". *Proceedings of the Institution of Mechanical Engineers, Part C: Journal of Mechanical Engineering Science*, 221(10):1211–1222, 10 2007. URL `http://pic.sagepub.com/content/221/10/1211.abstract`.

[13] Curtis, David, Mark Reeder, Craig Svanberg, Richard Cobb, and Gregory Parker. "Flapping Wing Micro Air Vehicle Bench Test Setup". *International Journal of Micro Air Vehicles*, 4(1):51–78, 03 2012. URL `http://dx.doi.org/10.1260/1756-8293.4.1.51`.

[14] Dantec Dynamics. *FlowManager Software and Introduction to PIV Instrumentation.* Dantec Dynamics A/S, P.O. Box 121, Tonsbakken 18, DK–2740 Skovlunde, Denmark, September 2002.

[15] Dantec Dynamics. *3D Stereoscopic PIV Reference Manual.* Dantec Dynamics A/S, P.O. Box 121, Tonsbakken 18, DK-2740 Skovlunde, Denmark, 2006.

[16] Dantec Dynamics. *DynamicStudio v3.12 User's Guide.* Dantec Dynamics A/S, P.O. Box 121, Tonsbakken 18, DK-2740 Skovlunde, Denmark, v3.12 edition, April 2010.

[17] Davis, William R., Bernard B. Kosicki, Don M. Boroson, and Daniel F. Kostishack. "Micro Air Vehicles for Optical Surveillance". *The Lincoln Laboratory Journal*, 9(2):17, 1996.

[18] De Clercq, Kristien, Roeland de Kat, Bart Remes, Bas van Oudheusden, and Hester Bijl. "Aerodynamic Experiments on DelFly II: Unsteady Lift Enhancement". *International Journal of Micro Air Vehicles*, 1(4):255–262, 12 2009. URL `http://dx.doi.org/10.1260/175682909790291465`.

[19] DeLeón, Nathanial E. *Manufacturing and Evaluation of a Biologically Inspired Engineered MAV Wing Compared to the Manduca Sexta Wing Under Simulated Flapping Conditions.* Thesis, Air Force Institute of Technology, 2950 Hobson Way, WPAFB, OH 45433, March 2011.

[20] DeLeón, N.E. and A. Palazotto. "The Evaluation of a Biologically Inspired Engineered MAV Wing Compared to the Manduca Sexta Wing under Simulated Flapping Conditions". *International Journal of Micro Air Vehicles*, 3(3):149–168, 2011.

[21] DeLuca, Anthony, Mark Reeder, and Richard Cobb. "An Experimental Investigation into the Effect of Flap Angles for a Piezo-Driven Wing". *International Journal of Micro Air Vehicles*, 5(1):55–92, 03 2013. URL `http://dx.doi.org/10.1260/1756-8293.5.1.55`.

[22] DeLuca, Anthony M. *Experimental Investigation into the Aerodynamic Performance of Both Flexible and Rigid Structured Micro-Air-Vehicles*. Master's thesis, Air Force Institute of Technology, 2950 Hobson Way, WPAFB, OH 45433, March 2004.

[23] DeLuca, Anthony M., Mark F. Reeder, and Richard G. Cobb. "Force Measurements and Flow Visualization of Biomimetically Designed Manduca Sexta Class Engineered Wings". *51st AIAA Aerospace Sciences Meeting including the New Horizons Forum and Aerospace Exposition*. American Institute of Aeronautics and Astronautics, 5 Janurary 2013. URL `http://dx.doi.org/10.2514/6.2013-87`.

[24] Dickinson, Michael H., Fritz-Olaf Lehmann, and Sanjay P. Sane. "Wing Rotation and the Aerodynamic Basis of Insect Flight". *Science*, 284(5422):1954–1960, 06 1999. URL `http://www.sciencemag.org/content/284/5422/1954.abstract`.

[25] Dickson, William B. and Michael H. Dickinson. "The effect of advance ratio on the aerodynamics of revolving wings". *Journal of Experimental Biology*, 207(24):4269–4281, 11 2004. URL `http://jeb.biologists.org/content/207/24/4269.abstract`.

[26] Doman, David B., Michael W. Oppenheimer, and David O. Sigthorsson. "Dynamics and Control of a Minimally Actuated Biomimetic Vehicle: Part I. *Aerodynamic Model*". *AIAA Guidance, Navigation, and Control Conference , Chicago, Illinois*, (AIAA 2009-6160):30, 10 - 13 August 2009.

[27] Doman, David B., Michael W. Oppenheimer, and David O. Sigthorsson. "Dynamics and Control of a Minimally Actuated Biomimetic Vehicle: Part II. *Control*". *AIAA Guidance, Navigation, and Control Conference , Chicago, Illinois*, (AIAA 2009-6161):30, 10 - 13 August 2009.

[28] Doyle, D. D. and J. T. Black. "Determination of Feature Generation Methods for PTZ Camera Object Tracking". *Society of Photo-Optical Instrumentation Engineers (SPIE) Conference Series*, volume 8395 of *Society of Photo-Optical Instrumentation Engineers (SPIE) Conference Series*. May 2012.

[29] Doyle, Daniel D., Alan L. Jennings, and Jonathan T. Black. "Optical flow background subtraction for real-time PTZ camera object tracking". *Instrumentation and Measurement Technology Conference (I2MTC), 2013 IEEE International*, 866–871. 2013. ISSN 1091-5281.

[30] Dudley, Robert. *The Biomechanics of Insect Flight*—form, function, evolution. Princeton University Press, 41 William Street, Princenton, NJ, 08540, 2000.

[31] Ellington, C. P. "The Aerodynamics of Hovering Insect Flight. I. *The Quasi-Steady Analysis*". *Philosophical Transactions of the Royal Society of London. B, Biological Sciences*, 305(1122):1–15, 1984. URL `http://rstb.royalsocietypublishing.org/content/305/1122/1.abstract`.

[32] Ellington, C. P. "The Aerodynamics of Hovering Insect Flight. II. *Morphological Parameters*". *Philosophical Transactions of the Royal Society of London. B, Biological Sciences*, 305(1122):17–40, 1984. URL `http://rstb.royalsocietypublishing.org/content/305/1122/17.abstract`.

[33] Ellington, C. P. "The Aerodynamics of Hovering Insect Flight. III. *Kinematics*". *Philosophical Transactions of the Royal Society of London. B, Biological Sciences*, 305(1122):41–78, 1984. URL `http://rstb.royalsocietypublishing.org/content/305/1122/41.abstract`.

[34] Ellington, C. P. "The Aerodynamics of Hovering Insect Flight. IV. *Aeorodynamic Mechanisms*". *Philosophical Transactions of the Royal Society of London. B, Biological Sciences*, 305(1122):79–113, 1984. URL `http://rstb.royalsocietypublishing.org/content/305/1122/79.abstract`.

[35] Ellington, C. P. "The Aerodynamics of Hovering Insect Flight. V. *A Vortex Theory*". *Philosophical Transactions of the Royal Society of London. B, Biological Sciences*, 305(1122):115–144, 1984. URL `http://rstb.royalsocietypublishing.org/content/305/1122/115.short`.

[36] Ellington, C. P. "The Aerodynamics of Hovering Insect Flight. VI. *Lift and Power Requirements*". *Philosophical Transactions of the Royal Society of London. B, Biological Sciences*, 305(1122):145–181, 1984. URL `http://rstb.royalsocietypublishing.org/content/305/1122/145.abstract`.

[37] Ellington, C. P. "The novel aerodynamics of insect flight: applications to micro-air vehicles". *Journal of Experimental Biology*, 202(23):3439–3448, 12 1999. URL `http://jeb.biologists.org/content/202/23/3439.abstract`.

[38] Ellington, Charles P., Coen Van Den Berg, Alexander P. Willmott, and Adrian L. Thomas. "Leading-edge Vortices in Insect Flight". *Nature*, 384(6610):626–630, 12 1996. URL `http://dx.doi.org/10.1038/384626a0`.

[39] Finio, B.M., J.K. Shang, and R.J. Wood. "Body torque modulation for a microrobotic fly". *Robotics and Automation, 2009. ICRA '09. IEEE International Conference on*, 3449 –3456. Mayay 2009. ISSN 1050-4729.

[40] Franklin, Benjamin. "Preface To The First Publishing of the Society". *Transactions of the American Philosophical Society*, 1:i–xix, 01 1769. URL `http://www.jstor.org/stable/1004999`.

289

[41] Hirsch, Charles. *Numerical Computation of Internal & External Flows—The Fundamentals of Computational Fluid Dynamics*. Butterworth-Heinemann, The Boulevard, Langford Lane, Kidlington, Oxford, OX5 1GB, 2nd edition, 2007.

[42] Hollenbeck, Alex and Anthony Palazotto. "Methods Used to Evaluate the Hawkmoth *Manduca Sexta* as a Flapping-Wing Micro Air Vehicle". *International Journal of Micro Air Vehicles*, 4(2):119–132, 06 2012. URL `http://dx.doi.org/10.1260/1756-8293.4.2.119`.

[43] Hollenbeck, Alex C. *Evaluation of the Thorax of the Manduca Sexta for Flapping Wing Micro Air Vehicle Applications*. Thesis, Air Force Institute of Technology, 2950 Hobson Way, WPAFB, OH 45433, March 2011.

[44] Huber, Arthur F. *Death By A Thousand Cuts: Micro Air Vehicles In the Service of Air Force Missions*. Occasional Paper No. 29, Air War College, 325 Chennault Circle, Maxwell AFB, AL, 36112, July 2002.

[45] Joint Chiefs of Staff. "*Joint Vision 2020*". Government Printing Office, June 2000. URL `http://www.dtic.mil/jv2020`.

[46] Jordan, T., Z. Ounaies, J. Tripp, and P. Tcheng. "Electrical Properties and Power Considerations of a Piezoelectric Actuator". *Proceedings of the MRS fall meetings*, volume 604, 203–210. Materials Research Society, Cambridge University Press, 1999.

[47] Jr., John D. Anderson. *Fundamentals of Aerodynamics*. Mcgraw Hill Series in Aeronautical and Aerospace Engineering. McGraw-Hill Science, 5th edition, February 2012.

[48] von Kármán, Theodore. *Phrophecy Fulfilled: "Toward New Horizons"–and It's Legacy–Science, the Key to Air Supremacy*. AAF Technical Report #1, AAF Scientific Advisory Group, 25 Washington DC, 1945.

[49] Keuthe, Arnold M. and Chuen-Yen Chow. *Foundations of Aerodynamics–Bases of Aerodynamic Design*. John Wiley and Sons, Inc., 111 River Street, Hoboken, NJ 07030, 5th edition, 1998.

[50] Khan, Z.A. and S.K. Agrawal. "Force and moment characterization of flapping wings for micro air vehicle application". *Proceedings of the American Control Conference, Portland, Oregon.*, volume 3, 1515 – 1520. June 2005. ISSN 0743-1619.

[51] Khan, Z.A. and S.K. Agrawal. "Optimal Hovering Kinematics of Flapping Wings for Micro Air Vehicles". *AIAA Journal*, 49:257–268, February 2011.

[52] Lehmann, Fritz-Olaf, Sanjay P. Sane, and Michael Dickinson. "The aerodynamic effects of wing–wing interaction in flapping insect wings". *Journal of Experimental Biology*, 208(16):3075–3092, August 2005. URL http://jeb.biologists.org/content/208/16/3075.abstract.

[53] Liu, H, C Ellington, K Kawachi, and c. "A computational fluid dynamic study of hawkmoth hovering". *Journal of Experimental Biology*, 201(4):461–477, 02 1998. URL http://jeb.biologists.org/content/201/4/461.abstract.

[54] Madangopal, Rajkiran, Zaeem Khan, and Sunil Agrawal. "Biologically Inspired Design Of Small Flapping Wing Air Vehicles Using Four-Bar Mechanisms And Quasi-steady Aerodynamics". *Journal of Mechanical Design*, 127(4):809–816, 2005. URL http://dx.doi.org/10.1115/1.1899690.

[55] Massey, Kevin, Ashley Flick, and Gautam Jadhav. "Force Measurements and Flow Visualization for a Flexible Flapping Wing Mechanism". *International Journal of Micro Air Vehicles*, 1(3):183–202, 11 2009. URL http://dx.doi.org/10.1260/175682909789996168.

[56] Maybury, Will J. and Fritz-Olaf Lehmann. "The fluid dynamics of flight control by kinematic phase lag variation between two robotic insect wings". *Journal of Experimental Biology*, 207(26):4707–4726, December 2004. URL http://jeb.biologists.org/content/207/26/4707.abstract.

[57] McClung, Aaron M. *Influence of Structural Flexibility On Flapping Wing Propulsion*. Dissertation, Air Force Institute of Technology, 2950 Hobson Way, WPAFB, OH 45433, June 2009.

[58] McMichael, James M. and Michael S. Francis *(Col. Ret.)* . *Micro Air Vehicles– Toward a New Dimension in Flight*. Technical report, Defense Advanced Projects Research Agency, 675 North Randolph Street, Arlington, Va, 22203-2114, August 1997.

[59] Mises, Richard Von. *Theory of Flight*. Dover Publishing Inc., 31 East 2nd Street, Mineola, NY, 11501, 1959.

[60] Muelller, Thomas J. "An Overview of Micro Air Vehicle Aerodynamics". Thomas J. Muelller and Paul Zarchan (editors), *Fixed and Flapping Wing Aerodynamics for Micro Air Vehicle Applications*, volume 195 of *Progress in Astronautics and Aeronautics*, 574. AIAA, American Institute of Aeronautics and Astronautics, 1801 Alexander Bell Drive, Suite 500, Reston, VA, 20191-4344, USA,, July 2001.

[61] Nakata, T., H. Liu, Y. Tanaka, N. Nishihashi, X. Wang, and A Sato. "Aerodynamics of a bio-inspired flexible flapping-wing micro air vehicle". *Bioinspiration & Biomimetics*, 6(4), December 2011. ISSN 1748-3182. URL http://dx.doi.org/10.1088/1748-3182/6/4/045002.

[62] Normayati Nordin, Vijay R. Raghavan, Safiah Othman and Zainal Ambri Abdul Karim. "Verification of 3-D Stereoscopic PIV Operation Verification of 3-D Stereoscopic PIV Operation and Procedures". *Internation Journal of Engineering & Technology 125804-9595-IJET-IJENS*, 12(04):8, August 2012.

[63] Norris, Aaron G. *Experimental characterization of the structural dynamics and aero-structural sensitivity of a hawkmoth wing toward the development of design rules for flapping-wing micro air vehicles.* Dissertation, Air Force Institute of Technology, 2950 Hobson Way, WPAFB, OH 45433, 2013.

[64] O'Hara, R., N. DeLeon, and A. Palazotto. "Structural Identification and Simulation of the Manduca Sexta Forewing". *AIAA 52nd Structural Dynamics and Modeling Conference, Denver, Colorado*, 4-7 April 2011.

[65] O'Hara, R P and A N Palazotto. "The morphological characterization of the forewing of the *Manduca Sexta* species for the application of biomimetic flapping wing micro air vehicles." *Bioinspir Biomim*, 7(4):046011, December 2012. ISSN 1748-3190 (Electronic); 1748-3182 (Linking).

[66] O'Hara, Ryan P. *The Characterization of Material Properties and Structural Dynamics of the Manduca Sexta Forewing for Application to Flapping Wing Micro Air Vehicle Design.* Dissertation, Air Force Institute of Technology, 2950 Hobson Way, WPAFB, OH 45433, September 2012.

[67] O'Hara, Ryan P. *The Material Property and Structural Dynamic Characteristics of the Manduca Sexta Forewing for Application to Flapping Micro Air Vehicle Design.* Prospectus, Air Force Institute of Technology, 2950 Hobson Way, WPAFB, OH 45433, December 2012.

[68] OpenCV development team. "OpenCV 2.4.6.0 documentation (OpenCV tutorial.image processing.canny)", July 2011. URL http://docs.opencv.org/doc/tutorials/imgproc/imgtrans/canny_detector/canny_detector.html.

[69] Patil, M. J. "From Fluttering Wings To Flapping Flight... *The Energy Connection*". *42nd AIAA ASME/ASCE/AHS/ASC Structures, Structural Dynamics and Materials Conference & Exhibit*, (AIAA-2001-1460), 13-17 April 2001.

[70] Pope, Alan. *Basic Wing and Airfoil Theory.* McGraw-Hill, 31 East 2nd Street, Mineola, NY, 11501, 1951.

[71] Sane, Sanjay P. "The aerodynamics of insect flight". *Journal of Experimental Biology*, 206(23):4191–4208, 12 2003. URL http://jeb.biologists.org/content/206/23/4191.abstract.

[72] Sane, Sanjay P. "Induced airflow in flying insects I. *A theoretical model of the induced flow*". *Journal of Experimental Biology*, 209(1):32–42, Janurary 2006. URL http://jeb.biologists.org/content/209/1/32.abstract.

[73] Sane, Sanjay P. and Michael H. Dickinson. "The control of flight force by a flapping wing: lift and drag production". *Journal of Experimental Biology*, 204(15):2607–2626, 08 2001. URL `http://jeb.biologists.org/content/204/15/2607.abstract`.

[74] Sane, Sanjay P. and Michael H. Dickinson. "The aerodynamic effects of wing rotation and a revised quasi-steady model of flapping flight". *Journal of Experimental Biology*, 205(8):1087–1096, 04 2002. URL `http://jeb.biologists.org/content/205/8/1087.abstract`.

[75] Sane, Sanjay P. and Nathaniel P. Jacobson. "Induced airflow in flying insects II. *Measurement of induced flow*". *Journal of Experimental Biology*, 209(1):43–56, Janurary 2006. URL `http://jeb.biologists.org/content/209/1/43.abstract`.

[76] Shyy, Wei, Patrick Trizila, Chang kwon Kang, and Hikaru Aono. "Can Tip Vortices Enhance Lift of a Flapping Wing?" *AIAA Journal 0001-1452*, Volume 47(2):(289–293), 2009.

[77] Sigthorsson, David O., Michael W. Oppenheimer, and David B. Doman. "Flapping Wing Micro Air Vehicle Aerodynamic Modeling Including Flapping and Rigid Body Velocity". *50th AIAA Aerospace Sciences Meeting including the New Horizons Forum and Aerospace Exposition, Nashville, Tennessee*, (AIAA-2012-26), Jan. 9-12 2012.

[78] Singh, B., M. Ramasamy, I. Chopra, and J. G. Leishman. "Experimental studies on insect-based flapping wings for micro hovering air vehicles". *AIAA*, 20742, 2004.

[79] Sladek, Nathanael, Michael Anderson, and Richard Cobb. "Aero and Structural-dynamic Repeatability of a Novel MAV Wing Manufacturing Process". *AIAA Atmospheric Flight Mechanics Conference, Portland, Oregon*, (AIAA-2011-6393):978–990, August 8-11, 2011.

[80] Sladek, Nathanael J. *Flapping Wing Micro Air Vehicle Wing Manufacture and Force Testing*. Thesis, Air Force Institute of Technology, 2950 Hobson Way, WPAFB, OH 45433, March 2011.

[81] Stepniweski, W.Z. and C.N. Keys. *Rotary-Wing Aerodynamics*, volume I & II. Dover Publishing Inc., 31 East 2nd Street, Mineola, NY, 11501, 2nd edition, 1984.

[82] Svanberg, Craig E. *Biomimetic Micro Air Vehicle Testing Development and Small Scale Flapping-Wing Analysis*. Master's thesis, Air Force Institute of Technology, 2950 Hobson Way, WPAFB, OH 45433, March 2008.

[83] Tannehill, John C., Dale A. Anderson, and Richard H. Pletcher. *Computational Fluid Mechanics and Heat Transfer*. Series in Computational and Physical Processes in Mechanics and Thermal Sciences. Taylor & Francis, 325 Chestnut Street, Suite 800, Philadelphia, PA 19106, 2nd edition, 1997.

[84] Usherwood, JR and CP Ellington. "The aerodynamics of revolving wings I. *Model hawkmoth wings*". *The Journal of experimental biology*, 205(Part 11):1547–1563, June 2002. URL `http://ukpmc.ac.uk/abstract/MED/12000800`.

[85] Van Den Berg, Coen and Charles P. Ellington. "The three-dimensional leading-edge vortex of a 'hovering' model hawkmoth". *Philosophical Transactions of the Royal Society of London. Series B: Biological Sciences*, 352(1351):329–340, 03 1997. URL `http://rstb.royalsocietypublishing.org/content/352/1351/329.abstract`.

[86] Van Den Berg, Coen and Charles P. Ellington. "The vortex wake of a 'hovering' model hawkmoth". *Philosophical Transactions of the Royal Society of London. Series B: Biological Sciences*, 352(1351):317–328, 03 1997. URL `http://rstb.royalsocietypublishing.org/content/352/1351/317.abstract`.

[87] Wang, Z. J. "Dissecting Insect Flight". *Annual Review of Fluid Mechanics*, 37:183–210, January 2005.

[88] White, Frank M. *Viscous Fluid Flow*. Number 2 in McGraw-Hill series in mechanical engineering. McGraw-Hill, 2nd edition, 1991. ISBN 9780070697126. URL `http://books.google.com/books?id=G6IeAQAAIAAJ`.

[89] Whitney, J.P. and R. J. Wood. "Aeromechanics of Passive Rotation in Flapping Flight". *Journal of Fluid Mechanics*, 660:197–220, 27 July 2010.

[90] Whitney, JP and RJ Wood. "Conceptual design of flapping-wing micro air vehicles". *Bioinspiration & Biomimetics*, 7(3):036001, 09 2012. URL `http://dx.doi.org/10.1088/1748-3182/7/3/036001`.

[91] Willmott, A P and C P Ellington. "The mechanics of flight in the hawkmoth Manduca sexta. I. *Kinematics of hovering and forward flight*". *Journal of Experimental Biology*, 200(21):2705–2722, 11 1997. URL `http://jeb.biologists.org/content/200/21/2705.abstract`.

[92] Willmott, A P and C P Ellington. "The mechanics of flight in the hawkmoth Manduca sexta. II. *Aerodynamic consequences of kinematic and morphological variation*". *Journal of Experimental Biology*, 200(21):2723–2745, November 1997. URL `http://jeb.biologists.org/content/200/21/2723.abstract`.

[93] Willmott, Alexander P., Charles P. Ellington, and Adrian L. Thomas. "Flow visualization and unsteady aerodynamics in the flight of the hawkmoth, Manduca sexta". *Philosophical Transactions of the Royal Society of London. Se-*

ries B: Biological Sciences, 352(1351):303–316, 1997. URL `http://rstb.royalsocietypublishing.org/content/352/1351/303.abstract`.

[94] Wood, R.J. "Design, fabrication, and analysis of a 3DOF, 3cm flapping-wing MAV". *Proceedings of the 2007 IEEE/RSJ International Conference on Intelligent Robots and Systems San Diego, CA*, 1576 –1581, Oct 29-Nov 2 2007.

[95] Wood, R.J. "The First Takeoff of a Biologically Inspired At-Scale Robotic Insect". *Robotics, IEEE Transactions on*, 24(2):341 –347, april 2008. ISSN 1552-3098.

[96] Wood, R.J., E. Steltz, and R.S. Fearing. "Optimal Energy Density Piezo-electric Bending Actuators". *Elsevier*, 119:476–488, 2005.

[97] Zivkovic, Z. "Improved adaptive Gaussian mixture model for background subtraction". *Pattern Recognition, 2004. ICPR 2004. Proceedings of the 17th International Conference on*, volume 2, 28 – 31 Vol.2. aug. 2004. ISSN 1051-4651.

Vita

Lieutenant Colonel DeLuca was born in Detroit, Michigan. He graduated from Henry For II high school in 1991, and attended the United States Military Academy at West Point the following year. He graduated from West Point in 1995 with a Bachelor's of Science in Mechanical Engineering, and was commissioned as a Lieutenant in the Air Force immediately thereafter.

In his professional career he has had numerous assignments across the Air Force, including a joint assignment in the Defense Intelligence Agency, and as a Commander at Eielson AFB, AK. He holds three Master's Degrees: A Masters of Business of Administration & Technology Management from the Albuquerque Campus of the University of Phoenix; a Masters of Science in Aeronautical Engineering from the Air Force Institute of Technology, and a Masters in Military Science from American Military University. He is a graduate of the National Test Pilot school, Squadron Office school, Air Command and Staff school, and the US Army Airborne and Air Assault schools. He was named the Kirtland Air Force Base 1998 Company Grade Officer of the year.

Lt Col DeLuca married a wonderful woman in 2002 and together they have a six year old son. Following graduation, Lt Col DeLuca will remain at the Air Force Institute Technology as part of the military faculty in the Department of Aeronautics and Astronautics.

REPORT DOCUMENTATION PAGE

1. REPORT DATE (DD–MM–YYYY)	2. REPORT TYPE	3. DATES COVERED (From — To)
13-09-2013	Dissertation	09-2010 - 13-09-2013

4. TITLE AND SUBTITLE

Aerodynamic Performance and Particle Image Velocimetery of Piezo Actuated Biomimetic *Manduca Sexta* Engineered Wings Towards the Design and Application of a Flapping Wing Flight Vehicle.

5a. CONTRACT NUMBER

5b. GRANT NUMBER

5c. PROGRAM ELEMENT NUMBER

6. AUTHOR(S)

DeLuca, Anthony, M, Lieutenant Colonel

5d. PROJECT NUMBER

11Y188

5e. TASK NUMBER

5f. WORK UNIT NUMBER

7. PERFORMING ORGANIZATION NAME(S) AND ADDRESS(ES)

Air Force Institute of Technology
Graduate School of Engineering and Management (AFIT/EN)
2950 Hobson Way
Wright-Patterson AFB, OH, 45433-7765

8. PERFORMING ORGANIZATION REPORT NUMBER

AFIT-ENY-DS-13-D-01

9. SPONSORING / MONITORING AGENCY NAME(S) AND ADDRESS(ES)

Dr. Gregory Parker
Air Force Research Laboratory
2145 5TH ST
B20024C R220
WPAFB, OH 45433
Gregory.Parker@wpafb.mil

10. SPONSOR/MONITOR'S ACRONYM(S)

AFRL/RBAA

11. SPONSOR/MONITOR'S REPORT NUMBER(S)

12. DISTRIBUTION / AVAILABILITY STATEMENT

13. SUPPLEMENTARY NOTES   This material is declared a work of the U.S. Government and is not subject to copyright protection in the United States.

14. ABSTRACT

Considerable research and investigation has been conducted on the aerodynamic performance, and the predominate flow physics of the *Manduca Sexta* size of biomimetically designed and fabricated wings as part of the AFIT FWMAV design project. Despite a burgeoning interest and research into the diverse field of flapping wing flight and biomimicry, the aerodynamics of flapping wing flight remains a nebulous field of science with considerable variance into the theoretical abstractions surrounding aerodynamic mechanisms responsible for aerial performance. Traditional FWMAV flight models assume a form of a quasi-steady approximation of wing aerodynamics based on an infinite wing element model (BEM). An accurate estimation of the lift, drag, and side force coefficients is a critical component of autonomous stability and control models. This research focused on two separate experimental avenues into the aerodynamics of AFIT's engineered hawkmoth wings---forces and flow visualization.

15. SUBJECT TERMS

micro air vehicles, flapping wing aerodynamics, Manduca Sexta, biomimetic wing design, fluid mechanics of flapping flight, Particle Image Velocimetry, PIV, lift and drag of flapping wings, stereoscopic velocity measurements, FWMAV, PIV, piezoelectric actuators

16. SECURITY CLASSIFICATION OF:			17. LIMITATION OF ABSTRACT	18. NUMBER OF PAGES	19a. NAME OF RESPONSIBLE PERSON
a. REPORT	b. ABSTRACT	c. THIS PAGE	UU	328	Dr. Mark F. Reeder, AFIT/ENY
U	U	U			19b. TELEPHONE NUMBER (Include Area Code) (937) 255-3636 x3065 mark.reeder@afit.edu